

Single Cell Analysis and Tissue Imaging by Laser Ablation and Mass Spectrometry

by Bindesh Shrestha

B.S. in Chemistry, Moravian College, Bethlehem, PA

M.Phil. in Chemistry, The George Washington University, Washington DC

a Dissertation submitted to

the Faculty of
Columbian College of Arts and Sciences
of The George Washington University
in partial satisfaction of the requirements
for the degree of Doctor of Philosophy

January 31, 2010

Dissertation directed by

Akos Vertes
Professor of Chemistry

The Columbian College of Arts and Sciences of The George Washington University certifies that Bindesh Shrestha has passed the Final Examination for the degree of Doctor of Philosophy as of January 12, 2010. This is the final and approved form of the dissertation.

Single Cell Analysis and Tissue Imaging by Laser Ablation and Mass Spectrometry

Bindesh Shrestha

Dissertation Research Committee:

Akos Vertes, Professor of Chemistry, Dissertation Director

John H. Miller, Professor of Chemistry, Committee Member

Cynthia S. Dowd, Assistant Professor of Chemistry, Committee Member

Dedicated to my parents,

Govinda Ram Shrestha and Sharada Shrestha

Acknowledgements

I would like to express my sincere gratitude to my research director, Professor Akos Vertes. I have learned from him how to explore a scientific question, scientifically investigate the problem, analyze the research outcome, and clearly communicate meaningful results. I benefitted from Professor Vertes' insight, guidance, knowledge, organizational aptitude, and communicational skills. Moreover, his curiosity, enthusiasm, and passion to understand nature have provided a lifelong inspiration for me.

Special acknowledgements are due to the members of the examination committee, who took the effort to read my dissertation and improve it by useful suggestions: Professor J. Houston Miller and Professor Cynthia Dowd.

It is a great pleasure to mention colleagues I worked with during my years as a graduate student. I had a fruitful collaboration with Dr. Yue Li, reflected in two publications on atmospheric pressure infrared matrix assisted laser desorption/ionization mass spectrometry. The research efforts with my colleague, Dr. Peter Nemes, on laser ablation electrospray mass spectrometry were very productive as well. I also want to acknowledge other former members of the Vertes' research group for their interest in my work and the exchange of ideas: Dr. Prabhakar Sripadi, Ms. Lida Parvin, Dr. Zhaoyang Chen, Dr. Ioan Marginean, Dr. Yong Chen, and Dr. Guanghong Luo. Recognition is due to the current members of the group with whom I had productive discussions: Mr. Bennett N. Walker, Ms. Jessica A. Stolee, Ms. Jelena Lusic, and Ms. Hehua Huang. I am also grateful to Dr. Javad N. Nazarian of Children's National medical Center in Washington, DC, for his help.

I am indebted to the United States National Science Foundation, the United States Department of Energy, the William Myron Keck Foundation, and the George Washington University for providing the financial support for my graduate work.

Last, but not least, no words of gratitude can sufficiently express my thankfulness to my parents, Mr. Govinda Ram Shrestha and Mrs. Sharada Shrestha, and my younger sister, Bindee Shrestha, who gave me their unconditional love, support and encouragement.

ABSTRACT OF DISSERTATION

Single Cell Analysis and Tissue Imaging by Laser Ablation and Mass Spectrometry

The direct analysis of biochemicals in tissues and single cells is critical for understanding living organisms. Due to excellent selectivity and sensitivity, mass spectrometry (MS) has proven to be an invaluable tool for the analysis of the biomolecules. Recent developments in atmospheric pressure direct ionization sources have enabled the *in situ* analysis of biological samples without external influences (e.g., purification, extraction, matrix addition etc.) that might alter their biochemical makeup. The work presented in this dissertation shows my efforts to utilize two novel atmospheric pressure (AP) direct ionization methodologies, AP infrared (IR) matrix-assisted laser desorption ionization (MALDI) and laser ablation electrospray ionization (LAESI) MS, for metabolomics, tissue imaging and single cell analysis.

Chapter 1 introduces analytical techniques used for the analysis of tissues and single cells. The fundamental aspects of IR laser ablation and its utilization in two direct ionization techniques, AP IR-MALDI and LAESI, are reviewed.

Chapter 2 introduces AP IR-MALDI for MS. It presents proof-of-principle molecular imaging of mock peptide samples at atmospheric pressure. The utility of AP IR-MALDI for plant tissue imaging and metabolomics are also discussed.

Chapter 3 describes the AP IR-MALDI analysis of various pharmaceuticals directly in their commercial formulations, as well as endogenous metabolites, exogenous drug metabolites and synthetic polymers in urine.

Chapter 4 presents the application of mid-infrared laser ablation for molecular imaging. The dynamics of the ablation plume and ion production in AP IR-MALDI and LAESI are compared.

In Chapter 5 metabolites and lipids are identified in mouse brain sections using MS with AP IR-MALDI and LAESI ion production. Reactive LAESI relies on interactions between the laser ablated species and reactants, e.g., Li^+ , introduced through the electrospray. This new modality of LAESI enables the analysis of samples with otherwise low ion yields.

Chapter 6 discusses the metabolic analysis of single cells by MS at atmospheric pressure. This breakthrough is made possible by the tight focusing of mid-IR laser light through an etched optical fiber tip and accurate aiming of cells for ablation through visualization and micromanipulation. Similar to conventional LAESI, the ablated plume is positioned by an electrospray.

Chapter 7 surveys the major challenges in the field of atmospheric pressure ion production based on mid-IR laser ablation. The need for the analysis of smaller cells, reactive LAESI-MS, ultrahigh resolution LAESI-MS, and the potential application of LAESI-MS in laser surgery are discussed.

TABLE OF CONTENTS

Content	Page
Dedication	ii
Acknowledgement	iii
Abstract	vi
Table of Contents	viii
List of Figures	xi
List of Tables	xxiii
Foreword	xxv
Chapter 1. Introduction	1
References	11
Chapter 2. Atmospheric Pressure Molecular Imaging by Infrared MALDI Mass Spectrometry for Plant Metabolomics.....	15
Abstract	15
Introduction	16
Experimental Section	21
Results and discussion	25

	Conclusions	57
	Acknowledgements	59
	References	59
Chapter 3.	Rapid analysis of pharmaceuticals and excreted xenobiotic and endogenous metabolites with atmospheric pressure infrared MALDI mass spectrometry.....	66
	Abstract	66
	Introduction	67
	Experimental Section	69
	Results and discussion	74
	Conclusions	100
	Acknowledgements	101
	References	101
Chapter 4.	Molecular Imaging by Mid-IR Laser Ablation Mass Spectrometry...	107
	Abstract	107
	Introduction	108
	Experimental Section	110
	Results and discussion	114
	Acknowledgements	126
	References	126

Chapter 5	Direct analysis of lipids and small metabolites in mouse brain tissue by AP IR-MALDI and reactive LAESI mass spectrometry	129
	Abstract	129
	Introduction	130
	Experimental Section	133
	Results and discussion	141
	Conclusions	170
	Acknowledgements	171
	References	171
Chapter 6	In Situ Metabolic Profiling of Single Cells by Laser Ablation Electrospray Ionization Mass Spectrometry	178
	Abstract	178
	Introduction	179
	Experimental Section	181
	Results and discussion	188
	Conclusions	208
	Acknowledgements	211
	References	211
Chapter 7.	Future Directions	215
Biography	224

LIST OF FIGURES

Figures	Page
Chapter 1	
Figure 1.1 Absorption coefficient of water made at room temperature ($\sim 20^\circ\text{C}$) in the wavelength range between 200 nm and 200 μm based on the experimental data compiled by Irvine and Pollack in 1968. The arrow shows the absorption coefficient peak at the wavelength of 2940 nm.....	4
Figure 1.2 Bright-field time-resolved images of atmospheric pressure water ablation at 2940 nm wavelength by a Q-switched Er:YAG laser pulse (70 ns pulse duration, 0.12 J/cm ² fluence, and an ablation spot size of 1 mm in diameter) Reprinted with permission by Springer-Verlag from Figure 1a of I. Apitz. and A. Vogel, Material ejection in nanosecond Er:YAG laser ablation of water, liver, and skin, Appl. Phys. A, 81, 2005, 329	6
Chapter 2	
Figure 2.1 (a) Signal-to-noise ratio for potassiated sucrose ions (m/z 381.1) from aqueous matrix using AP IR-MALDI shows ~ 3 fmol/pixel detection limit. Inset shows the marginal signal at m/z 381 and its vicinity in the corresponding mass spectrum. (b) AP IR-MALDI mass spectrum of	

equimolar bradykinin (m/z 1060.4), substance P (m/z 1347.6), and bovine insulin (m/z 5733.5) mixture with DHB as a matrix. Bovine insulin ions are low in abundance and appear as doubly and triply charged species at m/z 2867.2 and 1912.1, respectively..... 26

Figure 2.2 (a) AP IR-MALDI mass spectrum of substance P from DHB matrix based on 10 laser shots. **(b)** Molecular image of the three characters in the word “ION” at m/z 1347.6 corresponding to the substance P molecular ion. The characters were created by a paper mask over the sample surface. The scanning step size and the dwell time were 125 μm and 8 s/pixel, respectively..... 30

Figure 2.3 (a) Left panel: optical image of the electron microscope grid used as a mask to create chemical contrast with 92 μm features (gap width). Right panel: AP IR-MALDI molecular image of toluidine blue O in the exposed areas under the grid based on the m/z 270.1 ion obtained using the “oversampling” method. **(b)** Averaged ion intensity profile perpendicular to the grid bars indicated a lateral resolution of 40 μm 32

Figure 2.4 SEM images of ablation craters created by **(a)** a single and **(b)** six laser pulses of 0.27 (0.03 J/cm² fluence each, impinging on the upper surface of a peace lily plant (*Spathiphyllum*) leaf. After a single laser pulse, the tissue damage is localized to an elliptical area with 180 and 640 μm for the small and large axes, respectively. The top waxy cuticle layer and part of the upper epidermal cells were removed, but no damage to the underlying tissue was apparent. Upon exposure to six laser pulses, the laser crater

became slightly larger (230 μm by 720 μm), and some of the palisade and spongy mesophyll was also removed. 36

Figure 2.5 AP IR-MALDI mass spectra obtained in the positive ion mode from **(a)** the lamina of a cilantro leaf; **(b)** garlic bulb sections that exposed the storage tissue in the expanded leaf bases; **(c)** a segment of a white lily flower petal; and **(d)** sections of the outer wall of the pericarp of a tomato fruit. The inset in panel b shows the tandem mass spectrum of the m/z 175 ion that corresponds to protonated arginine. The isotopic distribution pattern for the m/z 219 ion in the inset of panel d is consistent with the presence of potassium..... 39

Figure 2.6 AP IR-MALDI mass spectra collected from the longitudinal section of an almond kernel for **(a)** low fluence (1.7 J/cm²) and **(b)** high fluence (3.3 J/cm²) exposures. The top inset in panel a shows triacylglycerol lipid distributions TG(52:4) to TG(52:2) and TG(54:6) to TG(54:3). The bottom inset in panel a zooms in on the potassiated dimers from these lipids. The inset in panel b indicates the formation of lipid trimers at elevated fluences..... 41

Figure 2.7 AP IR-MALDI mass spectra obtained in the negative ion mode for **(a)** the storage tissue in the outer medulla section of potato tubers, **(b)** onion storage leaf; **(c)** a segment of a white lily flower petal, and **(d)** a longitudinal section of an almond kernel. The insets in panels a and c are the tandem mass spectra of the ions with m/z 133 and 145 that are identified as malic acid and R-ketoglutaric acid, respectively. The inset in

panel d depicts the zoomed triacylglycerol lipid distributions starting from TG(54:6)..... 43

Figure 2.8 Optical image of a strawberry skin (top left) compared to AP IR-MALDI images for three major components, sucrose (top right), glucose/fructose (bottom right), and citric acid (bottom left) around embedded seeds. The false color intensities were assigned according to integrated areas of the associated potassium peaks. Although the distributions of these water-soluble components are similar, the position of the two seeds, with lower concentrations of these compounds, is clearly discernible 51

Figure 2.9 (a) Comparison of the tandem mass spectra of the nominal m/z 270 ion observed in the AP IR-MALDI mass spectra of toluidine blue O dye solution (left panel) and white lily flower petal after 48 h (right panel). **(b)** Optical and AP IR-MALDI images of the white lily flower petal section stained in the fluid transport experiment. Spatial distributions of GABA, glutamine, hexose sugars, toluidine blue O, and sucrose in the petal show a higher concentration of nutrients and metabolites in the vasculature..... 55

Chapter 3

Figure 3.1 Signal-to-noise ratio for pseudoephedrine ions as a function of the analyte amount in the ablated volume. The limit of detection (LOD) of AP IR-MALDI for aqueous solutions of pseudoephedrine was in the sub-

femtomole range. The inset shows the mass spectrum of pseudoephedrine at its detection limit 72

Figure 3.2 Sodiated sucrose ion was used as an internal standard to construct a calibration curve for fructose in water using AP IR-MALDI. The amount of fructose in a sample was determined with ~12% accuracy (solid circle)..... 76

Figure 3.3 Single scan mass spectrum of a generic cough medicine formulated as a gelatin capsule acquired in 1 second (10 laser shots). It demonstrates the possibility of using AP IR-MALDI for the high-throughput analysis of pharmaceuticals. The molecular ions of all active ingredients (acetaminophen, dextromethorphan, guaifenesin and pseudoephedrine) as well as the oligomers of an excipient (polyethylene glycol) were detected in the mass spectrum. In the inset, the isotope distribution was revealed by zooming in on the dextromethorphan molecular ion (m/z 272.2036)..... 79

Figure 3.4 Typical averaged mass spectra of 3 μ l of the urine sample collected **(a)** 2.5 h after drug ingestion clearly shows the molecular ion for unmetabolized pseudoephedrine in the urine as well as peaks related to an excipient, polyethylene glycol (PEG). In the inset the accuracy of the mass measurement, Δm , in mDa units for the metabolites in urine as a function of the theoretical m/z value indicates that most species are detected within 20 mDa of the theoretical m/z value. Panels (b), (c) and (d) show the mass

spectrum in the vicinity of the protonated pseudoephedrine molecule before and 2.5 h and 24 h following the ingestion of the drug, respectively.. 86

Figure 3.5 Fragmentation pattern of the nominal m/z 166 ion was obtained by collision activated dissociation to confirm structure of the corresponding metabolite in urine. Tandem mass spectrum of the nominal m/z 166 ion is presented in panel **(a)** from urine 2.5 h after the ingestion of the pseudoephedrine containing drug. It produced identical fragments as the tandem mass spectra of **(b)** pure pseudoephedrine analyte and **(c)** pseudoephedrine in the ingested medicine. Similar strategy can be applied to confirm the structure of each unknown metabolite detected in the urine.. 96

Chapter 4

Figure 4.1 Schematics of two atmospheric pressure IR laser ablation systems used in biomedical analysis based on **(a)** AP IR-MALDI and **(b)** LAESI configuration. System components include C - capillary; SP - syringe pump; HV - high-voltage power supply; M - mirror; FL - focusing lens; CE - counter electrode; OSC - digital oscilloscope; SH - sample holder; X-Y-Z - motorized micropositioning system; mid-IR laser - Nd:YAG laser driven OPO or Er:YAG laser; MS - mass spectrometer; and DA – data acquisition system 111

Figure 4.2 (a) Relative ion intensities in AP IR-MALDI as a function of sampling orifice distance from the surface and in LAESI as a function of the position where the spray axis intercepts the laser ablation plume. **(b)** Plume number density distributions for 1.4 J/cm² Er:YAG laser ablation of water into 1 atm nitrogen gas at 800 ns. The expanding plume distribution (solid line) shows a high density region close to the shock front and the pile-up of background gas (dashed line) in front of the interface..... 115

Figure 4.3 AP IR-MALDI imaging of mock pattern produced by pencil on paper. The optical image (top left) shows the letters “IR” before rastering the surface with the laser. Chemical image (top right) constructed from the intensity of m/z 365 ions as a function of position on the surface. A typical mass spectrum is shown in the bottom panel. The ions m/z 365 and 381 correspond to a sodiated and a potassiated disaccharide, respectively 120

Figure 4.4 Imaging of a mock pattern produced on an Easter lily (*Lilium longiflorum*) leaf by red (vertical line) and blue (horizontal line) permanent markers. Optical images show the marked leaf section before (left panel) and after (right panel) LAESI imaging. LAESI images for the dye cations indicate a vertical line for the m/z 443 species (Rhodamine 6G in the red marker) (top middle panel) and a horizontal line for the m/z 478 species (Basic Blue 7 in the blue marker) (bottom middle panel) 123

Chapter 5

Figure 5.1 Schematics of AP IR-MALDI and LAESI-MS. Pulses from the mid-IR Nd-YAG laser-driven OPO is focused onto the brain tissue sample (S) mounted on a Peltier stage (PS) using Au-coated mirrors (M) and a CaF₂ lens (L) generating the infrared ablation products (red dots). **(a)** In AP IR-MALDI, ions from the infrared ablation plume are directly sampled into the mass spectrometer (MS) with the help of pulsed high voltage (HV) produced by a pulse generator (PG) and timed by a delay generator (DG). **(b)** In LAESI-MS, the neutrals in the ablation plume are intercepted by the electrospray plume (black dots) and post-ionized to form ions (green dots), which are sampled by the MS. The electrospray is created by applying a high voltage (HV) to the emitter (E) capillary at a constant flow rate controlled by a syringe pump (SP) 136

Figure 5.2 Ambient mass spectra of PC (18:1/18:1) synthetic model lipid by **(a)** AP IR-MALDI and **(b)** LAESI indicate softer ion generation via the latter method. The inset in panel (a) shows the lipid fragmentation through the loss of the phosphocholine headgroup in AP IR-MALDI 139

Figure 5.3 Positive ion AP IR-MALDI mass spectrum from a transverse section of mouse brain cerebrum. Endogenous metabolite ions are observed in the $m/z < 400$ range. The spectrum was dominated by potassiumated and sodiumated phospholipids in the $m/z > 700$ range. The cholesterol was detected in its alkalinated form or after a water loss 143

Figure 5.4 Positive ion LAESI mass spectrum recorded from a transverse 145

section of mouse brain cerebrum. Phosphocholine, at m/z 184.0654, also found in the polar headgroup of PCs, was the base peak in the spectrum. Endogenous metabolite ions from the brain were observed in the $m/z < 400$ range and the $m/z > 700$ region revealed the presence of various protonated phospholipids

Figure 5.5 (a) Tandem MS of the protonated PC (18:1/18:1) generated by LAESI produced a single fragment.. **(b)** Tandem MS of the lithiated PC(18:1/18:1) generated by reactive LAESI produced structure-specific fragments 157

Figure 5.6 Reactive LAESI experiments facilitated the structural elucidation of several lipid species. Some of the ablated lipid molecules were converted into lithium adducts upon coalescence with electrospayed droplets seeded with Li^+ ions (see panel a). These lithiated lipid ions readily fragmented by collision-activated dissociation yielding fragments characteristic of the parent ion. For example in panel b, the ion measured at m/z 766.5912 produced fragment ions at m/z 707.5248, 583.5308, and 577.5198, corresponding to the loss of the trimethylamine $[\text{N}(\text{CH}_3)_3, \Delta m$ 59.0735], phosphocholine $[\text{C}_5\text{H}_{14}\text{NO}_4\text{P}, \Delta m$ 183.0660], and lithiated phosphocholine $[\text{C}_5\text{H}_{13}\text{NO}_4\text{PLi}, \Delta m/z$ 189.0742], respectively. Other fragment ions, including those registered at m/z 510.3568 and 484.3512 were formed through the neutral loss of palmitic acid (16:0) and oleic acid (18:1), respectively. This fragmentation pattern was consistent with the

CAD fragmentation of the PC(16:0/18:1)+Li ⁺ lipid ion	160
Figure 5.7 LAESI mass spectra of a solution containing PC(16:0), PE(18:1/16:0), PC(18:1/16:0), and PC(18:1/18:1) at equimolar concentration shows that differences in glycerophospholipid ionization efficiencies depend on the structure of their headgroups and on the length and degree of saturation of their acyl chains	166
Figure 5.8 Ion count ratio for deuterated PC(d-31)(34:1) and PC(32:0) expressed as $I(m/z\ 790)/I(m/z\ 734)$ vs. PC(d-31)(34:1) concentration in the mouse brain tissue. The inset shows the relevant part of the LAESI spectrum of the tissue spiked with PC(d-31)(34:1)	168

Chapter 6

Figure 6.1 Schematics of instrumental setup for single cell analysis by LAESI-MS. The mid-IR ablation products (red dots) generated by the etched optical fiber tip (F) are intercepted by the electrospray plume (black dots) and positioned to form ions (green dots) sampled by the mass spectrometer (MS). A long-distance video microscope (fiber monitor, FMM) is utilized to maintain constant distance between the fiber tip and the sample surface (S). The sample is placed on a 3-axis translation stage (TS), and a second video microscope (cell spotting microscope, CSM) is used to target the cells. The electrospray is produced by applying high voltage (HV) to the capillary emitter (E) and by maintaining constant solution flow rate by a syringe pump (SP). Pulses from the mid-IR OPO

are coupled to the optical fiber, adjusted by a fiber chuck (C) and a 5-axis fiber mount (FM), using two Au-coated mirrors (M) and a CaF₂ lens (L) ... 183

Figure 6.2 (a) Etched optical fiber tip and the raised surface of turgid epidermal cells of *A. cepa* were ~30 μm apart. For optimum coupling of the laser energy, this distance was similar to the diameter of the tip. Further removal of the fiber tip from the cell surface resulted in no ablation, whereas closer approach often led to damage to the cell or the fiber tip. **(b)** Cell targeting for ablation was carried out by adjusting the lateral position of the fiber tip over the selected turgid cell in the tissue 189

Figure 6.3 Single cell ablation marks on epidermal cell of **(a)** *A. cepa* (unpigmented cell) and **(c)** *N. pseudonarcissus* produced through an etched optical fiber tip. In panel **(a)** the first ablation (marked A) was performed on a turgid cell, whereas the second ablation (marked B) occurred after the loss of cytoplasm when the cell became flaccid. Panels **(b)** and **(d)** show the corresponding LAESI mass spectra produced by 100 laser pulses for *A. cepa* and *N. pseudonarcissus*, respectively. The inset in panel **(b)** depicts the eight fragments in the tandem MS of the nominal m/z 175 ion produced by CAD. The inset in panel **(d)** shows the zoomed portion of the daffodil spectrum at higher m/z 192

Figure 6.4 Positive ion LAESI mass spectrum of a single sea urchin (*L. pictus*) egg of ~100 μm in diameter. The inset shows the sessile egg immobilized by the holding pipette and touched by the sharpened optical

fiber	195
Figure 6.5 Single cell LAESI mass spectra of neighboring (a) colorless and (b) pigmented epidermal cells of the purple <i>A. cepa</i> cultivar with the optical image of the cells in the inset	205

Chapter 7

Figure 7.1 (a) Optical micrograph of epidermal tissue from purple cultivar of <i>A. Cepa</i> showing colorless and pigmented cells. (b) Cell-by-cell chemical image based on the intensity of protonated quercetin at nominal m/z 303 superimposed on the microscope image	218
--	-----

LIST OF TABLES

Tables	Page
Chapter 3	
Table 3.1 Comparison of measured and calculated monoisotopic m/z values for the analyzed active ingredients	83
Table 3.2 Suggested identification of the metabolites detected in the positive ion mass spectra of normal human urine	89
Table 3.3 Suggested identification of metabolites detected in the negative ion mass spectrum of normal human urine.....	93
Chapter 5	
Table 5.1 Tentative peak assignments for ions in the AP IR-MALDI mass spectrum of normal mouse brain tissue	147
Table 5.2 Tentative peak assignments for ions in the LAESI mass spectrum of normal mouse brain tissue	150
Table 5.3 Mass accuracy of fragment ions produced by CAD of lithiated DOPC generated by reactive LAESI	163

Chapter 6

Table 6.1 Tentative peak assignments in the mass spectrum of a single unpigmented epidermal cell from <i>A. cepa</i> bulb	199
Table 6.2 Tentative peak assignments in the mass spectrum of a single epidermal cell from <i>N. pseudonarcissus</i> bulb	201
Table 6.3 Comparative list of tentative peak assignments for the LAESI mass spectra of the colorless and pigmented cells in the onion bulb epidermis. The purple background in the table indicates ions found exclusively in the pigmented cells	203
Table 6.4 Relative ion intensities for some metabolites in single cells of an <i>A. cepa</i> bulb averaged for four cells	209

FOREWORD

The understanding of nature comes through the development of new analytical tools and the new insight they bring. Humanity has been probing the nature of “matter” since antiquity. The notion of four elemental substances—earth, air, fire and water—had been accepted until Boyle dispelled it based on observations with the analytical tools of his time.¹ The development of the mass spectrometer by Joseph John Thomson and his student Francis William Aston, approximately a century ago, commenced a way to investigate the nature of matter by analyzing its ions.^{2, 3}

REFERENCES

- (1) Boyle, R. *The Sceptical Chymist*: London, 1661.
- (2) *Nobel Lectures, Physics 1901-1921*; Elsevier Publishing Company: Amsterdam, 1967.
- (3) *Nobel Lectures, Chemistry 1922-1941*; Elsevier Publishing Company: Amsterdam, 1966.

CHAPTER 1

INTRODUCTION

Chemical analysis of metabolites directly from biological tissues and single cells is critical in the understanding of living organisms. The analysis of the metabolome complements genomics and proteomics analysis by elucidating biochemical pathways for small molecules in organisms.¹⁻³ Based on current genomic, biochemical, and physiological knowledge, the number of metabolites range from 584 in *Saccharomyces cerevisiae* to ~200,000 in the plant kingdom.^{4,5} An initial study of the human metabolome suggests even higher diversity and complexity.

A robust chemical analysis tool capable of sensitive, selective, high throughput and direct analysis is desired for metabolomics, the emerging field of the systematic study of all metabolites in an organism. Many techniques, such as infrared spectroscopy, Raman spectroscopy, fluorescence spectrometry and nuclear magnetic resonance, provide useful and complementary information on the chemical composition of tissues.⁶⁻⁸

Mass spectrometry can be used to study the biomolecules in tissues and cells by analyzing the mass-to-charge ratios (m/z) of the related ions with high sensitivity and selectively.⁹ Molecular weight analysis of a biomolecule by mass spectrometry requires an intact ion. Until the introduction of two soft ionization techniques, electrospray ionization (ESI) and matrix-assisted laser desorption ionization (MALDI), ionization of a biomolecule without fragmentation presented a major challenge.¹⁰⁻¹² In recognition of

the breakthrough achievements enabled by these techniques, "*for their development of soft desorption ionization methods for mass spectrometric analyses of biological macromolecules*" the Nobel Foundation awarded the 2002 Nobel Prize in chemistry to John Bennett Fenn and Koichi Tanaka.

ESI mass spectrometry (MS) enables the analysis of large biomolecules through the production of multiply charged ions.¹⁰ However, as a liquid phase technique, ESI requires the solubilization of the sample. MALDI-MS has also been used as a tool for the analysis of thermally labile biomolecules. However, the analysis of small molecules, such as metabolites, was often limited due to interferences from the applied organic matrix ions.

In 1999 Siuzdak *et al.* introduced a matrix-free soft laser desorption method called desorption ionization on silicon (DIOS).¹³ DIOS and other matrix-free laser ionization platforms, such as laser-induced silicon micro-column arrays (LISMA), have successfully demonstrated the analysis of biomolecules by MS without the addition of an external matrix.¹⁴

Conventionally, MALDI ionization is performed in vacuum with an ultraviolet (UV) laser at 337 nm (nitrogen laser) or at 355 nm (frequency tripled Nd:YAG laser) wavelengths. Hillenkamp *et al.* demonstrated the use of infrared (IR) MALDI to produce intact ions of large molecules by using ice as a matrix.¹⁵ Due to the lack of affordable and stable mid-IR lasers, IR-MALDI did not offer unique advantages over the UV version until the development of atmospheric pressure (AP) MALDI by Laiko and coworkers.¹⁶ With the introduction of AP MALDI, IR excitation became more attractive because it enabled the investigation of aqueous solutions.

Conventional mass spectrometric methods usually require extensive sample preparation. Multiple samples also involve extended analysis time due to the need to introduce them into the vacuum. Moreover, these requirements exclude the possibility of *in vivo* biochemical analysis. This limitation can be overcome by producing ions directly from the sample at atmospheric pressure.

The multitude of recently introduced atmospheric pressure or ambient ionization methods including AP IR-MALDI,¹⁷ desorption electrospray ionization (DESI),¹⁸ direct analysis in real time (DART),¹⁹ desorption atmospheric pressure chemical ionization (DAPCI),²⁰ electrospray-assisted laser desorption ionization (ELDI),²¹ extractive electrospray ionization (EESI),²² plasma-assisted desorption ionization (PADI),^{22, 23} laser assisted electrospray ionization (LAESI)²⁴, probe electrospray ionization (PESI),²⁵ and desorption electrospray metastable-induced ionization (DEMI)²⁶ have demonstrated the capability of ion production directly from various samples at atmospheric pressure without extensive sample preparation.

The major component in most biological tissues and cells is water. For example, the average water content in small rodent tissue was determined to be 76%, with the highest percentage found in the testes at 86% and the lowest in the adipose tissue at 18%.²⁷ Similarly, the average water content in typical plant tissues, e. g., in apple plantlets, was found to be 78%.²⁸ Due to the strong absorption peak of water at 2940 nm wavelength (see Figure 1.1), the native water content in tissues and cells can serve as an efficient matrix to couple the laser energy into the sample. The absorption coefficient of water increases six orders of magnitude, from an average of $7.0 \times 10^{-3} \text{ cm}^{-1}$ in the visible

Figure 1.1 Absorption coefficient of water made at room temperature($\sim 20^\circ\text{C}$) in the wavelength range between 200 nm and 200 μm based on the experimental data compiled by Irvine and Pollack in 1968.²⁹ The arrow shows the absorption coefficient peak at the wavelength of 2940 nm.

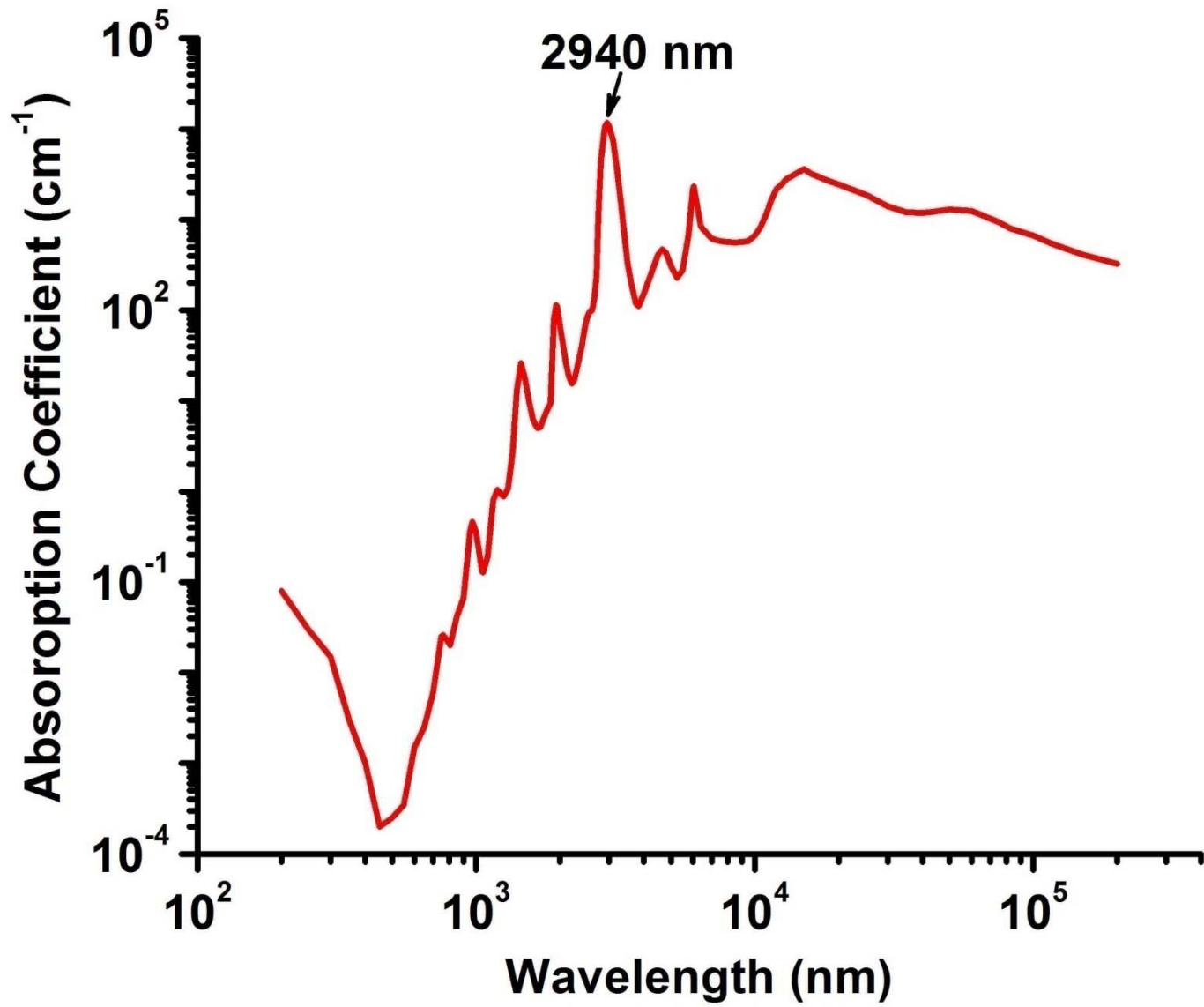
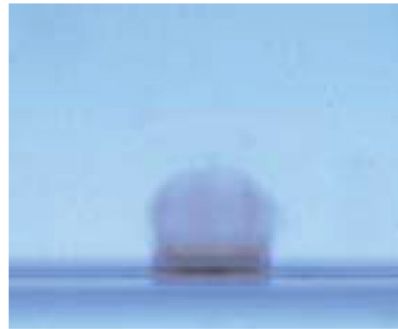


Figure 1.2 Bright-field time-resolved images of atmospheric pressure water ablation at 2940 nm wavelength by a Q-switched Er:YAG laser pulse (70 ns pulse duration, 0.12 J/cm² fluence, and an ablation spot size of 1 mm in diameter). Reprinted with permission by Springer-Verlag from Figure 1a of I. Apitz. and A. Vogel, Material ejection in nanosecond Er:YAG laser ablation of water, liver, and skin, *Appl. Phys. A*, 81, **2005**, 329.

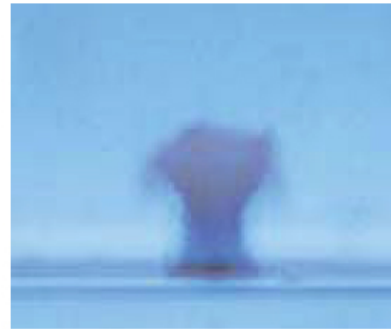
— = 1 mm



770 ns



1.5 μ s



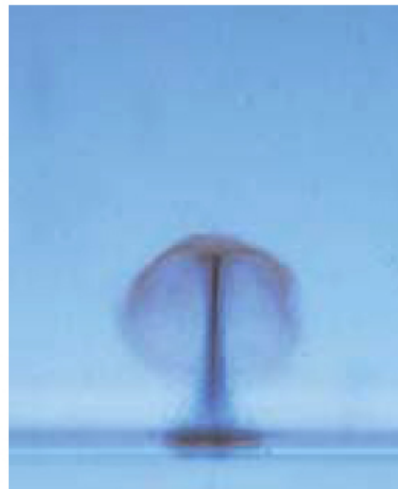
4 μ s



5 μ s



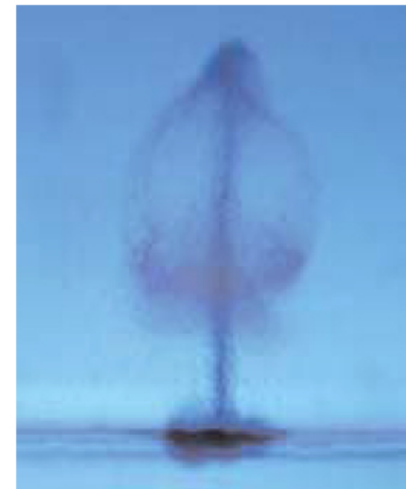
6 μ s



8 μ s



13 μ s



18 μ s

range (400 to 760 nm) to $\sim 1.2 \times 10^4$ at 2940 nm.²⁹ The resonance of the symmetric stretch mode, asymmetric stretch mode and symmetric bend mode of water molecules at wave numbers 3652 cm^{-1} , 3756 cm^{-1} and 1595 cm^{-1} , respectively, affect the absorption spectrum of water. The indicated vibration modes and their combination modes result in absorptions peaks at 0.96, 1.44, 1.95, 2.94, 4.68, and 6.1 μm wavelengths.³⁰

The work presented in this dissertation discusses my efforts to directly analyze tissues and single cells by mass spectrometry at atmospheric pressure using mid-IR laser ablation. The mid-IR laser ablation based methods were chosen because a focused laser beam can sample a well defined and sufficiently small volume of the specimen and the native water content in tissues and cells can provide an efficient means of coupling the laser energy.

The interaction of mid-IR laser radiation with water and water-rich targets, such as sections of soft tissues, exhibits three overlapping temporal phases (see Figure 1.2).³¹ At the beginning of the laser pulse, non-equilibrium surface evaporation occurs and leads to the gradual removal of material. For nanosecond laser pulses, fast energy deposition into the water target leads to temporary superheating beyond the boiling point. When the temperature reaches the spinodal limit, the liquid water is abruptly transformed into a mixture of vapor and liquid droplets. The resulting increase in volume leads to the ejection of material from the target through phase explosion. This phase explosion and other fluid instabilities, in turn, induce a recoil pressure causing secondary material removal by the recoil-induced material expulsion. This process results in increased ablation efficiency and can often last up to one second after the laser pulse, which is $\sim 10^8$ times longer than the pulse that caused it.^{32,33}

Figure 1.2 shows the consequences of all three phases of the mid-IR ablation at a laser fluence of 0.1 J/cm^2 , which is similar to the values used in my work. The first phase of the ablation lasts for one to two μs (microseconds), when a spherical plume is created through surface evaporation and phase explosion. This plume induces strong shock waves³² and is decelerated and eventually (at around $5 \mu\text{s}$) stopped by the background gas (air) pressure. In the third phase lasting up to tens of microseconds, the recoil pressure expels additional material in the form small particulate matter. The analytically useful information for AP IR-MALDI stems from the initial hemispherical plume because it directly produces ions for analysis, whereas the LAESI process relies on the secondary material ejection that can be post-ionized by ESI.

Atmospheric pressure ionization methods, such as DESI, have been successfully used to produce ions directly from biological samples, such as tissues (e. g., human liver, plant tissue, rat brain sections and histological sections of rat lung), bodily fluids (e. g., urine and blood), human skin, etc.^{34, 35} Application of ELDI-MS was reported for direct chemical analysis from tissue sections (e. g., porcine liver and heart), dried bodily fluids (e. g., blood, saliva and tear), cell cultures, etc.²¹

AP IR-MALDI has been utilized to directly analyze plant tissues, animal tissues, and human bodily fluid providing detailed information on metabolites and lipids.³⁶⁻³⁸ The detailed study of biological tissues with the AP IR-MALDI method is discussed in Chapters 2, 3, 4 and 5. LAESI-MS has been used to directly analyze chemicals in various plant organs, human bodily fluids, the electric organ of torpedo fish, and rodent brain tissues.^{24, 39-41} The details of LAESI-MS analysis of biological tissue are provided in Chapters 5 and 6.

The chemical analysis of a single cell by MS presents further challenges, as well as an opportunity to study the heterogeneity of biochemical processes in cells. Other analytical techniques for single cell analysis, such as fluorescence microscopy, Fourier transform infrared (FTIR) spectroscopic imaging, coherent anti-Stokes Raman scattering (CARS) microscopy, nuclear magnetic resonance spectrometry, require extensive sample preparation, chemical tagging or the genetic incorporation of a fluorophore, and generally do not provide simultaneous detection of multiple chemical species.^{42, 43}

Chemical analyses of a single cell by MS was been performed by coupling capillary electrophoresis with ESI to analyze hemoglobin in a single human erythrocyte.⁴⁴ The high spatial resolution of the ion sputtering process and improvements in secondary ion mass spectrometry (SIMS) have enabled single cell and subcellular analysis in vacuum.⁴⁵ Single cell analysis in vacuum by UV-MALDI has also been demonstrated for neuropeptides in a single isolated neuron and in single dense core vesicles of the exocrine atrial gland of *Aplysia californica*.^{46, 47}

Most of the single cell analysis by MS is performed on isolated cells or cell extracts in vacuum.⁴⁸ Many techniques have been developed to isolate single cells for analysis. For example, laser capture microdissection has been applied to isolate cells from tissue sections for mass spectrometric analysis.^{49, 50} All the above mentioned single cell chemical analysis techniques need extensive sample preparation and/or sample introduction into the vacuum. However, the processing of the single cells away from their natural environment potentially affects their metabolic profile.

In order to analyze single cells with LAESI-MS, the diameter of the laser ablation spot should be smaller than an individual cell. Since conventional long working distance

mid-IR focusing optics (e. g., a single ZnSe or CaF₂ lens) did not produce an ablation spot smaller than most single cells, in our approach the laser pulses were delivered through the etched tip of a GeO₂-based glass fiber.⁵¹ The results of single plant and animal cell analysis by LAESI-MS are discussed in Chapter 6.

REFERENCES

- (1) Glassbrook, N.; Beecher, C.; Ryals, J. *Nature Biotechnology* **2000**, *18*, 1157-1161.
- (2) Fiehn, O.; Kopka, J.; Dörmann, P.; Altmann, T.; Trethewey, R. N.; Willmitzer, L. *Nature Biotechnology* **2000**, *18*, 1157-1161.
- (3) Nicholson, J. K.; Connelly, J.; Lindon, J. C.; Holmes, E. *Nature Reviews Drug Discovery* **2002**, *1*, 153.
- (4) Förster, J.; Famili, I.; Fu, P.; Palsson, B.; Nielsen, J. *Genome Research* **2003**, *13*, 244.
- (5) Fiehn, O. *Comparative and Functional Genomics* **2001**, *2*, 155-168.
- (6) Dunn, W. B.; Bailey, N. J. C.; Johnson, H. E. *The Analyst* **2005**, *130*, 606-625.
- (7) Ellis, D. I.; Goodacre, R. *The Analyst* **2006**, *131*, 875-885.
- (8) Reo, N. V. *Drug and Chemical Toxicology* **2002**, *25*, 375-382.
- (9) ASMS.
- (10) Fenn, J. B.; Mann, M.; Meng, C. K.; Wong, S. F.; Whitehouse, C. M. *Science* **1989**, *246*, 64-71.
- (11) Tanaka, K.; Ido, H. W. Y.; Akita, S.; Yoshida, Y.; Yoshida, T.; Matsuo, T. *Rapid Communications in Mass Spectrometry* **1988**, *2*, 151-153.
- (12) Karas, M.; Hillenkamp, F. *Analytical Chemistry* **1988**, *60*, 2299-2301.
- (13) Wei, J.; Buriak, J. M.; Siuzdak, G. *Nature* **1999**, *399*, 243-246.
- (14) Chen, Y.; Vertes, A. *Analytical Chemistry* **2006**, *78*, 5835-5844.

- (15) Berkenkamp, S.; Karas, M.; Hillenkamp, F. *Proceedings of the National Academy of Sciences* **1996**, *93*, 7003-7007.
- (16) Laiko, V. V.; Baldwin, M. A.; Burlingame, A. L. *Analytical Chemistry* **2000**, *72*, 652-657.
- (17) Laiko, V. V.; Taranenko, N. I.; Berkout, V. D.; Yakshin, M. A.; Prasad, C. R.; Lee, H. S.; Doroshenko, V. M. *Journal of the American Society for Mass Spectrometry* **2002**, *13*, 354-361.
- (18) Takats, Z.; Wiseman, J. M.; Gologan, B.; Cooks, R. G. *Science* **2004**, *306*, 471 - 473.
- (19) Cody, R. B.; Laramée, J. A.; Durst, H. D. *Analytical Chemistry* **2005**, *77*, 2297-2302.
- (20) Takats, Z.; Cotte-Rodriguez, I.; Talaty, N.; Chen, H.; Cooks, R. G. *Chem. Commun* **2005**, *1950*, 1952.
- (21) Huang, M.-Z.; Hsu, H.-J.; Lee, J.-Y.; Jeng, J.; Shiea, J. *Journal of Proteome Research* **2006**, *5*, 1107-1116.
- (22) Chen, H.; Venter, A.; Cooks, R. G. *Chemical Communications* **2006**, 2042-2044.
- (23) Ratcliffe, L. V.; Rutten, F. J. M.; Barrett, D. A.; Whitmore, T.; Seymour, D.; Greenwood, C.; Aranda-Gonzalvo, Y.; Robinson, S.; McCoustra, M. *Analytical Chemistry* **2007**, *79*, 6094-6101.
- (24) Nemes, P.; Vertes, A. *Analytical Chemistry* **2007**, *79*, 8098-8106.
- (25) Lee Chuin, C.; Kentaro, Y.; Zhan, Y.; Rikiya, I.; Hajime, I.; Hiroaki, S.; Kunihiko, M.; Osamu, A.; Sen, T.; Takeo, K.; Kenzo, H. *Journal of Mass Spectrometry* **2009**, *44*, 1469-1477.
- (26) Nyadong, L.; Galhena, A. S.; Fernandez, F. M. *Analytical Chemistry* **2009**, *81*, 7788-7794.

- (27) Reinoso, R. F.; Telfer, B. A.; Rowland, M. *Journal of Pharmacological and Toxicological Methods* **1997**, *38*, 87-92.
- (28) Diaz-Pérez, J. C.; Shackel, K. A.; Sutter, E. G. *J. Exp. Bot.* **1995**, *46*, 111-118.
- (29) Irvine, W. M.; Pollack, J. B. *Icarus* **1968**, *8*, 324-360.
- (30) Vogel, A.; Venugopalan, V. *Chemical Reviews* **2003**, *103*, 577-644.
- (31) Apitz, I.; Vogel, A. *Applied Physics A: Materials Science & Processing* **2005**, *81*, 329-338.
- (32) Chen, Z.; Bogaerts, A.; Vertes, A. *Applied Physics Letters* **2006**, *89*, 041503-041503.
- (33) Chen, Z.; Vertes, A. *Physical Review E (Statistical, Nonlinear, and Soft Matter Physics)* **2008**, *77*, 036316.
- (34) Cooks, R. G.; Ouyang, Z.; Takats, Z.; Wiseman, J. M. *Science* **2006**, *311*, 1566-1570.
- (35) Wiseman, J. M.; Ifa, D. R.; Zhu, Y.; Kissinger, C. B.; Manicke, N. E.; Kissinger, P. T.; Cooks, R. G. *Proceedings of the National Academy of Sciences* **2008**, *105*, 18120-18125.
- (36) Li, Y.; Shrestha, B.; Vertes, A. *Analytical Chemistry* **2007**, *79*, 523-532.
- (37) Li, Y.; Shrestha, B.; Vertes, A. *Analytical Chemistry* **2008**, *80*, 407-420.
- (38) Shrestha, B.; Li, Y.; Vertes, A. *Metabolomics* **2008**, *4*, 297-311.
- (39) Nemes, P.; Barton, A. A.; Li, Y.; Vertes, A. *Analytical Chemistry* **2008**, *80*, 4575-4582.
- (40) Nemes, P.; Barton, A. A.; Vertes, A. *Analytical Chemistry* **2009**, *81*, 6668-6675.
- (41) Sripadi, P.; Nazarian, J.; Hathout, Y.; Hoffman, E.; Vertes, A. *Metabolomics* **2009**, *5*, 263-276.
- (42) Navratil, M.; Mabbott, G. A.; Arriaga, E. A. *Analytical Chemistry* **2006**, *78*, 4005-4020.
- (43) Aguayo, J. B.; Blackband, S. J.; Schoeniger, J.; Mattingly, M. A.; Hintermann, M. *Nature* **1986**, *322*, 190-191.
- (44) Steven, A. H.; Joanne, C. S.; Richard, D. S.; Franklin, D. S.; Andrew, G. E. *Rapid Communications in Mass Spectrometry* **1996**, *10*, 919-922.

- (45) Ostrowski, S. G.; Van Bell, C. T.; Winograd, N.; Ewing, A. G. *Science* **2004**, *305*, 71-73.
- (46) Li, L.; Garden, R. W.; Sweedler, J. V. *Trends in Biotechnology* **2000**, *18*, 151-160.
- (47) Rubakhin, S. S.; Garden, R. W.; Fuller, R. R.; Sweedler, J. V. *Nat Biotech* **2000**, *18*, 172-175.
- (48) Monroe, E. B.; Jurchen, J. C.; Rubakhin, S. S.; Sweedler, J. V. In *New Frontiers in Ultrasensitive Bioanalysis*; Xiao-Hong Nancy, X., Ed., 2007, pp 269-293.
- (49) Emmert-Buck, M. R.; Bonner, R. F.; Smith, P. D.; Chuaqui, R. F.; Zhuang, Z.; Goldstein, S. R.; Weiss, R. A.; Liotta, L. A. *Science* **1996**, *274*, 998-1001.
- (50) Xu, B. J.; Caprioli, R. M.; Sanders, M. E.; Jensen, R. A. *Journal of the American Society for Mass Spectrometry* **2002**, *13*, 1292-1297.
- (51) Shrestha, B.; Vertes, A. *Analytical Chemistry* **2009**, *81*, 8265-8271.

CHAPTER 2

ATMOSPHERIC PRESSURE MOLECULAR IMAGING AND PLANT METABOLOMICS BY INFRARED MALDI MASS SPECTROMETRY

Based on material published by Y. Li, B. Shrestha, and A. Vertes in
Anal. Chem., **2007**, *79*, 523-532. and *Anal. Chem.*, **2008**, *80*, 407-420.

ABSTRACT

An atmospheric pressure (AP) MALDI imaging interface was developed for an orthogonal acceleration time-of-flight mass spectrometer and utilized to analyze peptides, carbohydrates, and other small biomolecules using infrared (IR) laser excitation. In molecular imaging experiments, the spatial distribution of mock peptide patterns was recovered with a detection limit of ~ 1 fmol/pixel from a variety of MALDI matrixes. With the use of oversampling for the image acquisition, a spatial resolution of 40 μm , 5 times smaller than the laser spot size, was achieved. This approach, however, required that the analyte was largely removed at the point of analysis before the next point was interrogated. Native water in plant tissue was demonstrated to be an efficient natural matrix for AP IR-MALDI. Tissue sections from plant organs, including flowers, ovaries, aggregate fruits, fruits, leaves, tubers, bulbs, and seeds were studied in both positive and negative ion modes. For leaves, single laser pulses sampled the cuticle and upper

epidermal cells, whereas multiple pulses were demonstrated to ablate some mesophyll layers. Tandem mass spectra were obtained with collision-activated dissociation to aid with the identification of some observed ions. In the positive mode, most ions were produced as potassium, proton or sometimes sodium ion adducts, whereas proton loss was dominant in the negative ion mode. Over 50 small metabolites and various lipids were detected in the mass spectra. Key components of the glycolysis pathway occurring in the plant cytosol were found along with intermediates of phospholipid biosynthesis and reactants or products of amino acid, nucleotide, oligosaccharide, and flavonoid biosynthesis. Molecular imaging of a strawberry skin sample revealed distribution of sucrose, glucose/fructose, and citric acid species around the embedded seeds. AP IR-MALDI was also used to follow the fluid transport driven by transpiration and image the spatial distributions of several metabolites in a white lily (*Lilium candidum*) flower petal.

INTRODUCTION

Molecular imaging with mass spectrometry (MS) has attracted the attention of scientists for over 3 decades because it offers the benefit of excellent sensitivity combined with the ability to uniquely identify an array of chemical species in the image. The top contenders to deliver on this promise are secondary ion mass spectrometry (SIMS) and matrix-assisted laser desorption ionization (MALDI). Excellent recent reviews on the development and application of these methods are available in the literature.¹⁻⁵ In many respects the two techniques are complementary. For example, SIMS produces high lateral resolution (<20 nm) of distributions of elemental and small organic ions ($m/z < 1000$), whereas MALDI-MS imaging using an ultraviolet (UV) laser reports

on larger species ($1000 < m/z < 50000$ for proteins) with coarser resolution (typically 30–200 μm). The demonstrated ability of MALDI-MS imaging to reveal protein distributions in tissue sections⁶ resulted in heightened interest and the rapid growth of related publications during the past 5 years.⁷⁻²⁰

Tissue sections are prepared for MALDI imaging by uniformly covering the surface with matrix solution. An alternative method is to blot the species of interest onto the target followed by the application of matrix. Although necessary, these steps, perhaps, are the most critical, as the analyzed species have to be transferred into the matrix overlay without significant degradation of its lateral distribution by diffusion and/or mixing. After air-drying, the treated sample is transferred into the vacuum system of the mass spectrometer where an automated X – Y stage moves the sample in the laser desorption ion source. By synchronizing the target movement to the ultraviolet laser shots, spatially correlated mass spectra are acquired. Application of MALDI imaging to large biomolecules critically depends on sample preparation. Depending on crystallization conditions a layer of more or less fine crystallite of the UV-absorbing matrix is formed over the biological material. During their formation, these crystallites incorporate some of the proteins from the tissue section.^{6, 21-26} This approach has been successfully used to profile and image peptides and proteins from mammalian cells and tissue sections including samples from colon tumors.²⁷

There are significant efforts underway to refine molecular imaging methods based on MALDI-MS technology.^{4, 8, 12, 14, 19, 20, 28-35} The spatial resolution of MALDI imaging depends on laser spot size. The theoretical smallest laser spot size is determined by the size of the Airy disc due to diffraction. Depending on numerical aperture, diffraction

limit is typically about one-half to one-quarter of the wavelength of the beam. Recent advances in instrumentation pioneered on a home-built system promise close to diffraction-limited lateral resolution ($0.6\ \mu\text{m}$ for $\lambda = 337\ \text{nm}$ laser wavelength), rapid image collection (up to 50 pixels per second), and the combination of MALDI imaging with confocal microscopy.¹⁹ With the use of a high repetition rate (8 kHz) Nd:YLF laser and a fast piezoelectric nanostage a 100×100 pixel image can be acquired within 4–15 min. On this system, inorganic ion distributions in pine tree root tissue sections were recorded with excellent spatial resolution. Probing the surface point by point has two important disadvantages. First, it is inherently slow due to the limitations in the rate of laser pulses and/or data acquisition. Second, the above-mentioned diffraction-limited focusing reduces the spatial resolution. Both of these obstacles can be resolved by switching to the “microscope mode” known from SIMS imaging.^{14, 32} In this mode the highly focused laser beam is replaced by large area illumination and spatially resolved ion detection. In a single shot experiment mass-resolved images are obtained for the intact peptide and protein ions of a $200\ \mu\text{m}$ spot with a spatial resolution of $4\ \mu\text{m}$ in less than 1 millisecond. This powerful approach, however, can only be applied in a vacuum environment for at atmospheric pressure the congruence of ion trajectories is spoiled by the collisions of the ions with the background gas molecules.

Despite the growing success of MALDI-MS as a molecular imaging technique, two major obstacles stand in the way of its widespread application. First, mixing and cocrystallizing the sample with the light-absorbing matrix material can significantly obscure the original spatial distribution of analytes (e.g., through lateral mixing). Second, the need to transfer the sample into a vacuum environment for mass analysis

considerably restricts the choice of samples. Both of these requirements for successful MALDI analysis exclude the possibility of *in vivo* measurements. The information on the spatial distributions and temporal variations of chemical species in biological systems is essential to understand metabolic pathways and, in general, complex biological processes in plants. These metabolites play a critical role in biological function, such as energy production and the biosynthesis of macromolecules.^{36, 37} Knowledge of the structure, function, and biosynthetic pathways for metabolites in plants is important for various areas including energy production, agriculture, environmental processes, and pharmacology. Often complementary information from several techniques is used for the identification or quantitation of metabolites. The analytical techniques used in the emerging field of metabolomics have recently been reviewed.³⁸

Due to its inherently high sensitivity and molecular specificity, mass spectrometry has become an increasingly important tool for the analysis of biological systems. Several separations and mass spectrometry approaches, such as GC/MS, LC/MS, and CE/MS, were developed to enable better metabolite identification and quantitation.^{36, 39-47} In combination with soft ionization methods such as electrospray ionization (ESI) and matrix-assisted laser desorption/ionization (MALDI), mass spectrometry proved to be useful in the investigation of biological systems.⁴⁸⁻⁵¹ In these ESI studies, however, the plant tissues had to be extracted by solvents through laborious procedures. Sample preparation protocols for the conventional MALDI analysis of plant metabolites usually start with extraction followed by mixing the extract with a matrix solution. In imaging MALDI experiments, it is possible to directly analyze tissue sections; however, the sample surface needs to be uniformly covered with the matrix without significantly

altering the original molecular distributions. This task is particularly challenging in the case of water-soluble analytes and small molecules. Moreover, for analysis, the matrix-treated samples have to be transferred into the vacuum system of the mass spectrometer. These delicate and laborious procedures considerably restrict the choice of samples and exclude the possibility of *in vivo* studies.

Although the feasibility of atmospheric pressure (AP) MALDI has been demonstrated several years ago,⁵²⁻⁵⁸ its analytical applications are just beginning to emerge⁵⁹⁻⁶¹ Initially the enthusiasm was tempered by its reduced sensitivity compared to that of vacuum MALDI, but the recently reported subfemtomole detection limits (in combination with preconcentration methods, e.g., solid-phase microextraction) and the streamlined sample handling in the ambient rekindled the interest.⁶² Additional advantages of AP-MALDI include the possibility to use liquid matrixes and, in combination with a mid-IR laser, to efficiently study carbohydrates, their complexes, and noncovalent peptide–carbohydrate interactions.⁶³⁻⁶⁶

Conventional MALDI-MS relies on a UV laser to produce the ions. Although infrared (IR) MALDI had been demonstrated to produce intact ions of large nucleic acids and work with water ice as a matrix,^{67, 68} due to its less robust analytical performance compared to that of UV-MALDI and to the lack of inexpensive mid-IR laser sources, it was not universally embraced by the analytical community. Nevertheless, the inherent advantages of IR-MALDI for certain applications are compelling. Direct combination of IR-MALDI with liquid-phase separation techniques⁶⁹⁻⁷² and with thin-layer chromatography⁷³ have been demonstrated in the literature. There are also more potential matrixes for IR-MALDI because many compounds have a strong absorption in

the mid-IR spectral region. Recently, Laiko *et al.*⁷⁴ successfully used water and glycerol as a matrix with a 3 μm IR laser at atmospheric pressure to generate peptide ions.

In this contribution, we present a new approach to molecular imaging based on mid-IR laser excitation for AP-MALDI that mitigates both of these impediments. Molecular imaging of peptide distributions on surfaces and the distribution of various small molecules in biological tissue without the addition of a matrix are demonstrated. AP IR-MALDI experiments with diverse plant tissues in both positive and negative ion modes as well as on imaging results for fluid transport induced by plant transpiration demonstrate its ability to identify and image a wide variety of metabolites in plants and to gauge its potential for *in vivo* investigations.

EXPERIMENTAL SECTION

Mass Spectrometer and Infrared Laser. A Q-TOF Premier orthogonal acceleration time-of-flight (TOF) mass spectrometer (Waters Co., Milford, MA) was modified by replacing the electrospray source with a custom-made AP laser desorption ion source. The inlet capillary had a length of 30 mm and an internal diameter of 127 μm . The mid-IR output of a Nd:YAG laser-driven tunable optical parametric oscillator (OPO) (set to 2940 nm, 10 Hz) was projected onto the sample mounted on a stainless steel probe to produce the ions. The pulse duration of the laser was 4 ns. A single plano-convex focusing lens with 50 mm focal length produced an elliptical laser spot of ~ 250 μm average diameter. The closest possible distance, ~ 2 mm, between the mass spectrometer inlet and the target surface was selected to maximize the ion signal but still

avoid an electrical breakdown. All the experiments were performed in the positive ion mode.

Pulsed Dynamic Focusing. In order to improve the ion collection efficiency, pulsed dynamic focusing (PDF) was implemented.⁷⁵ In PDF when the ions in the expanding laser plume are sufficiently close to the mass spectrometer inlet, the extraction voltage is reduced to zero. Through the rest of the way to the inlet the ions are guided by the aerodynamic flow created by the suction of the orifice. Consistent with earlier results⁷⁵, our experiments showed that, compared to a static electric extraction field, the PDF improved the ion collection efficiency by approximately a factor of 5. There were several PDF and source parameters to optimize to achieve this improvement. These included the high voltage applied to the target plate, the temperature of the capillary, and the high-voltage pulse width. The best results were obtained at 3.0 kV target plate voltage held for 13 ms, 150 °C interface block temperature, and –50 V interface voltage.

Molecular Imaging. The imaging experiments were performed with a computer-controlled, stepper motor-driven, three-axis precision flexure stage (NanoMax TS, Thorlabs, Newton, NJ). The flexure stage with additional piezoelectric actuators and displacement sensors had a travel range of 4 mm, a theoretical resolution of 25 nm, and a repeatability of 1 μm . The sample surfaces mounted on the flexure stage were scanned in front of the mass spectrometer inlet orifice. The mass spectra obtained at each spot exposed to the laser beam (or a pixel) were averaged, typically for 50 laser pulses, and stored as a function of scanning time. Two-dimensional spatial distributions of the ion intensities were recovered from the ion chromatograms by a LabView program. A

scientific visualization package (Origin 7.0, OriginLab Co., Northampton, MA) was used to produce false color images representing ion abundances as a function of position.

Materials and Sample Preparation. HPLC-grade triacetate salt of bradykinin, acetate salt hydrate of substance P, bovine insulin, and 2,5-dihydroxybenzoic acid (DHB), as well as reagent-grade reserpine, succinic acid, thiourea, and glycerol were purchased from Sigma-Aldrich. The aqueous 1% solution of toluidine blue O was obtained from Home Training Tools, Ltd. Both the analytes and the matrixes were used without further purification. Deionized water was produced with an E-pure system (D4631, Barnstead, Dubuque, IA).

The conventional MALDI samples were produced by mixing 1 μ L of the diluted 2×10^{-4} M peptide stock solution prepared in 0.01% TFA with 1 μ L of the saturated matrix solution prepared in 70% (v/v) HPLC-grade aqueous acetonitrile solution. For crystalline matrixes, the samples were allowed to air-dry at room temperature.

Various plant organs including flowers (white lily, *Lilium candidum*), fruits (banana, *Musa paradisiaca*, and tomato, *Solanum lycopersicum*), aggregate fruits (strawberry, *Fragaria ananassa*), leaves (cilantro, *Coriandrum sativum*, and peace lily, *Spathiphyllum*), tubers (potato, *Solanum tuberosum*), bulbs (onion, *Allium cepa*, and garlic, *Allium sativum* L.), and seeds (almond, *Prunus amygdalus*) were obtained from a local supermarket. Except for the leaves and the flower petals that were studied without sectioning, tissue sections of 0.2–0.5 mm in thickness (measured with caliper) were prepared at room temperature with a scalpel, and without further treatment, they were carefully placed onto the sample stage. The wet tissue sections adhered to the sample holder through surface forces, whereas the samples with dry surfaces were attached with a double-sided tape.

Identification of Ions. Due to the inherent complexity of the plant samples, identification of the ions based on their nominal mass alone is not possible. In order to elucidate the structure of the detected ions, we performed accurate mass measurements, isotope distribution analysis, and in some cases collision activated dissociation (CAD) for the comparison of fragmentation patterns. Accurate mass measurements were performed using internal calibration based on common ions that were known to be produced from plant samples. These included potassiated sugars, their clusters, and some organic acids. The mass accuracies for $m/z < 195$, $195 < m/z < 800$ and $800 < m/z < 1500$ are within ± 0.012 , ± 0.049 , and ± 0.005 , respectively. This enabled the selection of a short list of compounds for every peak using the AraCyc 3.5 metabolic pathways database at TAIRs - The Arabidopsis Information Resource: <http://www.arabidopsis.org/> for *Arabidopsis thaliana* (accessed June 7, 2007). Some assignments were made using the broader MetaCyc7272 combined database for 261 organisms at <http://biocyc.org/> (accessed August 4, 2007). Lipid assignments were aided by the LIPID Metabolites and Pathways Strategy database maintained by the LIPID MAPS consortium. The database was accessed on August 6, 2007, at <http://www.lipidmaps.org/>.

Individual peak assignments were further aided by the comparison of $M + n$ peak intensities to the calculated patterns obtained from the abundances of natural isotopes. Most of the product ions in the positive mode were formed through protonation or alkylation, whereas in the negative ion mode, deprotonation was dominant. For high-fidelity structure assignments, the fragmentation patterns due to CAD in tandem mass spectra were compared to the corresponding spectra in the NIST library (NIST Mass Spectral Search Program for the NIST/EPA/NIH Mass Spectral Library, Version 2.0).

Even with the combination of the three methods, there are clear limitations for the structure assignments. For example, stereoisomers and some structural isomers cannot be distinguished.

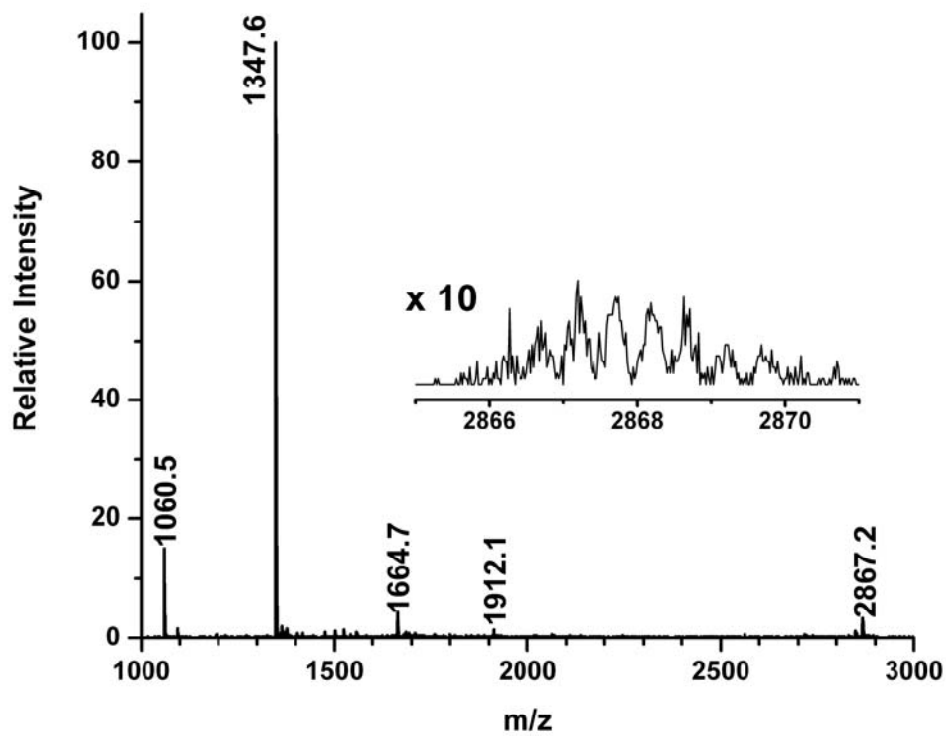
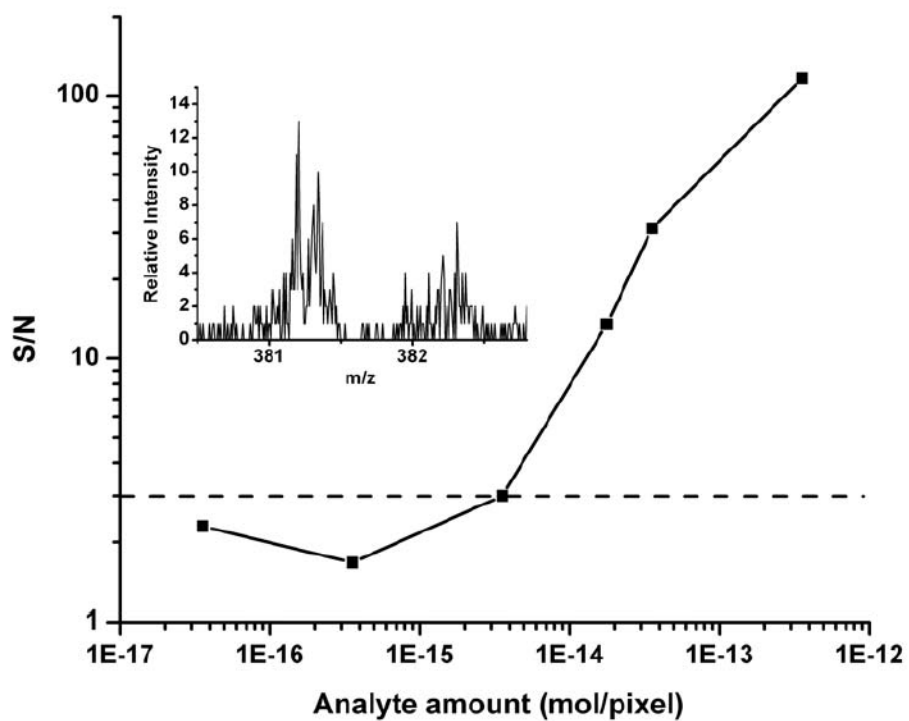
RESULTS AND DISCUSSION

Sensitivity and Interferences. Due to ion production, collection, and transport losses in the AP environment and within the interface itself, the AP-MALDI ion sources are perceived as less efficient than their vacuum counterparts. To test the utility of our AP-MALDI system, the sensitivity and spectral interferences were assessed. A series of dilution experiments using reserpine (m/z 608.7) and bradykinin (m/z 1060.4) analyte and saturated DHB matrix solutions showed that for the entire sample spot the sensitivity was 300 fmol, whereas in imaging experiments for individual pixels ~ 1 fmol/pixel sensitivity was achieved using $S/N > 3$ as the detection criterion. In the presence of potassium ions, somewhat higher detection limit, ~ 3 fmol/pixel, was found for the direct desorption of sucrose from aqueous environment. Figure 2.1a shows the dependence of the signal-to-noise ratio (S/N) for the potassiated sucrose ions as a function of solution concentrations. At ~ 3 fmol/pixel the S/N drops below 3 and the signal becomes commensurate with the noise. The inset depicts the marginal signal at m/z 381 and its vicinity in the corresponding mass spectrum.

Both in the case of DHB and water as a matrix, matrix-related interferences were

Figure 2.1 (a) Signal-to-noise ratio for potassiated sucrose ions (m/z 381.1) from aqueous matrix using AP IR-MALDI shows ~ 3 fmol/pixel detection limit. Inset shows the marginal signal at m/z 381 and its vicinity in the corresponding mass spectrum.

(b) AP IR-MALDI mass spectrum of equimolar bradykinin (m/z 1060.4), substance P (m/z 1347.6), and bovine insulin (m/z 5733.5) mixture with DHB as a matrix. Bovine insulin ions are low in abundance and appear as doubly and triply charged species at m/z 2867.2 and 1912.1, respectively.



A

B

absent. This is consistent with the general notion of efficient matrix suppression in AP-MALDI reported in the literature.^{55, 76} The sensitivity in our system also depended on the mass of the analyte. Figure 2.1b shows the AP IR-MALDI mass spectrum for an equimolar (100 pmol each) mixture of bradykinin, substance P (m/z 1347.6), and insulin (m/z 5733.5). While the bradykinin and substance P peaks were strong, no singly charged insulin signal was detected. The weak peaks at m/z 2867.2 and 1912.1 corresponded to the doubly and triply protonated forms of insulin, respectively. Although analyte suppression effects by the low-mass peptides could account for reduced insulin intensities, experiments with insulin alone confirmed that these observations were mostly due to the reduced sensitivity in the $m/z > 3000$ region.

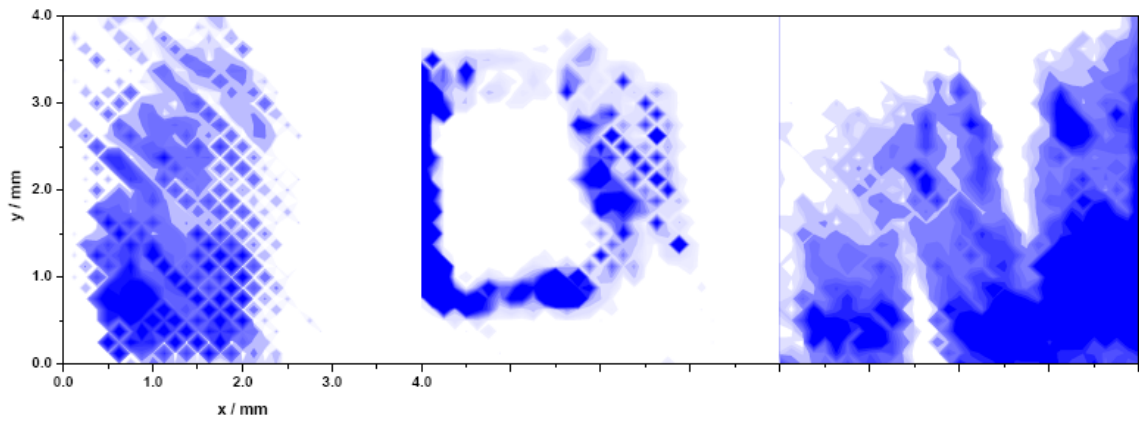
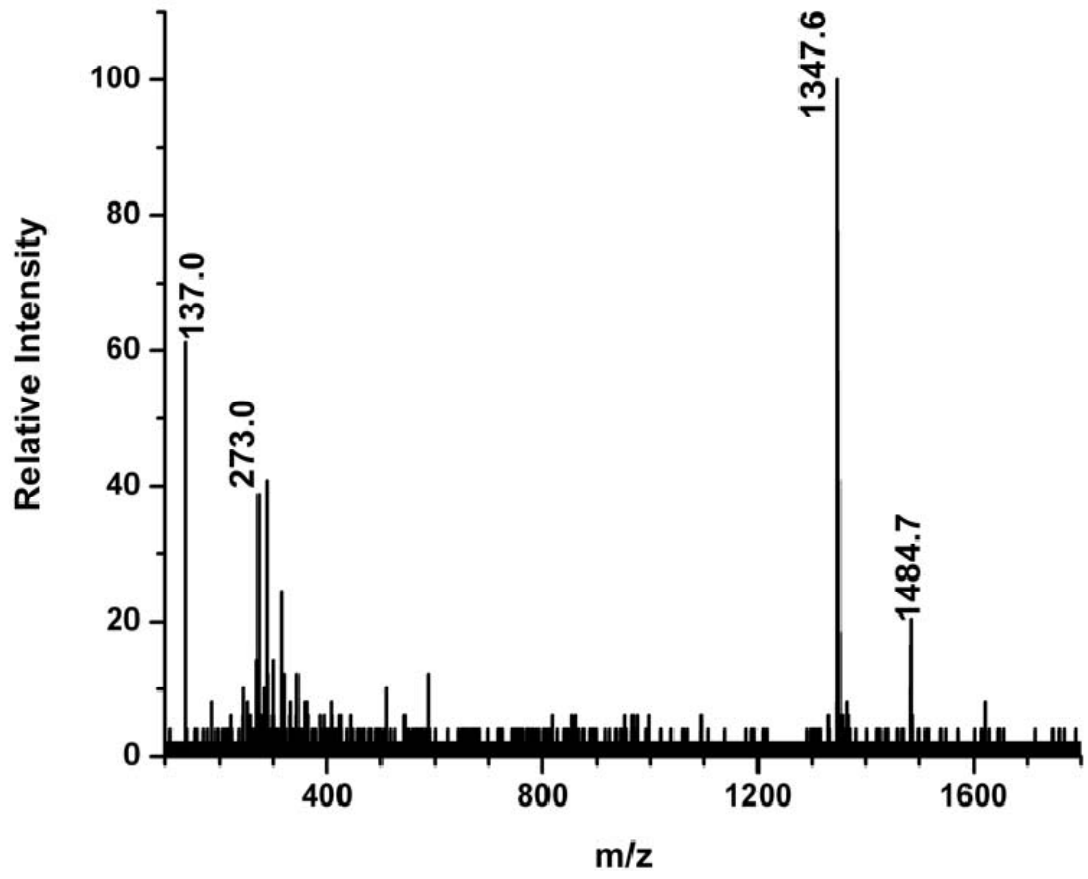
For vacuum UV-MALDI and IR-MALDI, the typical sensitivity values are in the low femtomole and subpicomole range, respectively.⁷⁷ For ion trap instruments in AP UV-MALDI experiments absolute sensitivity values were reported at the low femtomole level.⁵⁴ Direct AP analysis of oligosaccharides with an IR laser from the solution phase also indicated femtomole sensitivity.⁶⁶ Thus, it seems, for AP-MALDI ion sources (including ours) the current challenge is not the absolute sensitivity for the best case compounds but the demonstration of consistent analytical performance for broad classes of molecules.

Molecular Imaging of Mock Peptide Distributions. Several known IR matrixes, including DHB, succinic acid, thiourea, glycerol, and water, were tested in AP laser desorption experiments. Although all of these matrixes produced analyte ion signal, for the small peptides studied, DHB and water offered the strongest peaks and the best signal-to-noise ratio. Encouraged by the robust AP-MALDI signal, imaging experiments

on mock peptide distributions were performed. Figure 2.2 shows the molecular images of the three characters in the word “ION”, with the intensity of substance P at m/z 1347.6 represented on a false color scale. In these experiments, 1 μ L of the analyte DHB mixture was transferred onto the target plate and allowed to air-dry. An adhesive paper mask with the letters “I”, “O”, and “N” excised was attached to the sample surface. As our flexure stage had a range of 4 mm in the X and Y directions, scanning of the surface was performed one character at a time. Because the focal spot of our IR laser was 250 μ m, initially a 125 μ m scanning step size was selected. Although spectral features were already discernible after 1 s (10 laser shots), to achieve high signal-to-noise ratio, each surface position was interrogated for 8 s and the spectra from the 80 laser shots were averaged.

Figure 2.2a displays a mass spectrum obtained by averaging the signal for 10 laser shots. The base peak at m/z 1347.6 corresponds to substance P. It is accompanied by the dehydroxylated DHB fragment ion at m/z 137.0 and by its adducts with a substance P molecule at m/z 1484.7 and with a neutralized DHB fragment at m/z 273.0. To determine the substance P distribution over the surface, the m/z 1347.6 peaks were integrated for every position of the translation stage, the corresponding pixels were colored according to the peak areas and mapped to the surface to produce an image (see Figure 2.2b). Although the original pattern and the three characters are clearly discernible, due to the uneven mask surface and probably due to the charging of the insulating paper mask during the experiments, the image in Figure 2.2b is fairly crude. We estimated the spatial resolution to be \sim 200 μ m on the basis of the measurement of the size differences between the actual and imaged patterns. This, in part, is attributed to

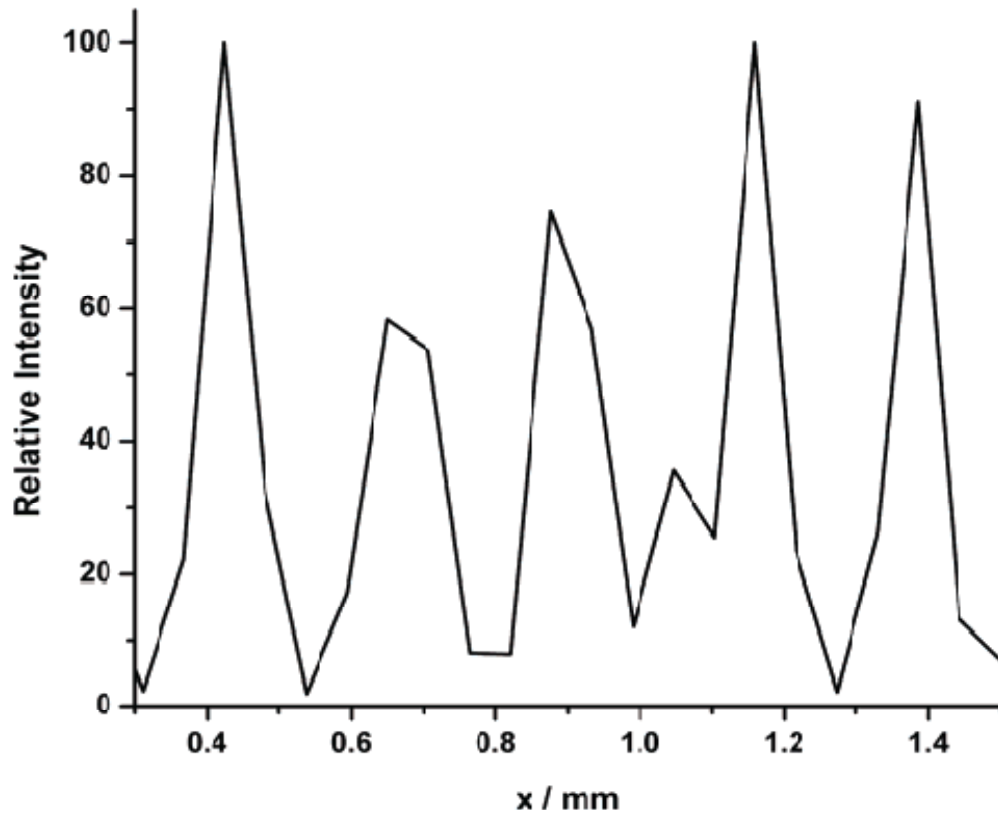
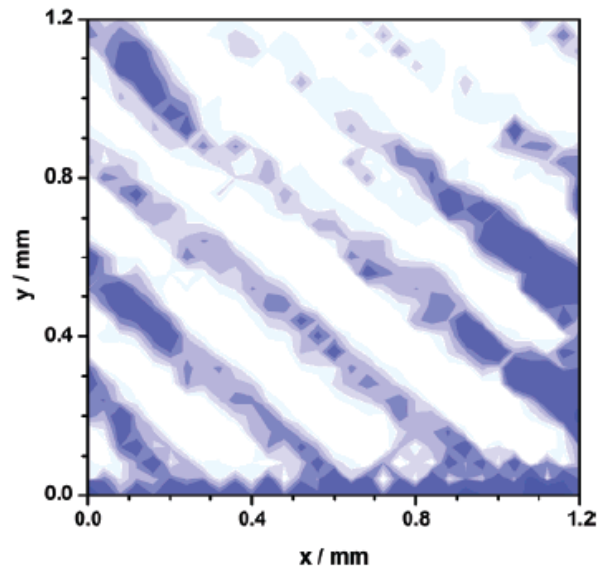
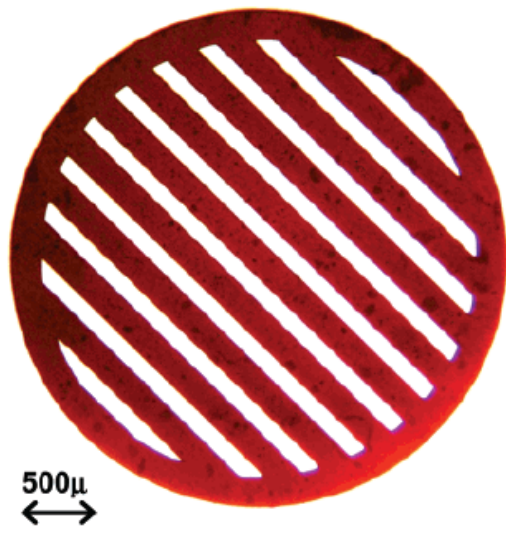
Figure 2.2 (a) AP IR-MALDI mass spectrum of substance P from DHB matrix based on 10 laser shots. **(b)** Molecular image of the three characters in the word “ION” at m/z 1347.6 corresponding to the substance P molecular ion. The characters were created by a paper mask over the sample surface. The scanning step size and the dwell time were 125 μm and 8 s/pixel, respectively.



A

B

Figure 2.3 (a) Left panel: optical image of the electron microscope grid used as a mask to create chemical contrast with 92 μm features (gap width). Right panel: AP IR-MALDI molecular image of toluidine blue O in the exposed areas under the grid based on the m/z 270.1 ion obtained using the “oversampling” method. **(b)** Averaged ion intensity profile perpendicular to the grid bars indicated a lateral resolution of 40 μm .



$\frac{A}{B}$

the rudimentary method of producing the distribution and to the inherent limitation on the spatial resolution imposed by the size of the laser focal spot. The focusing of the laser beam in our system is limited by the optical arrangement to ~ 250 μm spot size. Significant improvement can be expected from optics with higher numerical aperture. Short of complex designs and precision optical components this cannot be achieved with the long working distance (~ 5 cm) necessary to accommodate the sample inlet of our mass spectrometer. Thus, in order to improve the spatial resolution, we implemented the oversampling technique described by Jurchen *et al.* for vacuum UV-MALDI imaging.³¹ This method can only be used if the analyte is largely depleted in every interrogated point. By moving the translation stage to the next point with an increment smaller than the laser spot size, fresh sample surface is exposed. Collecting mass spectra from these partially fresh areas provides a higher spatial resolution limited by the step size of the translation stage.

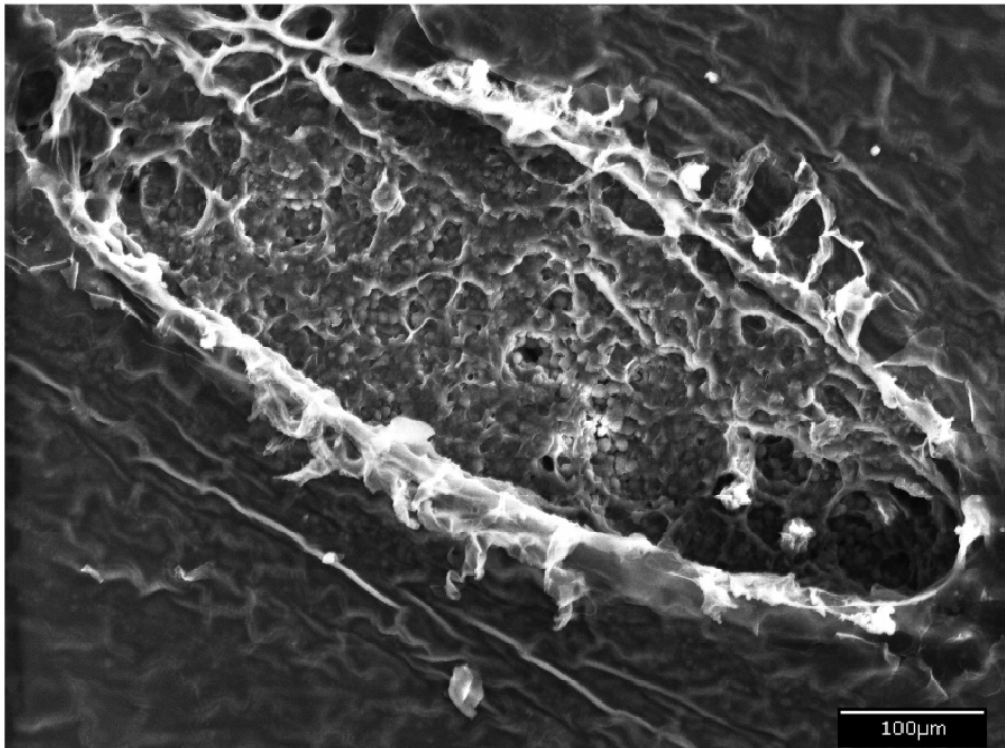
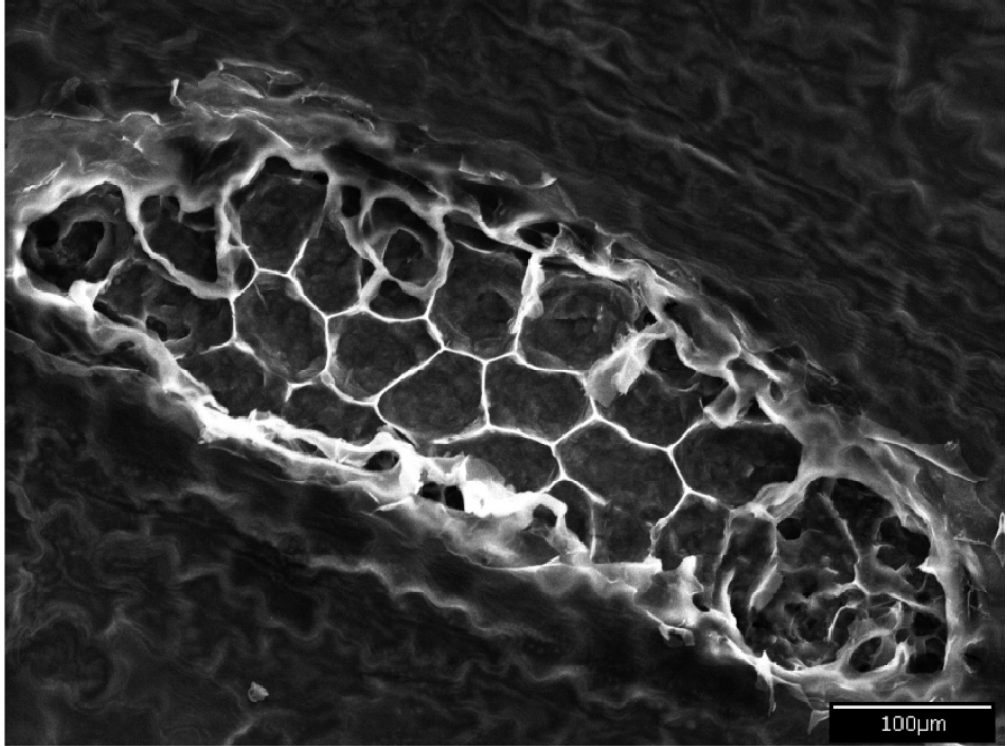
The left panel in Figure 2.3a shows the optical image of the electron microscope grid with 92 μm bar spacing used as a mask to cover a homogeneous toluidine blue surface. The created pattern was imaged by AP IR-MALDI with oversampling at a 40 μm step size (see the right panel in Figure 2.3a). In order to deplete the sample in a particular point a dwell time of 8 s was selected for each pixel. The image was constructed using the m/z 270.1 base peak representing the organic cation from the toluidine blue O salt. In Figure 2.3a the pattern created by the grid is clearly seen. Figure 2.3b corresponds to an ion intensity profile perpendicular to the grid bars. To get a rough estimate of the spatial resolution, we determined the distance along the profile for which the ion intensity increased from 20% to 80% of the maximum value. By this

definition, the spatial resolution in Figure 2.3b was $\sim 40\ \mu\text{m}$, approximately 5–6 times better than what was obtained with the limitation imposed by the laser spot size. As the smallest imaged details of the sample, the $92\ \mu\text{m}$ gaps were smaller than the diameter of the laser spot, these results clearly indicated the power of oversampling, i.e., without oversampling no features could be distinguished in this image.

It is interesting to note that oversampling is more likely to work with IR-than with UV-MALDI. It is known that the thickness of removed material for DHB in IR-MALDI is at least 10 times larger than in UV-MALDI.⁷⁸ Thus, the condition of largely depleted spots is easier to achieve with the IR laser. Indeed, for most of the samples in this study, the analyte ion signal decreased significantly upon multiple laser exposure of the same spot. Typically, after 50 laser shots, the signal intensity dropped by at least 1 order of magnitude.

Laser Ablation of Plant Tissue. To test the damage induced by the laser, the lamina of a peace lily leaf was mounted on a target plate and exposed to laser pulses that produced $0.27 \pm 0.03\ \text{J}/\text{cm}^2$ fluence in the elliptical focal area. Scanning electron microscope investigation of the interrogated area indicated the removal of the cuticle, the upper epidermis, part of the mesophyll, and the vascular bundles. Figure 2.4a shows the ablated area on a peace lily leaf after a single laser pulse. The tissue damage is localized to an elliptical area (due to the 45° angle of incidence) with 180 and $640\ \mu\text{m}$ for the small and large axes, respectively. The top waxy cuticle layer and part of the upper epidermal cells were removed, but no damage to the underlying tissue was apparent. Upon exposure to six laser pulses, the laser crater became slightly larger ($230\ \mu\text{m}$ by $720\ \mu\text{m}$) and some of the palisade and spongy mesophyll was also removed (see Figure 2.4 b). The

Figure 2.4 SEM images of ablation craters created by **(a)** a single and **(b)** six laser pulses of 0.27 (0.03 J/cm² fluence each, impinging on the upper surface of a peace lily plant (*Spathiphyllum*) leaf. After a single laser pulse, the tissue damage is localized to an elliptical area with 180 and 640 μm for the small and large axes, respectively. The top waxy cuticle layer and part of the upper epidermal cells were removed, but no damage to the underlying tissue was apparent. Upon exposure to six laser pulses, the laser crater became slightly larger (230 μm by 720 μm), and some of the palisade and spongy mesophyll was also removed.



A

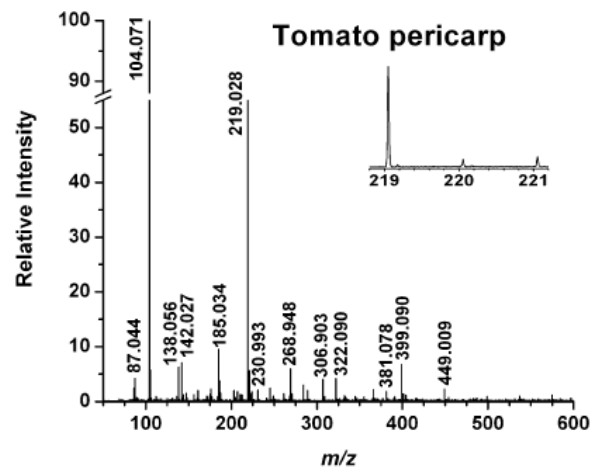
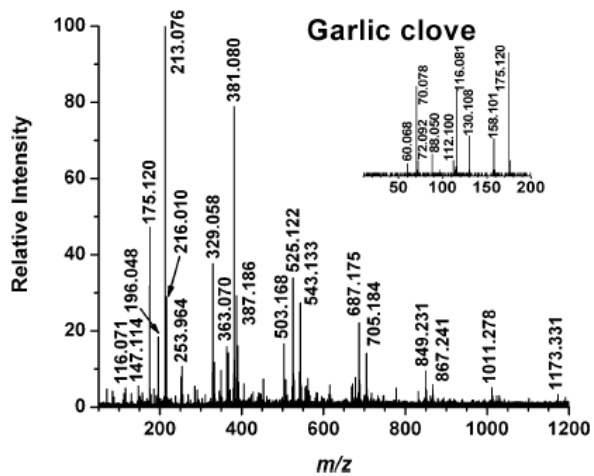
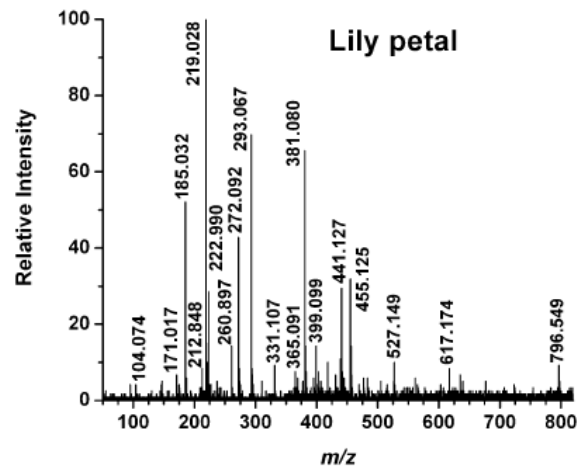
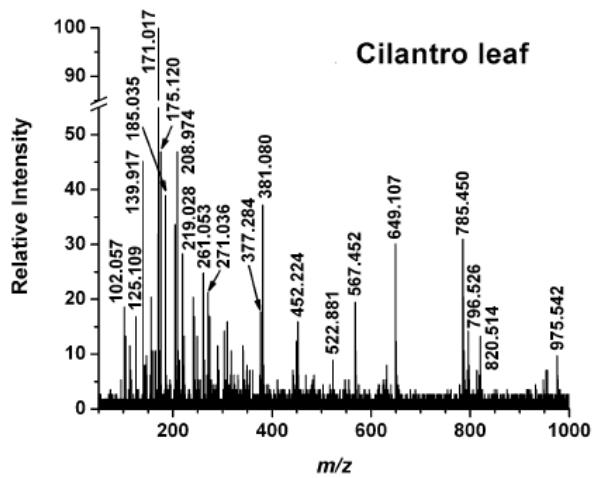
B

opening close to the center of the crater appears to be a stoma essential for gas exchange of the leaf.

Overall, it seemed the damage caused by the laser was localized with a fairly well-defined boundary and, in case of probing individual points, did not interfere with the viability of the plant. The vicinity of the ablation crater did not show the redeposition of ablated material. From the analytical and especially from the imaging point of view, this was advantageous because it lowered the risk of point-to-point cross-contamination. The multiple-exposure case indicated that the consecutive laser pulses sampled increasing depths through the gradual removal of the tissue.

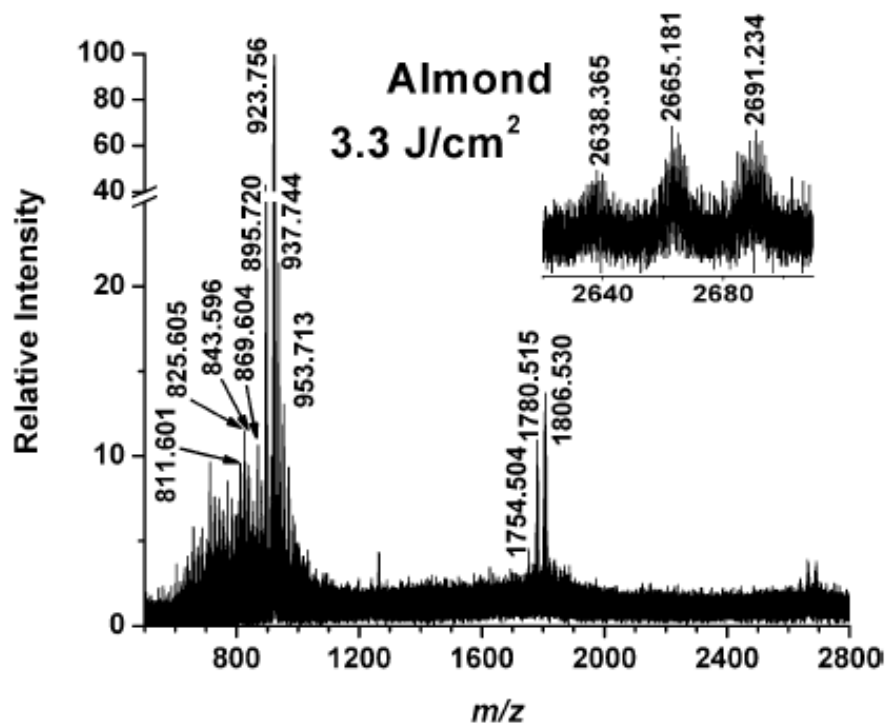
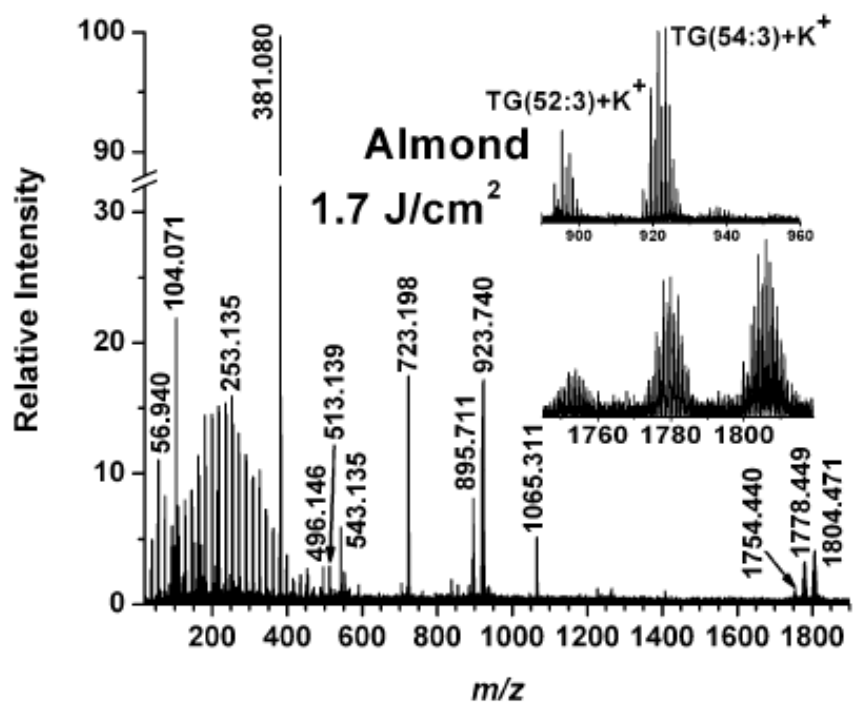
Ambient Plant Metabolomics. Water is a native component of biological samples. In particular, plants, especially fruits, are rich in water. On the basis of our experience with water as a matrix, AP IR-MALDI experiments were conducted on fruit tissue sections. To survey the range of detected metabolites, tissue sections were prepared from plant organs of various species and positive (see Figures 2.5 and 2.6) and negative ion AP IR-MALDI spectra (see Figure 2.7) were recorded. Figures 2.5 and 2.7 compare different plant organs in positive and negative modes, respectively. The effect of fluence, which is energy density measured in energy per area, was also investigated. Figure 2.6 contrasts low fluence (1.7 J/cm^2 in panel a) and high fluence (3.3 J/cm^2 in panel b) mass spectra from the same sample. We collected spectra from sections of the outer wall of the pericarp of a tomato fruit (Figure 2.5d); a segment of a white lily flower petal (Figures 2.5c and 2.7c); the storage tissue in the outer medulla section of potato tubers (Figure 2.7a); ground tissue in the cross section of banana fruit; onion (Figure

Figure 2.5 AP IR-MALDI mass spectra obtained in the positive ion mode from **(a)** the lamina of a cilantro leaf; **(b)** garlic bulb sections that exposed the storage tissue in the expanded leaf bases; **(c)** a segment of a white lily flower petal; and **(d)** sections of the outer wall of the pericarp of a tomato fruit. The inset in panel b shows the tandem mass spectrum of the m/z 175 ion that corresponds to protonated arginine. The isotopic distribution pattern for the m/z 219 ion in the inset of panel d is consistent with the presence of potassium.



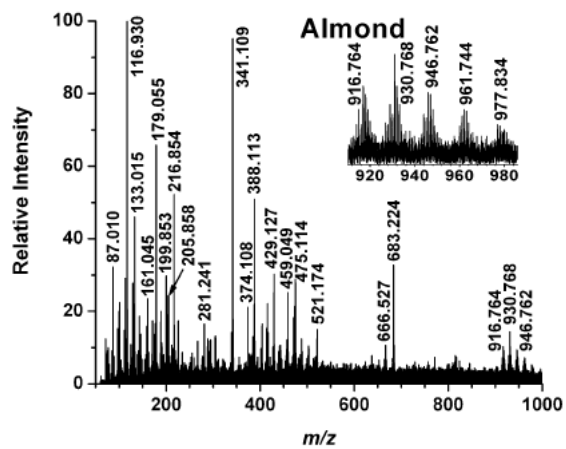
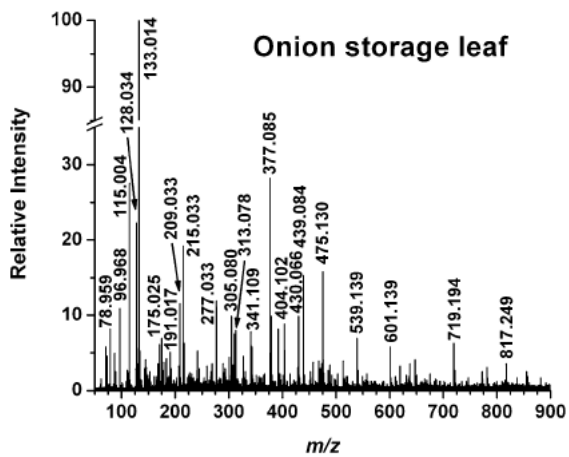
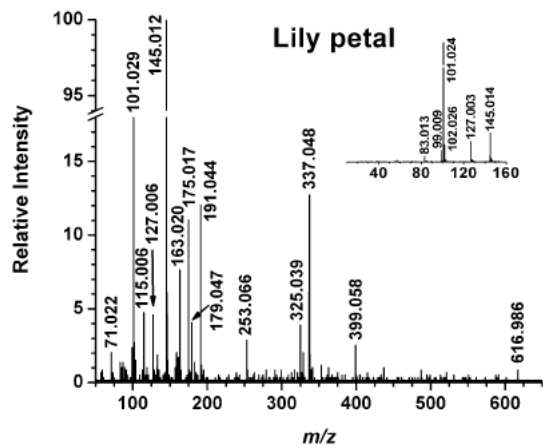
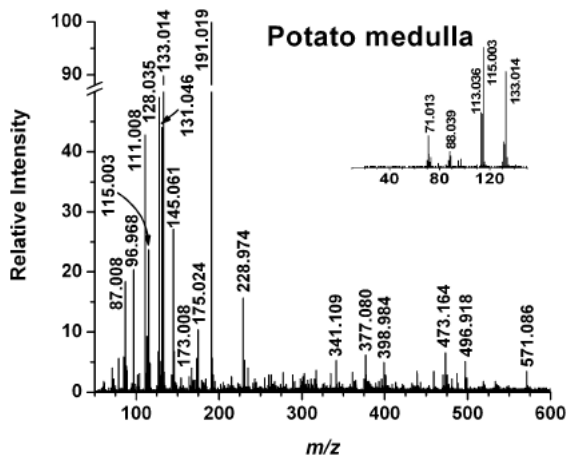
A/C
B/D

Figure 2.6 AP IR-MALDI mass spectra collected from the longitudinal section of an almond kernel for **(a)** low fluence (1.7 J/cm²) and **(b)** high fluence (3.3 J/cm²) exposures. The top inset in panel a shows triacylglycerol lipid distributions TG(52:4) to TG(52:2) and TG(54:6) to TG(54:3). The bottom inset in panel a zooms in on the potassiumated dimers from these lipids. The inset in panel b indicates the formation of lipid trimers at elevated fluences.



A
—
B

Figure 2.7 AP IR-MALDI mass spectra obtained in the negative ion mode for **(a)** the storage tissue in the outer medulla section of potato tubers, **(b)** onion storage leaf; **(c)** a segment of a white lily flower petal, and **(d)** a longitudinal section of an almond kernel. The insets in panels a and c are the tandem mass spectra of the ions with m/z 133 and 145 that are identified as malic acid and R-ketoglutaric acid, respectively. The inset in panel d depicts the zoomed triacylglycerol lipid distributions starting from TG(54:6).



A/C
B/D

2.7b) and garlic bulb (Figure 2.5b) sections that exposed the storage tissue in the expanded leaf bases; the cortex of a strawberry aggregate fruit containing several achenes and part of the accessory tissue of the receptacle; the lamina of a cilantro leaf (Figure 2.5a); and a longitudinal section of an almond kernel (Figures 2.6a and b, and 2.7d).

Tandem mass spectrometry results for selected ions are shown in the insets of Figures 2.5b, and 2.7a and c.

(a) Carbohydrates and Oligosaccharide Synthesis. Over 30 peaks were observed in the AP IR-MALDI mass spectra of most samples with cationized carbohydrates, important primary metabolites, prominent in most them. For example, the potassiated sucrose ion with m/z 381.077 was observed for all of the organs and all the species. In the mass spectra of tuber, fruit, and bulb tissues, this ion produced the most abundant peak, indicating high sucrose content. Sucrose is the major product of photosynthesis in plants and the dominant form in which carbohydrates are transferred from the leaves to the rest of the plant, to supply carbon and energy for growth and the accumulation of storage reserves. At m/z 365.106, the sodiated sucrose ion was also observed with lower intensity, consistent with the lower concentration of sodium than potassium in these tissues (See <http://www.nal.usda.gov>).

With the exception of spectra from potato tuber and garlic bulb tissues, another abundant ion was observed at m/z 219.028 corresponding to the potassiated hexose sugars ($[C_6H_{12}O_6 + K]^+$). In addition to the accurate mass value (4 ppm mass accuracy), the presence of potassium in this ion was also confirmed by the isotope pattern (see the inset in Figure 2.5d). In the positive ion spectra, the formation of oligosaccharides ($C_{6n}H_{10n}+2O_{5n+1}$) was detected up to $n = 5$ through the presence of tri-, tetra-, and

pentasaccharides (e.g., raffinose, stachyose, and verbascose, respectively) in bulbs and for the trisaccharides in fruits and seeds. In bulbs, starting from α -D-fructofuranose β -D-fructofuranose 1,2':1,2'-dianhydride ($C_{12}H_{20}O_{10}$), a series of fructans with a formula of $(C_6H_{10}O_5)_n$ was identified up to $n = 7$. A quantitative measure for the reliability of the peak assignments was expressed by the absolute deviation of measured and calculated monoisotopic mass values, Δm expressed in millidaltons. In this respect, all the carbohydrate assignments above were accurate within $\Delta m < \pm 7$ mDa. In some spectra, phosphorylated (m/z 261.053 and 268.948) and aminosugars (m/z 196.048) were also identified, although the fidelity of these assignments ($\Delta m < \pm 35$ mDa) was lower than that for the carbohydrates discussed above.

Due to the high abundance of hexose and sucrose in fruits, extensive clustering of these species was observed in the form of potassiated hexose dimers and sucrose dimers, trimers, and tetramers. In the negative ion spectra, hexose, sucrose, their clusters, and some mixed clusters with other molecules (water, and small organic acids) appeared through proton loss.

(b) Amino Acids. Amino acids were the second large group of observed primary metabolites. They appeared prominent in both the positive and negative ion spectra through cationization and proton loss, respectively. Glutamine, lysine, histidine, asparagine, and arginine in the positive ion mode were identified with $\Delta m < \pm 3$ mDa, whereas asparagine, aspartic acid, glutamine, glutamic acid, and histidine were observed in the negative ion spectra with $\Delta m < \pm 1$ mDa accuracy. The excellent mass accuracy in combination with the knowledge of the metabolic role of these compounds verified by their presence in the Arabidopsis database provided strong reinforcement in their

assignment. For example, the distinction of glutamine and lysine is usually problematic as both produce protonated molecular ions at nominal m/z 147. There is, however, a calculated $\Delta m = 36$ mDa difference in their monoisotopic masses. The accuracies for the measured glutamine and the lysine protonated ion m/z values were $\Delta m = 3$ and 1 mDa, respectively; thus, these amino acids could also be distinguished.

The inset in Figure 2.5b shows the tandem MS of the m/z 175.120 ion from garlic clove tissue. Based on accurate mass measurements, we assigned it as protonated arginine with a $\Delta m < \pm 1$ mDa accuracy. Comparison of the tandem mass spectrum in the inset with the NIST/EPA/NIH Mass Spectral Library revealed strong similarity with MS/MS fragmentation of protonated arginine through the presence of fragments with nominal m/z 175, 158, 130, 116, 112, 88, 72, 70, and 60. Although the peak intensities in the library spectrum were different from the ones we observed, the almost complete agreement of the fragmentation patterns provided yet another piece of evidence for the assignment of the parent ion.

In the negative ion spectra of glutamine, the deprotonated molecular ion with m/z 145.061 could be identified based on the good agreement with the calculated monoisotopic value of m/z 145.0613. In flower petals, however, there was a very abundant ion within $\Delta m = 49$ mDa. To further elucidate the structure of the $[M - H]^-$ ion, CAD was performed to produce the tandem mass spectrum (see the inset in Figure 2.7c). The dominant fragment ions with nominal m/z 127, 101, and 83 corresponded to neutral losses of H_2O , CO_2 , and $[H_2O + CO_2]$, respectively. Comparing this fragmentation pattern with the literature data⁷⁹ for the CAD of the glutamate ion revealed that the presence of the m/z 83 species was inconsistent with this

assignment. Due to the presence of the two carboxyl groups in α -ketoglutaric acid, the loss of both CO_2 and H_2O was more likely from its $[\text{M} - \text{H}]^-$ ion. The accurate mass of this ion, m/z 145.012, was also convincingly close to the calculated m/z 145.0137.

(c) Organic Acids. The third group of metabolites observed in the spectra can be classified as organic acids. The positive ions with m/z 104.071, 138.056, 169.029, and 230.993 were assigned as cationized γ -aminobutyric acid (GABA), aminobenzoic acid, 2-oxoisocaproic acid, and citric acid, respectively. The mass accuracy of these assignments was within $\Delta m < \pm 2$ mDa. In the negative ion spectra, the deprotonated forms of pyruvic acid (m/z 87.008), 2-furoic acid (m/z 111.008), fumaric acid (m/z 115.003), pyrrolinehydroxycarboxylate (m/z 128.035), malic acid (m/z 133.014), α -ketoglutaric acid (m/z 145.012), aconitic acid (m/z 173.008), ascorbic acid (m/z 175.017), oxalosuccinic acid (m/z 189.002), citric acid (m/z 191.019), quinic acid (m/z 191.044), and 5-hydroxyferulic acid (m/z 209.033) were noted. The m/z 101.029 ion could be derived from α - or β -ketobutyric acid or succinic acid semialdehyde through proton loss. The peak assignments were within $\Delta m < \pm 12$ mDa the measured m/z values.

(d) Lipids. Higher laser fluences were required to obtain mass spectra from almond seed tissue. Figure 2.6 compares the spectra at 1.7 J/cm² in panel a and 3.3 J/cm² in panel b. The need for higher fluence could be rationalized in terms of the lower water content of the seed tissue. In addition to the seed metabolites, typical lipid mass spectral patterns were observed in the vicinity of the most abundant m/z 895.711 and 923.740 ions. Comparison of these patterns with data from the LIPID MAPS database revealed the presence of unsaturated triacylglycerol (TG) mixtures. For example, the m/z 895.711 peak was consistent with the potassiumated TG(17:1(9Z)/17:1(9Z)/18:1(9Z)) with

calculated monoisotopic m/z 895.7157. In reality, any combination of acyl chain lengths that added up to 52 and any arrangement of the 3 double bonds along those chains would be consistent with the observed m/z within $\Delta m = -5$ mDa. To designate all possible structural isomers with the same m/z , this lipid can be denoted as TG(52:3). The neighboring peaks at m/z 893.7000 and 897.7313 corresponded to the potassiated TG(52:4) and TG(52:2) molecules, respectively. The lipid distribution was convoluted with the carbon isotope patterns for all three species.

Similarly, the m/z 923.740 ion could be identified as potassiated TG(18:1(9Z)/18:1(9Z)/18:1(9Z)) along with all of its structural isomers. The calculated monoisotopic mass for this ion produced m/z 923.7469. The notation for all isomers of this species included was TG(54:3). The neighboring peaks were produced by a convolution of TG(54:4), TG(54:5), and TG(54:6) with the carbon isotope distribution patterns. Three sets of peaks were observed at m/z 1754.440, 1778.449, and 1804.471.

These three groups could be explained as potassiated lipid dimers. For example, mixing two of the lighter lipids, [TG(52:2) + TG(52:3) + K]⁺ produced an m/z 1754.483 ion. Combining two heavier species, [2TG(54:4) + K]⁺, resulted in m/z 1804.499, whereas dimers mixed from both the light and heavy group, [TG(52:4) + TG(54:3) + K]⁺, produced m/z 1778.483. Further increasing the laser fluence to 3.3 J/cm² favored the formation of clusters. This is demonstrated in Figure 2.6b, where the intensity of dimer peaks is increased and the formation trimer patterns can be observed at m/z 2638.365, 2665.181, and 2691.234.

(e) Miscellaneous Metabolites. This is a diverse group that includes a few primary as well as secondary metabolites. Several nucleotides (thymidine diphosphate-d-

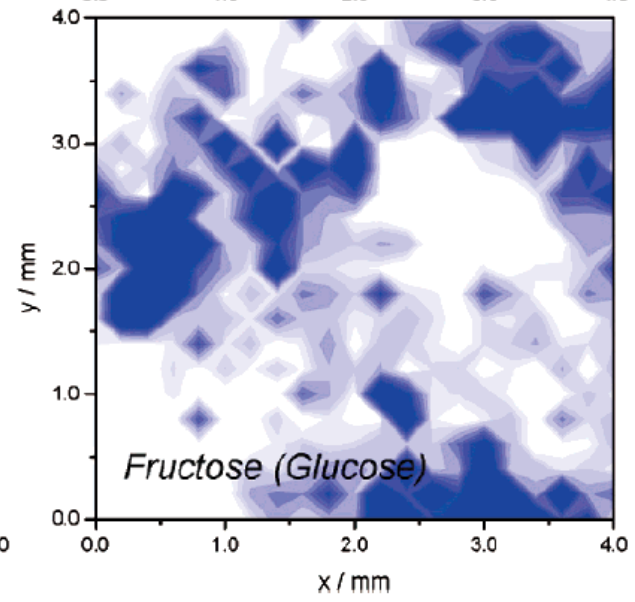
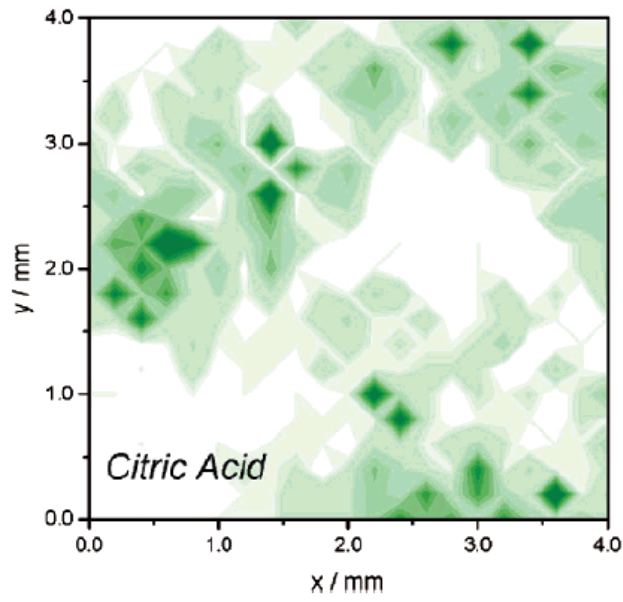
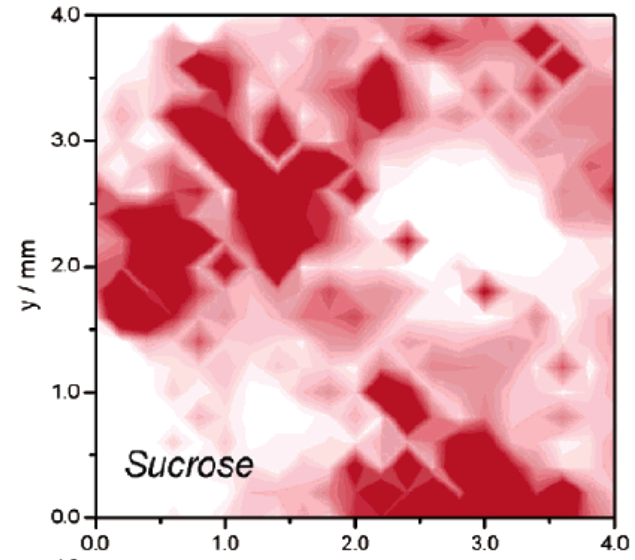
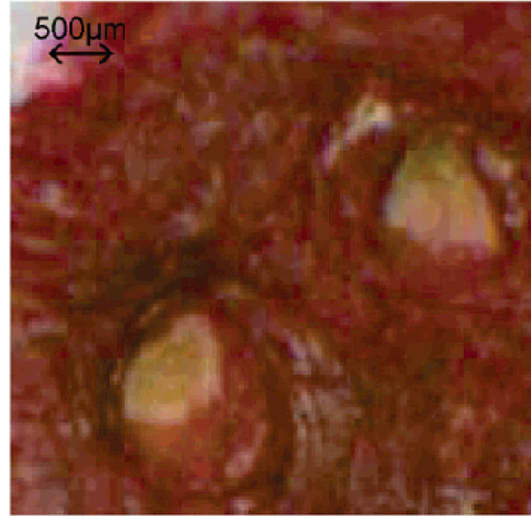
glucose, 2,4-dioxotetrahydropyrimidine d-ribonucleotide and aminoimidazole carboxamide ribonucleotide), and a nucleoside (guanosine), various phosphates (dihydroxyacetonephosphate, erythronate-4-phosphate, arginine phosphate, 2-C-methyl-d-erythritol-4-phosphate, 2-C-methyl-d-erythritol-2,4-cyclodiphosphate, and geranyl diphosphate), an amino acid derivative (alliin in garlic), and lipid-related compounds (β -D-galactopyranosyl-1-glycerol and 18:1–18:1-phosphatidylethanolamine) were found.

Among the secondary metabolites, we assigned some flavonoids and flavonoid precursors (e.g., quercetin 3-*O*-rutinoside, and 3,4-dihydroxy-2-butanone-4-phosphate), plant hormones (GA14, GA15, GA53, and GA110), a lignan (sesamolol), and a precursor of lignin biosynthesis (chlorogenic acid).

Molecular Imaging of Plant Tissue. On the basis of the robust signal from the main components in the studied fruits, low-resolution imaging experiments were performed on strawberry skin tissue. To complete the imaging in less than 30 min, a 21×21 pixel array was used with a 4 s/pixel dwell time and a 200 μm step size. It was found that longer scanning time led to significant dehydration of the sample, resulting in decreased signal intensity and skewed component distributions. To introduce chemical heterogeneity, the field of view was selected to include some seeds.

Together with the optical image, the distribution of the potassiumated sucrose, $[\text{Glc}\alpha(1\text{--}4)\beta\text{Fru} + \text{H}_2\text{O} + \text{K}]^+$, glucose and/or fructose, $[\text{Glc}/\text{Fru} + \text{K}]^+$, and citric acid are shown in Figure 2.8. Although the distributions of these water-soluble components are similar, the position of the two seeds, with lower concentrations of these compounds, is clearly discernible. The signal in the seed region was marginal and did not

Figure 2.8 Optical image of a strawberry skin (top left) compared to AP IR-MALDI images for three major components, sucrose (top right), glucose/fructose (bottom right), and citric acid (bottom left) around embedded seeds. The false color intensities were assigned according to integrated areas of the associated potassium peaks. Although the distributions of these water-soluble components are similar, the position of the two seeds, with lower concentrations of these compounds, is clearly discernible.



allow the identification of the chemical components present. As the scanning step size of 200 μm was comparable to the dimensions of the seeds their shape is not reflected accurately in the molecular images. Nevertheless the information on the spatial distribution of these small metabolites can be useful in exploring biosynthesis and metabolic pathways in plants.

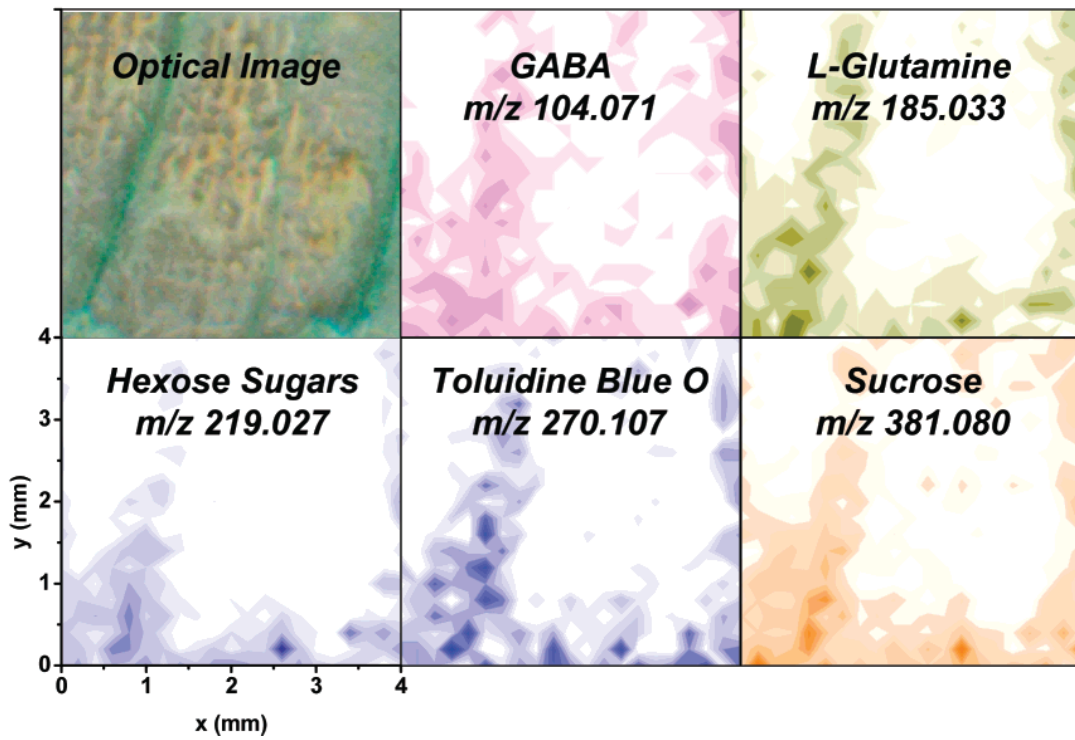
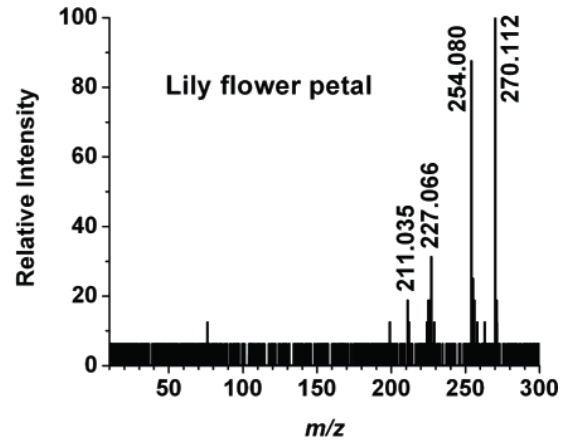
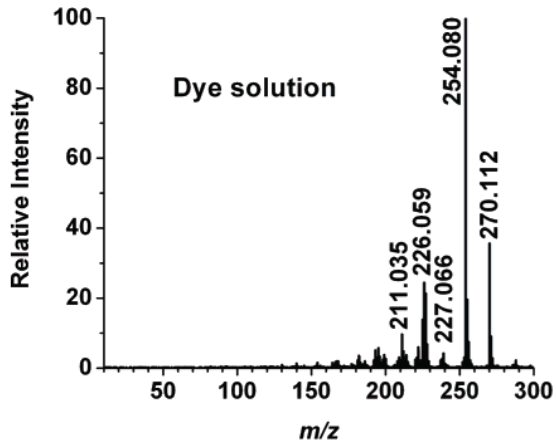
The ability to perform AP IR-MALDI using native water as the matrix enables the in vivo investigation of the spatial distributions and temporal variations of chemical components in plant and animal tissues. The current limitations on the step size are not fundamental as both the laser focal spot and the translation stage step size can be reduced. Drying of the tissue during data acquisition can be mitigated by using a higher repetition rate laser and by providing an environment of controlled humidity, for example in an environmental chamber, for the analysis. Spatial correlations of unknown constituents can be used in deciphering their role in the organism.

Metabolic Imaging and Fluid Transport Induced by Plant Transpiration.

The stability of the AP IR-MALDI signal and the obtained ion intensities enabled us to perform imaging experiments on plant tissues. To produce a known chemical contrast, the cut end of a white lily plant stem was immersed into toluidine blue O chloride dye solution (1 drop of 1% dye solution in 200 mL of deionized water). In 48 h, a visual observation of the originally white flower petals indicated light blue discoloration. Correspondingly, a positive ion with m/z 270.112 was observed in the AP IR-MALDI mass spectrum, very close to the monoisotopic m/z 270.1065 calculated for the organic cation of the toluidine blue O ion. To further confirm the identity of this species, tandem AP IR-MALDI mass spectra of the nominal m/z 270 ion produced from the dye

solution and from the flower petal were compared (see Figure 2.9a). The good agreement between the two fragmentation patterns supported the assignment of the m/z 270.112 ion from the flower petal as the toluidine blue O cation. This further confirmed the visual observation that the blue dye was absorbed by the plant stem and transported to the flower petals by the transpirational pull. A $10 \times 20 \text{ mm}^2$ section of the flower petal was removed and transferred onto the target plate for the imaging experiment. A coarse array of 21×21 pixels was used for AP IR-MALDI imaging with the dwell time and scanning step size set to 5 s and $200 \text{ }\mu\text{m}$, respectively. The image acquisition was completed in under 45 min. Figure 2.9b shows the optical image of the lily flower petal after the imaging experiment along with the distributions of GABA, glutamine, hexose sugars, toluidine blue O, and sucrose. Close inspection of the stained flower petal under the optical microscope revealed that the dye concentration was higher in the vasculature. The primary and secondary veins in the petal appeared to be stained stronger, and this, observation was reflected in the optical image (top left panel in Figure 2.9b). Correspondingly, the distribution of toluidine blue O molecules indicated higher concentrations in the vasculature. The blue color in the optical image and the toluidine blue O distribution reflected by AP IR-MALDI appeared to be highly correlated (see Figure 2.9b). Somewhat lower, but still strong spatial correlation was observed for the nutrients (sucrose and hexose) as well as for the other two metabolites (GABA and glutamine). Indeed, it is known that these components are transported and distributed in the plant by the phloem within the vascular bundle. The correlation between the vascular architecture and nutrient availability within a plant had been demonstrated by observing isotope and dye distributions.⁸⁰ This so-called sectoriality has far-reaching implications

Figure 2.9 (a) Comparison of the tandem mass spectra of the nominal m/z 270 ion observed in the AP IR-MALDI mass spectra of toluidine blue O dye solution (left panel) and white lily flower petal after 48 h (right panel). **(b)** Optical and AP IR-MALDI images of the white lily flower petal section stained in the fluid transport experiment. Spatial distributions of GABA, glutamine, hexose sugars, toluidine blue O, and sucrose in the petal show a higher concentration of nutrients and metabolites in the vasculature.



A

B

for plant development and even ecology. The spatial resolution in the molecular image is not sufficient to discern details on the cellular level. This limitation, however, can be resolved by tighter focusing of the laser beam. To obtain smaller focal spots, a shorter focal length focusing lens is needed and the laser beam divergence has to be reduced. This latter can be achieved by using a beam expander. Further improvement can be expected from taking advantage of aspherical optics or fiber optics.

CONCLUSIONS

Molecular imaging with MALDI mass spectrometry is a rapidly developing field. Most imaging work in the literature focuses on UV-MALDI imaging in vacuum environment with the help of an external matrix overlayer. In this contribution our first results with AP IR-MALDI are described that enable imaging at atmospheric pressure without the addition of an artificial matrix. Instead, the native water content of the biological tissue is utilized as an energy absorbing matrix. The results are encouraging as the major water-soluble components in various fruits have been detected, identified, and their molecular distributions were imaged. It is essential, however, to explore if components with lower concentration and/or water-insoluble molecules are amenable for AP IR-MALDI. On the basis of studies in artificial matrixes, the sensitivity of our interface and mass spectrometer was verified at the ~ 1 fmol/pixel level. This indicates that the instrument is capable of detecting trace constituents of a sample.

An important limitation of UV-MALDI imaging in vacuum environment is the reduced amount of information in the low mass ($m/z < 1000$) region. Due to matrix interferences, this limitation becomes most apparent in the $m/z < 500$ domain. This

might present a serious impediment in its application to following low molecular components, such as amino acids, organic acids, and saccharides, in metabolomics studies. We also demonstrated that AP IR-MALDI mass spectrometry can serve as an effective tool for quick identification of a wide array of metabolites, including simple carbohydrates, oligosaccharides, amino acids, organic acids, lipids, and a variety of other compounds, in plant tissues. An unexplored aspect of AP IR-MALDI is its potential for depth profiling in biological systems. Comparing Figure 1a and b shows how consecutive laser pulses sample deeper and deeper layers of the tissue. To take advantage of this capability, the removal rates of various tissues through laser ablation have to be established.

This work can in part rely on the extensive data available for laser surgery applications. Indeed, ultimately the AP IR-MALDI chemical sampling can be combined with laser surgery. The analytical technique could be used to accurately monitor the removal of abnormal tissue through the mass spectrometric analysis of the ablated plume. There are diverse potential applications for AP IR-MALDI in the life sciences. For example in plant biology, AP IR-MALDI imaging can be utilized to follow metabolism changes in genetically modified plants. In plant physiology experiments, the plant metabolic response to stress, such as starvation or drought conditions, can be monitored. In plant ecology, the understanding of plant–herbivore and plant–insect interactions can be facilitated by AP IR-MALDI mass spectrometry.

As water is a native component of plant and animal tissues, the ability to perform AP IR-MALDI using water as the matrix enables the *in vivo* investigation of complex biological systems in their natural state. The damage inflicted on the tissue during

imaging experiments is superficial (a few micrometers in depth); thus, larger organisms (e.g., plants) can survive the imaging experiments. Improvements in focusing and instrumental sensitivity can further enhance the applicability of this method for in vivo investigations by minimizing this damage.

ACKNOWLEDGEMENTS

The authors are grateful for the support of this work by the W. M. Keck Foundation (041904), the U.S. Department of Energy (DEFG02-01ER15129), and the George Washington University Research Enhancement Fund. B.S. is grateful to B. N. Walker and J. Stolee for helping with taking the SEM images.

REFERENCES:

- (1) Pacholski, M. L.; Winograd, N. *Chem.Rev.* **1999**, *99*, 2977-3005.
- (2) Todd, P. J.; Schaaff, T. G.; Chaurand, P.; Caprioli, R. M. *Journal of Mass Spectrometry* **2001**, *36*, 355-369.
- (3) Rubakhin, S. S.; Jurchen, J. C.; Monroe, E. B.; Sweedler, J. V. *Drug Discov. Today* **2005**, *10*, 823-837.
- (4) Caldwell, R. L.; Caprioli, R. M. *Molecular & Cellular Proteomics* **2005**, *4*, 394-401.
- (5) McPhail, D. S. *Journal of Materials Science* **2006**, *41*, 873-903.
- (6) Stoeckli, M.; Chaurand, P.; Hallahan, D. E.; Caprioli, R. M. *Nature Medicine* **2001**, *7*, 493-496.

- (7) Hsieh, Y.; Casale, R.; Fukuda, E.; Chen, J. W.; Knemeyer, I.; Wingate, J.; Morrison, R.; Korfmacher, W. *Rapid Communications in Mass Spectrometry* **2006**, *20*, 965-972.
- (8) Altelaar, A. F. M.; Klinkert, I.; Jalink, K.; de Lange, R. P. J.; Adan, R. A. H.; Heeren, R. M. A.; Piersma, S. R. *Analytical Chemistry* **2006**, *78*, 734-742.
- (9) Wang, H. Y. J.; Jackson, S. N.; McEuen, J.; Woods, A. S. *Analytical Chemistry* **2005**, *77*, 6682-6686.
- (10) Rohner, T. C.; Staab, D.; Stoeckli, M. *Mechanisms of Ageing and Development* **2005**, *126*, 177-185.
- (11) Maddalo, G.; Petrucci, F.; Iezzi, M.; Pannellini, T.; Del Boccio, P.; Ciavardelli, D.; Biroccio, A.; Forli, F.; Di Ilio, C.; Ballone, E.; Urbani, A.; Federici, G. *Clinica Chimica Acta* **2005**, *357*, 210-218.
- (12) Crecelius, A. C.; Cornett, D. S.; Caprioli, R. M.; Williams, B.; Dawant, B. M.; Bodenheimer, B. *Journal of the American Society for Mass Spectrometry* **2005**, *16*, 1093-1099.
- (13) Touboul, D.; Piednoel, H.; Voisin, V.; De La Porte, S.; Brunelle, A.; Halgand, F.; Laprevote, O. *European Journal of Mass Spectrometry* **2004**, *10*, 657-664.
- (14) Luxembourg, S. L.; Mize, T. H.; McDonnell, L. A.; Heeren, R. M. A. *Analytical Chemistry* **2004**, *76*, 5339-5344.
- (15) Brunelle, A.; Touboul, D.; Piednoel, H.; Voisin, V.; De La Porte, S.; Tallarek, E.; Hagenhoff, B.; Halgand, F.; Laprevote, O. *Molecular Biology of the Cell* **2004**, *15*, 103A-104A.

- (16) Reyzer, M. L.; Hsieh, Y. S.; Ng, K.; Korfmacher, W. A.; Caprioli, R. M. *Journal of Mass Spectrometry* **2003**, *38*, 1081-1092.
- (17) Kruse, R.; Sweedler, J. V. *Journal of the American Society for Mass Spectrometry* **2003**, *14*, 752-759.
- (18) Chaurand, P.; Fouhecourt, S.; DaGue, B. B.; Xu, B. G. J.; Reyzer, M. L.; Orgebin-Crist, M. C.; Caprioli, R. M. *Proteomics* **2003**, *3*, 2221-2239.
- (19) Spengler, B.; Hubert, M. *Journal of the American Society for Mass Spectrometry* **2002**, *13*, 735-748.
- (20) Chaurand, P.; Schwartz, S. A.; Caprioli, R. M. *Current Opinion in Chemical Biology* **2002**, *6*, 676-681.
- (21) Koomen, J. M.; Russell, W. K.; Hettick, J. M.; Russell, D. H. *Analytical Chemistry* **2000**, *72*, 3860-3866.
- (22) Chaurand, P.; Stoeckli, M.; Caprioli, R. M. *Anal.Chem.* **1999**, *71*, 5263-5270.
- (23) Zhang, H.; Stoeckli, M.; Andren, P. E.; Caprioli, R. M. *Journal of Mass Spectrometry* **1999**, *34*, 377-383.
- (24) Stoeckli, M.; Farmer, T. B.; Caprioli, R. M. *Journal of the American Society for Mass Spectrometry* **1999**, *10*, 67-71.
- (25) Chaurand, P.; Caprioli, R. M. *Electrophoresis* **2002**, *23*, 3125-3135.
- (26) Caprioli, R. M.; Farmer, T. B.; Gile, J. *Analytical Chemistry* **1997**, *69*, 4751-4760.
- (27) Chaurand, P.; DaGue, B. B.; Pearsall, R. S.; Threadgill, D. W.; Caprioli, R. M. *Proteomics* **2001**, *1*, 1320-1326.
- (28) Luxembourg, S. L.; McDonnell, L. A.; Duursma, M. C.; Guo, X. H.; Heeren, R. M. A. *Analytical Chemistry* **2003**, *75*, 2333-2341.

- (29) Altelaar, A. F. M.; van Minnen, J.; Jimenez, C. R.; Heeren, R. M. A.; Piersma, S. R. *Analytical Chemistry* **2005**, *77*, 735-741.
- (30) James, A.; Dindyal-Popescu, A.; Scott, G.; Zhao, J. Y. *Clinical Chemistry* **2005**, *51*, A204-A205.
- (31) Jurchen, J. C.; Rubakhin, S. S.; Sweedler, J. V. *Journal of the American Society for Mass Spectrometry* **2005**, *16*, 1654-1659.
- (32) Luxembourg, S. L.; McDonnell, L. A.; Mize, T. H.; Heeren, R. M. A. *Journal of Proteome Research* **2005**, *4*, 671-673.
- (33) McCombie, G.; Staab, D.; Stoeckli, M.; Knochenmuss, R. *Analytical Chemistry* **2005**, *77*, 6118-6124.
- (34) Crossman, L.; McHugh, N. A.; Hsieh, Y. S.; Korfmacher, W. A.; Chen, J. W. *Rapid Communications in Mass Spectrometry* **2006**, *20*, 284-290.
- (35) Lemaire, R.; Tabet, J. C.; Ducoroy, P.; Hendra, J. B.; Salzet, M.; Fournier, I. *Analytical Chemistry* **2006**, *78*, 809-819.
- (36) Lisec, J.; Schauer, N.; Kopka, J.; Willmitzer, L.; Fernie, A. R. *Nature Protocols* **2006**, *1*, 387-396.
- (37) Wink, M. *Theor. Appl. Genet.* **1988**, *75*, 225-233.
- (38) Dunn, W. B.; Overy, S.; Quick, W. P. *Metabolomics* **2005**, *1*, 137-148.
- (39) Roessner, U.; Wagner, C.; Kopka, J.; Trethewey, R. N.; Willmitzer, L. *The Plant Journal* **2000**, *23*, 131-142.
- (40) Tolstikov, V. V.; Lommen, A.; Nakanishi, K.; Tanaka, N.; Fiehn, O. *Anal. Chem.* **2003**, *75*, 6737-6740.

- (41) Edwards, E. L.; Rodrigues, J. A.; Ferreira, J.; Goodall, D. M.; Rauter, A. P.; Justino, J.; Thomas-Oates, J. *Electrophoresis* **2006**, *27*, 2164-2170.
- (42) Wolfender, J.; Ndjoko, K.; Hostettmann, K. *Journal of Chromatography A* **2003**, *1000*, 437-455.
- (43) Garratt, L. C.; Linforth, R.; Taylor, A.; Lowe, K. C.; Power, J. B.; Davey, M. R. *Plant Biotechnology Journal* **2005**, *3*, 165-174.
- (44) Zhou, R.; Squires, T. M.; Ambrose, S. J.; Abrams, S. R.; Ross, A. R. S.; Cutler, A. J. *Journal of Chromatography A* **2003**, *1010*, 75-85.
- (45) Fiehn, O.; Kopka, J.; Threthewey, R. N.; Willmitzer, L. *Anal. Chem.* **2000**, *72*, 3573-3580.
- (46) Keurentjes, J. J. B.; Fu, J.; Ric de Vos, C. H.; Lommen, A.; Hall, R. D.; Bino, R. J.; van der Plas, L. H. W.; Jansen, R. C.; Vreugdenhil, D.; Koornneef, M. *Nature Genetics* **2006**, *38*, 842-849.
- (47) El-Zohri, M. H. A.; Cabala, R.; Frank, H. *Anal. Bioanal. Chem.* **2005**, *382*, 1871-1876.
- (48) Fenselau, C. *Anal. Chem.* **1997**, *69*, A661-A665.
- (49) Kahn, M. L.; Parra-Colmenares, A.; Ford, C. L.; Kaser, F.; McCaskill, D.; Ketchum, R. E. *Analytical Biochemistry* **2002**, *307*, 219-225.
- (50) Allen, J.; Davey, H. M.; Broadhurst, D.; Heald, J. K.; Rowland, J. J.; Oliver, S. G.; Kell, D. B. *Nature Biotechnology* **2003**, *21*, 692-696.
- (51) Li, L.; Garden, R. W.; Sweedler, J. V. *Trends Biotechnol.* **2000**, *18*, 151-160.
- (52) Laiko, V. V.; Baldwin, M. A.; Burlingame, A. L. *Analytical Chemistry* **2000**, *72*, 652-657.

- (53) Galicia, M. C.; Vertes, A.; Callahan, J. H. *Analytical Chemistry* **2002**, *74*, 1891-1895.
- (54) Doroshenko, V. M.; Laiko, V. V.; Taranenko, N. I.; Berkout, V. D.; Lee, H. S. *International Journal of Mass Spectrometry* **2002**, *221*, 39-58.
- (55) Callahan, J. H.; Galicia, M. C.; Vertes, A. *Applied Surface Science* **2002**, *197*, 130-137.
- (56) Laiko, V. V.; Moyer, S. C.; Cotter, R. J. *Analytical Chemistry* **2000**, *72*, 5239-5243.
- (57) Moyer, S. C.; Cotter, R. J.; Woods, A. S. *Journal of the American Society for Mass Spectrometry* **2002**, *13*, 274-283.
- (58) Moyer, S. G.; Cotter, R. J. *Analytical Chemistry* **2002**, *74*, 468A-476A.
- (59) Zhang, J. H.; LaMotte, L. T.; Dodds, E. D.; Lebrilla, C. B. *Analytical Chemistry* **2005**, *77*, 4429-4438.
- (60) Hanton, S. D.; Parees, D. M.; Zweigenbaum, J. *Journal of the American Society for Mass Spectrometry* **2006**, *17*, 453-458.
- (61) Creaser, C. S.; Ratcliffe, L. *Current Analytical Chemistry* **2006**, *2*, 9-15.
- (62) Wang, Y.; Schneider, B. B.; Covey, T. R.; Pawliszyn, J. *Analytical Chemistry* **2005**, *77*, 8095-8101.
- (63) Von Seggern, C. E.; Cotter, R. J. *J. Mass Spectrom.* **2004**, *39*, 736-742.
- (64) Von Seggern, C. E.; Moyer, S. C.; Cotter, R. J. *Anal. Chem.* **2003**, *75*, 3212-3218.
- (65) Von Seggern, C. E.; Zarek, P. E.; Cotter, R. J. *Analytical Chemistry* **2003**, *75*, 6523-6530.
- (66) Tan, P. V.; Taranenko, N. I.; Laiko, V. V.; Yakshin, M. A.; Prasad, C. R.; Doroshenko, V. M. *Journal of Mass Spectrometry* **2004**, *39*, 913-921.
- (67) Berkenkamp, S.; Kirpekar, F.; Hillenkamp, F. *Science* **1998**, *281*, 260-262.

- (68) Berkenkamp, S.; Karas, M.; Hillenkamp, F. *Proceedings of the National Academy of Sciences of the United States of America* **1996**, *93*, 7003-7007.
- (69) Daniel, J. M.; Laiko, V. V.; Doroshenko, V. M.; Zenobi, R. *Analytical and Bioanalytical Chemistry* **2005**, *383*, 895-902.
- (70) Daniel, J. M.; Ehala, S.; Friess, S. D.; Zenobi, R. *Analyst* **2004**, *129*, 574-578.
- (71) Xu, Y. C.; Little, M. W.; Murray, K. K. *Journal of the American Society for Mass Spectrometry* **2006**, *17*, 469-474.
- (72) Lawson, S. J.; Murray, K. K. *Rapid Communications in Mass Spectrometry* **2000**, *14*, 129-134.
- (73) Dreisewerd, K.; Kolbl, S.; Peter-Katalinic, J.; Berkenkamp, S.; Pohlentz, G. *Journal of the American Society for Mass Spectrometry* **2006**, *17*, 139-150.
- (74) Laiko, V. V.; Taranenko, N. I.; Berkout, V. D.; Yakshin, M. A.; Prasad, C. R.; Lee, H. S.; Doroshenko, V. M. *J. Am. Soc. Mass Spectrom* **2002**, *13*, 354-361.
- (75) Tan, P. V.; Laiko, V. V.; Doroshenko, V. M. *Analytical Chemistry* **2004**, *76*, 2462-2469.
- (76) Moyer, S. C.; Marzilli, L. A.; Woods, A. S.; Laiko, V. V.; Doroshenko, V. M.; Cotter, R. J. *International Journal of Mass Spectrometry* **2003**, *226*, 133-150.
- (77) Kirpekar, F.; Berkenkamp, S.; Hillenkamp, F. *Analytical Chemistry* **1999**, *71*, 2334-2339.
- (78) Kampmeier, J.; Dreisewerd, K.; Schurenberg, M.; Strupat, K. *Int. J. Mass Spectrom. Ion Proc.* **1997**, *169/170*, 31-41.
- (79) Kulik, W.; Heerma, W. *Biomedical and Environmental Mass Spectrometry* **1988**, *15*, 419-427.
- (80) Orians, C. M.; Ardon, M.; Mohammad, B. A. *Am. J. Bot.* **2002**, *89*, 270-278.

CHAPTER 3

RAPID ANALYSIS OF PHARMACEUTICALS AND EXCRETED XENOBIOTIC AND ENDOGENOUS METABOLITES WITH ATMOSPHERIC PRESSURE INFRARED MALDI MASS SPECTROMETRY

Based on material published by B. Shrestha, Y. Li, and A.

Vertes in *Metabolomics*, **2008**, *4*, 297-311.

ABSTRACT

Atmospheric pressure (AP) infrared (IR) matrix-assisted laser desorption/ionization (MALDI) mass spectrometry (MS) was demonstrated for the rapid direct analysis of pharmaceuticals, and excreted human metabolites. More than 50 metabolites and excreted xenobiotics were directly identified in urine samples with high throughput. As the water content of the sample was serving as the matrix, AP IR-MALDI showed no background interference in the low mass range. The structure of targeted ions was elucidated from their fragmentation pattern using collision activated dissociation. The detection limit for pseudoephedrine was found to be in the sub-femtomole range and the semi-quantitative nature of the technique was tentatively demonstrated for a metabolite, fructose, by using a homologous internal standard, sucrose. A potential application of AP IR-MALDI for intestinal permeability studies was also explored using polyethylene glycol.

INTRODUCTION

Advances in combinatorial chemistry have led to a remarkable increase in the synthesis of drug candidates. As a result high-throughput analytical techniques are needed for drug detection and structural identification during synthesis and assessment of biological activity. ¹ Mass spectrometry is a well established tool for the analysis of xenobiotic and endogenous metabolites. ²⁻⁵ Many other non-mass spectrometric techniques, such as infrared spectrometry, ⁶⁻⁸ Raman spectroscopy, ⁹ terahertz imaging, ¹⁰ fluorescence spectroscopy, ¹¹ and nuclear magnetic resonance, ¹²⁻¹⁴ provide useful and complementary information on their chemical composition. Mass spectrometry gives unique insights into metabolism due to its high sensitivity and the ability to selectively identify these molecules through fragmentation studies. The detection of metabolites for medical diagnosis and for clinical or forensic toxicology is dominated by hyphenated approaches, ^{5, 15, 16} such as gas chromatography-MS, ¹⁷ liquid chromatography-MS, ^{18, 19} and capillary electrophoresis-MS. ²⁰ The conventional mass spectrometric methods for drug and metabolite studies require extensive sample preparation and/or extended analysis time.

Sample preparation and analysis time can be reduced by using ambient ion sources. A variety of recently introduced methods, including desorption electrospray ionization (DESI), ²¹⁻²⁴ direct analysis in real time (DART), ²⁵ desorption atmospheric pressure chemical ionization (DAPCI), ²⁶ extractive electrospray ionization (EESI), ^{27, 28} plasma-assisted desorption/ionization (PADI), ²⁹ and laser ablation electrospray ionization (LAESI), ³⁰ have demonstrated the capability of ambient analysis of complex samples without extensive sample preparation. A recent comparative study of DESI,

DART, and DAPCI has shown that the three methods provide complementary information for a range of pharmaceuticals.³¹

Since its inception in 1988, matrix-assisted laser desorption/ionization (MALDI) mass spectrometry (MS) has been used as a tool for analysis of large biomolecules and synthetic polymers.^{32, 33} The application of MALDI MS for low mass compounds of biological interest,^{34, 35} such as carbohydrates, amino acids etc., has been recently reviewed.³⁶ The use of MALDI for the analysis of small molecules is primarily limited by often overwhelming background interference from the matrix molecules in the low mass region. To overcome this limitation, Siuzdak and coworkers introduced a matrix-free approach called desorption ionization on silicon (DIOS).³⁷ DIOS and other matrix-free laser ionization methods, e.g., laser-induced silicon micro-column arrays (LISMA), have demonstrated excellent sensitivity for small molecule analysis.^{38, 39} With these methods, however, the direct analysis of biological fluids has not been demonstrated.

At mid-infrared laser wavelengths (2.94 μm), a non-interfering MALDI matrix, such as ice or water can also be used to analyze proteins and small metabolites.^{40, 41} As most cells and tissues contain 60 to 90% water, it is an attractive matrix to study biological samples. Many pharmaceutical formulations (e.g., syrups, ointments and gels) and mother liquors in pharmaceutical synthesis also contain significant amounts of water. Atmospheric pressure (AP) IR-MALDI could enable the rapid direct analysis of these samples with little or no sample preparation.^{42, 43}

Soft laser desorption ionization techniques use a focused laser beam to ionize the sample. This local analysis capability enables chemical imaging of biological tissues to spatially map the distribution of pharmaceutical compounds in various tissues.⁴⁴⁻⁴⁶ In

addition to providing an attractive alternative for imaging the distribution of pharmaceuticals and their metabolites in tissue without the need to apply an external matrix, AP IR-MALDI could also enable high-throughput analysis of samples in a multi-well plate under ambient conditions. We have recently described the utility of AP IR-MALDI for the analysis and imaging of plant metabolites directly from tissue samples.⁴¹,⁴⁷ The present study explores the use of AP IR-MALDI for the analysis of selected pharmaceuticals in their commercial formulations, and the related metabolites in human urine.

EXPERIMENTAL SECTION

AP IR-MALDI Instrumentation. All the experiments were carried out with an orthogonal acceleration time-of-flight mass spectrometer, Q-TOF Premier (Waters Co., Milford, MA), utilizing a custom made AP MALDI interface similar to one described on the experimental section of chapter 2. The sample deposited on a stainless steel target was ionized by a Nd:YAG laser-driven optical parametric oscillator (Opotek, Carlsbad, CA) running at 2.94 μm wavelength, 10 Hz repetition rate, and 5 ns pulse width. The laser beam was steered and aligned by SiO protected gold mirrors (Thorlabs, Newton, NJ) with >97.5% reflectivity to a plano-convex calcium fluoride lens with 50 mm focal length (Infrared Optical Products, Farmingdale, NY). The laser beam was focused with the lens to the target surface at an approximately 45° incidence angle producing an elliptical laser spot with $\sim 250 \times 650 \mu\text{m}^2$ dimensions. The average pulse energy was 240 $\pm 10 \mu\text{J}$, which corresponded to a fluence of 0.20 $\pm 0.02 \text{ J/cm}^2$. The target was placed on a 3-axis translation stage for sample positioning and geometry optimization. The distance

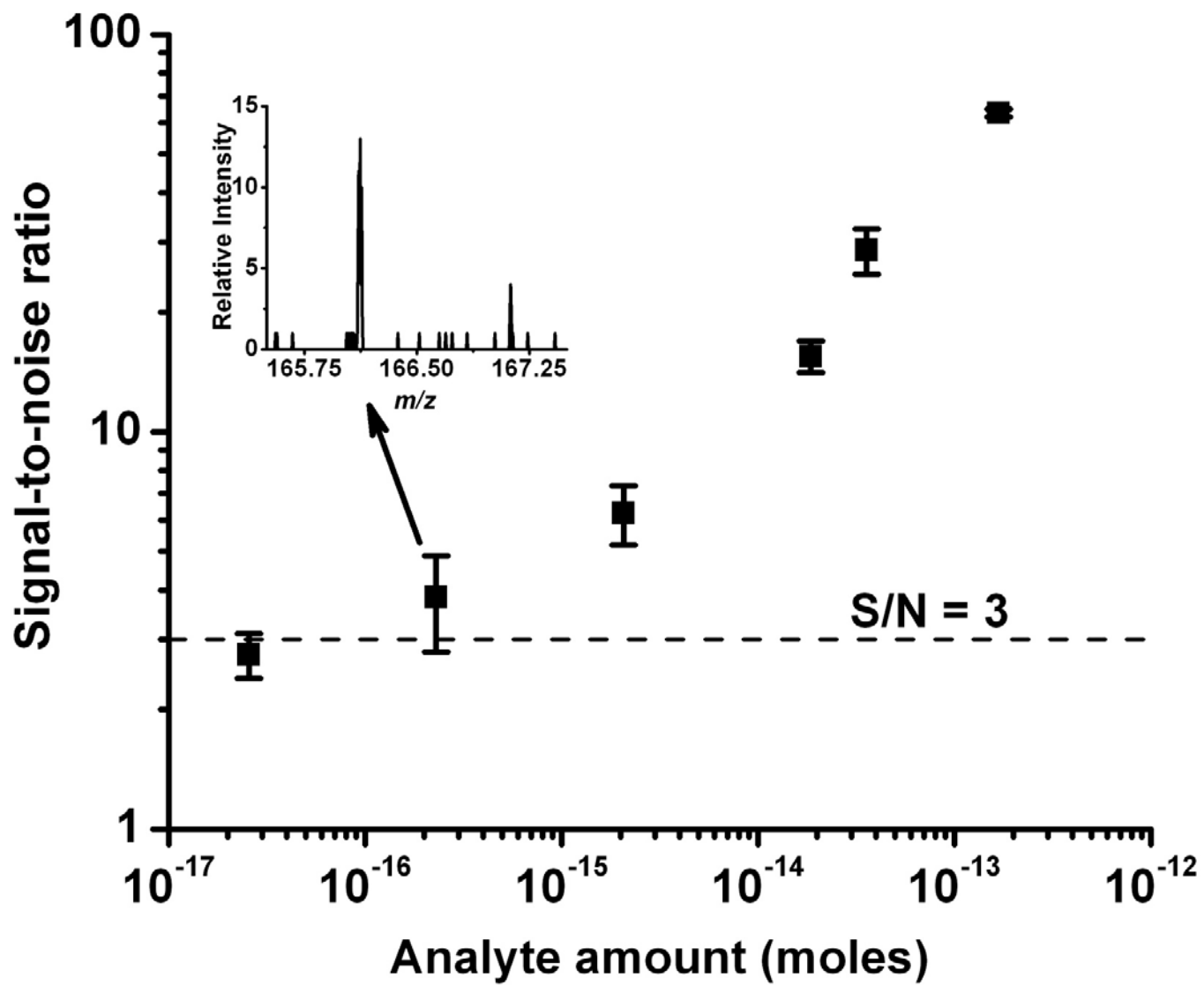
between the mass spectrometer inlet orifice and the target surface was set to ~ 2 mm to maximize the ion signal intensity without producing an electrical breakdown or adversely effecting the focusing. A pulsed voltage of ± 3.0 kV was applied to the target in order to improve the ion collection efficiency. In this technique, known as pulsed dynamic focusing, the high voltage on the target is reduced to zero after ~ 10 μ s as expanding plume approaches the inlet orifice of the mass spectrometer. This results in the optimal combination of electric field and aerodynamic flow for ion collection ⁴⁸. Typically, the mass spectrometer orifice was heated to 50 °C and kept at constant -50 V or 50 V potential for positive or negative ions, respectively. Prior to the analyses, the mass spectrometer was calibrated with sodium iodide cluster ions from 0.01 M solution. Additionally internal calibration was performed in each analysis based on the m/z values of certain known metabolites. The fragments for tandem mass spectrometry were generated by collision activated dissociation (CAD) with argon gas using typical collision energies between 15 and 30 eV, and 4×10^{-3} mbar pressure.

Materials and Sample Preparation. Pure active ingredients (pseudoephedrine, ketoprofen, loratadine, melatonin, naphthoquinone, propranolol, and verapamil) of the formulated drugs were purchased from Sigma-Aldrich (St. Louis, MO). All reagents were at least 98% pure and they were used without the further purification. Over-the-counter tablets (ibuprofen), syrup (acetaminophen, dextromethorphan, doxylamine, and pseudoephedrine), gelatin capsule (acetaminophen, dextromethorphan, guaifenesin, and pseudoephedrine), and powder (aspirin, caffeine, and salicylamide) drugs were obtained from a local pharmacy (Washington, D.C.). The concentrations of the active ingredients among the formulations varied, typically anywhere from 1 to 100 mM. When needed

deionized water from a D4631 E-pure system (Barnstead, Dubuque, IA) was used for the sample preparations. Only a few microliters or a few milligrams of the samples were placed on the stainless steel target for analysis. Medications in solid form (e.g., tablets or powders) were analyzed either by mounting a fragment on the target with a double sided conductive tape or applied as an aqueous solution. In order to prevent spectral interferences from the conductive tape, the solid samples were kept at least a few hundred micrometers thick. The target was cleaned with ~50% ethanol/water mixture between analyses to avoid any cross-contamination or carryover.

Sample preparation in most cases was not necessary. For coated tablets and capsules, prior to analysis by mass spectrometry the inside contents had to be exposed. Multiple laser shots at a single spot were utilized to ablate the coating, and provided mass spectra for the different layers of the tablet. Alternatively the coating was removed by physical abrasion, which only added a few seconds of analysis time. Fresh urine sample was obtained from a presumably healthy Asian male volunteer in his mid-20s with normal medical history. There were no dietary restrictions except for total abstinence from alcoholic beverages and smoking 24 h prior to the administration of the medicine. The urine samples were collected at various times before and after (2.5 h, and 24 h) the single-dose oral administration of a gelatin capsule containing the following active ingredients; acetaminophen (250 mg), dextromethorphan (10 mg), guaifenesin (100 mg), and pseudoephedrine (10 mg). For the analysis of metabolites in urine, two parallel trials were performed on the same individual within two weeks from each other. The presented m/z values for the metabolites in urine were obtained from typical mass spectra averaged over two hundred scans from a single sample.

Figure 3.1 Signal-to-noise ratio for pseudoephedrine ions as a function of the analyte amount in the ablated volume. The limit of detection (LOD) of AP IR-MALDI for aqueous solutions of pseudoephedrine was in the sub-femtomole range. The inset shows the mass spectrum of pseudoephedrine at its detection limit.



RESULTS AND DISCUSSION

Sensitivity and Quantitative Analysis. Initially AP MALDI was considered less sensitive than its vacuum counterpart due to the inefficiency of the ion collection, and transportation through the atmospheric interface. Recently attomole range sensitivity has been reported for ultraviolet AP MALDI using an electrospray matrix deposition technique.⁴⁹ The same experimental setup gave low femtomole range sensitivity when the conventional dried droplet method was used for matrix deposition. To evaluate the detection limit of our AP IR-MALDI setup for small molecules, solutions of pseudoephedrine (molecular weight: 165.1153 g/mol) were prepared in deionized water containing 0.1 % trifluoroacetic acid. At the limit of detection (LOD), defined as signal-to-noise ratio greater than 3, the total amount of pseudoephedrine deposited on a cold finger target was 1 pmol. For a single analyzed spot on the target, the LOD was calculated to be 230 amol, which approached the performance of vacuum MALDI ion sources. Figure 3.1 shows the signal-to-noise ratio for the pseudoephedrine solutions as a function of analyte amount in the probed area. The inset in the figure presents a typical mass spectrum of pseudoephedrine for 230 amol analyte.

Generally quantitative analysis by MALDI is complicated by variable signal intensity due to laser pulse energy fluctuations, and as a consequence of inhomogeneous analyte distribution in the sample. Above the ion generation threshold, the signal amplitude of the analyte as a function of laser irradiance follows a power law relationship with ~ 6 in the exponent.⁵⁰ Thus small variations in the laser output result in disproportionately magnified MALDI signal variations. Structural isomer or stable isotope

analogues as internal standards can be used to factor out this variability and enhance quantitation.^{34, 51}

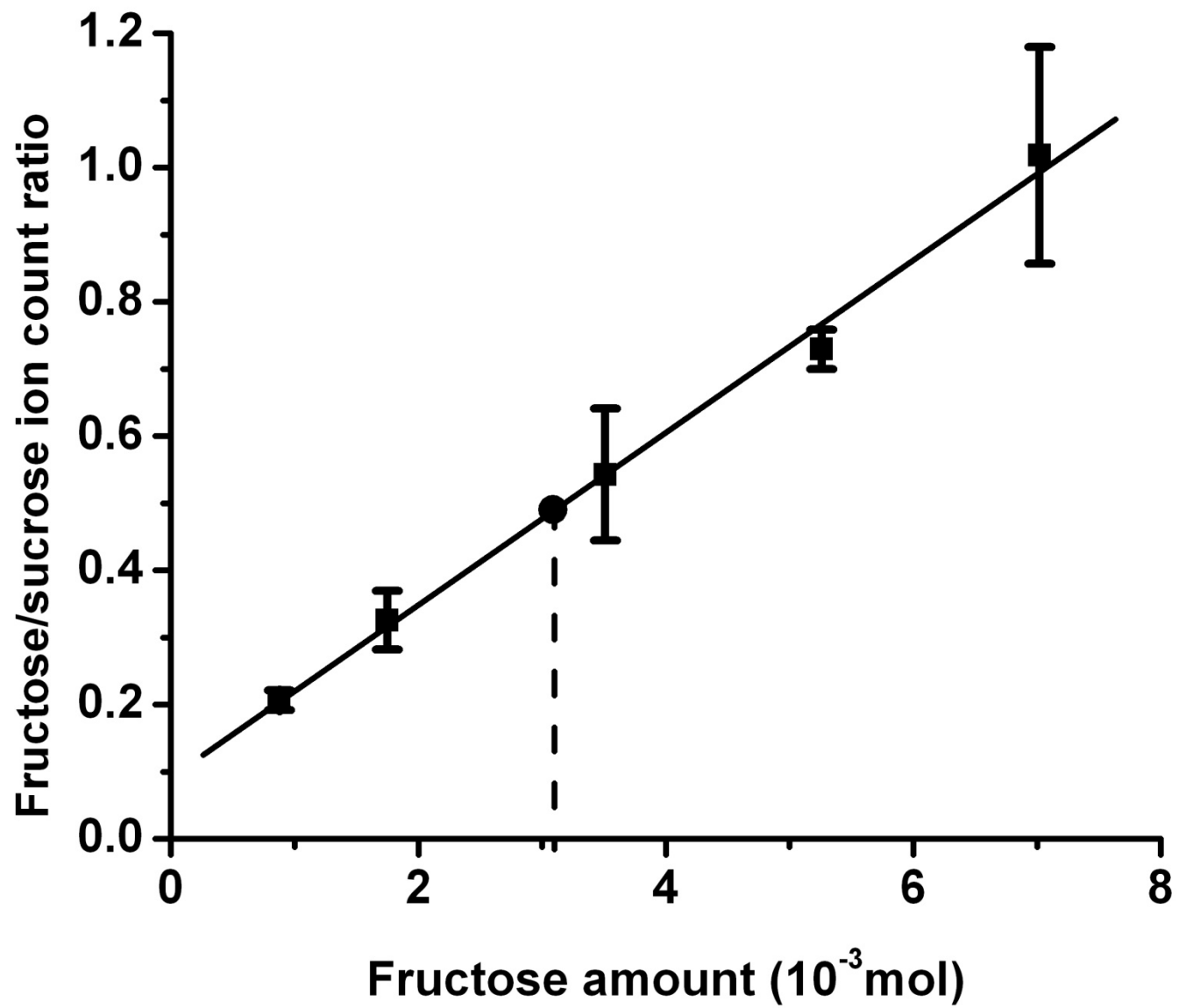
To gauge the dynamic range of AP IR-MALDI, samples with different amounts of fructose were dissolved and analyzed in an aqueous sucrose/Na⁺ solution. As shown in Figure 3.2, the ratio of sodiated fructose to sucrose ion counts increased linearly with increasing the amount of fructose in the solution. Thirty mass spectra were averaged to improve the signal-to-noise ratio. Using Figure 3.2 as a calibration curve to estimate the amount of fructose present in a test sample (denoted with a solid circle in Figure 3.2) yielded ~12% accuracy. This preliminary result is encouraging, but extended studies on multiple analytes with variety of interferences and systems are needed to establish the quantitation capabilities of AP IR-MALDI.

The effect of the various ion source parameters, such as the laser fluence, target voltage, axial and radial position of the laser focal spot versus the inlet orifice, and the orifice temperature, on the ion yield was studied to establish optimum conditions.^{41, 47}

The laser fluence dependence of the ion signal showed a threshold behavior and an initial rapid rise. Increasing the laser fluence significantly beyond the threshold fluence of 0.20 ± 0.02 J/cm², however, did not substantially increase the ion signal. At the same time, the secondary material ejection induced by the recoil pressure expelled more material in the form of particulate matter leading to the depletion of the sample and the clogging of the mass spectrometer orifice. Thus, a fluence just above the threshold value, which also corresponded to a weak phase explosion regime,⁵² was chosen for the analysis.

Above a certain threshold, the voltage applied to the target did not significantly affect the signal intensity. The threshold voltage for ion detection usually fell in the 50 to

Figure 3.2 Sodiated sucrose ion was used as an internal standard to construct a calibration curve for fructose in water using AP IR-MALDI. The amount of fructose in a sample was determined with ~12% accuracy (solid circle).



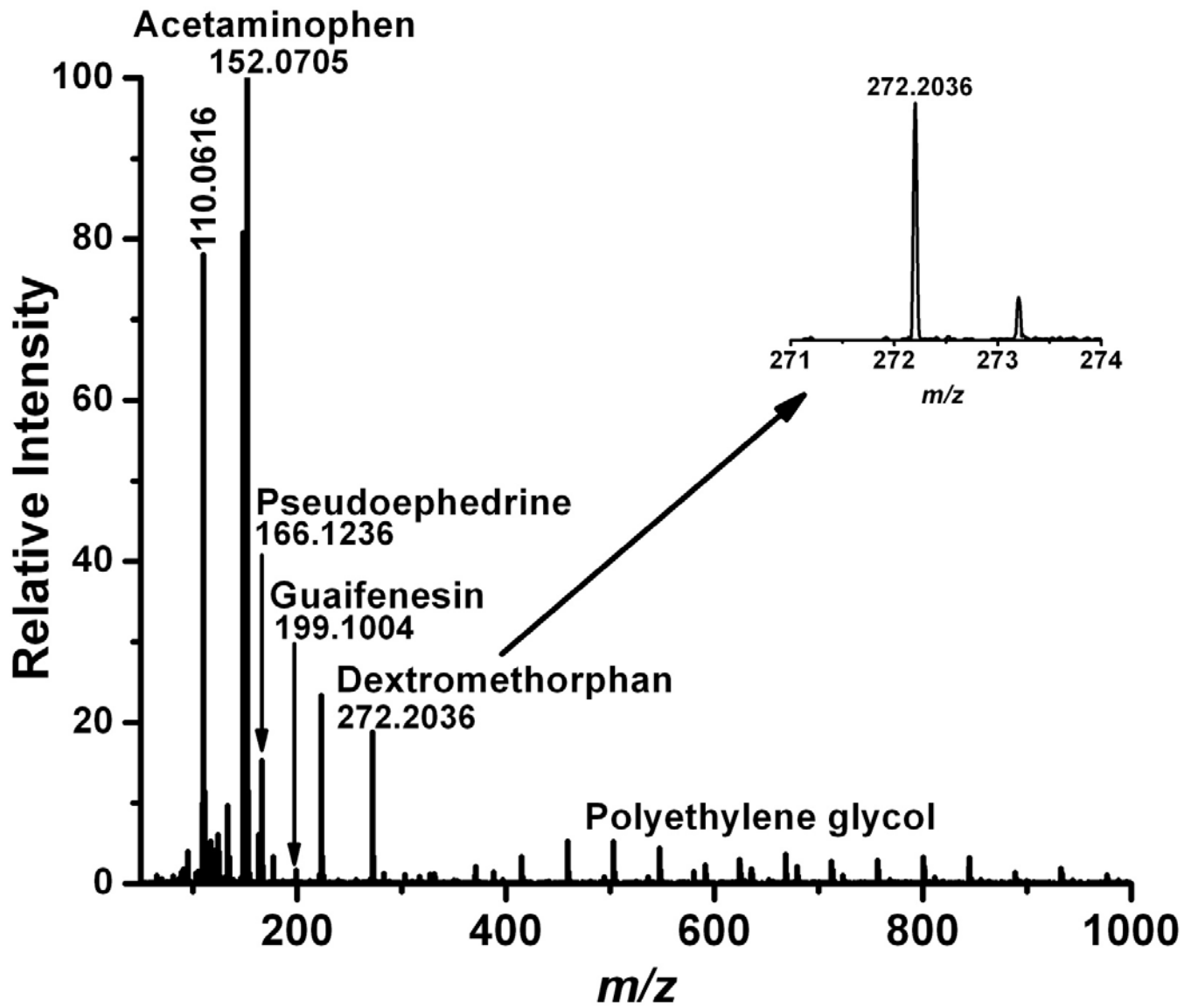
2500 V range with a polarity that agreed with the charge of the collected ions. Its value depended on the target-orifice distance, the laser fluence, and the type and concentration of the analyte. Typically, ± 3.0 kV was applied to the target, which was higher than any observed threshold. Further increasing the voltage was avoided as it increased the possibility of electrical breakdown and instrument failure.

The ion yield dramatically increased as target was moved closer to the inlet orifice. This was demonstrated by measuring the ion yields as a function of target-orifice distance (not shown). However, due to two factors the target could not be moved closer than 2.0 mm to the orifice. First, the dimensions of the laser focusing system presented a physical limitation on the minimum distance between the target and the orifice. Second due to the high voltage on the target, below 2.0 mm the possibility of electric breakdown increased significantly.

The signal intensity was very sensitive to the radial position of the laser focal spot with respect to the inlet orifice axis. Moving the focal spot off-axis by a fraction of a millimeter dramatically decreased the ion signal.

Changing the orifice temperature between room temperature and 80 °C did not significantly affect the analyte ion intensities. At lower temperatures, however, the orifice was more susceptible to clogging and close to room temperature abundant water cluster peaks appeared in the low mass region. Higher temperatures resulted in faster drying of the aqueous samples, which led to rapid diminishing of the ion signal with time. Thus, an optimum temperature of 50 °C was chosen for these studies as it provided the longest lasting signal from the sample without clogging the inlet orifice.

Figure 3.3 Single scan mass spectrum of a generic cough medicine formulated as a gelatin capsule acquired in 1 second (10 laser shots). It demonstrates the possibility of using AP IR-MALDI for the high-throughput analysis of pharmaceuticals. The molecular ions of all active ingredients (acetaminophen, dextromethorphan, guaifenesin and pseudoephedrine) as well as the oligomers of an excipient (polyethylene glycol) were detected in the mass spectrum. In the inset, the isotope distribution was revealed by zooming in on the dextromethorphan molecular ion (m/z 272.2036).



Preingestion analysis of pharmaceuticals. To ascertain the composition of the studied drug formulations and to test the utility of the AP IR-MALDI method, the active ingredients of various pharmaceuticals, administered as gelatin capsule, syrup, tablet and powder, were analyzed using AP IR-MALDI mass spectrometry. The first set of analysis was performed on a thin layer of gel excised from a generic gelatin capsule containing four active ingredients against the common cold and related ailments; acetaminophen (250 mg), dextromethorphan (10 mg), guaifenesin (100 mg), and pseudoephedrine (10 mg). As shown in the Figure 3.3, a single scan obtained in one second (corresponding to 10 laser shots) showed the molecular ion peaks of all four active ingredients. Some of their common fragments were also observed. For example, acetaminophen is observed at m/z 152.0705 as a protonated molecular species and at m/z 110.0616 as the corresponding fragment due to ketene loss. As it is described by Chen *et al.*, the loss of ketene from acetaminophen has also been found in DESI mass spectra.²² Other identified peaks included excipients, for example polyethylene glycol (PEG) used in the formulation of the drug. The signal from PEG is further analyzed in the following section.

The formulations of the active ingredients with different excipients (inactive ingredients) or the presence of other active ingredients did not affect the analysis by AP IR-MALDI. For example, pseudoephedrine formulated as gel, syrup, solution, tablet and powder produced the same protonated ion at nominal m/z 166, and the same fragmentation pattern upon collision activated dissociation. Compared to the wet samples, the positive ion mass spectra of nonwetted tablet/powder samples showed lower intensities for the protonated molecular ions. A few of the drugs, such as

ibuprofen, did not produce signal for protonated molecular ions in the positive ion mode. Instead, a fragment ion was observed at m/z 161.1328, due to the loss of HCOOH (formic acid).

In the negative ion mode, for ibuprofen the deprotonated molecular ion was observed at m/z 205.1271, as expected. The negative ion mode proved to be a useful complementary tool in the detection of compounds that are not easily ionized as protonated species. All of the active ingredients listed in the table 3.1 were detected within a few seconds of analysis per sample. These preliminary results suggest that automated AP IR-MALDI can be used for the high-throughput detection of ingredients in diverse formulations of pharmaceuticals.

Detection of xenobiotic and endogenous metabolites in urine. Urine is an easily and noninvasively collected biofluid rich in both endogenous and xenobiotic metabolites. The rapid detection of drug metabolites in urine can be challenging due to their low concentrations and interferences from endogenous biomolecules. Two of the major components in urine, water and urea, exhibit strong absorption at the 2.94 μm laser wavelength and thus can act as a matrix for AP IR-MALDI. To determine the role of water in the ionization process of urine samples, it was eliminated through drying and reintroduced. The air-dried urine sample failed to produce any mass spectrum while the sample re-wetted with a few microliters of water produced nearly identical mass spectra to the original. This simple experiment indicated that water acted as a matrix in the mid-infrared laser desorption ionization of the molecular components in urine.

Table 3.1 Comparison of measured and calculated monoisotopic m/z values for the analyzed active ingredients

Active ingredient	Chemical formula	Monoisotopic mass	Measured m/z^a	Δm mDa	Studied formulations
Acetaminophen	C ₈ H ₉ NO ₂	152.0712	152.0705 (+H)	-0.70	gelatin capsule*, pure analyte, syrup, tablet
Aspirin	C ₉ H ₈ O ₄	181.0501	181.0489 (+H)	-1.20	powder*
Caffeine	C ₈ H ₁₀ N ₄ O ₂	195.0882	195.0926 (+H)	4.40	powder*, tablet
Dextromethorphan	C ₁₈ H ₂₅ NO	272.2014	272.2036 (+H)	2.20	gelatin capsule*, syrup
Doxylamine	C ₁₇ H ₂₂ N ₂ O	271.1810	271.1737 (+H)	-7.30	syrup*
Guaifenesin	C ₁₀ H ₁₄ O ₄	199.0970	199.0952 (+H)	-1.80	gelatin capsule*, syrup
Ibuprofen	C ₁₃ H ₁₈ O ₂	205.1229	205.1271 (-H)	4.20	tablet*
Ketoprofen	C ₁₆ H ₁₄ O ₃	255.1021	255.0988 (+H)	-3.30	pure analyte*
Loratadine	C ₂₂ H ₂₃ ClN ₂ O ₂	383.1526	383.1516 (+H)	-1.00	pure analyte*, tablet
Melatonin	C ₁₃ H ₁₆ N ₂ O ₂	233.1290	233.1231 (+H)	-5.90	pure analyte*
Naphthoquinone	C ₁₀ H ₆ O ₂	159.0446	159.0359 (+H)	-8.70	pure analyte*
Propranolol	C ₁₆ H ₂₁ NO ₂	260.1650	260.1649 (+H)	-0.10	pure analyte*
Pseudoephedrine	C ₁₀ H ₁₅ NO	166.1232	166.1236 (+H)	0.40	gelatin capsule*, pure analyte, syrup, tablet
Verapamil	C ₂₇ H ₃₈ N ₂ O ₄	455.2910	455.2910 (+H)	0.00	pure analyte*

*Formulation of the active ingredient used to obtain the measured m/z value.

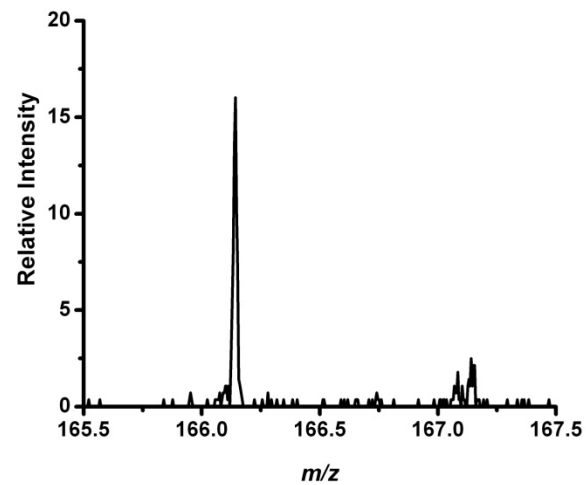
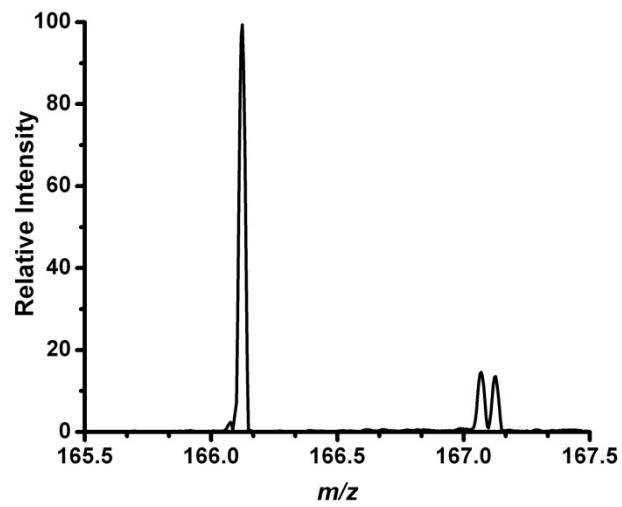
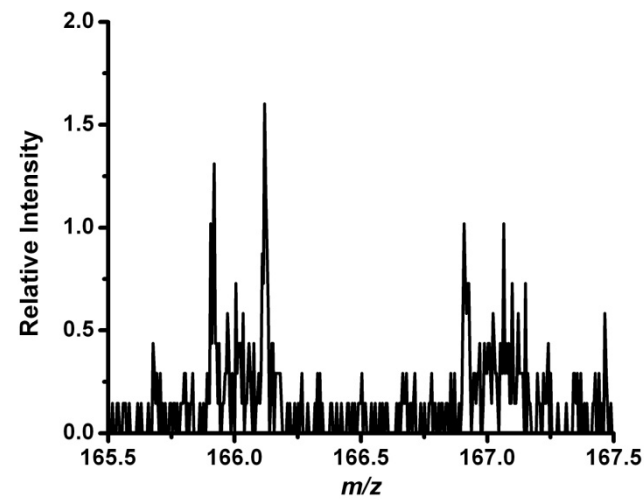
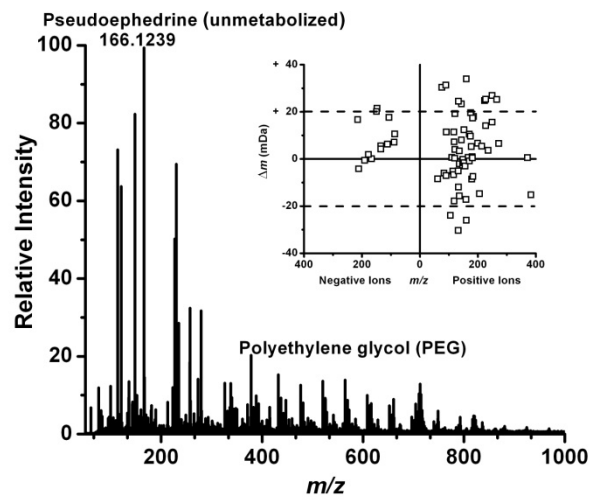
^aSymbols in parentheses: (+H) indicate protonated and (-H) indicate deprotonated species.

The pharmacokinetics of absorption, distribution, metabolism and excretion (ADME) of a drug molecule is pivotal in drug development ⁵³. To follow the excretion of xenobiotic compounds, an over-the-counter cough medicine, containing pseudoephedrine (10 mg) and three other active ingredients described previously, was orally administered to a healthy volunteer. Urine samples were collected before and 2.5 h and 24 h after the ingestion of the medication. Pseudoephedrine is a common nasal decongestant used for the treatment of common cold and other related ailments. It is known that more than eighty percent of the administered pseudoephedrine is excreted unchanged in the urine within 24 h, peaking at 4 h following its oral administration. ⁵⁴ Only a small fraction of the pseudoephedrine is metabolized to norpseudoephedrine through N-demethylation. ⁵⁴

Small volumes (3 μL) of the unprocessed urine sample were analyzed directly without drying, extraction or any other sample preparation steps. For the investigation of xenobiotics and endogenous metabolites in the urine, an average of more than 200 mass spectra was collected. The target was continuously rastered to ensure even sampling of the target surface. The mass spectra were further validated by multiple analyses of the same sample as well as by a parallel study on the same individual within two weeks.

In the urine collected after 2.5 h, the protonated pseudoephedrine was detected at m/z 166.1239 along with its fragment after OH loss at m/z 148.1124. As shown in figure 3.4a, the metabolites for dextromethorphan at m/z 272.208, guaifenesin at m/z 199.1037 and acetaminophen at m/z 152.0696, as well as the excipients such as polyethylene glycol and mannitol/sorbitol (m/z 183.0795) were also detected in the urine spectra. Panels b, c and d in figure 3.4 compare the relative intensities of pseudoephedrine peaks at before,

Figure 3.4 Typical averaged mass spectra of 3 μl of the urine sample collected **(a)** 2.5 h after drug ingestion clearly shows the molecular ion for unmetabolized pseudoephedrine in the urine as well as peaks related to an excipient, polyethylene glycol (PEG). In the inset the accuracy of the mass measurement, Δm , in mDa units for the metabolites in urine as a function of the theoretical m/z value indicates that most species are detected within 20 mDa of the theoretical m/z value. Panels (b), (c) and (d) show the mass spectrum in the vicinity of the protonated pseudoephedrine molecule before and 2.5 h and 24 h following the ingestion of the drug, respectively.



A	B
C	D

and 2.5 h and 24 h following taking the medication, respectively. It is discernable from figure 3.4b that the control urine sample taken before the oral administration of the medication did not contain any peaks for pseudoephedrine. Compared to the 2.5 h level, the urine sample collected at 24 h showed a relative ion intensity reduced by ~84% for pseudoephedrine.

Along with the xenobiotic drug metabolites, many ions related to endogenous compounds were also observed in the urine mass spectrum. The identification of the endogenous metabolites was based on matching the observed monoisotopic mass (within $\pm \Delta m$ 35 mDa), and isotope distribution with those of known metabolites for normal human urine listed in the Human Metabolome Database (<http://www.hmdb.ca/> accessed on March 8, 2008)⁵⁵. The list of metabolites directly detected by AP IR-MALDI in the urine with their suggested identifications and biological activities are listed in table 3.2 (positive ions), and in table 3.3 (negative ions). Except for a few noted instances, the reported biological activities of the listed metabolites were obtained from the KEGG (Kyoto Encyclopedia of Genes and Genomes) pathway database (<http://www.genome.jp/kegg/pathway.html> accessed on March 8, 2008).⁵⁶

The most abundant components in the urine samples were detected both as protonated and as sodiated species. For example, urea, which accounts for half of the total urinary solid, was detected both as m/z 61.0318 (M+H⁺) and m/z 83.0161 (M+Na⁺). The positive ion AP IR-MALDI spectrum of urine showed peaks for diverse chemical species such as amino acids, organic acids, amines, ketones, carbohydrates, steroids, etc. Compared to the positive ion spectra, fewer ions were identified in the

Table 3.2 Suggested identification of the metabolites detected in the positive ion mass spectra of normal human urine.

Metabolite ^a	Chemical Formula	Mono. mass	Meas. m/z ^c		Δm mDa	Biological Activity ^b
Urea	CH ₄ N ₂ O	61.0402	61.0318	(+H)	-8.4	Urea cycle and metabolism of amino groups, Purine metabolism, Pyrimidine metabolism, Arginine and proline metabolism, etc.
		83.0221	83.0161	(+Na)	-6.0	
Glycine	C ₂ H ₅ NO ₂	76.0399	76.0703	(+H)	30.4	Bile acid biosynthesis, Purine metabolism, Glycine, serine and threonine metabolism, Lysine degradation, Cyanoamino acid metabolism, etc.
Pyruvic acid	C ₃ H ₄ O ₃	89.0239	89.0552	(+H)	31.3	Glycolysis / Gluconeogenesis, Citrate cycle (TCA cycle), Pentose phosphate pathway, Pentose and glucuronate interconversions, etc.
Alanine	C ₃ H ₇ NO ₂	90.0555	90.0485	(+H)	-7.0	Alanine and aspartate metabolism, Cysteine metabolism, Taurine and hypotaurine metabolism, D-Alanine metabolism, etc.
Dihydroxyacetone	C ₃ H ₆ O ₃	91.0395	91.0509	(+H)	11.4	Glycerolipid metabolism, Methane metabolism
Lactic acid			91.0509	(+H)		Glycolysis / Gluconeogenesis, Pyruvate metabolism, Propanoate metabolism, Styrene degradation
Hydroxybutyric acid	C ₄ H ₈ O ₃	105.0552	105.0313	(+H)	-23.9	Propanoate metabolism, in urine during ketosis*
Aminophenol	C ₆ H ₇ NO	110.0606	110.0613	(+H)	0.7	Acetaminophen Metabolite*
Creatinine	C ₄ H ₇ N ₃ O	114.0667	114.0615	(+H)	-5.2	Arginine and proline metabolism
		136.0487	136.0466	(+Na)	-2.1	
Proline	C ₅ H ₉ NO ₂	116.0712	116.0645		-6.7	Arginine and proline metabolism, Novobiocin biosynthesis, Aminoacyl-tRNA biosynthesis, ABC transporters - General
Dimethylpyruvate	C ₅ H ₈ O ₃	117.0552	117.0666	(+H)	11.4	Valine, leucine and isoleucine biosynthesis, Pantothenate and CoA biosynthesis *
Betaine	C ₅ H ₁₁ NO ₂	118.0868	118.0690	(+H)	-17.8	Glycine, serine and threonine metabolism, ABC transporters - General
Valine						Valine, leucine and isoleucine degradation / biosynthesis, Propanoate metabolism, Pantothenate and CoA biosynthesis, etc.
Guanidoacetic acid	C ₃ H ₇ N ₃ O ₂	118.0617	118.0690	(+H)	7.3	Precursor of Creatine, * glycine, serine and threonine metabolism, Arginine and proline metabolism
Threonine	C ₄ H ₉ NO ₃	120.0661	120.0664	(+H)	0.3	Glycine, serine and threonine metabolism, Valine, leucine and isoleucine biosynthesis, Porphyrin and chlorophyll metabolism, etc.
Dihydroxybutyric acid	C ₄ H ₈ O ₄	121.0501	121.0693	(+H)	19.2	Pentose phosphate pathway*
		143.0320	143.0554	(+Na)	23.4	
Hydroxystyrene	C ₈ H ₈ O	121.0653	121.0693	(+H)	4.0	Phenylpropanoid biosynthesis; metabolite of wines, foods and berries*
		143.0473	143.0554	(+Na)	8.1	
Creatine	C ₄ H ₉ N ₃ O ₂	132.0773	132.0722	(+H)	-5.1	Glycine, serine and threonine metabolism, Arginine and proline metabolism
Leucine	C ₆ H ₁₃ NO ₂	132.1025	132.0722	(+H)	-30.3	Valine, leucine and isoleucine degradation / biosynthesis, Aminoacyl-tRNA biosynthesis, ABC transporters - General

Isoleucine						Valine, leucine and isoleucine degradation / biosynthesis, Alkaloid biosynthesis II, Aminoacyl-tRNA biosynthesis, etc.
Asparagine	C ₄ H ₈ N ₂ O ₃	133.0613	133.0858	(+H)	24.5	Alanine and aspartate metabolism, Tetracycline biosynthesis, Cyanoamino acid metabolism, Nitrogen metabolism, etc.
Ureidopropionic acid						Pyrimidine metabolism, beta-Alanine metabolism, Pantothenate and CoA biosynthesis
Ornithine	C ₅ H ₁₂ N ₂ O ₂	133.0977	133.0858	(+H)	-11.9	Urea cycle and metabolism of amino groups, Arginine and proline metabolism, D-Arginine and D-ornithine metabolism, etc.
Methylcysteine	C ₄ H ₉ NO ₂ S	136.0432	136.0466	(+H)	3.4	Garlic Metabolite*
Adenine (Vitamin B4)	C ₅ H ₅ N ₅	136.0623	136.0466	(+H)	-15.7	Urea cycle and metabolism of amino groups, Purine metabolism
Tyramine	C ₈ H ₁₁ NO	160.0738	160.1078	(+Na)	34.0	Tyrosine metabolism, Alkaloid biosynthesis I, Neuroactive ligand-receptor interaction
Glutamine	C ₅ H ₁₀ N ₂ O ₃	147.0770	147.0744	(+H)	-2.6	Purine metabolism, Pyrimidine metabolism, Glutamate metabolism, D-Glutamine and D-glutamate metabolism, Nitrogen metabolism, etc.
Pseudoephedrine fragment	C ₁₀ H ₁₄ N	148.1126	148.1124	(+H)	-0.2	Pseudoephedrine Metabolite*
Guanine	C ₅ H ₅ N ₅ O	152.0572	152.0696	(+H)	12.4	Purine metabolism
Acetaminophen	C ₈ H ₉ NO ₂	152.0712	152.0696	(+H)	-1.6	Acetaminophen Metabolite*
Histidine	C ₆ H ₉ N ₃ O ₂	156.0773	156.0743	(+H)	-3.0	Histidine metabolism, beta-Alanine metabolism, Aminoacyl-tRNA biosynthesis, ABC transporters - General
Oenanthic ether	C ₉ H ₁₈ O ₂	159.1385	159.1213	(+H)	-17.2	Human Sweat*
Aminooctanoic acid	C ₈ H ₁₇ NO ₂	160.1338	160.1078	(+H)	-26.0	Urine metabolite*
Nicotine	C ₁₀ H ₁₄ N ₂	185.1055	185.1235	(+Na)	18.0	Nicotine metabolite, Alkaloid biosynthesis II
Pseudoephedrine	C ₁₀ H ₁₅ NO	166.1232	166.1239	(+H)	0.7	Pseudoephedrine Metabolite*
Hydroxydopamine	C ₈ H ₁₁ NO ₃	170.0817	170.0922	(+H)	10.5	Tyrosine metabolism, Amine in human urine
Norepinephrine				(+H)		Tyrosine metabolism, Neuroactive ligand-receptor interaction, Gap junction
Methylhistidine	C ₇ H ₁₁ N ₃ O ₂	170.0930	170.0922	(+H)	-0.8	Histidine metabolism
Oxoarginine	C ₆ H ₁₁ N ₃ O ₃	174.0879	174.0976	(+H)	9.7	Urea cycle and metabolism of amino groups
Arginine	C ₆ H ₁₄ N ₄ O ₂	175.1195	175.1391	(+H)	19.6	Urea cycle and metabolism of amino groups, Arginine and proline metabolism, Clavulanic acid biosynthesis, D-Arginine and D-ornithine metabolism, etc.
Ascorbic acid	C ₆ H ₈ O ₆	177.0399	177.0452	(+H)	5.3	Ascorbate and aldarate metabolism, Phosphotransferase system (PTS)
Cysteinylglycine	C ₅ H ₁₀ N ₂ O ₃ S	179.0490	179.0405	(+H)	-8.5	Glutathione metabolism
Succinoylpyridine	C ₉ H ₉ NO ₃	180.0661	180.0670	(+H)	0.9	Nicotine metabolite*
D-hexose sugar	C ₆ H ₁₂ O ₆	181.0712	181.0717	(+H)	0.5	Urine Metabolite*
Tyrosine	C ₉ H ₁₁ NO ₃	182.0817	182.0991	(+H)	17.4	Tyrosine metabolism, Phenylalanine, tyrosine and tryptophan biosynthesis,

							Novobiocin biosynthesis, Thiamine metabolism, etc.
4-Hydroxy-4-(3-pyridyl)-butanoic acid							
Mannitol/Sorbitol	C ₆ H ₁₄ O ₆	183.0869	183.0795		-7.4	Excipient in medicine*	
Guaifenesin	C ₁₀ H ₁₄ O ₄	199.0970	199.1037	(+H)	6.7	Guaifenesin Metabolite*	
Tryptophan	C ₁₁ H ₁₂ N ₂ O ₂	205.0977	205.0830	(+H)	-14.7	Tryptophan metabolism, Phenylalanine, tyrosine and tryptophan biosynthesis, Indole and ipecac alkaloid biosynthesis, Aminoacyl-tRNA biosynthesis	
Vanillic acid	C ₁₀ H ₁₂ O ₅	213.0763	213.0817	(+H)	5.4	Acidic catecholamine metabolite*	
		235.0583	235.0620	(+Na)	3.7		
Cystathionine	C ₇ H ₁₄ N ₂ O ₄ S	223.0753	223.1001	(+H)	24.8	Associated with Cystathioninuria,* Glycine, serine and threonine metabolism, Methionine metabolism	
Porphobilinogen	C ₁₀ H ₁₄ N ₂ O ₄	227.1032	227.1285	(+H)	25.3	Porphyrin and chlorophyll metabolism	
		249.0851	249.1120	(+Na)	26.9		
Carnosine	C ₉ H ₁₄ N ₄ O ₃	227.1144	227.1285	(+H)	14.1	Alanine and aspartate metabolism, Histidine metabolism, beta-Alanine metabolism	
		249.0964	249.1120	(+Na)	15.6		
Eugenol	C ₁₄ H ₁₆ O ₅	265.1076	265.1328	(+H)	25.2	Food Metabolite*	
Dextromethorphan	C ₁₈ H ₂₅ NO	272.2014	272.2080	(+H)	6.6	Dextromethorphan metabolite*	
Aldosterone	C ₂₁ H ₂₈ O ₅	383.1834	383.1682	(+Na)	-15.2	C21-Steroid hormone metabolism	
Thromboxane B2	C ₂₀ H ₃₄ O ₆	371.2434	371.2440	(+H)	0.6	Arachidonic acid metabolism	
6-keto-Prostaglandin F1a	C ₂₀ H ₃₄ O ₆	371.2434	371.2440	(+H)	0.6	Arachidonic acid metabolism	

*Listed metabolites are obtained from the Human Metabolome Database (<http://www.hmdb.ca/> accessed on March 8, 2008) after matching the m/z value (within Δm 35 mDa) and the isotopic distribution with the metabolites found in normal human urine.

^bBiological activities are based on the KEGG (Kyoto Encyclopedia of Genes and Genomes) pathway database (<http://www.genome.jp/kegg/pathway.html> accessed on March 8, 2008) except where marked with * which are based on the Human Metabolome Database (<http://www.hmdb.ca/> accessed on March 8, 2008).

^cSymbols in parentheses, indicate protonated (+H), and sodiated (+Na) species.

Table 3.3 Suggested identification of metabolites detected in the negative ion mass spectrum of normal human urine.

Metabolites ^a	Chemical Formula	Monoisotopic mass	Measured m/z	Δm (10^{-3})	Biological Activity ^b
Pyruvic Acid	C ₃ H ₄ O ₃	87.0082	86.9976 (-H)	-10.6	Glycolysis / Gluconeogenesis, Citrate cycle (TCA cycle), Pentose phosphate pathway, Pentose and glucuronate interconversions, etc.
Lactic Acid	C ₃ H ₆ O ₃	89.0239	89.0168 (-H)	-7.1	Glycolysis / Gluconeogenesis, Pyruvate metabolism, Propanoate metabolism, Styrene degradation
Dihydroxyacetone					Glycerolipid metabolism, Methane metabolism
Cresol	C ₇ H ₈ O	107.0497	107.0321 (-H)	-17.6	Toluene and xylene degradation
Creatinine	C ₄ H ₇ N ₃ O	112.0511	112.0448 (-H)	-6.3	Arginine and proline metabolism
Hypoxanthine	C ₅ H ₄ N ₄ O	135.0307	135.0252 (-H)	-5.5	Purine metabolism
Threonic acid	C ₄ H ₈ O ₅	135.0294	135.0252 (-H)	-4.2	Degradation of ascorbic acid*
Erythronic acid			(-H)		Degradation of ascorbic acid*
Methionine	C ₅ H ₁₁ NO ₂ S	148.0432	148.0217 (-H)	-21.5	Methionine metabolism, Aminoacyl-tRNA biosynthesis
Guanine	C ₅ H ₅ N ₅ O	150.0416	150.0215 (-H)	-20.1	Purine metabolism
Uric acid	C ₅ H ₄ N ₄ O ₃	167.0205	167.0204 (-H)	-0.1	Purine metabolism
3-succinoylpyridine	C ₉ H ₉ NO ₃	178.0504	178.0485 (-H)	-1.9	Nicotine Metabolite*
Citric acid	C ₆ H ₈ O ₇	191.0192	191.0198 (-H)	0.6	Citrate cycle (TCA cycle), Glutamate metabolism, Alanine and aspartate metabolism, Glyoxylate and dicarboxylate metabolism, etc.
Isocitric acid					
Vanillic acid	C ₁₀ H ₁₂ O ₅	211.0607	211.0649 (-H)	4.2	Catecholamine metabolite*
Bisnorbiotin	C ₈ H ₁₂ N ₂ O ₃ S	215.0490	215.0323 (-H)	-16.7	Biotin metabolite*

^aListed metabolites are obtained from the Human Metabolome Database (<http://www.hmdb.ca/> accessed on March 8, 2008) after matching the m/z value (within Δm 35 mDa) and the isotopic distribution with the metabolites found in normal human urine.

^bBiological activities are based on the KEGG (Kyoto Encyclopedia of Genes and Genomes) pathway database (<http://www.genome.jp/kegg/pathway.html> accessed on March 8, 2008) except where marked with * which are based on the Human Metabolome Database (<http://www.hmdb.ca/> accessed on March 8, 2008).

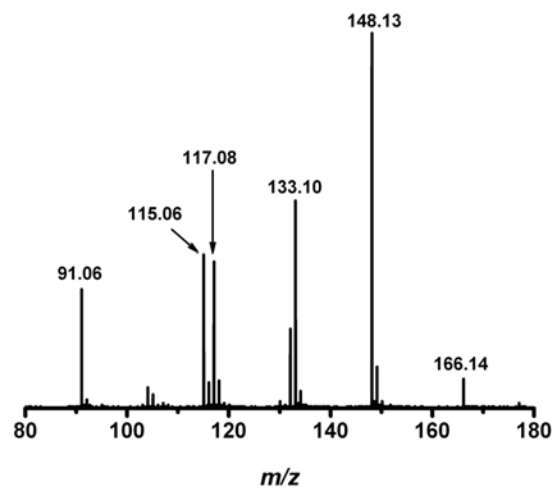
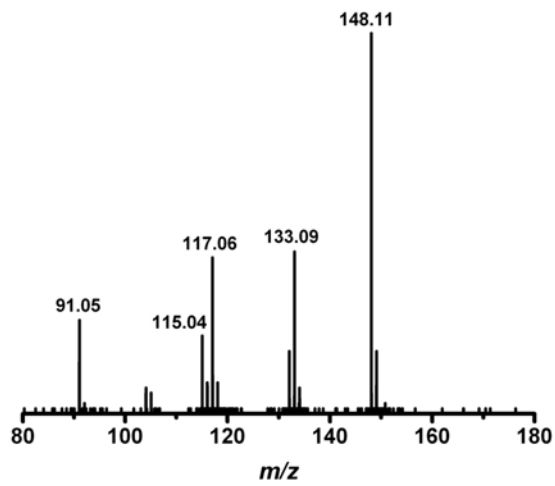
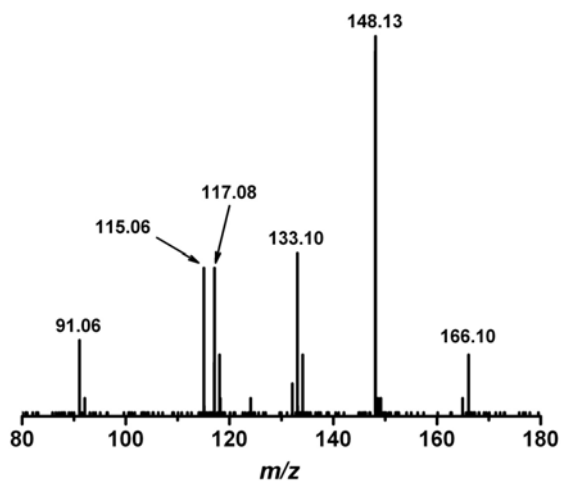
^cSymbols in parentheses indicate deprotonated (-H) species.

negative ion mode, which mainly derived ions from organic acids and amines. A complementary set of metabolites were found in the positive and negative ion spectra.

Some metabolites have close m/z values and similar chemical composition. Accurate m/z values and isotopic distributions alone might not be sufficient to identify them. For example, the m/z 166.1239 ion might correspond to either unmetabolized pseudoephedrine or to hordenine, a phenylethylamine alkaloid found in human urine after consumption of beer brewed using barley.⁵⁵ Both have the same chemical formula and thus the same monoisotopic mass of 165.1154. The m/z 166.1239 ion was identified as pseudoephedrine after it had produced a CAD fragmentation pattern identical to pseudoephedrine from the formulated medicine. The CAD spectra for the m/z 166.1239 ion from urine, pure analytical standard and medicine formulation are shown in panels (a), (b) and (c) of figure 3.5, respectively. This example shows that AP IR-MALDI combined with tandem mass spectrometry can be used to unambiguously identify detected metabolites. Tandem mass spectrometric analysis was not performed on all detected metabolites, thus, some of the m/z values have more than one assignment.

Detecting xenobiotic metabolites originating from pharmaceuticals can help to assess the pharmacological and toxicological effects of drug candidates, while identifying endogenous metabolites might have essential diagnostic applications in the biomedical sciences and in clinical applications. Mass spectrometers have already been successfully used in the diagnosis of many metabolic disorders, e.g., in screening for inborn metabolic disorders in infants.⁵⁷⁻⁵⁹ For example, the more than a dozen amino acids that have been identified in the ~ 3 μ l of urine sample within seconds can be used in gastrointestinal nutritional assessment, and in the diagnosis of metabolic disorders.^{60, 61} The detection of

Figure 3.5 Fragmentation pattern of the nominal m/z 166 ion was obtained by collision activated dissociation to confirm structure of the corresponding metabolite in urine. Tandem mass spectrum of the nominal m/z 166 ion is presented in panel **(a)** from urine 2.5 h after the ingestion of the pseudoephedrine containing drug. It produced identical fragments as the tandem mass spectra of **(b)** pure pseudoephedrine analyte and **(c)** pseudoephedrine in the ingested medicine. A similar strategy can be applied to confirm the structure of each unknown metabolite detected in the urine.



$$\frac{A}{B}$$

$$\frac{B}{C}$$

amino acids by AP IR-MALDI is faster than any of the classical methods of analysis by specialized assays for each analyte or the simultaneous detection afforded by hyphenated mass spectrometric techniques. With an appropriate internal standard, AP IR-MALDI tandem mass spectrometry might be used as a screening tool for the diagnosis and prognosis of disease states. Even with tandem mass spectrometric capability, AP IR-MALDI cannot distinguish between stereoisomers. Online coupling of AP IR-MALDI with chiral separation techniques can be helpful in these cases.⁶²

Potential application in the study of intestinal permeability. Non-invasive intestinal permeability tests using polyethylene glycol (e.g., PEG 400 with MW 280-634) are administered clinically to screen and monitor various gastrointestinal diseases such as the irritable bowel syndrome and Crohn's disease as well as to study gastrointestinal reactions to cytotoxic drugs and food allergens. One form of the intestinal permeability tests includes measuring the urinary excretion of orally administered PEG to give insight into the adsorption and transport of chemicals in the intestine.^{63, 64} Although there is an ongoing controversy about the suitability of this test for reliable diagnosis, which we are not addressing here, below we follow the changes upon excretion in the oligomer size distribution of the PEG ingested with cold medication.

PEG oligomers were detected by AP IR-MALDI in both the formulated gelatin capsule and in the urine collected after its oral administration. Without the addition of water, the standard PEG failed to produce any signal, indicating that water played a critical role as the matrix. The PEG ions were observed as a protonated species in the medicine and as sodiated species in the urine. The predominately sodiated PEG peaks in the urine can be explained by the high level of sodium ions excreted in the urine (~170

mmol per 24 h).⁶⁵ For example, the PEG peak at m/z 459.2787 in the gelatin capsule is observed as m/z 481.2900 in the urine. The difference in m/z value between the two peaks is equal to the mass difference between the protonated and the sodiated species within Δm 29.5 mDa.

Polymers are usually characterized by their repeat units and molecular weight distributions. The molecular weight distribution is described by two average values; the number-average molecular weight, M_N , and the weight-average molecular weight, M_W , as well as by their polydispersity, PD . The average molecular weights and polydispersity are defined as:

$$M_N = \frac{\sum M_i N_i}{\sum N_i},$$

(1)

$$M_W = \frac{\sum M_i^2 N_i}{\sum M_i N_i} \text{ and}$$

(2)

$$PD = \frac{M_W}{M_N},$$

(3)

where M_i is the mass of the i -th oligomer and N_i is its abundance represented by the relative intensity in the mass spectrum.⁶⁶

The average molecular weights and polydispersity were calculated from the ion intensities and ion masses using equations 1-3. The calculated values for the PEG in the cough medicine were; $M_N = 548$ g/mol, $M_W = 575$ g/mol, $PD = 1.05$. The metabolized PEG excreted in the urine exhibited $M_N = 496$ g/mol, $M_W = 510$ g/mol, $PD = 1.03$.

This simple comparison is not intended to actually characterize the intestinal permeability in this case; rather it demonstrates the ability of AP IR-MALDI mass spectrometry to recover oligomer size distribution changes in excreted samples. Further testing of the AP IR-MALDI approach can establish this method for the rapid diagnosis of intestinal permeability. It is worth noting that current techniques require much larger doses of PEG, for example 0.1 g of PEG 400 mixed with 2.5 g of PEG 1000, and the analysis often relies on HPLC analysis.⁶⁷ Establishing AP IR-MALDI for the testing of intestinal permeability can substantially reduce the quantity of the administered polymer and significantly shorten the time required for analysis.

CONCLUSIONS

Analysis of biofluids is extensively used to follow metabolic changes. In this communication we demonstrated how the water content of these fluids enables the rapid direct analysis of endogenous metabolites and xenobiotics with AP IR-MALDI mass spectrometry. The wide range of metabolites detected in urine points to diverse applications in metabolism research and to potential clinical uses. For example, the rapid mass spectrometric detection lends itself to large scale stable isotope studies. The minimal sample preparation requirement and extremely fast analysis time are ideal for high throughput studies and population screening. The analysis at atmospheric pressure outside of the vacuum of the mass spectrometer also provides an opportunity to work with non-traditional samples, e.g., to conduct *in vivo* pharmacokinetic and diagnostic studies. By coupling the AP IR-MALDI ion source with a translation stage, the analysis method can be used to detect the spatial distributions of metabolites in a tissue⁴¹.

Although the preliminary results presented in this study are encouraging, further improvement is necessary to expand the range of metabolites, and increase both the sensitivity and selectivity. Enhancements in the AP ionization and in the ion collection/transport will increase the sensitivity and possibly the diversity of the collected biomolecules. An automated AP IR-MALDI system with a higher repetition rate laser and the integration of online separation techniques, e.g., ion mobility spectrometry, should enable the swifter detection of a wider variety of biomolecules.

ACKNOWLEDGEMENTS

The authors would like to recognize the financial support from the W. M. Keck Foundation (041904), the U.S. Department of Energy (DEFG02-01ER15129), and the George Washington University Research Enhancement Fund for this work. Modified capillary inlets for the mass spectrometer were kindly provided by D. Kenny of the Waters Co.

REFERENCES

- (1) Triolo, A.; Altamura, M.; Cardinali, F.; Sisto, A.; Maggi, C. A. *Journal of Mass Spectrometry* **2001**, *36*, 1249-1259.
- (2) Nicholson, J. K.; Connelly, J.; Lindon, J. C.; Holmes, E. *Nature Reviews Drug Discovery* **2002**, *1*, 153.
- (3) Siuzdak, G. *Proceedings of the National Academy of Sciences* **1994**, *91*, 11290-11297.
- (4) Glassbrook, N.; Beecher, C.; Ryals, J. *Nature Biotechnology* **2000**, *18*, 1157-1161.

- (5) Dettmer, K.; Aronov, P. A.; Hammock, B. D. *Mass Spectrometry Reviews* **2007**, *26*, 51-78.
- (6) MacDonald, B. F.; Prebble, K. A. *Journal of Pharmaceutical and Biomedical Analysis* **1993**, *11*, 1077-1085.
- (7) Blanco, M.; Coello, J.; Iturriaga, H.; Maspoch, S.; de la Pezuela, C. *The Analyst* **1998**, *123*, 135R-150R.
- (8) Guimarães, A. E.; Pacheco, M. T. T.; Silveira Jr, L.; Barsottini, D.; Duarte, J.; Villaverde, A. B.; Zângaro, R. A. *Spectroscopy: An International Journal* **2006**, *20*, 185-194.
- (9) Strachan, C. J.; Rades, T.; Gordon, K. C.; Rantanen, J. *Journal of Pharmacy and Pharmacology* **2007**, *59*, 179-192.
- (10) Kawase, K.; Ogawa, Y.; Watanabe, Y.; Inoue, H. *Opt. Express* **2003**, *11*, 2549-2554.
- (11) Moreira, A. B.; Oliveira, H. P. M.; Atvars, T. D. Z.; Dias, I. L. T.; Neto, G. O.; Zagatto, E. A. G.; Kubota, L. T. *Analytica Chimica Acta* **2005**, *539*, 257-261.
- (12) Popchapsky, S. S.; Popchapsky, T. C. *Current Topics in Medicinal Chemistry* **2001**, *1*, 427-441.
- (13) Maher, A. D.; Zirah, S. F. M.; Holmes, E.; Nicholson, J. K. *Analytical Chemistry* **2007**, *79*, 5204-5211.
- (14) Balchin, E.; Malcolme-Lawes, D. J.; Poplett, I. J.; Rowe, M. D.; Smith, J. A. S.; Pearce, G. E. S.; Wren, S. A. C. *Analytical chemistry* **2005**, *77*, 3925-3930.
- (15) Papac, D. I.; Shahrokh, Z. *Pharmaceutical Research* **2001**, *18*, 131-145.
- (16) Bowers, L. D. *Clinical Chemistry* **1997**, *43*, 1299-1304.

- (17) Wolthers, B. G.; Kraan, G. P. B. *Journal of Chromatography A* **1999**, *843*, 247-274.
- (18) Niessen, W. M. A. *Journal of Chromatography A* **1999**, *856*, 179-197.
- (19) Kostianen, R.; Kotiaho, T.; Kuuranen, T.; Auriola, S. *Journal of Mass Spectrometry* **2003**, *38*, 357-372.
- (20) Smyth, W. F.; Rodriguez, V. *Journal of Chromatography A* **2007**, *1159*, 159-174.
- (21) Takats, Z.; Wiseman, J. M.; Gologan, B.; Cooks, R. G. *Science* **2004**, *306*, 471 - 473.
- (22) Chen, H.; Talaty, N. N.; Takáts, Z.; Cooks, R. G. *Analytical Chemistry* **2005**, *77*, 6915-6927.
- (23) Kauppila, T. J.; Wiseman, J. M.; Ketola, R. A.; Kotiaho, T.; Cooks, R. G.; Kostianen, R. *Rapid Communications in Mass Spectrometry* **2006**, *20*, 387-392.
- (24) Leuthold, L. A.; Mandscheff, J. F.; Fathi, M.; Giroud, C.; Augsburg, M.; Varesio, E.; Hopfgartner, G. *Rapid Communications in Mass Spectrometry* **2006**, *20*, 103-110.
- (25) Cody, R. B.; Laramee, J. A.; Durst, H. D. *Analytical Chemistry* **2005**, *77*, 2297-2302.
- (26) Takats, Z.; Cotte-Rodriguez, I.; Talaty, N.; Chen, H.; Cooks, R. G. *Chem. Commun* **2005**, *1950*, 1952.
- (27) Chen, H.; Venter, A.; Cooks, R. G. *Chemical Communications* **2006**, 2042-2044.
- (28) Chen, H. W.; Wortmann, A.; Zenobi, R. *J. Mass Spectrom.* **2007**, *42*, 1123-1135.
- (29) Ratcliffe, L. V.; Rutten, F. J. M.; Barrett, D. A.; Whitmore, T.; Seymour, D.; Greenwood, C.; Aranda-Gonzalvo, Y.; Robinson, S.; McCoustra, M. *Analytical Chemistry* **2007**, *79*, 6094-6101.
- (30) Nemes, P.; Vertes, A. *Analytical Chemistry* **2007**, *79*, 8098-8106.

- (31) Williams, J. P.; Patel, V. J.; Holland, R.; Scrivens, J. H. *Rapid Communications in Mass Spectrometry* **2006**, *20*, 1447-1456.
- (32) Karas, M.; Hillenkamp, F. *Analytical Chemistry* **1988**, *60*, 2299-2301.
- (33) Tanaka, K.; Ido, H. W. Y.; Akita, S.; Yoshida, Y.; Yoshida, T.; Matsuo, T. *Rapid Communications in Mass Spectrometry* **1988**, *2*, 151-153.
- (34) Duncan, M. W.; Matanovic, G.; Cerpa-Poljak, A. *Rapid Communications in Mass Spectrometry* **1993**, *7*, 1090-1094.
- (35) Lidgard, R.; Duncan, M. W. *Rapid Communications in Mass Spectrometry* **1995**, *9*, 128-132.
- (36) Cohen, L. H.; Gusev, A. I. *Analytical and Bioanalytical Chemistry* **2002**, *373*, 571-586.
- (37) Wei, J.; Buriak, J. M.; Siuzdak, G. *Nature* **1999**, *399*, 243-246.
- (38) Go, E. P.; Prenni, J. E.; Wei, J.; Jones, A.; Hall, S. C.; Witkowska, H. E.; Shen, Z.; Siuzdak, G. *Analytical Chemistry* **2003**, *75*, 2504-2506.
- (39) Chen, Y.; Vertes, A. *Analytical Chemistry* **2006**, *78*, 5835-5844.
- (40) Berkenkamp, S.; Karas, M.; Hillenkamp, F. *Proceedings of the National Academy of Sciences* **1996**, *93*, 7003-7007.
- (41) Li, Y.; Shrestha, B.; Vertes, A. *Anal. Chem.* **2008**, *80*, 407-420.
- (42) Laiko, V. V.; Baldwin, M. A.; Burlingame, A. L. *Analytical Chemistry* **2000**, *72*, 652-657.
- (43) Laiko, V. V.; Taranenko, N. I.; Berkout, V. D.; Yakshin, M. A.; Prasad, C. R.; Lee, H. S.; Doroshenko, V. M. *Journal of the American Society for Mass Spectrometry* **2002**, *13*, 354-361.

- (44) Reyzer, M. L.; Hsieh, Y.; Ng, K.; Korfmacher, W. A.; Caprioli, R. M. *Journal of Mass Spectrometry* **2003**, *38*, 1081-1092.
- (45) Bunch, J.; Clench, M. R.; Richards, D. S. *Rapid Communications in Mass Spectrometry* **2004**, *18*, 3051-3060.
- (46) Hsieh, Y.; Casale, R.; Fukuda, E.; Chen, J.; Knemeyer, I.; Wingate, J.; Morrison, R.; Korfmacher, W. *Rapid Communications in Mass Spectrometry* **2006**, *20*, 965-972.
- (47) Li, Y.; Shrestha, B.; Vertes, A. *Analytical Chemistry* **2007**, *79*, 523-532.
- (48) Tan, P. V.; Laiko, V. V.; Doroshenko, V. M. *Analytical Chemistry* **2004**, *76*, 2462-2469.
- (49) Wei, H.; Nolkrantz, K.; Powell, D. H.; Woods, J. H.; Ko, M.-C.; Kennedy, R. T. *Rapid Communications in Mass Spectrometry* **2004**, *18*, 1193-1200.
- (50) Ens, W.; Mao, Y.; Mayer, F.; Standing, K. G. *Rapid Commun Mass Spectrom* **1991**, *5*, 117-123.
- (51) Tang, K.; Allman, S. L.; Jones, R. B.; Chen, C. H. *Analytical Chemistry* **1993**, *65*, 2164-2166.
- (52) Chen, Z.; Bogaerts, A.; Vertes, A. *Applied Physics Letters* **2006**, *89*, 041503.
- (53) Caldwell, J.; Gardner, I.; Swales, N. *Toxicologic Pathology* **1995**, *23*, 102-114.
- (54) Chester, N.; Mottram, D. R.; Reilly, T.; Powell, M. *British Journal of Clinical Pharmacology* **2004**, *57*, 62-67.
- (55) Wishart, D. S.; Tzur, D.; Knox, C.; Eisner, R.; Guo, A. C.; Young, N.; Cheng, D.; Jewell, K.; Arndt, D.; Sawhney, S.; Fung, C.; Nikolai, L.; Lewis, M.; Coutouly, M.-A.; Forsythe, I.; Tang, P.; Shrivastava, S.; Jeroncic, K.; Stothard, P.; Amegbey, G.; Block, D.; Hau, D. D.; Wagner, J.; Miniaci, J.; Clements, M.; Gebremedhin, M.;

- Guo, N.; Zhang, Y.; Duggan, G. E.; MacInnis, G. D.; Weljie, A. M.; Dowlatabadi, R.; Bamforth, F.; Clive, D.; Greiner, R.; Li, L.; Marrie, T.; Sykes, B. D.; Vogel, H. J.; Querengesser, L. *Nucleic Acids Research* **2007**, *35*, D521-526.
- (56) Kanehisa, M.; Goto, S. *Nucleic Acids Research* **2000**, *28*, 27-30.
- (57) Millington, D. S.; Kodo, N.; Norwood, D. L.; Roe, C. R. *Journal of Inherited Metabolic Disease* **1990**, *13*, 321-324.
- (58) Kuhara, T. *Journal of Chromatography B* **2007**, *855*, 42-50.
- (59) Wilcken, B.; Wiley, V.; Hammond, J.; Carpenter, K. *New England Journal of Medicine* **2003**, *348*, 2304-2312.
- (60) Brand, H. S.; Jorning, G. G. A.; Chamuleau, R. A. F. M.; Abraham-Inpijn, L. *Clinica Chimica Acta* **1997**, *264*, 37-47.
- (61) Strauss, A. W. *Journal of Clinical Investigation* **2004**, *113*, 354-356.
- (62) McCooeye, M.; Ding, L.; Gardner, G. J.; Fraser, C. A.; Lam, J.; Sturgeon, R. E.; Mester, Z. *Analytical Chemistry* **2003**, *75*, 2538-2542.
- (63) Bjarnason, I.; Macpherson, A.; Hollander, D. *Gastroenterology* **1995**, *108*, 1566-1581.
- (64) Camilleri, M.; Gorman, H. *Neurogastroenterol. Motil.* **2007**, *19*, 545-552.
- (65) Bingham, S. A.; Williams, R.; Cole, T. J.; Price, C. P.; Cummings, J. H. *Annals of Clinical Biochemistry* **1988**, *25*, 610-619.
- (66) Hanton, S. D. *Chemical Reviews* **2001**, *101*, 527-569.
- (67) Lahesmaarantala, R.; Magnusson, K. E.; Granfors, K.; Leino, R.; Sundqvist, T.; Toivanen, A. *Ann. Rheum. Dis.* **1991**, *50*, 91-94.

CHAPTER 4

MOLECULAR IMAGING BY MID-IR LASER ABLATION

MASS SPECTROMETRY

Based on material published by A. Vertes, P. Nemes, B. Shrestha, A. A. Barton, Z. Chen and Y. Li in *Appl. Phys. A*, **2008**, *93*, 885-891.

ABSTRACT

Mid-IR laser ablation at atmospheric pressure (AP) produces a mixture of ions, neutrals, clusters, and particles with a size distribution extending into the nanoparticle range. Using external electric fields the ions can be extracted and sampled by a mass spectrometer. In AP infrared (IR) matrix-assisted laser desorption ionization (MALDI) experiments, the plume was shown to contain an appreciable proportion of ionic components that reflected the composition of the ablated target and enabled mass spectrometric analysis. Detected ion intensities rapidly declined with increasing the distance of sampling from the ablated surface to ~ 4 mm. This was rationalized in terms of ion recombination and the stopping of plume expansion by the background gas. In laser ablation electrospray ionization (LAESI) experiments, the ablation plume was intercepted by an electrospray. The neutral particles in the plume were ionized by the charged droplets in the spray and enabled the detection of large molecules (up to 66 kDa). Maximum ion production in LAESI was observed at large (~ 15 mm) spray axis to

ablated surface distance indicating radically different ion formation mechanism compared to AP IR-MALDI. The feasibility of molecular imaging by both AP IR-MALDI and LAESI was demonstrated on targets with mock patterns.

INTRODUCTION

In recent years atmospheric pressure (AP) laser ablation has been increasingly used in chemical analysis. As its vacuum counterpart, AP laser ablation can be utilized to produce ions, neutrals, clusters, nanoparticles and particulate matter from diverse targets. Depending on the applied laser wavelength, pulse duration and fluence and on the properties of the target and the background gas, the relative amount and the nature of these species can be vastly different. The laser-target interactions exhibit numerous regimes that are governed by the prevailing energy deposition, redistribution and dissipation mechanisms. Due to its low ion yield, preferential evaporation and ionization, direct AP laser ablation has rarely been used for chemical analysis. Instead, the established methods rely on converting other species in the laser plume into detectable ions.

In elemental analysis the combination of AP laser ablation with inductively coupled plasma mass spectrometry proved itself valuable for the microanalysis of solids.^{1, 2} This high energy postionization method is based on converting neutrals, clusters and particles into elemental ions in a high temperature plasma supported by radio frequency current. In molecular analysis, emerging methods include AP matrix-assisted laser desorption ionization (MALDI) mass spectrometry using ultraviolet

(UV)^{3, 4} and infrared (IR) lasers.^{5, 6} These methods rely on the presence of an energy absorbing matrix material that dramatically enhances the coupling of the laser energy into the target. While these techniques improved the ease of analysis for broad sample classes (including in vivo analysis), persistent debates about their lower sensitivity and especially their reduced high-mass limits compared to the corresponding vacuum methods continued to limit their acceptance. For example, AP IR-MALDI mass analysis of a peptide mixture containing bradykinin (m/z 1060.4), substance P (m/z 1347.6), and insulin (m/z 5733.5) showed discrimination against $m/z > 3,000$ ions.⁷

Although it is known from vacuum MALDI studies that both the UV and the IR laser ablation plume can contain ions from large molecules ($m/z > 100,000$), the ion yield is known to be 10^{-4} or less even for small molecules at the laser fluence threshold for ion generation.⁸ As this number results from postionization experiments based on photoexcitation, it is an upper limit for the degree of ionization because it does not account for the extensive amount of neutrals ablated as nanoparticles and particulate matter.⁹ Further factors that limit the efficiency of ion detection are the enhanced recombination of the laser generated ions in the expanding plume under AP conditions^{10, 11} and the limited ion collection efficiency of the mass spectrometer.¹² Clearly, efficient but gentle postionization is necessary to improve the ion yield in these experiments without extensive fragmentation and plasma formation.

Although postionization in vacuum environment based on a second laser beam that intercepts the ablation plume produced by the first laser has a long history,¹³⁻¹⁷ the application of this technique at atmospheric pressure has not been explored. Furthermore, the results in the vacuum experiments indicate that the overall gain in the

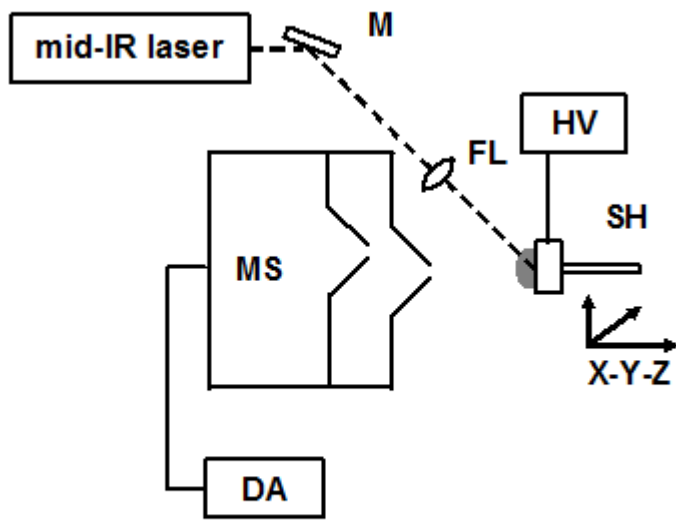
total ion yield is modest, probably due to the inability of the postionization laser to efficiently disperse and ionize the clusters, nanoparticles and particulate matter in the plume. Postionization of the ablated plume at atmospheric pressure is much less studied. Recent advances in photoionization¹⁸ and chemical ionization of the ablated material using reactive ions produced by a corona discharge indicate up to two orders of magnitude increase in ionization efficiency.^{19, 20} In a different approach, the laser ablation plume was intercepted by an electrospray plume to achieve ion production from nanoparticles and particulates produced by UV^{21, 22} and IR²³ lasers. This latter method, termed laser ablation electrospray ionization (LAESI), proved to be capable of *in vivo* analysis of plant organs as well as direct analysis of biological fluids.

In this contribution we compare ion production in AP IR-MALDI and in LAESI from diverse targets, including plant organs and bodily fluids. Optimization of ion sampling in the two methods reveals some of their mechanistic differences. Molecular imaging capabilities are demonstrated for both methods.

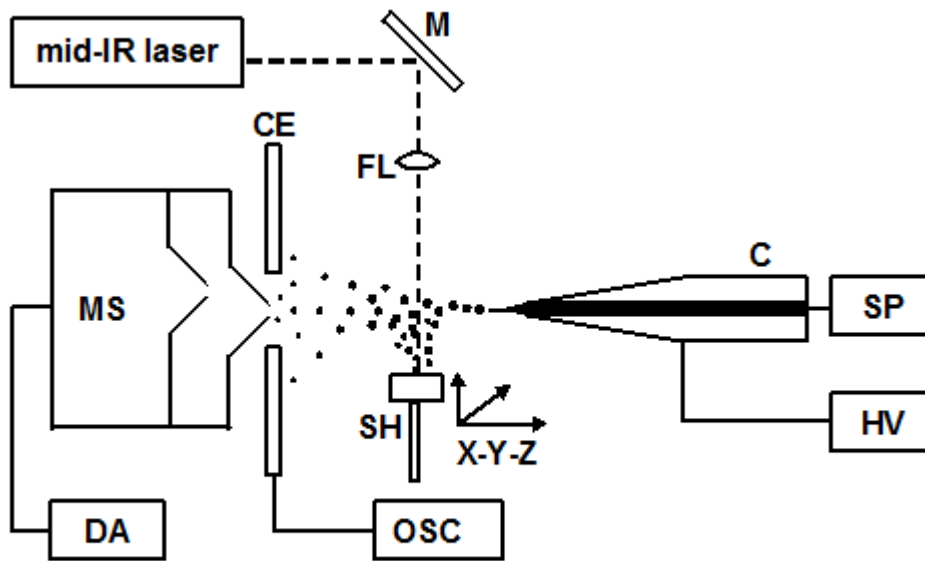
EXPERIMENTAL SECTION

The two experimental arrangements used in this study are shown in Figure 4.1. Both the AP IR-MALDI and the LAESI system are similar to the system described in chapter 2 and Nemes *et al.*,²³ respectively. The laser ablation was achieved by a Nd:YAG laser driven optical parametric oscillator (OPO) and in some LAESI experiments by an Er:YAG laser. The radiation at 2940 nm wavelength from the OPO source had a pulse length of 4 ns, whereas the Er:YAG laser produced 100 ns pulses. In the AP IR-MALDI

Figure 4.1 Schematics of two atmospheric pressure IR laser ablation systems used in biomedical analysis based on **(a)** AP IR-MALDI and **(b)** LAESI configuration. System components include C - capillary; SP - syringe pump; HV - high-voltage power supply; M - mirror; FL - focusing lens; CE - counter electrode; OSC - digital oscilloscope; SH - sample holder; X-Y-Z - motorized micropositioning system; mid-IR laser - Nd:YAG laser driven OPO or Er:YAG laser; MS - mass spectrometer; and DA – data acquisition system.



AP IR-MALDI



LAESI

A
B

experiments the elliptical focal spots resulting from the 45° angle of incidence exhibited 200 μm and 650 μm small and large axes, respectively. In the LAESI configuration the laser pulses impinged on the target surface under a right angle and circular focal spots were produced with 350-400 μm diameter. The laser fluences produced at the target were 0.3–1.0 J/cm^2 for AP IR-MALDI and 0.8–3.6 J/cm^2 for LAESI experiments.

Two orthogonal acceleration time-of-flight (oa-TOF) mass spectrometers, an AccuTOF (JEOL, Peabody, MA) and a Q-TOF Premier (Waters Co., Milford, MA) were used to detect the ions. The initial LAESI experiments were performed on the AccuTOF system in combination with the Er:YAG laser. For tandem mass spectrometry used to study the structure of unknown ions and for LAESI imaging, the Q-TOF mass spectrometer was equipped with the OPO laser source. All the AP IR-MALDI experiments were performed on the latter system.

For the molecular imaging experiments, the sample holder was mounted on a NanoMax TS motorized positioning stage. Imaging was achieved by scanning the target in the X-Y plane with a travel range of 4 mm in both directions. Positioning in the Z direction for signal optimization was achieved with a manual translation stage.

In the LAESI experiments, a home-built electrospray source was used for post-ionization. Details of this source are available in Ref. ²⁴. For best performance, that is for the highest postionization yield, the 100 μm i.d. and 320 μm o.d. tapered tip metal emitter (New Objective, Woburn, MA) was operated in the cone-jet mode. The spraying mode was monitored through the spray current measured on the stainless steel counter electrode using a digital oscilloscope. The sprayed 50 % methanol solution containing 0.1 % (v/v) acetic acid was supplied by a syringe pump.

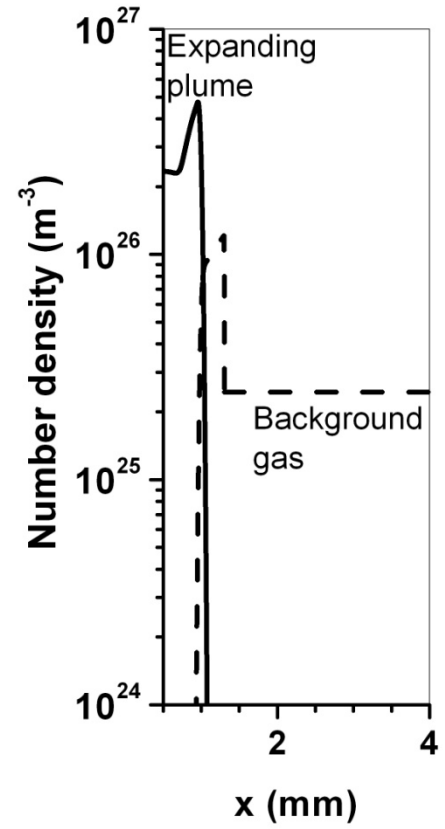
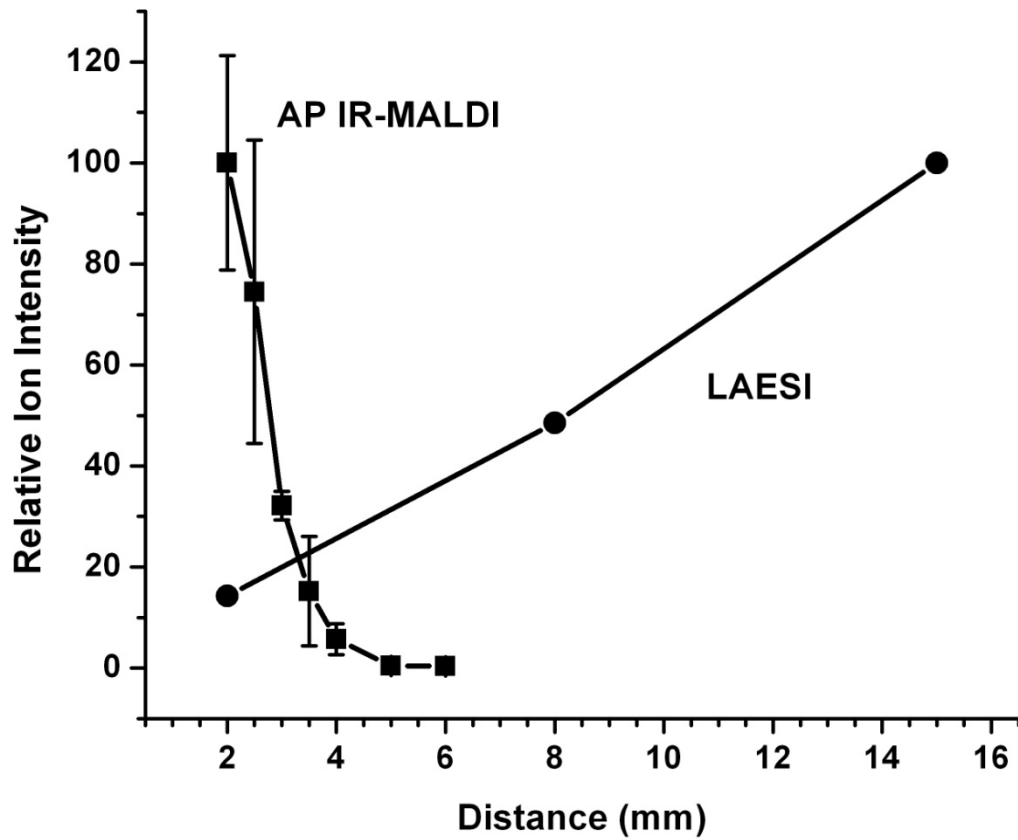
RESULTS AND DISCUSSION

Direct and postionization in the ablation plume. Based on the two experimental configurations in Figure 4.1, we compare the travel range of ions and neutral particles produced by the mid-IR laser ablation. The AP IR-MALDI system enables us to monitor the directly produced ion abundances as a function of the distance between the ablation site on the target surface and the inlet orifice of the mass spectrometer. The neutral particles can be postionized by the electrospray plume in the LAESI configuration. By changing the distance between the ablation site on the target and the axis of the electrospray plume, the travel range of the most efficiently ionized particles can be determined.

Studies on the AP mid-IR laser ablation of biological tissues indicate the presence of two phases.^{25, 26} In the early phase of the ablation (first 1 to 2 μs), vaporization of the water and the biomolecules from the tissue produces a hemispherical plume that exhibits partial ionization. This expanding plume drives a shock wave at its interface with the background gas. Eventually the energy of this plume dissipates through the work exerted on the background gas and its expansion is stopped.²⁷ Most of the ion content of this plume neutralizes through recombination.

An indication of plume stopping is the rapid decline of ion collection as the sampling orifice of the mass spectrometer is moved away from the target surface. Typical stopping distances in our experiments were 2 to 4 mm depending on the laser fluence.

Figure 4.2 (a) Relative ion intensities in AP IR-MALDI as a function of sampling orifice distance from the surface and in LAESI as a function of the position where the spray axis intercepts the laser ablation plume. **(b)** Plume number density distributions for 1.4 J/cm² Er:YAG laser ablation of water into 1 atm nitrogen gas at 800 ns. The expanding plume distribution (solid line) shows a high density region close to the shock front and the pile-up of background gas (dashed line) in front of the interface.



A|B

The curve labeled as AP IR-MALDI in Figure 4.2a shows the precipitous decline of the relative ion intensity for protonated bradykinin molecules produced from 2,5-dihydroxybenzoic acid (DHB) matrix. The OPO was tuned to 2940 nm to deliver 0.58 mJ pulses at 10 Hz repetition rate to a ~ 300 μm diameter area on the target surface, which corresponded to an 0.8 J/cm^2 fluence. The highest ion intensities were detected at the 2 mm minimum distance from the target. The standoff of the mass spectrometer was not reduced further to avoid electrical breakdown between the target held at +3000 V and the sampling cone held at -55 V. As the sampling distance from the surface increased to 4 mm the relative ion intensity dropped to $\sim 6\%$ of the value at 2 mm.

Using a one dimensional fluid dynamic model to describe the competition of surface evaporation and phase explosion ²⁶, we followed the plume density distributions in the mid-IR laser ablation of water. Figure 4.2b shows the shock wave at the water plume background gas (nitrogen) interface at 800 ns into the expansion. At the position of the large density gradient, ~ 1 mm above the surface, the water vapor density dramatically drops and the background gas density rises. Due to the so called “snowplow effect” in front of the vapor plume the background gas density is elevated in a thin layer. This early phase of the plume development is terminated when the displacement of this interface stops and the vapor plume dissipates.

Depending on target properties, the early phase is followed by the expulsion of neutral nanoparticles and small particulates driven by phase explosion and the following recoil pressure induced ejection. This ejection process can last for hundreds of microseconds. Due to the momentum of the ejected particles, this second phase produces a plume with significantly extended range. Although no data is available on

how far these particles travel, they are expected to be projected beyond ~ 10 mm above the surface.

The results of our LAESI experiments indicate that ion production through the interaction of the electrospray plume and the laser ablation plume steadily increases as the ablation spot is moved away from the common axis of the spray and the mass spectrometer. The ablation axis, positioned ~ 4 mm ahead of the emitter tip, was perpendicular to the spray axis. The strongest signal for hemoglobin alpha chain carrying 15 charges produced from human blood was detected with the spray axis at 15 mm above the ablated surface (see the curve labeled LAESI in Figure 4.2a). Further increase of the distance resulted in declining ion signal (not shown) but ions were produced as far as 30 mm away from the ablated surface. Although the IR matrixes of the target material are different (DHB vs. water), the disparate travel range of the ablation produced ions and the ejected particles is obvious in Figure 4.2a. While the laser produced ions traveling with the vapor plume almost completely disappear by the time the plume reaches ~ 4 mm, the ion yield from neutral particles increases in this range.

The decrease in AP IR-MALDI signal with the sampling distance can be explained by the combined effect of recombination and the arresting of the plume expansion. The positive ions detected in this experiment efficiently recombine with the electrons and the negative ions in the plume. The presence of these processes is indicated by the strong effect of the target potential on the detected ion signal. When the target potential was lowered close to ground, the ion signal disappeared. Sufficiently high target potential separates the charges in the plume and, in combination with the gas dynamics in the region, guides the extracted positive ions toward the sampling orifice.

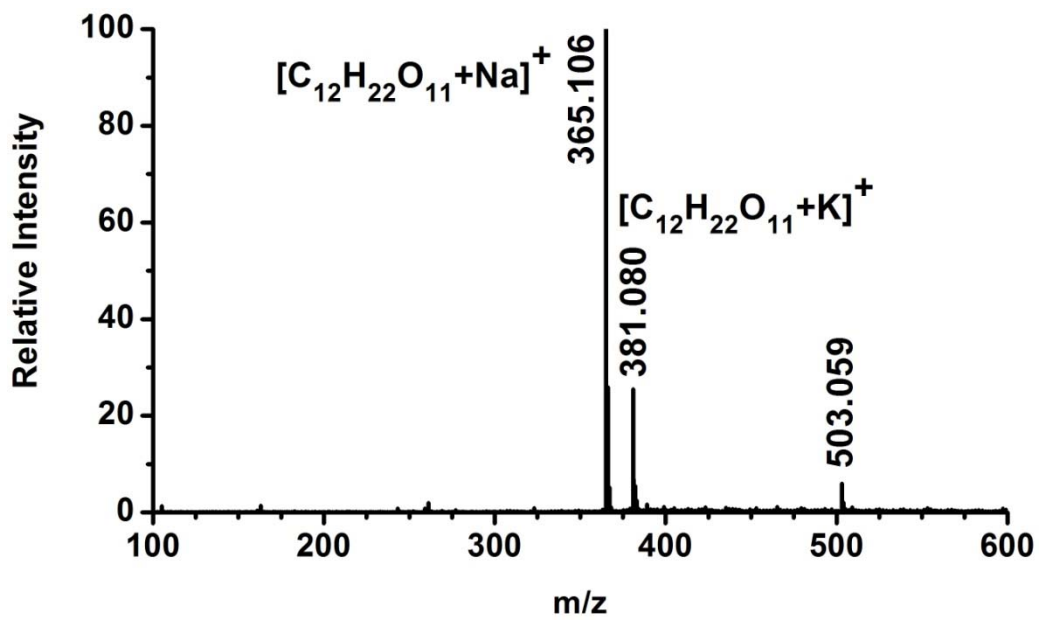
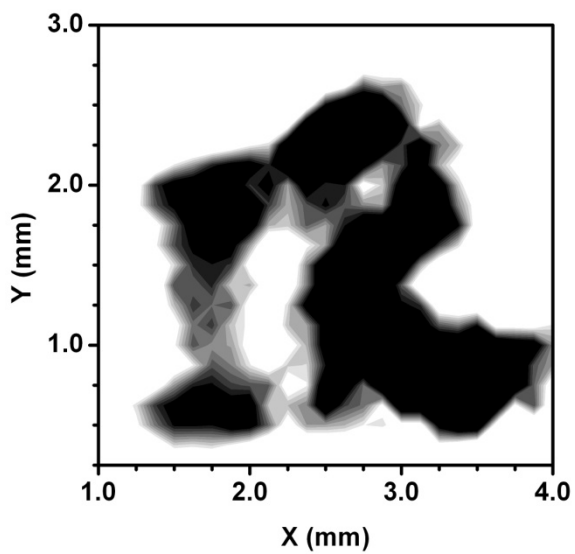
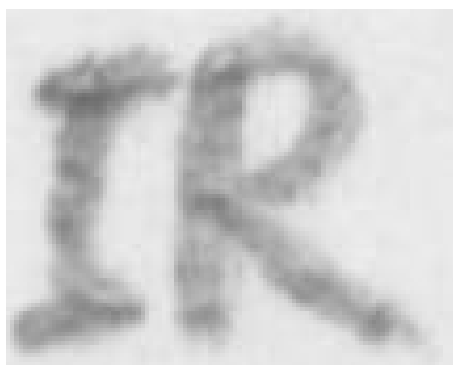
Recombination in the plume can also explain the bias against large molecules detection ($m/z > 3000$) in AP IR-MALDI.⁷ As the reaction cross section of the positive ions scales with their size, preferential recombination of large ions is expected. This effect in combination with the declining performance of the ion transfer optics at higher masses in our mass spectrometer can account for the lack of $m/z > 3000$ ions in the observed AP IR-MALDI spectra.

The dynamics of the ejected neutral particles is significantly different. Their trajectories are governed by the dissipation of the initial kinetic energy due to the drag force in the background gas. Initial particle velocities can be several hundred m/s.²⁵ From the growing trend of the detected ion intensity with increasing intercept distance in Figure 4.2a it can be inferred that this velocity is too high for efficient interaction with the charged droplets in the electrospray. As the particles are slowed down by the drag force the efficiency of coalescence increases. Alternatively, the optimum spatial overlap between the laser ablation plume and the electrospray plume can also account for the highest ion signal observed at 15 mm.

The small particles captured by the charged droplets are efficiently dissolved or their soluble components are extracted by the droplet. These charged droplets, seeded by the particles, undergo Coulomb fission and eventually produce ions from the constituents of the ablated particles. This ion production follows the rules of electrospray ionization and, for example, generates multiply charged ions from large molecules of up to 66 kDa molecular weight.

As in LAESI the sampled ablation products are neutral, there is no need to bias the target and the deleterious effect of recombination does not affect ion production.

Figure 4.3 AP IR-MALDI imaging of mock pattern produced by pencil on paper. The optical image (top left) shows the letters “IR” before rastering the surface with the laser. Chemical image (top right) constructed from the intensity of m/z 365 ions as a function of position on the surface. A typical mass spectrum is shown in the bottom panel. The ions m/z 365 and 381 correspond to a sodiated and a potassiated disaccharide, respectively.



The ion yield in LAESI strongly depends on the properties of the spray plume (spray plume density and duty cycle, as well as droplet size and composition). For example, maintaining the spray in cone-jet mode significantly improved the ion yield compared to pulsating spraying modes.^{23,24}

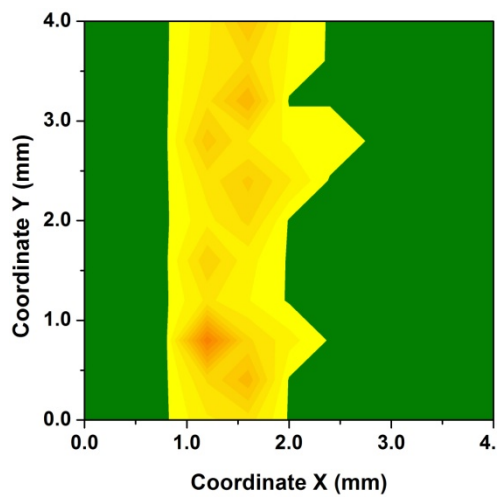
AP IR-MALDI and LAESI imaging. Lateral scanning of patterned targets in front of the laser beam produced position dependent mass spectra with both methods. To show the feasibility of molecular imaging with LAESI and to compare its capabilities with AP IR-MALDI mock patterns were created and studied.

For the AP IR-MALDI imaging, a graphite pencil was used to write the letters “IR” on a white adhesive paper label (Fisher Scientific). The top left panel in Figure 4.3 shows the optical image of the pattern before rastering the surface with the laser. The collected mass spectra showed three prominent peaks in the areas marked by the pencil (bottom panel). Two of the three ions, m/z 365 and 381, were identified as a sodiated and a potassiated disaccharide ($C_{12}H_{22}O_{11}$), respectively.²⁸ To produce the molecular image of a 4×4 mm² area, spectra were collected on a 33×33 grid with a 125 μ m step size in both directions. The image constructed from the intensity of the m/z 365 ions as a function of position on the surface is shown in the top right panel. The correlation between the optical and the molecular image is acceptable.

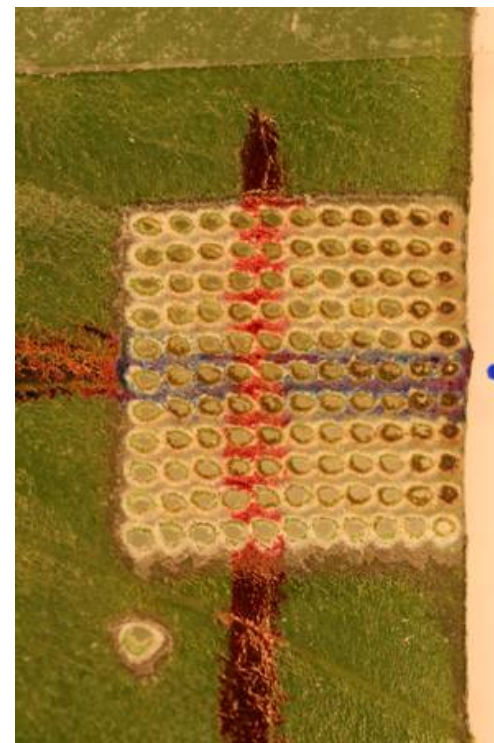
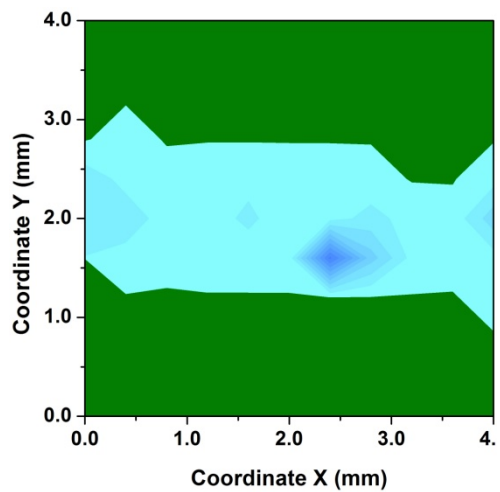
The resolution of the molecular image is limited by the laser focal spot size. The extent of the focal area is currently defined by the properties of the focusing optics (focal length, numerical aperture and spherical aberration) and, more importantly, by the wavelength and the divergence of the laser beam. In future refined versions of the

FIGURE 4.4 Imaging of a mock pattern produced on an Easter lily (*Lilium longiflorum*) leaf by red (vertical line) and blue (horizontal line) permanent markers. Optical images show the marked leaf section before (left panel) and after (right panel) LAESI imaging. LAESI images for the dye cations indicate a vertical line for the m/z 443 species (Rhodamine 6G in the red marker) (top middle panel) and a horizontal line for the m/z 478 species (Basic Blue 7 in the blue marker) (bottom middle panel).

Vertical line with
Rhodamine 6G – m/z 443



Horizontal line with
Basic Blue 7 – m/z 478



system, a beam expander could significantly reduce the latter and help to produce a significantly smaller focal spot.

For the LAESI imaging experiment a mock pattern of two lines was produced by red (vertical line) and blue (horizontal line) permanent markers (Sharpie, Sanford Co.) on an Easter lily (*Lilium longiflorum*) leaf (see the left panel of Figure 4.4). In this arrangement the laser beam aligned perpendicular to the target surface illuminated the leaf with an 0.8 J/cm² fluence and produced a circular crater of 350 μm in diameter. Mass spectra were collected on an 11×11 grid with a 400 μm step size to produce molecular images in a 4×4 mm² area. The collected mass spectra showed the typical ions of primary and secondary metabolites found in leaves and, where marked, the cations from the two dyes. Spectra corresponding to the red vertical line exhibited the m/z 443 species corresponding to the [C₂₈H₃₁N₂O₃]⁺ cation of the Rhodamine 6G ionic dye. When the sampled areas overlapped with the blue horizontal line, the m/z 478 species was observed, consistent with the [C₃₃H₄₀N₃]⁺ cation of the Basic Blue 7 common cationic dye. The molecular images for the m/z 443 and 478 ions are shown in the top and bottom middle panels of Figure 4.4, respectively. A comparison of the optical and molecular images showed good agreement. Very importantly, in the center where the two lines intercept the cations of both dyes are present in the spectra along with the plant metabolites. Furthermore, the unmarked areas on the leaf also produced metabolite ions indicating the presence of a true chemical contrast.

Inspection of the leaf after the LAESI experiment revealed the presence of tissue damage. The optical image of the exposed area is shown in the right panel of Figure 4.4. Although the array of ablation craters can be damaging to small organisms, larger ones

can remain viable after a LAESI imaging experiment. Thus, in principle, LAESI is capable of in vivo analysis and ultimately molecular imaging. The extent of tissue damage largely depends on the focal spot size. Similarly to AP IR-MALDI, the spatial resolution is also limited by the size of the ablation crater. Reducing the laser focal spot size, while maintaining the sensitivity of the method, is an important challenge in achieving these goals. Comparing the absolute ion counts on similar samples studied by AP IR-MALDI and LAESI indicates that the latter can achieve one to two orders of magnitude higher ion yields. Nevertheless, the complementary nature of the ions detected from plant tissues using the two methods requires further exploration of their utility for any given application.

ACKNOWLEDGEMENTS

This work was supported by the U.S. Department of Energy (DEFG02-01ER15129), by the W. M. Keck Foundation (041904) and in part by the U.S. National Science Foundation (grant No. 0719232). Any opinions, findings, and conclusions or recommendations expressed in this material are those of the authors and do not necessarily reflect the views of the supporting organizations.

REFERENCES

- (1) Gunther, D.; Jackson, S. E.; Longerich, H. P. *Spectrochimica Acta Part B-Atomic Spectroscopy* **1999**, *54*, 381-409.
- (2) Russo, R. E.; Mao, X. L.; Mao, S. S. *Analytical Chemistry* **2002**, *74*, 70A-77A.

- (3) Laiko, V. V.; Baldwin, M. A.; Burlingame, A. L. *Analytical Chemistry* **2000**, *72*, 652-657.
- (4) Galicia, M. C.; Vertes, A.; Callahan, J. H. *Analytical Chemistry* **2002**, *74*, 1891-1895.
- (5) Laiko, V. V.; Taranenko, N. I.; Berkout, V. D.; Yakshin, M. A.; Prasad, C. R.; Lee, H. S.; Doroshenko, V. M. *Journal of the American Society for Mass Spectrometry* **2002**, *13*, 354-361.
- (6) Von Seggern, C. E.; Cotter, R. J. *Journal of the American Society for Mass Spectrometry* **2003**, *14*, 1158-1165.
- (7) Li, Y.; Shrestha, B.; Vertes, A. *Analytical Chemistry* **2007**, *79*, 523-532.
- (8) Mowry, C. D.; Johnston, M. V. *Rapid Communications in Mass Spectrometry* **1993**, *7*, 569-575.
- (9) Leisner, A.; Rohlfing, A.; Rohling, U.; Dreisewerd, K.; Hillenkamp, F. *Journal of Physical Chemistry B* **2005**, *109*, 11661-11666.
- (10) Le, H. C.; Zeitoun, D. E.; Parisse, J. D.; Sentis, M.; Marine, W. *Physical Review E* **2000**, *62*, 4152-4161.
- (11) Knochenmuss, R.; Zhigilei, L. V. *Journal of Physical Chemistry B* **2005**, *109*, 22947-22957.
- (12) Tan, P. V.; Laiko, V. V.; Doroshenko, V. M. *Analytical Chemistry* **2004**, *76*, 2462-2469.
- (13) Spengler, B.; Bahr, U.; Karas, M.; Hillenkamp, F. *Analytical Instrumentation* **1988**, *17*, 173-193.
- (14) Lykke, K. R.; Wurz, P.; Parker, D. H.; Pellin, M. J. *Applied Optics* **1993**, *32*, 857-866.

- (15) Tang, X. D.; Sadeghi, M.; Olumee, Z.; Vertes, A. *Rapid Communications in Mass Spectrometry* **1997**, *11*, 484-488.
- (16) Voumard, P.; Zhan, Q.; Zenobi, R. *Review of Scientific Instruments* **1993**, *64*, 2215-2220.
- (17) Leisner, A.; Rohlfing, A.; Berkenkamp, S.; Hillenkamp, F.; Dreisewerd, K. *Journal of the American Society for Mass Spectrometry* **2004**, *15*, 934-941.
- (18) Robb, D. B.; Covey, T. R.; Bruins, A. P. *Analytical Chemistry* **2000**, *72*, 3653-3659.
- (19) Coon, J. J.; McHale, K. J.; Harrison, W. W. *Rapid Communications in Mass Spectrometry* **2002**, *16*, 681-685.
- (20) Coon, J. J.; Harrison, W. W. *Analytical Chemistry* **2002**, *74*, 5600-5605.
- (21) Shiea, J.; Huang, M. Z.; Hsu, H. J.; Lee, C. Y.; Yuan, C. H.; Beech, I.; Sunner, J. *Rapid Communications in Mass Spectrometry* **2005**, *19*, 3701-3704.
- (22) Huang, M. Z.; Hsu, H. J.; Lee, L. Y.; Jeng, J. Y.; Shiea, L. T. *Journal of Proteome Research* **2006**, *5*, 1107-1116.
- (23) Nemes, P.; Vertes, A. *Anal. Chem.* **2007**, *79*, 8098-8106.
- (24) Nemes, P.; Marginean, I.; Vertes, A. *Analytical Chemistry* **2007**, *79*, 3105-3116.
- (25) Apitz, I.; Vogel, A. *Applied Physics a-Materials Science & Processing* **2005**, *81*, 329-338.
- (26) Chen, Z. Y.; Bogaerts, A.; Vertes, A. *Applied Physics Letters* **2006**, *89*, 041503.
- (27) Arnold, N.; Gruber, J.; Heitz, J. *Applied Physics a-Materials Science & Processing* **1999**, *69*, S87-S93.
- (28) Li, Y.; Shrestha, B.; Vertes, A. *Analytical Chemistry* **2008**, *80*, 407-420.

CHAPTER 5

DIRECT ANALYSIS OF LIPIDS AND SMALL METABOLITES IN MOUSE BRAIN TISSUE BY AP IR-MALDI AND REACTIVE LAESI MASS SPECTROMETRY

Based on material submitted by B. Shrestha, P. Nemes, J. Nazarian,
Y. Hathout, E. P. Hoffman, and A. Vertes.

ABSTRACT

Ambient analysis of metabolites and lipids from unprocessed animal tissue by mass spectrometry remains a challenge. The utility of the two novel ambient ionization techniques, atmospheric pressure infrared matrix-assisted laser desorption ionization (AP IR-MALDI) and laser ablation electrospray ionization (LAESI), is demonstrated for the direct mass spectrometric analysis of lipids and other metabolites from mouse brain. Major brain lipids including cholesterol, various phospholipid species (glycerophosphocholines, sphingomyelin and phosphatidylethanolamines) along with numerous metabolites, for example γ -aminobutyric acid (GABA), creatine and choline, were identified in a typical mass spectrum. In a new ionization modality of LAESI, termed reactive LAESI, in-plume reactions with a solute of choice (lithium sulfate) enhanced structure-specific fragmentation of lipid ions for improved molecular assignment in collision-activated dissociation experiments. In-plume processes in reactive

LAESI provide additional structural information without contaminating the biological sample with the reactant.

INTRODUCTION

Lipidomics is broadly defined as the analysis of lipids and lipid-associated species. Apart from their structural role, lipids also act as signaling molecules or precursors to such molecules in the nervous system. As such, many neurological disorders such as schizophrenia and Alzheimer's disease, are linked to abnormal lipid metabolism.¹⁻⁴ The mammalian brain is not only rich in lipid content but also contains a structurally diverse lipid population.¹ More than half of the dry weight of a normal human brain is composed of lipids, predominantly glycerophospholipids.^{5, 6} These species play vital roles such as the generation of second messengers, apoptosis, regulation of transporters and membrane-bound enzymes, and the maintenance of neuronal wellbeing.⁷

Imbalances in brain metabolites are responsible for many neurological diseases and neurocognitive conditions.^{8, 9} Since many small metabolites are directly or indirectly involved with lipid metabolism, their detection helps to gain a better understanding of lipid function. Currently the *in vivo* analysis of metabolites is achieved by microdialysis sampling¹⁰ or by non-invasive measurements with nuclear magnetic resonance (NMR)^{11, 12} or positron emission tomography (PET)¹³ that exhibit low sensitivity. Improved detection limits for brain neurotransmitters and metabolites can be achieved using mass spectrometric techniques, such as LC/MS,¹⁴ CE-ESI-MS/MS¹⁵ and LC/ESI MS/MS,¹⁶ which require extensive sample

preparation and long analysis time. Recently, the utility of atmospheric pressure photoionization and atmospheric pressure chemical ionization was demonstrated for neurotransmitters.¹⁷

Several techniques are available for the analysis of lipids *in vivo* and *in vitro*. Nuclear magnetic resonance (NMR) based on ³¹P nuclei for phospholipids and protons for all other lipids has demonstrated excellent capabilities for the *in vivo* analysis of lipids.¹⁸ Chromatographic techniques, such as thin layer chromatography (TLC),^{19, 20} high performance liquid chromatography (HPLC) and gas chromatography (GC), are often used for the analysis of extracted lipid samples.²¹ Mass spectrometry (MS) is another powerful approach for the investigation of lipids,²² for example, in combination with traditional ionization techniques such as secondary ion mass spectrometry (SIMS)²³ and fast atom bombardment (FAB)²⁴. Two soft ionization techniques, electrospray ionization (ESI)²⁵⁻²⁷ and matrix-assisted laser desorption ionization (MALDI),²⁸⁻³⁰ have been utilized to analyze lipids from processed biological samples. The direct analysis of lipids from brain tissue using vacuum or intermediate pressure MALDI requires the application of an external matrix and the transfer of the sample into the low pressure environment.³¹⁻³⁶ Sample processing as well as the postmortem cellular disintegration of autopsied biological samples require special care to maintain the molecular integrity of samples.^{37, 38} Clearly, technical developments are needed in the way sampling and molecular analysis to mitigate such effects.

Novel MS-based approaches employing ambient ion sources present unique advantages for the investigation of biological samples, including brain

sections. As these methods probe the molecular content of tissues under atmospheric-pressure conditions, they can help to minimize or eliminate artifacts linked to freeze-thawing and postmortem tissue disintegration and provide the much desired capability of studying biological samples with minimal pretreatment. For example, desorption electrospray ionization (DESI) MS has already shown outstanding capabilities in assessing the chemical distribution in positive and negative ion mode of various lipids from brain and liver sections.³⁹⁻⁴³ Similarly, electrospray-assisted laser desorption ionization (ELDI) MS has been utilized to characterize lipids in porcine brain tissue.⁴⁴

At 2.94 μm wavelength, the strong absorption of the water molecules due to OH vibrations can be utilized to directly analyze tissue samples with a high water content including mammalian brains with $\sim 80\%$ water content.⁴⁵ Atmospheric pressure infrared matrix-assisted laser desorption ionization (AP IR-MALDI) MS, which directly samples ions generated by the infrared laser pulse, has been utilized to analyze metabolites and lipids from various plant organs and human bodily fluids.⁴⁶⁻⁴⁸ Laser ablation electrospray ionization (LAESI) samples neutrals produced by the laser ablation followed by postionization by an electrospray. LAESI-MS has been employed for the analysis of metabolites from various plant organs, human bodily fluids, and the electric organ of the torpedo fish.⁴⁹⁻⁵¹ A technique similar to LAESI, IR matrix-assisted laser desorption electrospray ionization (MALDESI) was utilized to analyze carbohydrates and lipids in milk and egg yolk.⁵² More recently, with the help of a sharpened optical fiber to reduce the focal spot size, we have demonstrated

the capability of LAESI-MS to directly analyze metabolites from single plant and animal cells.⁵³

In this contribution we demonstrate the utility of AP IR-MALDI and LAESI in the direct analysis of metabolites and lipids in mouse brain samples. To facilitate the structure elucidation of glycerophosphocholines (PC), we present a new variant of LAESI, termed reactive LAESI. Other reactive ambient ionization methods, reactive DESI and reactive ELDI,⁵⁴⁻⁵⁷ have demonstrated success in the analysis of antimalarial drugs, phosphonate hydrolysis, cholesterol, and proteins. In this approach, a reactant, i.e., lithium salt, is dissolved in the electrosprayed solution to produce droplets seeded with lithium ions. As the particulates from the laser ablation plume coalesce with the electrosprayed droplets, lithium adducts are produced from the molecules of the sample. For the lipid class, the formation of lithiated ions is especially beneficial as these ions readily undergo structure-specific fragmentation enabling enhanced molecular assignments. The cationization of PC in reactive LAESI also reveals some mechanistic details of the interaction between the electrospray plume and the neutrals produced by the infrared laser ablation.

EXPERIMENTAL SECTION

Mass Spectrometer and Infrared Laser. Positive ions generated by AP IR-MALDI and LAESI (see below) were detected by an orthogonal acceleration time-of-flight mass spectrometer (Q-TOF Premier, Waters Co., Milford, MA) with a custom made interface (see Figure 5.1). The infrared 5 ns laser pulse at 2.94 μm wavelength was

generated by a Nd:YAG laser-driven optical parametric oscillator (Vibrant IR, Opotek, Carlsbad, CA) running at 10 Hz repetition rate. The laser beam was aligned by gold-coated mirrors (**Thorlabs, Newton, NJ**) and focused by a 50 mm focal length plano-convex calcium fluoride lens (Infrared Optical Products, Farmingdale, NY). Fragmentation of selected ions was achieved by collision activated dissociation (CAD) in tandem MS experiments. The primary ions with typical collision energies between 15 and 50 eV were introduced into a collision cell filled with argon gas at 4×10^{-3} mbar pressure. The mass spectrometer was calibrated using standards for some lipid or metabolite species. The accurate m/z values were obtained from a mass spectrum averaged over 10 scans.

AP IR-MALDI MS. For improved ion collection efficiency, our home-built AP IR-MALDI interface used pulsed dynamic focusing⁵⁸ based on fast switching of a high voltage power supply (PS350, Stanford Research Systems, Sunnyvale, CA) from +3 kV to ground at a particular delay time triggered by a digital delay generator (DG535, Stanford Research Systems, Sunnyvale, CA). The target plate was kept at a distance of 2 mm from the mass spectrometer orifice to maximize ion collection efficiency, while allowing access by the focused laser beam under 45° angle. Although reducing this distance would increase the ion yield, further approaching the orifice with the sample at high voltage could induce an electrical breakdown. The laser fluence in the AP IR-MALDI experiments was 0.7 ± 0.1 J/cm².

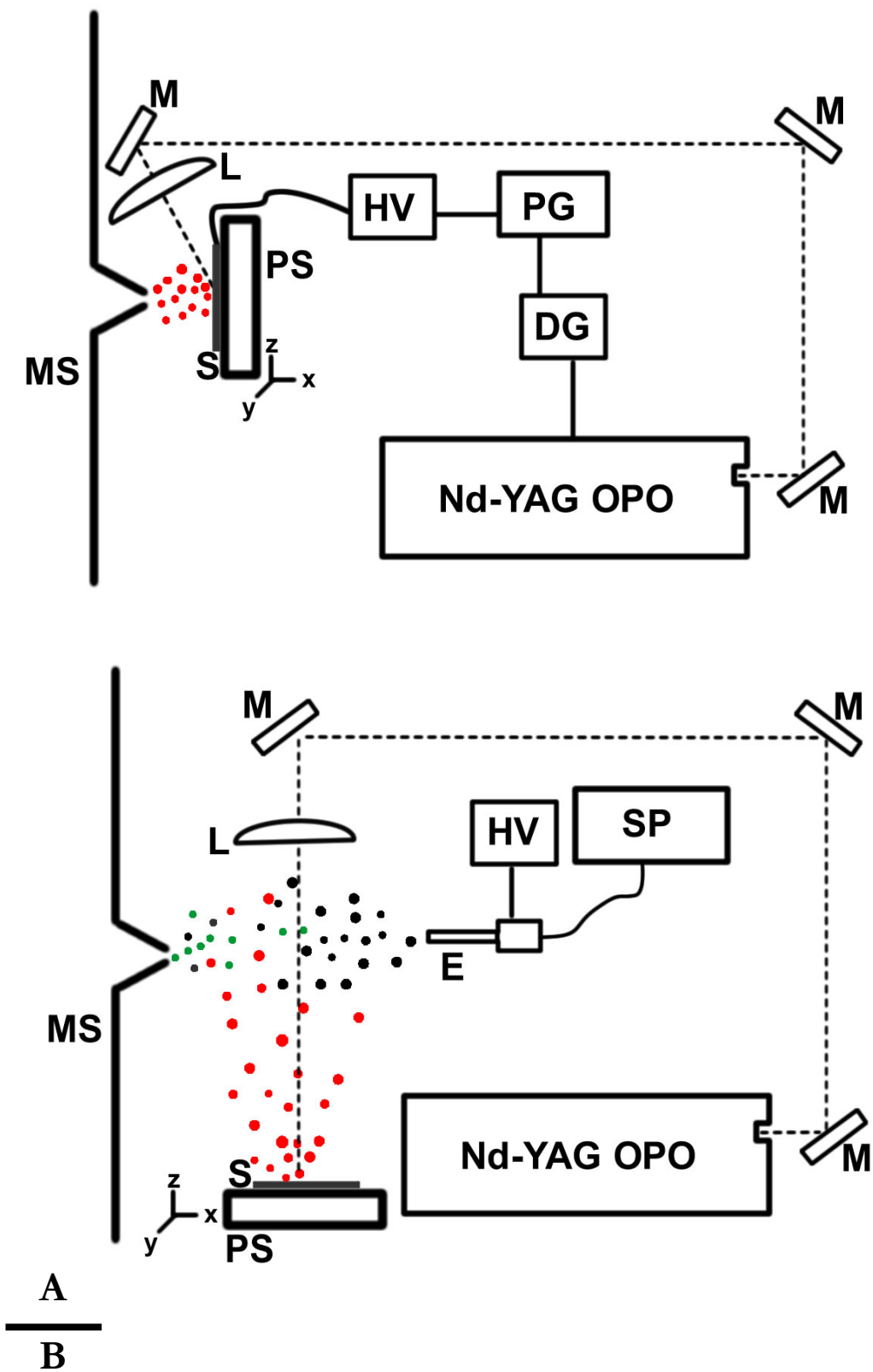
LAESI-MS. The LAESI ion source is based on an electrospray setup with the emitter biased by a regulated high voltage powersupply (PS350, Stanford Research Systems, Sunnyvale, CA). Methanol/water (1:1) mixture containing 0.1% (v/v)

trifluoroacetic acid was pumped through a blunt tip emitter (130 μm i.d., 260 μm , o.d., model 90531, Hamilton Co., Reno, NV) by a syringe pump (Harvard 22, Harvard Apparatus, Holliston, MA) at 2-5 $\mu\text{l}/\text{min}$ flow rate and stable electrospray was maintained at 3000 V potential. The emitter was lined up with the orifice of the mass spectrometer and was located at a distance of 10-12 mm from it. The distance between the target and the emitter axis was varied between 10 and 15 mm. The laser beam, with 90° incidence angle, was focused on the target \sim 5 mm downstream from the emitter tip and delivered a fluence of 0.8 ± 0.1 J/cm².

Chemicals. Lipid standard samples were obtained from Avanti Polar Lipids Inc., Alabaster, AL. All other chemicals were purchased from Fisher Scientific (Boston, MA) and used without further purification. Lipid standards of various concentrations were prepared in 50% (v/v) MeOH solution by adding lipid stock solutions prepared in CHCl₃.

Mouse Brain Tissue. Mouse brain samples were obtained from a healthy C57Bl/10 mouse strain from the Jackson Laboratory (Bar Harbor, ME). The mice were euthanized by cervical dislocation at average ages of 12-14 months. Appropriate national regulations concerning animal welfare were followed during the study. Their brains were removed and immediately snap-frozen using liquid nitrogen and stored at -80 °C until the analysis. The samples were prepared by manually excising 400 μm thick transverse sections through the middle of the cerebrum with a sharp surgical scalpel. Brain sections were directly used for mass spectrometric analysis without any pretreatment.

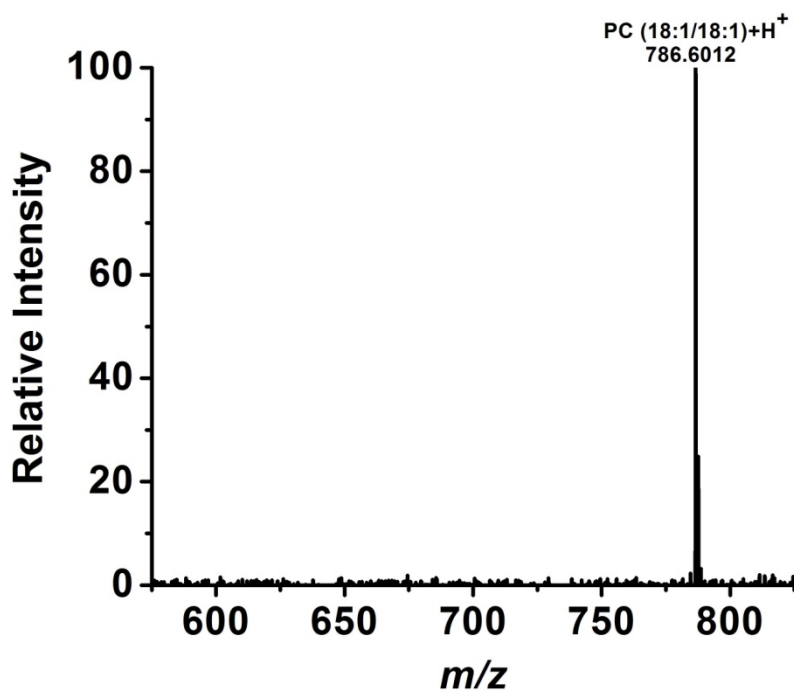
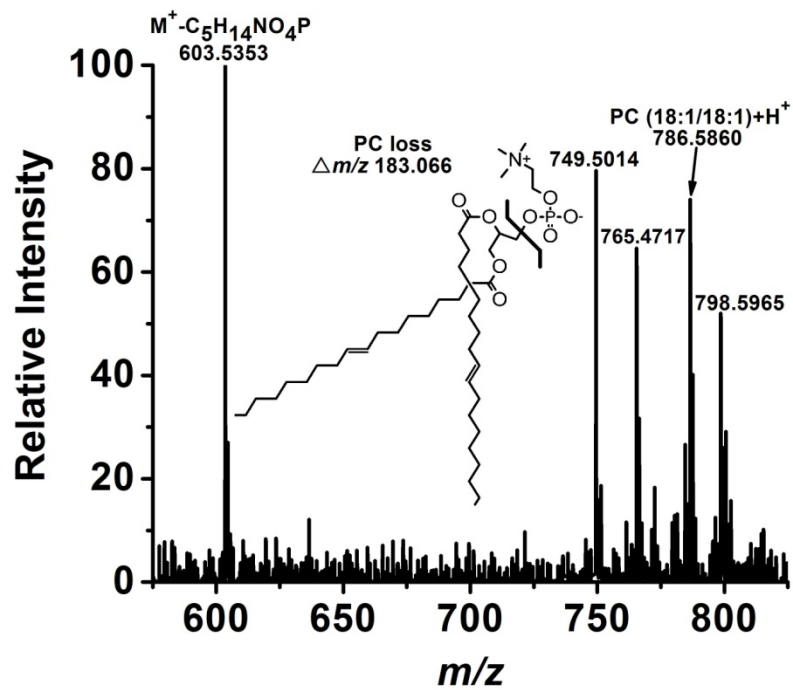
Figure 5. 1 Schematics of AP IR-MALDI and LAESI-MS. Pulses from the mid-IR Nd-YAG laser-driven OPO is focused onto the brain tissue sample (S) mounted on a Peltier stage (PS) using Au-coated mirrors (M) and a CaF₂ lens (L) generating the infrared ablation products (red dots). **(a)** In AP IR-MALDI, ions from the infrared ablation plume are directly sampled into the mass spectrometer (MS) with the help of pulsed high voltage (HV) produced by a pulse generator (PG) and timed by a delay generator (DG). **(b)** In LAESI-MS, the neutrals in the ablation plume are intercepted by the electrospray plume (black dots) and post-ionized to form ions (green dots), which are sampled by the MS. The electrospray is created by applying a high voltage (HV) to the emitter (E) capillary at a constant flow rate controlled by a syringe pump (SP).



Peltier Cooling Stage. Brain tissue kept at room temperature can undergo rapid biochemical changes and dehydration. To avoid such changes, the sections were kept just below the freezing temperature of the tissue at ~ -5 °C during the analysis by using a Peltier cooling stage.⁵⁹ The Peltier cooling stage was based on a ceramic thermoelectric module (Ferrotec Corp., Bedford, NH) attached by glue (Henkel Loctite, Cleveland, OH) to a metal heat sink (Aavid Thermalloy, Concord, NH) and a DC fan (Comair Rotron, San Diego, CA). The thermoelectric module and the fan were powered by DC supplies (R.S.R. Electronics, Avenel, NJ).

Protocol for Molecular Assignments. Due to the large number of chemical species present in the biological tissue, the assignment of the detected ions required special attention. The tentative assignments of metabolites and lipids was obtained by a combination of accurate monoisotopic mass measurements, isotope distribution analysis, the use of metabolomic and lipid databases and, in some cases, CAD tandem MS. The theoretical monoisotopic masses were calculated using the NIST Isotope Calculator package (ISOFORM, Version 1.02). Metabolomic and lipid databases were searched for species within a ± 15 mDa accuracy window of our mass spectrometric results. In particular, the detected molecules with low m/z were matched against known brain metabolites listed in the METLIN Metabolite Database⁶⁰ maintained by the Scripps Center for Mass Spectrometry (<http://metlin.scripps.edu>; last accessed on October 1, 2009) and in the Human Metabolome Database⁶¹ maintained by Genome Alberta and Genome Canada (<http://www.hmdb.ca>; last accessed on October 1, 2009). The lipid databases included the LIPID Metabolites and Pathways Strategy resource maintained by

Figure 5.2 Ambient mass spectra of PC(18:1/18:1) synthetic model lipid by **(a)** AP IR-MALDI and **(b)** LAESI indicate softer ion generation via the latter method. The inset in panel (a) shows the lipid fragmentation through the loss of the phosphocholine headgroup in AP IR-MALDI.



A
—
B

the LIPID MAPS Consortium⁶² (<http://www.lipidmaps.org>; last accessed on October 1, 2009), and the LipidBank⁶³ maintained by the Japanese Conference on the Biochemistry of Lipids (<http://www.lipidbank.jp>; last accessed on October 1, 2009). The results were reported following the comprehensive classification and nomenclature of lipids proposed by Fahy et al.⁶⁴ Even with extensive information, careful assignment of the metabolites and lipids is necessary due to the large number of possible structural isomers. The unambiguous identification of an ion needs comprehensive studies depending on multiple methods, such as separation techniques, ultrahigh resolution MS, NMR, FTIR, etc.

RESULTS AND DISCUSSION

AP IR-MALDI vs. LAESI-MS of a Lipid Standard. Initially, the production of lipid ions in AP IR-MALDI and LAESI experiments was assessed using a lipid standard. Figure 5.2 presents the mass spectrum of the synthetic model lipid, PC(18:1/18:1) acquired by AP IR-MALDI and LAESI-MS. Comparison of the two spectra revealed that in AP IR-MALDI (see Figure 5.2a) of PC(18:1/18:1) underwent fragmentation losing, among others, the phosphocholine (PC) headgroup (Figure 5.2a inset), whereas LAESI primarily produced the intact protonated molecular ion (see Figure 5.2b). Recalling the sampling conditions for the two ionization modes helps to understand the differences between these spectra. While in AP IR-MALDI the primary laser ablation plume, produced by the phase explosion of the liquid, is sampled for ions,⁶⁵ in LAESI, the neutral particulate matter ejected by the recoil pressure is post-

ionized by an electrospray source.⁴⁹ Thus, the lack of fragmentation observed in LAESI is consistent with the less energetic sample ejection process.

Analysis of brain metabolites. Direct AP IR-MALDI and LAESI analysis of mouse brain sections produced mass spectra dominated by small metabolites and phospholipids, such as PC (see Figures 5.3 and 5.4, respectively). Detailed analysis of the spectra further revealed the presence of mono-radiylglycerols (MG), diradiylglycerols (DG), phosphatidylethanolamines (PE), glycerophosphoglycerols (PG) and phosphosphingolipids (SM). Detailed lists of the metabolites and lipids detected by AP IR-MALDI and LAESI are provided in Tables 5.1 and 5.2, respectively. Consistent with earlier reports that indicated predominant alkalination instead of protonation for MALDI at elevated pressures,⁶⁶⁻⁶⁸ in AP IR-MALDI lipids were detected primarily as potassiumated and sodiumated molecules. In contrast, even though alkali cation concentrations were generally high in the brain tissue, the LAESI mass spectra were dominated by protonated peaks with sodiumated ions present in only a few cases.

In addition to lipids, small brain metabolites were also present in both the AP IR-MALDI and the LAESI spectra (see Tables 5.1 and 5.2, respectively). Accurate mass measurements with sufficient mass resolution were needed to make the assignments for 44 small metabolites. For example, γ -aminobutyric acid (GABA), a major inhibitory neurotransmitter in the mammalian brain⁶⁹ and choline, a precursor to many lipids and a neurotransmitter⁷⁰ were both expected to be present with a nominal m/z of 104. The calculated accurate monoisotopic masses of the protonated GABA ion and the choline cation were only 36.3 mDa apart.

Figure 5.3 Positive ion AP IR-MALDI mass spectrum from a transverse section of mouse brain cerebrum. Endogenous metabolite ions are observed in the $m/z < 400$ range. The spectrum was dominated by potassiated and sodiated phospholipids in the $m/z > 700$ range. The cholesterol was detected in its alkalinated form or after a water loss.

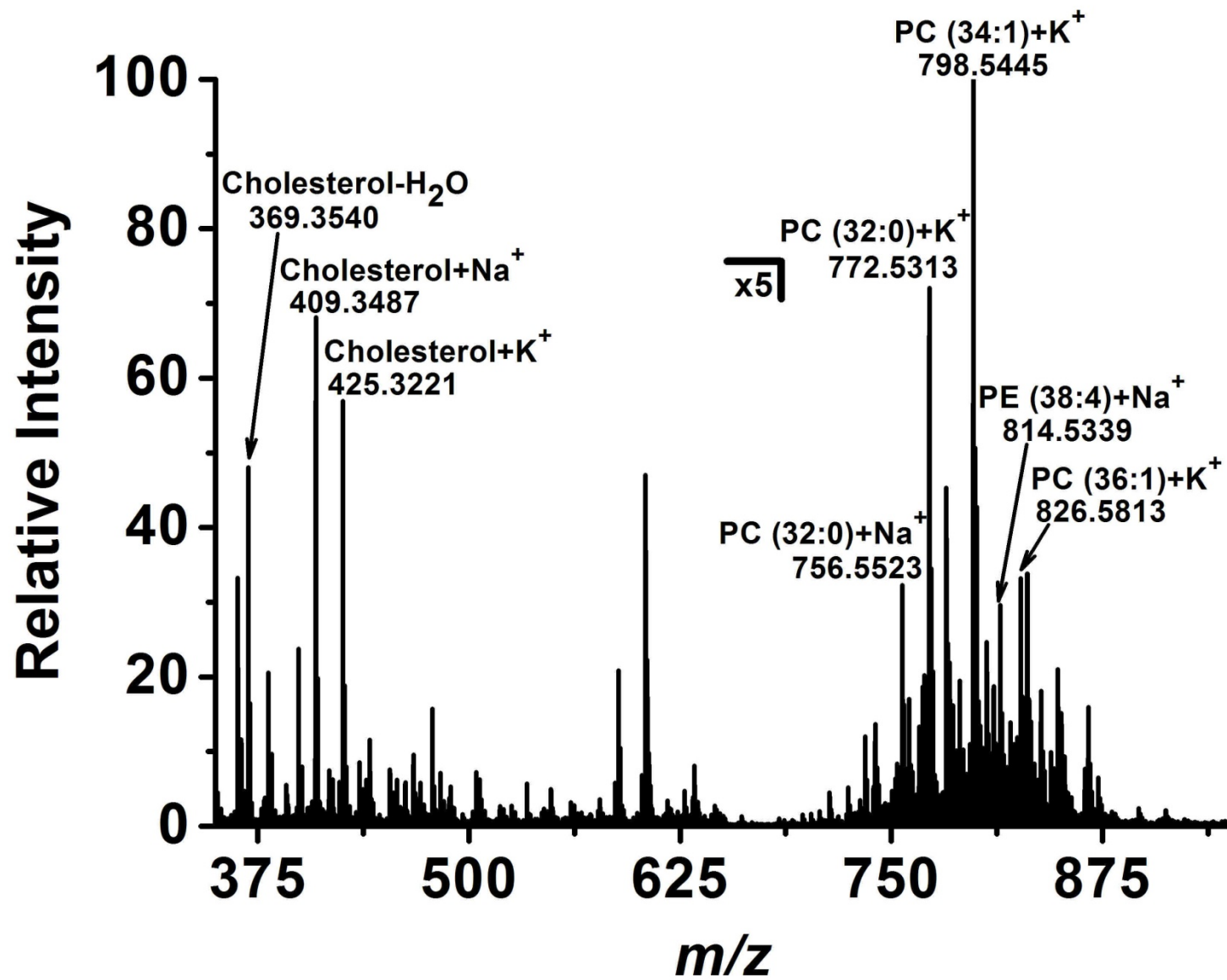


Figure 5.4 Positive ion LAESI mass spectrum recorded from a transverse section of mouse brain cerebrum. Phosphocholine, at m/z 184.0654, also found in the polar headgroup of PCs, was the base peak in the spectrum. Endogenous metabolite ions from the brain were observed in the $m/z < 400$ range and the $m/z > 700$ region revealed the presence of various protonated phospholipids.

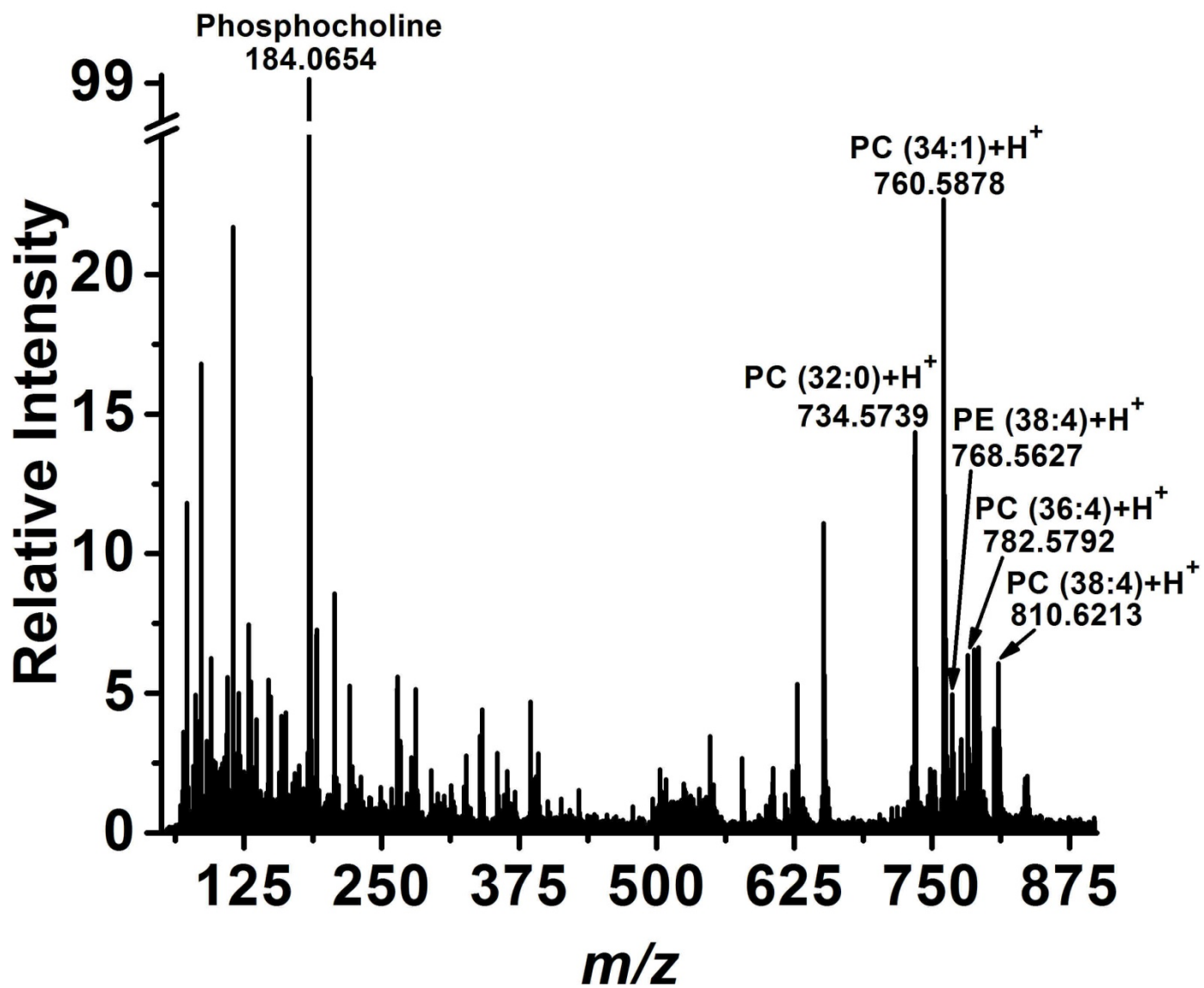


Table 5.1 Tentative peak assignments for ions in the AP IR-MALDI mass spectrum of normal mouse brain tissue.

Metabolites and Lipids ^a	Chemical formula	Ion	<i>m/z</i> _{calc.}	<i>m/z</i> _{meas.}	Δm (mDa)	ppm
pyrrolidinone	C ₄ H ₇ NO	M+H ⁺	86.0606	86.0597	-0.9	-10.5
alanine	C ₃ H ₇ NO ₂	M+H ⁺	90.0555	90.0551	-0.4	-4.4
γ -aminobutyric acid	C ₄ H ₉ NO ₂	M+H ⁺	104.0712	104.0731	1.9	18.3
choline	C ₅ H ₁₄ NO ⁺	(+)	104.1075	104.1075	0	0.0
creatine	C ₄ H ₉ N ₃ O ₂	M+H ⁺	132.0773	132.0775	0.2	1.5
hypoxanthine	C ₅ H ₄ N ₄ O	M+H ⁺	137.0463	137.0459	-0.4	-2.9
phosphoethanolamine	C ₂ H ₈ NO ₄ P	M+H ⁺	142.0269	142.0302	3.3	23.2
spermidine	C ₇ H ₁₉ N ₃	M+H ⁺	146.1657	146.1690	3.3	22.6
imidazolone propionic acid	C ₆ H ₈ N ₂ O ₃	M+H ⁺	157.0613	157.0642	2.9	18.5
dihydroorotate	C ₅ H ₆ N ₂ O ₄	M+H ⁺	159.0406	159.0291	-11.5	-72.3
dihydroxymandelaldehyde	C ₈ H ₈ O ₄	M+H ⁺	169.0501	169.0591	9	53.2
furoylglycine	C ₇ H ₇ NO ₄	M+H ⁺	170.0453	170.0362	-9.1	-53.5
arginine	C ₆ H ₁₄ N ₄ O ₂	M+H ⁺	175.1195	175.1199	0.4	2.3
methyltryptamine	C ₁₁ H ₁₄ N ₂	M+H ⁺	175.1235	175.1199	-3.6	-20.6
hydroxytryptophan	C ₁₁ H ₁₂ N ₂ O ₃	M+H ⁺	221.0926	221.0950	2.4	10.9
carosine	C ₉ H ₁₄ N ₄ O ₃	M+H ⁺	227.1144	227.1126	-1.8	-7.9
homocarnosine	C ₁₀ H ₁₆ N ₄ O ₃	M+H ⁺	241.1301	241.1284	-1.7	-7.1
glycerophosphocholine	C ₈ H ₂₀ NO ₆ P	M+H ⁺	258.1106	258.1133	2.7	10.5
inosine	C ₁₀ H ₁₂ N ₄ O ₅	M+H ⁺	269.0886	269.0917	3.1	11.5
		M+K ⁺	307.0445	307.0462	1.7	5.5
aminoimidazole ribonucleotide	C ₈ H ₁₄ N ₃ O ₇ P	M+H ⁺	296.0648	296.0662	1.4	4.7
arachidonic acid	C ₂₀ H ₃₂ O ₂	M+H ⁺	305.2481	305.2340	-14.1	-46.2
cholesterol	C ₂₇ H ₄₆ O	M-				
		H ₂ O+H ⁺	369.3521	369.3540	1.9	5.1
		M+Na ⁺	409.3446	409.3487	4.1	10.0
		M+K ⁺	425.3186	425.3221	3.5	8.2
N-arachidonoyl D-serine	C ₂₃ H ₃₇ NO ₄	M+H ⁺	392.2801	392.2833	3.2	8.2
hydroxycholesterol	C ₂₇ H ₄₆ O ₂	M+K ⁺	441.3135	441.3259	12.4	28.1
PC(O-16:1)	C ₂₄ H ₅₀ NO ₆ P	M+K ⁺	518.3013	518.3072	5.9	11.4
PC(16:0)	C ₂₄ H ₅₀ NO ₇ P	M+K ⁺	534.2962	534.3058	9.6	18.0
PC(20:4)	C ₂₈ H ₅₀ NO ₇ P	M+H ⁺	544.3403	544.3317	-8.6	-15.8
PC(18:1)	C ₂₆ H ₅₂ NO ₇ P	M+Na ⁺	544.3379	544.3317	-6.2	-11.4
Cer(d18:1/18:0)	C ₃₆ H ₇₁ NO ₃	M+Na ⁺	588.5331	588.5372	4.1	7.0
		M+K ⁺	604.5071	604.5123	5.2	8.6
DG(34:1)	C ₃₇ H ₇₀ O ₅	M+Na ⁺	617.5120	617.5239	11.9	19.3
DG(36:1)	C ₃₉ H ₇₄ O ₅	M+Na ⁺	645.5433	645.5369	-6.4	-9.9
		M+K ⁺	661.5173	661.5209	3.6	5.4
DG(38:4)	C ₄₁ H ₇₂ O ₅	M+Na ⁺	667.5277	667.5402	12.5	18.7
PA(34:1)	C ₃₇ H ₇₁ O ₈ P	M+Na ⁺	697.4784	697.4857	7.3	10.5
		M+K ⁺	713.4524	713.4602	7.8	10.9
PA(36:2)	C ₃₉ H ₇₃ O ₈ P	M+Na ⁺	723.4940	723.5016	7.6	10.5
		M+K ⁺	739.4680	739.4800	12	16.2
SM(18:0)	C ₄₁ H ₈₄ N ₂ O ₆ P ⁺	(+)	731.6067	731.6086	1.9	2.6
		M-H+Na ⁺	753.5886	753.5836	-5	-6.6
		M-H+K ⁺	769.5626	769.5598	-2.8	-3.6
PC(32:0)	C ₄₀ H ₈₀ NO ₈ P	M+H ⁺	734.5700	734.5776	7.6	10.3
		M+Na ⁺	756.5519	756.5523	0.4	0.5
		M+K ⁺	772.5258	772.5313	5.5	7.1
PC(34:1)	C ₄₂ H ₈₂ NO ₈ P	M+H ⁺	760.5856	760.5878	2.2	2.9
		M+Na ⁺	782.5675	782.5671	-0.4	-0.5
		M+K ⁺	798.5415	798.5445	3	3.8
PE(38:4)	C ₄₃ H ₇₈ NO ₈ P	M+H ⁺	768.5543	768.5493	-5	-6.5
		M+Na ⁺	790.5363	790.5342	-2.1	-2.7
PE(36:1)	C ₄₁ H ₈₀ NO ₈ P	M+Na ⁺	768.5519	768.5493	-2.6	-3.4
SM(24:0)	C ₄₂ H ₈₄ NO ₆ P	M+K ⁺	768.5673	768.5632	-4.1	-5.3

PC(36:4)	C ₄₄ H ₈₀ NO ₈ P	M+H ⁺	782.5700	782.5671	-2.9	-3.7
PC(O-34:1)	C ₄₂ H ₈₄ NO ₇ P	M+K ⁺	784.5622	784.5659	3.7	4.7
PS(36:2)	C ₄₂ H ₇₈ NO ₁₀ P	M+H ⁺	788.5441	788.5528	8.7	11.0
PC(O-36:5)	C ₄₄ H ₈₀ NO ₇ P	M+Na ⁺	788.5566	788.5528	-3.8	-4.8
PE(40:6)	C ₄₅ H ₇₈ NO ₈ P	M+H ⁺	792.5543	792.5460	-8.3	-10.5
PC(O-36:3)	C ₄₄ H ₈₄ NO ₇ P	M+K ⁺	808.5622	808.5589	-3.3	-4.1
		M+Na ⁺	814.5363	814.5339	-2.4	-2.9
		M+K ⁺	830.5101	830.5212	11.1	13.4
PG(36:0)	C ₄₂ H ₈₃ O ₁₀ P	M+H ⁺	801.5621	801.5630	0.9	1.1
		M+Na ⁺	817.5361	817.5458	9.7	11.9
PC(36:1)	C ₄₄ H ₈₆ NO ₈ P	M+Na ⁺	810.5989	810.6011	2.2	2.7
		M+K ⁺	826.5728	826.5813	8.5	10.3
PC(38:4)	C ₄₆ H ₈₄ NO ₈ P	M+H ⁺	810.6012	810.6011	-0.1	-0.1
		M+Na ⁺	832.5831	832.5697	-13.4	-16.1
PC(O-38:5)	C ₄₆ H ₈₄ NO ₇ P	M+K ⁺	832.5622	832.5697	7.5	9.0
PC(38:3)	C ₄₆ H ₈₆ NO ₈ P	M+Na ⁺	834.5989	834.5854	-13.5	-16.2
PC(O-38:4)	C ₄₆ H ₈₆ NO ₇ P	M+K ⁺	834.5779	834.5854	7.5	9.0
PC(38:6)	C ₄₆ H ₈₀ NO ₈ P	M+Na ⁺	828.5519	828.5660	14.1	17.0
		M+K ⁺	844.5258	844.5347	8.9	10.5
PS(36:0)	C ₄₂ H ₈₂ NO ₁₀ P	M+K ⁺	830.5313	830.5212	-10.1	-12.2
SM(24:1)	C ₄₇ H ₉₄ N ₂ O ₆ P	M-H+K ⁺	851.6408	851.6492	8.4	9.9
PC(40:6)	C ₄₈ H ₈₄ NO ₈ P	M+Na ⁺	856.5831	856.5961	13	15.2
		M+K ⁺	872.5571	872.5673	10.2	11.7
PC(40:1)	C ₄₈ H ₉₄ NO ₈ P	M+Na ⁺	866.6614	866.6537	-7.7	-8.9
PC(40:1)	C ₄₈ H ₉₄ NO ₈ P	M+K ⁺	882.6354	882.6407	5.3	6.0

^aDG, PA, PC, PE, PS, PG, and SM species are identified by the total length of the acyl chain(s) and the number of double bonds in parentheses.

Table 5.2 Tentative peak assignments for ions in the LAESI mass spectrum of normal mouse brain tissue.

Metabolites and Lipids ^a	Chemical formula	Ion	<i>m/z</i> _{calc.}	<i>m/z</i> _{meas.}	Δm (mDa)	ppm
pyrrolidinone	C ₄ H ₇ NO	M+H ⁺	86.0606	86.0597	-0.9	-10.5
alanine	C ₃ H ₇ NO ₂	M+H ⁺	90.0555	90.0551	-0.4	-4.4
γ -aminobutyric acid	C ₄ H ₉ NO ₂	M+H ⁺	104.0712	104.0731	1.9	18.3
choline	C ₅ H ₁₄ NO ⁺	(+)	104.1075	104.1075	0	0.0
creatine	C ₄ H ₉ N ₃ O ₂	M+H ⁺	132.0773	132.0775	0.2	1.5
hypoxanthine	C ₅ H ₄ N ₄ O	M+H ⁺	137.0463	137.0459	-0.4	-2.9
phosphoethanolamine	C ₂ H ₈ NO ₄ P	M+H ⁺	142.0269	142.0302	3.3	23.2
spermidine	C ₇ H ₁₉ N ₃	M+H ⁺	146.1657	146.1690	3.3	22.6
imidazolone propionic acid	C ₆ H ₈ N ₂ O ₃	M+H ⁺	157.0613	157.0642	2.9	18.5
dihydroorotate	C ₅ H ₆ N ₂ O ₄	M+H ⁺	159.0406	159.0291	-11.5	-72.3
dihydroxymandelaldehyde	C ₈ H ₈ O ₄	M+H ⁺	169.0501	169.0591	9	53.2
furoylglycine	C ₇ H ₇ NO ₄	M+H ⁺	170.0453	170.0362	-9.1	-53.5
arginine	C ₆ H ₁₄ N ₄ O ₂	M+H ⁺	175.1195	175.1199	0.4	2.3
methyltryptamine	C ₁₁ H ₁₄ N ₂	M+H ⁺	175.1235	175.1199	-3.6	-20.6
hydroxytryptophan	C ₁₁ H ₁₂ N ₂ O ₃	M+H ⁺	221.0926	221.0950	2.4	10.9
carosine	C ₉ H ₁₄ N ₄ O ₃	M+H ⁺	227.1144	227.1126	-1.8	-7.9
homocarnosine	C ₁₀ H ₁₆ N ₄ O ₃	M+H ⁺	241.1301	241.1284	-1.7	-7.1
glycerophosphocholine	C ₈ H ₂₀ NO ₆ P	M+H ⁺	258.1106	258.1133	2.7	10.5
inosine	C ₁₀ H ₁₂ N ₄ O ₅	M+H ⁺	269.0886	269.0917	3.1	11.5
		M+K ⁺	307.0445	307.0462	1.7	5.5
aminoimidazole	C ₈ H ₁₄ N ₃ O ₇ P					
ribonucleotide		M+H ⁺	296.0648	296.0662	1.4	4.7
arachidonic acid	C ₂₀ H ₃₂ O ₂	M+H ⁺	305.2481	305.2340	-14.1	-46.2
cholesterol	C ₂₇ H ₄₆ O	M-				
		H ₂ O+H ⁺	369.3521	369.3540	1.9	5.1
		M+Na ⁺	409.3446	409.3487	4.1	10.0
		M+K ⁺	425.3186	425.3221	3.5	8.2
N-arachidonoyl D-serine	C ₂₃ H ₃₇ NO ₄	M+H ⁺	392.2801	392.2833	3.2	8.2
hydroxycholesterol	C ₂₇ H ₄₆ O ₂	M+K ⁺	441.3135	441.3259	12.4	28.1
PC(O-16:1)	C ₂₄ H ₅₀ NO ₆ P	M+K ⁺	518.3013	518.3072	5.9	11.4
PC(16:0)	C ₂₄ H ₅₀ NO ₇ P	M+K ⁺	534.2962	534.3058	9.6	18.0
PC(20:4)	C ₂₈ H ₅₀ NO ₇ P	M+H ⁺	544.3403	544.3317	-8.6	-15.8
PC(18:1)	C ₂₆ H ₅₂ NO ₇ P	M+Na ⁺	544.3379	544.3317	-6.2	-11.4
Cer(d18:1/18:0)	C ₃₆ H ₇₁ NO ₃	M+Na ⁺	588.5331	588.5372	4.1	7.0
		M+K ⁺	604.5071	604.5123	5.2	8.6
DG(34:1)	C ₃₇ H ₇₀ O ₅	M+Na ⁺	617.5120	617.5239	11.9	19.3
DG(36:1)	C ₃₉ H ₇₄ O ₅	M+Na ⁺	645.5433	645.5369	-6.4	-9.9
		M+K ⁺	661.5173	661.5209	3.6	5.4
DG(38:4)	C ₄₁ H ₇₂ O ₅	M+Na ⁺	667.5277	667.5402	12.5	18.7
PA(34:1)	C ₃₇ H ₇₁ O ₈ P	M+Na ⁺	697.4784	697.4857	7.3	10.5
		M+K ⁺	713.4524	713.4602	7.8	10.9
PA(36:2)	C ₃₉ H ₇₃ O ₈ P	M+Na ⁺	723.4940	723.5016	7.6	10.5
		M+K ⁺	739.4680	739.4800	12	16.2
SM(18:0)	C ₄₁ H ₈₄ N ₂ O ₆ P ⁺	(+)	731.6067	731.6086	1.9	2.6
		M-H+Na ⁺	753.5886	753.5836	-5	-6.6
		M-H+K ⁺	769.5626	769.5598	-2.8	-3.6
PC(32:0)	C ₄₀ H ₈₀ NO ₈ P	M+H ⁺	734.5700	734.5776	7.6	10.3
		M+Na ⁺	756.5519	756.5523	0.4	0.5
		M+K ⁺	772.5258	772.5313	5.5	7.1
PC(34:1)	C ₄₂ H ₈₂ NO ₈ P	M+H ⁺	760.5856	760.5878	2.2	2.9
		M+Na ⁺	782.5675	782.5671	-0.4	-0.5
		M+K ⁺	798.5415	798.5445	3	3.8
PE(38:4)	C ₄₃ H ₇₈ NO ₈ P	M+H ⁺	768.5543	768.5493	-5	-6.5
		M+Na ⁺	790.5363	790.5342	-2.1	-2.7
PE(36:1)	C ₄₁ H ₈₀ NO ₈ P	M+Na ⁺	768.5519	768.5493	-2.6	-3.4

SM(24:0)	C ₄₂ H ₈₄ NO ₆ P	M+K ⁺	768.5673	768.5632	-4.1	-5.3
PC(36:4)	C ₄₄ H ₈₀ NO ₈ P	M+H ⁺	782.5700	782.5671	-2.9	-3.7
PC(O-34:1)	C ₄₂ H ₈₄ NO ₇ P	M+K ⁺	784.5622	784.5659	3.7	4.7
PS(36:2)	C ₄₂ H ₇₈ NO ₁₀ P	M+H ⁺	788.5441	788.5528	8.7	11.0
PC(O-36:5)	C ₄₄ H ₈₀ NO ₇ P	M+Na ⁺	788.5566	788.5528	-3.8	-4.8
PE(40:6)	C ₄₅ H ₇₈ NO ₈ P	M+H ⁺	792.5543	792.5460	-8.3	-10.5
PC(O-36:3)	C ₄₄ H ₈₄ NO ₇ P	M+K ⁺	808.5622	808.5589	-3.3	-4.1
		M+Na ⁺	814.5363	814.5339	-2.4	-2.9
		M+K ⁺	830.5101	830.5212	11.1	13.4
PG(36:0)	C ₄₂ H ₈₃ O ₁₀ P	M+H ⁺	801.5621	801.5630	0.9	1.1
		M+Na ⁺	817.5361	817.5458	9.7	11.9
PC(36:1)	C ₄₄ H ₈₆ NO ₈ P	M+Na ⁺	810.5989	810.6011	2.2	2.7
		M+K ⁺	826.5728	826.5813	8.5	10.3
PC(38:4)	C ₄₆ H ₈₄ NO ₈ P	M+H ⁺	810.6012	810.6011	-0.1	-0.1
		M+Na ⁺	832.5831	832.5697	-13.4	-16.1
PC(O-38:5)	C ₄₆ H ₈₄ NO ₇ P	M+K ⁺	832.5622	832.5697	7.5	9.0
PC(38:3)	C ₄₆ H ₈₆ NO ₈ P	M+Na ⁺	834.5989	834.5854	-13.5	-16.2
PC(O-38:4)	C ₄₆ H ₈₆ NO ₇ P	M+K ⁺	834.5779	834.5854	7.5	9.0
PC(38:6)	C ₄₆ H ₈₀ NO ₈ P	M+Na ⁺	828.5519	828.5660	14.1	17.0
		M+K ⁺	844.5258	844.5347	8.9	10.5
PS(36:0)	C ₄₂ H ₈₂ NO ₁₀ P	M+K ⁺	830.5313	830.5212	-10.1	-12.2
SM(24:1)	C ₄₇ H ₉₄ N ₂ O ₆ P	M-H+K ⁺	851.6408	851.6492	8.4	9.9
PC(40:6)	C ₄₈ H ₈₄ NO ₈ P	M+Na ⁺	856.5831	856.5961	13	15.2
		M+K ⁺	872.5571	872.5673	10.2	11.7
PC(40:1)	C ₄₈ H ₉₄ NO ₈ P	M+Na ⁺	866.6614	866.6537	-7.7	-8.9
PC(40:1)	C ₄₈ H ₉₄ NO ₈ P	M+K ⁺	882.6354	882.6407	5.3	6.0

The corresponding peaks were close to baseline resolved by both AP IR-MALDI and LAESI. Compared to LAESI, a higher propensity of alkylation was observed in AP IR-MALDI (see Tables 5.2 and 5.1). Mass accuracies for the ions identified in the mass spectra were uniformly below 15 mDa in the $m/z < 900$ mass range. Inspecting Tables 5.1 and 5.2 reveals that the two methods presented above offer complementary information for metabolite analysis directly from the brain tissue.

Cholesterol. Detection of cholesterol, one of the most abundant steroid lipids, by mass spectrometry is hindered by its inefficient ionization. In addition to being critical for the regulation of cell membrane properties in mammalian cells, cholesterol also acts as a precursor to other metabolites such as steroid hormones, bile acids and vitamin D.⁷¹ ⁷² Cholesterol was readily detected by AP IR-MALDI at m/z 369.3540, 409.3487 and 425.3221 as $[M-H_2O+H]^+$, $[M+Na]^+$ and $[M+K]^+$, respectively (see Figure 5.3). In wet samples the alkaline adduct ions were more abundant. Interestingly, cholesterol spectra were also produced from dried samples with the $[M-H_2O+H]^+$ ion becoming more prominent. The ionization of cholesterol with AP IR-MALDI in the absence of water could be explained by the absorption of the O-H bond in the cholesterol molecule at 2.94 μm laser wavelength as shown in the condensed phase FT-IR spectrum (see, e.g., <http://webbook.nist.gov/>).

In the positive ion mode, relatively non-polar molecules, such as cholesterol, are poorly ionized by electrospray ionization. Thus usually derivatization, for example, to cholesterol-3-sulfate, is carried out to facilitate their detection.⁷³ In the LAESI spectrum of the mouse brain sample, the cholesterol ion could be detected only as a minor $[M-H_2O+H]^+$ peak after scanning a wider sample surface. However, the

analysis of a wetted synthetic cholesterol sample by LAESI readily produced a peak at m/z 369.3482 indicating the presence of the $[M-H_2O+H]^+$ ion. The ionization of synthetic cholesterol showed that LAESI was capable of ionizing a compound that absorbed the mid-IR laser light, even though it could not be ionized directly by ESI. Further studies on the effect of laser wavelength, electrospray solution composition, negative ion modality, and ion source geometry are needed to assess the ability of LAESI to ionize such nonpolar analytes.

Glycerophosphocholines. Ion production from PC is efficient due to the presence of the positively charged quaternary amine moiety in these molecules. The brain tissue mass spectra from both AP IR-MALDI and LAESI are dominated by PC ions. The analysis of a standard phospholipid mixture by conventional MALDI showed the suppression of other lipids by PC.⁷⁴ Most of the ions in the 700 to 900 m/z range represent PC species with a variety of fatty acid moieties. Four PCs in brain tissue samples, PC(32:0), PC(34:1), PC(36:1), and PC(38:4), with some of the related DG ions appeared as major peaks in both the AP IR-MALDI and the LAESI mass spectra.

The DG structures can be independent species in the tissue, fragment ions, and/or natural degradation products of PC. Fragmentation of PC molecules has been reported under vacuum UV-MALDI conditions.²⁹ In AP IR-MALDI, based on the accurate mass measurement alone, the m/z 723.5016 ion can be viewed as a sodiated PA(36:2) molecule, $[C_{39}H_{73}O_8P+Na^+]$ or a sodiated fragment of PC(34:1) formed by the loss of trimethylamine ($-N(CH_3)_3$, Δm 59.0735), $[C_{39}H_{73}O_8P+Na^+]$, as both of these species have the same elemental composition. Similarly in LAESI, the m/z 577.5279 ion can be derived as a protonated fragment of PC(34:1) due to the loss of the polar

phosphocholine ($C_5H_{14}NO_4P$, Δm 183.0660) headgroup, $[C_{37}H_{68}O_4+H^+]$, or it can be rationalized as a protonated DG structure, such as DG(34:1) with the same elemental composition after water loss. Ion production from the model lipid PC(18:1/18:1) with LAESI did not show any evidence of phosphocholine loss, whereas AP IR-MALDI produced a protonated fragment with the loss of phosphocholine, $[C_{39}H_{70}O_4+H^+]$, resulting in an ion that was undistinguishable from the protonated DG(36:2) species after water loss. In Tables 5.1 and 5.2 we only listed the assignment for the detected ions that required the least amount of rearrangement, supported by the analysis of standards, and/or positive match in the related database. Due to the limited mass accuracy, in some cases even the elemental compositions could not be unambiguously discerned. For example, in the AP IR-MALDI spectra, m/z 810.6011 could be explained as a sodiated PC(36:1) and/or as a protonated PC(38:4) because the exact masses of these ions were only 2.3 mDa apart. Coupling AP IR-MALDI and LAESI with ultrahigh resolution MS should enable unambiguous identification in such cases.

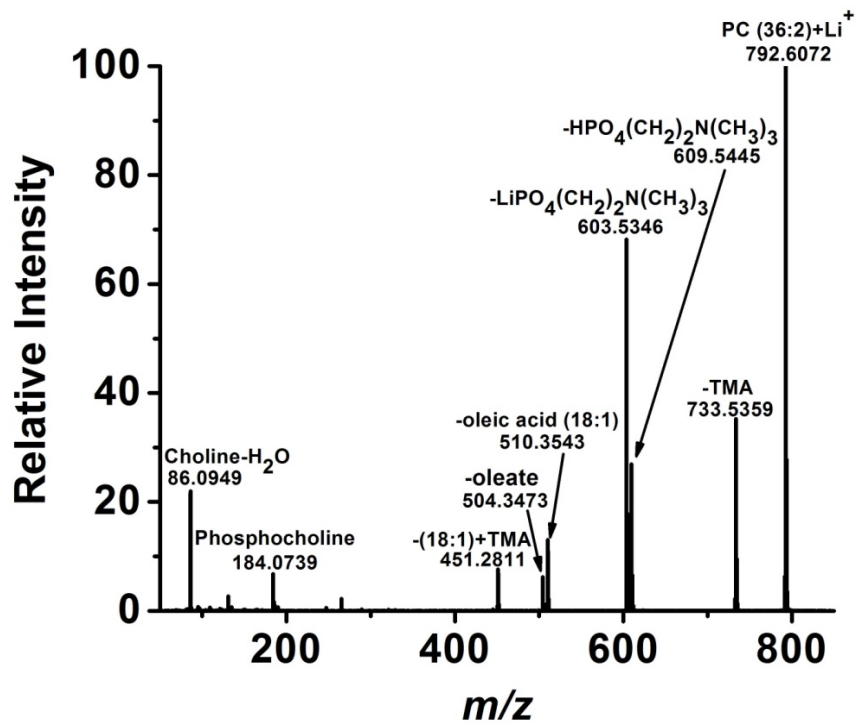
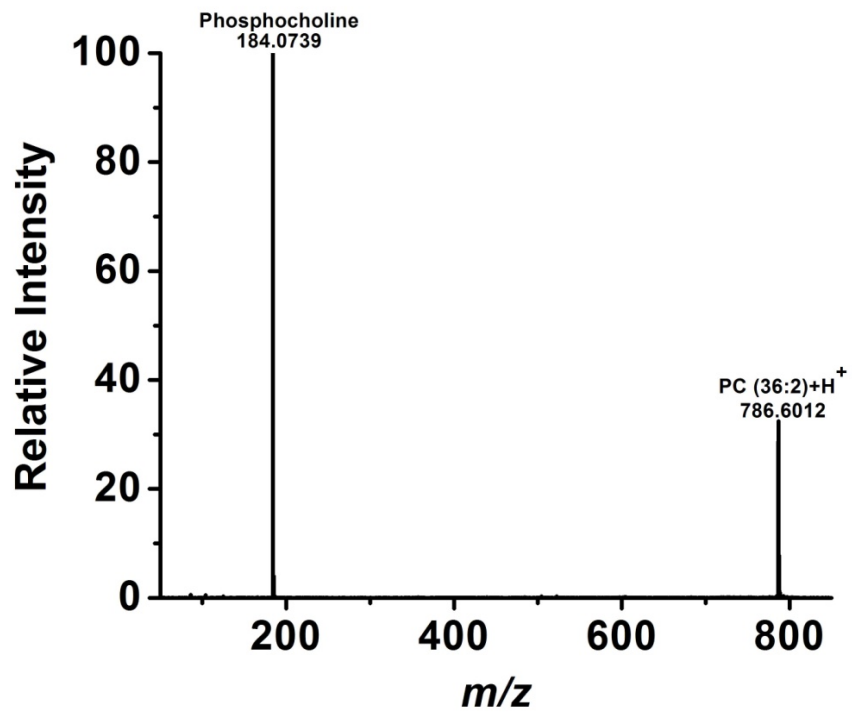
Other lipids. Lipids from two other major categories, PE and SM, were detected by both AP IR-MALDI and LAESI. Protonated and alkalinated PE(38:4) and PE(40:6) structures were observed in AP IR-MALDI with no fragmentation (see Table 5.1). In LAESI, PE were detected as protonated molecules (see Table 5.2). Similar to the case of the PC assignments, these measured m/z values were consistent with potential fragmentation of other lipids. For example in ESI, the loss of the phosphoethanolamine headgroup was used as a diagnostic tool for the detection of the PE.^{75, 76} Based on the accurate mass alone the produced ion could also be explained via a water loss from a DG. Other lipid assignments included a few instances of MG, glycerophosphates (PA),

glycerophosphoglycerols (PG), SM and ceramide (Cer), implicated in the hydrolysis of SM. The ability to detect diverse lipids through AP IR-MALDI and LAESI-MS directly from the tissue can be used to uncover brain lipid profiles.

Structural elucidation by reactive LAESI. In light of the complexity of analogous lipid structures and the ambiguity of assignments based on the accurate mass alone, ion dissociation strategies were explored in combination with tandem MS. Conventional CAD of lipid molecular ions, however, often produces little additional information. For example, the CAD of the standard PC(18:1/18:1), at nominal m/z 787, produces a single fragment ion with m/z 184 indicating the presence of the phosphocholine headgroup but leaving the individual lengths of the acyl chains unexplored (See Figure 5.5a). Structure-specific fragmentation at the ester bonds is necessary to identify the acyl chain lengths and to narrow the set of potential lipid structures compatible with the m/z value.

Several MS-based methods, including MALDI, ESI, etc., have noted that lithiated lipid molecules undergo extensive fragmentation by CAD that can enhance the identification of the fatty acyl chains.^{77, 78} In order to form the PC lithium adduct in AP IR-MALDI, it would be necessary to deposit the lithium salt onto the tissue, which might result in analyte redistribution in the sample. In contrast, LAESI enables the introduction of the lithiating agent through the electrospray process. Thus we added Li_2SO_4 to the electrospray solution in the LAESI source to produce lithiated ions from

Figure 5.5 (a) Tandem MS of the protonated PC(18:1/18:1) generated by LAESI produced a single fragment.. **(b)** Tandem MS of the lithiated PC(18:1/18:1) generated by reactive LAESI produced structure-specific fragments.



A
—
B

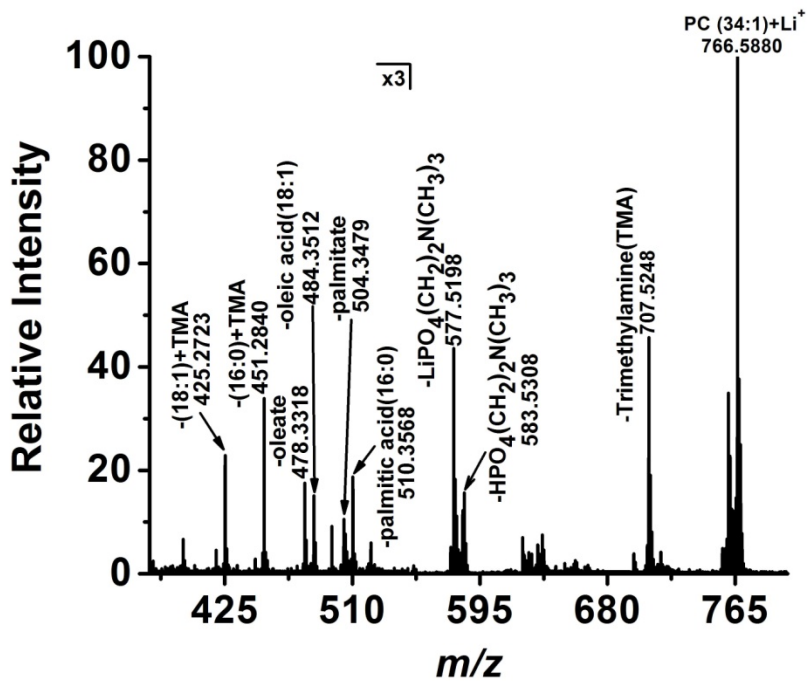
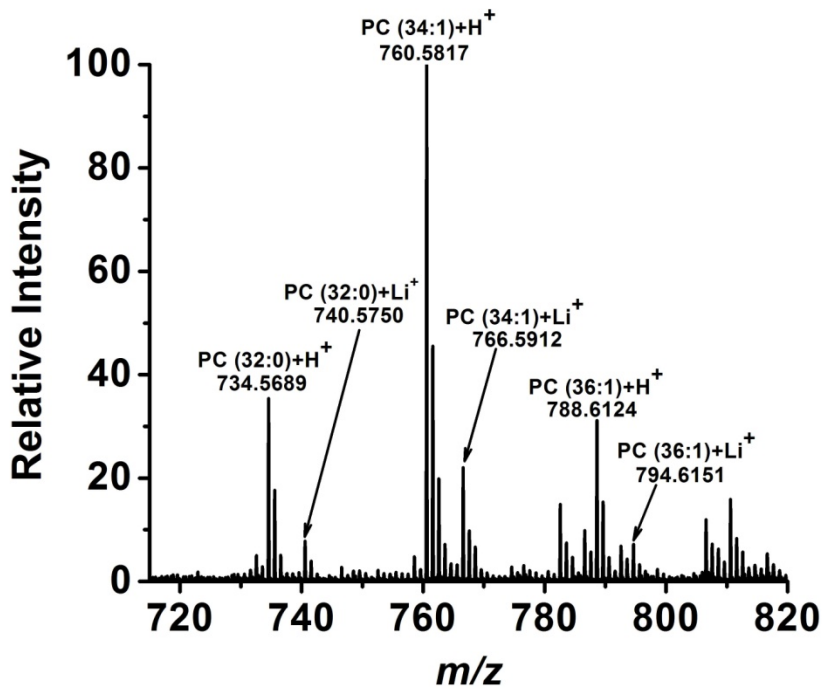
the ablated lipids. This new variant of LAESI, termed reactive LEASI provided an opportunity to introduce various reactions into the ion source.

To test the utility of reactive LAESI, CAD experiments were conducted on PC(18:1/18:1) with reactive LAESI ionization. The lithiated PC(18:1/18:1) generated by reactive LAESI with 500 μM Li_2SO_4 in the electrospray solution produced a variety of structure-specific fragments. This enabled the assignment of PC(18:1/18:1). See the Figure 5.5b.

The reactive LAESI approach enabled us to elucidate the structure of several lipids that were detected directly in the mouse brain tissue. For example, the ion measured at m/z 766.5912 (see Figure 5.6a) was subjected to CAD with 15-20 eV collision energy. As shown in Figure 5.6b, the recorded tandem mass spectrum revealed neutral losses corresponding to palmitic acid (16:0), oleic acid (18:1), lithium palmitate, lithium oleate, and the combined losses of the fatty acids with trimethylamine (TMA), (16:0)+TMA and (18:1)+TMA. Based on this information the ion in question was identified as PC(16:0/18:1). In these experiments, the reactive LAESI methodology, in combination with CAD and tandem MS, gave additional insight into the structure of lipid ions produced directly from the tissue sample. Independent methodologies, including liquid chromatography and NMR can help to elucidate the location of the double bond in the (18:1) chain and the stereochemistry of the molecule.

LAESI vs. reactive LAESI tandem MS of DOPC. Except for the following modifications, all experimental conditions were the same as in the main section. In the LAESI experiments, a nanospray source was used. The source featured a tapered tip stainless steel emitter (i.d. 50 μm , MT320-50-5-5, New Objective, Woburn, MA), held at

Figure 5.6 Reactive LAESI experiments facilitated the structural elucidation of several lipid species. Some of the ablated lipid molecules were converted into lithium adducts upon coalescence with electrosprayed droplets seeded with Li^+ ions (see panel a). These lithiated lipid ions readily fragmented by collision-activated dissociation yielding fragments characteristic of the parent ion. For example in panel b, the ion measured at m/z 766.5912 produced fragment ions at m/z 707.5248, 583.5308, and 577.5198, corresponding to the loss of the trimethylamine [$\text{N}(\text{CH}_3)_3$, Δm 59.0735], phosphocholine [$\text{C}_5\text{H}_{14}\text{NO}_4\text{P}$, Δm 183.0660], and lithiated phosphocholine [$\text{C}_5\text{H}_{13}\text{NO}_4\text{PLi}$, $\Delta m/z$ 189.0742], respectively. Other fragment ions, including those registered at m/z 510.3568 and 484.3512 were formed through the neutral loss of palmitic acid (16:0) and oleic acid (18:1), respectively. This fragmentation pattern was consistent with the CAD fragmentation of the $\text{PC}(16:0/18:1)+\text{Li}^+$ lipid ion.



A
—
B

2.8 kV high voltage. It sprayed methanol/water (1:1) mixture containing 0.1% (v/v) acetic acid at 200 nl/min flow rate. The mid-IR laser beam was focused with a 150 mm focal length CaF₂ lens (Infrared Optical Products, Farmingdale, NY). The >99% purity 1,2-dioleoyl-*sn*-glycero-3-phosphocholine (DOPC), corresponding to PC(18:1/18:1) in the LIPID MAPS nomenclature,⁶⁴ was obtained from Sigma Aldrich, St. Louis, MO, and used without further purification.

This model lipid was used to illustrate the utility of reactive LAESI for the determination of the acyl chain lengths and double bond counts in the PC. The CAD fragmentation of the protonated DOPC ion, at m/z 786.6012, produced a single fragment, the phosphocholine ion at m/z 184.0739 (see Figure 5.5a). This showed the presence of the phosphocholine headgroup, sufficient to assign the compound as PC(36:2), but lacked any information on the length of the individual acyl chains and the distribution of double bonds. In reactive LAESI with 500 μ M Li₂SO₄ in the electrospray solution, in addition to the protonated DOPC, the formation of lithiated DOPC at m/z 792.6072 was also observed. The tandem mass spectrum of the lithiated DOPC, obtained with CAD at 20-25 eV collision energy, showed the phosphocholine ion, and the ions due to the losses of trimethylamine (TMA), HPO₄(CH₂)₂N(CH₃)₃, LiPO₄(CH₂)₂N(CH₃)₃, oleic acid (18:1), oleate, and oleic acid + TMA from the lithiated molecule (Figure 5.5b and Table 5.3). The first four fragments indicated the presence of a phosphocholine headgroup and the last three fragments indicated the nature of the acyl chains. Thus, reactive LAESI using Li⁺ as a reactant in combination with CAD revealed that the standard DOPC molecule indeed had a PC(18:1/18:1) structure.

Table 5.3 Mass accuracy of fragment ions produced by CAD of lithiated DOPC generated by reactive LAESI.

Fragment ions	Chemical formula ^a	m/z calc.	m/z meas.	Δm (mDa)	ppm
PC(18:1/18:1) + Li ⁺	C ₄₄ H ₈₄ NO ₈ PLi ⁺	792.6094	792.6072	-2.2	-2.8
PC(18:1/18:1) – TMA + Li ⁺	C ₄₁ H ₇₅ O ₈ PLi ⁺	733.5359	733.5359	0	0.0
PC(18:1/18:1) – HPO ₄ (CH ₂) ₂ N(CH ₃) ₃ + Li ⁺	C ₃₉ H ₇₀ O ₄ Li ⁺	609.5434	609.5445	1.1	1.8
PC(18:1/18:1) – Li PO ₄ (CH ₂) ₂ N(CH ₃) ₃ + H ⁺	C ₃₉ H ₇₁ O ₄ ⁺	603.5353	603.5346	-0.7	-1.2
PC(18:1/18:1) – oleic acid + Li ⁺	C ₂₆ H ₅₀ NO ₆ PLi ⁺	510.3536	510.3543	0.7	1.4
PC(18:1/18:1) – oleate + H ⁺	C ₂₆ H ₅₁ NO ₆ P ⁺	504.3454	504.3473	1.9	3.8
PC(18:1/18:1) – (oleic acid + TMA) + Li ⁺	C ₂₃ H ₄₁ O ₆ PLi ⁺	451.2801	451.2811	1	2.2
phosphocholine	C ₅ H ₁₅ NO ₄ P ⁺	184.0739	184.0739	0	0.0
choline – H ₂ O	C ₅ H ₁₂ N ⁺	86.0970	86.0949	-2.1	-24.4

^a The monoisotopic masses were calculated using the NIST Isotope Calculator package (ISOFORM, Version 1.02), and the measured m/z values were obtained from a typical mass spectrum.

Relative quantitation of lipids in brain tissue. Earlier studies indicated that the ionization efficiency of phospholipid species by ESI MS depends on the length and the degree of saturation of its acyl chains, and most importantly on the structure of its headgroup.²⁶ To explore these potential disparities, LAESI mass spectra of the equimolar solution of PC(16:0), PE(18:1/16:0), PC(18:1/16:0), and PC(18:1/18:1) were recorded at 100 μ M concentration for each components (see Figure 5.7). The diacyl lipid ions with the same phosphocholine headgroup, PC(18:1/18:1) and PC(18:1/16:0), show similar ion counts in LAESI-MS, whereas diacyl lipid ions with the same acyl chains but different headgroups, PE(18:1/16:0) and PC(18:1/16:0), have significantly different ion counts.

The capability of quantitative analysis for small metabolites in *Torpedo californica* tissue by LAESI-MS had been demonstrated.⁷⁹ The tissue was spiked with deuterium labeled metabolites to aid quantitation. Similarly, to obtain concentration values for PC(34:1) in the mouse brain, spiking with deuterium labeled PC(d-31)(34:1) was used at different concentrations. Then spiked tissue was ground in liquid nitrogen resulting in a homogenous paste.

The inset in Figure 5.8 shows the typical LAESI spectrum of the ground tissue spiked with deuterated PC(d31)(34:1). To quantitate PC(34:1), ion counts for the PC(d31)(34:1) ion (m/z 790) and another ion, PC(32:0) at m/z 734, were measured. The ratio of ion counts for m/z 790/734 was plotted against the spiked concentration of PC(d31)(34:1) as shown in Figure 5.8. Linear regression produced a calibration curve with $R = 0.99$ correlation coefficient. Based on the regression, the concentration of PC(34:1) in the mouse brain was calculated to be 2.5×10^{-4} M.

Figure 5.7 LAESI mass spectra of a solution containing PC(16:0), PE(18:1/16:0), PC(18:1/16:0), and PC(18:1/18:1) at equimolar concentration shows that differences in glycerophospholipid ionization efficiencies depend on the structure of their headgroups and on the length and degree of saturation of their acyl chains.

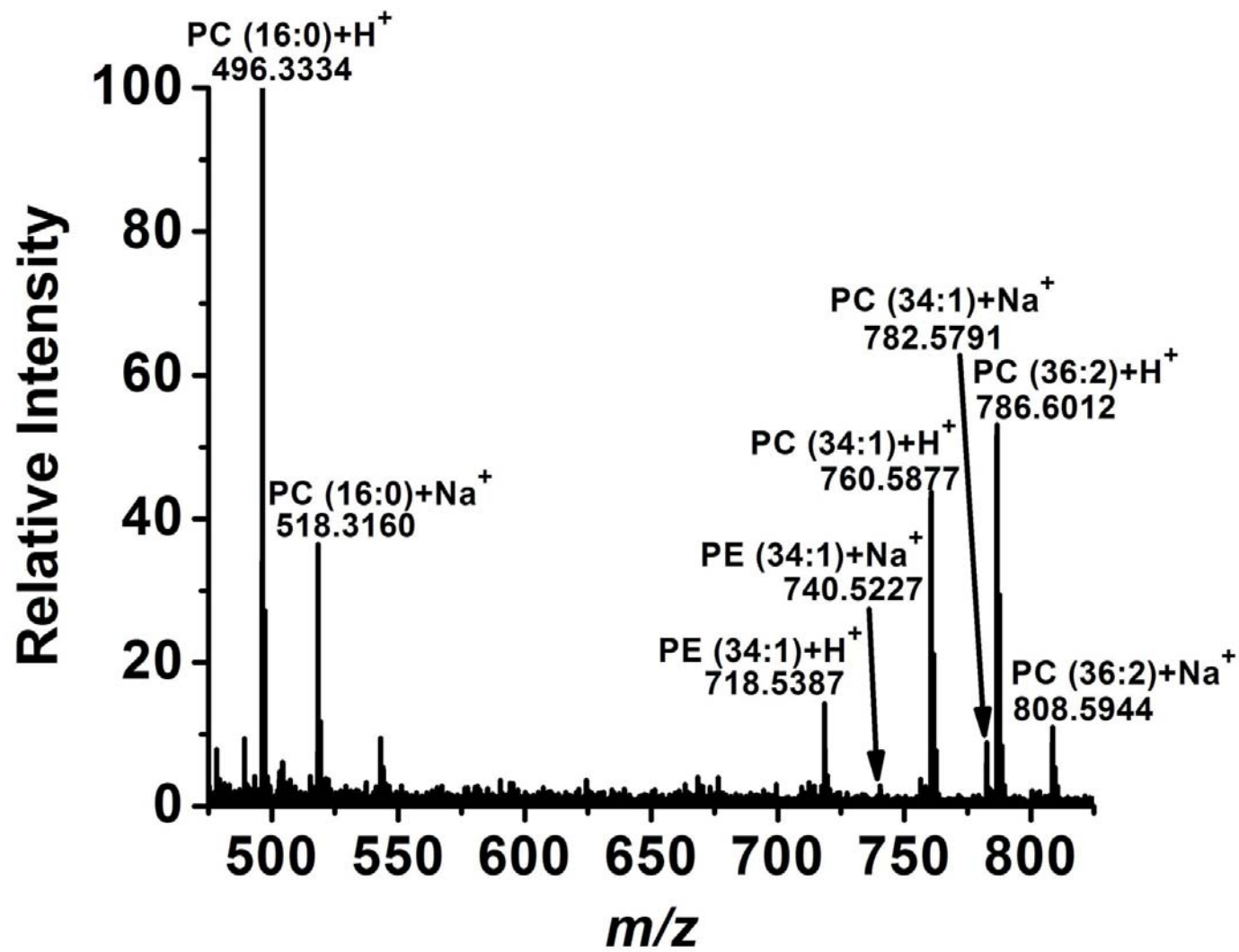
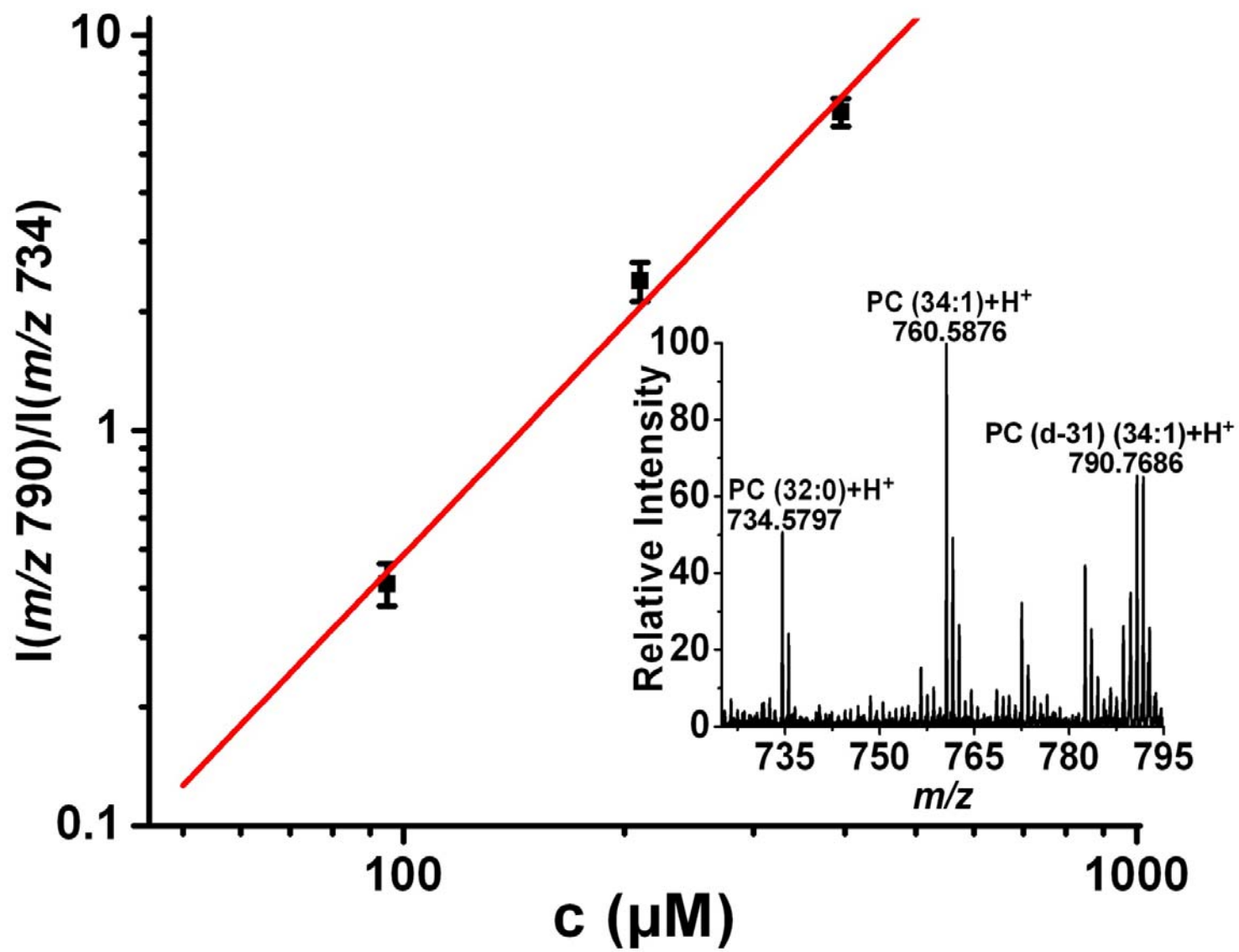


Figure 5.8 Ion count ratio for deuterated PC(d-31)(34:1) and PC(32:0) expressed as $I(m/z\ 790)/I(m/z\ 734)$ vs. PC(d-31)(34:1) concentration in the mouse brain tissue. The inset shows the relevant part of the LAESI spectrum of the tissue spiked with PC(d-31)(34:1).



CONCLUSIONS

Our results demonstrated the potential of AP IR-MALDI and LAESI for direct analysis of metabolites and lipids in neural tissues. The tentative assignment of 131 peaks, out of 206 detected ions, to more than 40 small metabolites and more than 45 species from diverse lipid classes (PC, MG, DG, PE, PG, SM and Cer) indicated the utility of these methods for applications in metabolomics. The ambient nature of the analysis also raised the prospect of studying physiological processes close to their native state, ultimately *ex vivo*, with minimal biochemical changes. Further development of this technique could lead to the identification of signaling molecules and their role in neurodegenerative diseases.

For lipid standards and in the analysis of brain tissue, reactive LAESI produced lithiated lipids that in CAD experiments readily fragmented at the ester bond. The produced structure-specific fragments enabled the determination of the acyl chain lengths and the number of double bonds within a chain. In order to achieve increased ion yields and desired fragmentation pathways, reactive LAESI can be extended by the use of a wide variety of reactants and/or surfactants in the electrospray solution. The modification of other experimental parameters, e.g., electrospray polarity and solvents, and laser fluence, may help to detect other biomolecules, such as neuropeptides in the brain tissue.

MS-based chemical mapping techniques have already been used to investigate the effect of diseases on tissue composition. For example, UV-MALDI imaging indicated abnormal distribution of phospholipids in the metastasis of colon cancer, whereas DESI detected tumor boundaries in metastatic human liver

adenocarcinoma.³⁹ Imaging by AP IR-MALDI can also be extended to brain and muscle tissue sections. LAESI-MS has recently shown success with molecular imaging of brain tissues.⁸⁰ Ambient spatial mapping of metabolites, lipids and, importantly, pharmaceuticals in animal tissues with IR laser ablation mass spectrometry holds the potential to enhance our understanding of metabolic response to diseases and the corrective action of drugs or drug candidates.

ACKNOWLEDGEMENTS

The authors recognize the financial support for this work from the National Science Foundation under grant 0719232, the W. M. Keck Foundation (041904) and the George Washington University Research Enhancement Fund. Any opinions, findings, and conclusions or recommendations expressed in this material are those of the authors and do not necessarily reflect the views of the supporting organizations. The PC(18:1/18:1) sample was kindly donated by Prof. Susan D. Gillmor of GWU.

REFERENCES

- (1) Sastry, P. S. *Progress in Lipid Research* **1985**, *24*, 69-176.
- (2) Wenk, M. R. *Nature Reviews Drug Discovery* **2005**, *4*, 594-610.
- (3) Fahy, E.; Subramaniam, S.; Brown, H. A.; Glass, C. K.; Merrill, A. H., Jr.; Murphy, R. C.; Raetz, C. R. H.; Russell, D. W.; Seyama, Y.; Shaw, W.; Shimizu, T.; Spener, F.; van Meer, G.; VanNieuwenhze, M. S.; White, S. H.; Witztum, J. L.; Dennis, E. A. *Journal of Lipid Research* **2005**, *46*, 839-862.

- (4) Watson, A. D. *Journal of Lipid Research* **2006**, *47*, 2101-2111.
- (5) O'Brien, J. S.; Sampson, E. L. *Journal of Lipid Research* **1965**, *6*, 537-544.
- (6) Adibhatla, R. M.; Hatcher, J. F.; Dempsey, R. J. *American Association of Pharmaceutical Scientists Journal* **2006**, *8*, E314-321.
- (7) Dowhan, W. *Annual Review of Biochemistry* **1997**, *66*, 199-232.
- (8) Hutchinson, P. J.; Connell, M. T. O.; Kirkpatrick, P. J.; Pickard, J. D. *Physiological Measurement* **2002**, R75.
- (9) Lyoo, I. K.; Renshaw, P. F. *Biological Psychiatry* **2002**, *51*, 195-207.
- (10) Westerink, B. H. C. *Behavioural Brain Research* **1995**, *70*, 103-124.
- (11) Henriksen, O. *NMR in biomedicine* **1995**, *8*, 139-148.
- (12) Jansen, J. F. A.; Backes, W. H.; Nicolay, K.; Kooi, M. E. *Radiology* **2006**, *240*, 318-332.
- (13) Phelps, M. E.; Mazziotta, J. C. *Science* **1985**, *228*, 799-809.
- (14) Bourcier, S.; Benoist, J. F.; Clerc, F.; Rigal, O.; Taghi, M.; Hoppilliard, Y. *Rapid Communications in Mass Spectrometry* **2006**, *20*, 1405-1421.
- (15) Jäverfalk-Hoyes, E. M.; Bondesson, U.; Westerlund, D.; Andrén, P. E. *Electrophoresis* **1999**, *20*, 1527-1532.
- (16) Tareke, E.; Bowyer, J. F.; Doerge, D. R. *Rapid Communications in Mass Spectrometry* **2007**, *21*, 3898-3904.
- (17) Kauppila, T. J.; Nikkola, T.; Ketola, R. A.; Kostainen, R. *Journal of Mass Spectrometry* **2006**, *41*, 781-789.
- (18) Kriat, M.; Vion-Dury, J.; Confort-Gouny, S.; Favre, R.; Viout, P.; Sciaky, M.; Sari, H.; Cozzone, P. J. *Journal of Lipid Research* **1993**, *34*, 1009-1019.

- (19) Kupke, I. R.; Zeugner, S. *Journal of Chromatography B: Biomedical Sciences and Applications* **1978**, *146*, 261-271.
- (20) Touchstone, J. C. *Journal of Chromatography B: Biomedical Sciences and Applications* **1995**, *671*, 169-195.
- (21) Peterson, B. L.; Cummings, B. S. *Biomedical Chromatography* **2006**, *20*, 227-243.
- (22) Murphy, R. C.; Fiedler, J.; Hevko, J. *Chemical Reviews* **2001**, *101*, 479-526.
- (23) Sjovall, P.; Lausmaa, J.; Johansson, B. *Analytical Chemistry* **2004**, *76*, 4271-4278.
- (24) Jensen, N.; Tomer, K.; Gross, M. *Lipids* **1986**, *21*, 580-588.
- (25) Han, X.; Gross, R. W. *Proceedings of the National Academy of Sciences* **1994**, *91*, 10635-10639.
- (26) Pulfer, M.; Murphy, R. C. *Mass Spectrometry Reviews* **2003**, *22*, 332-364.
- (27) Han, X.; Gross, R. W. *Mass Spectrometry Reviews* **2005**, *24*, 367-412.
- (28) Harvey, D. J. *Journal of Mass Spectrometry* **1995**, *30*, 1333-1346.
- (29) Marto, J. A.; White, F. M.; Seldomridge, S.; Marshall, A. G. *Analytical Chemistry* **1995**, *67*, 3979-3984.
- (30) Schiller, J.; Su, R.; Arnhold, J.; Fuchs, B.; Leig, J.; Muller, M.; Petkovic, M.; Spalteholz, H.; Zschornig, O.; Arnold, K. *Progress in Lipid Research* **2004**, *43*, 449-488.
- (31) Ishida, Y.; Nakanishi, O.; Hirao, S.; Tsuge, S.; Urabe, J.; Sekino, T.; Nakanishi, M.; Kimoto, T.; Ohtani, H. *Analytical Chemistry* **2003**, *75*, 4514-4518.
- (32) Rujoi, M.; Estrada, R.; Yappert, M. C. *Analytical Chemistry* **2004**, *76*, 1657-1663.
- (33) Jackson, S. N.; Wang, H. Y. J.; Woods, A. S. *Analytical Chemistry* **2005**, *77*, 4523-4527.

- (34) Garrett, T. J.; Yost, R. A. *Analytical Chemistry* **2006**, *78*, 2465-2469.
- (35) Cha, S.; Yeung, E. S. *Analytical Chemistry* **2007**, *79*, 2373-2385.
- (36) Dreisewerd, K.; Lemaire, R.; Pohlentz, G.; Salzet, M.; Wisztorski, M.; Berkenkamp, S.; Fournier, I. *Analytical Chemistry* **2007**, *79*, 2463-2471.
- (37) Perry, T. L.; Hansen, S.; Gandham, S. S. *Journal of Neurochemistry* **1981**, *36*, 406-412.
- (38) Banaschak, S.; Rzanny, R.; Reichenbach, J. R.; Kaiser, W. A.; Klein, A. *International Journal of Legal Medicine* **2005**, *119*, 77-79.
- (39) Wiseman, J. M.; Puolitaival, S. M.; Takáts, Z.; Cooks, R. G.; Caprioli, R. M. *Angewandte Chemie International Edition* **2005**, *44*, 7094-7097.
- (40) Wiseman, J. M.; Ifa, D. R.; Song, Q.; Cooks, R. G. *Angewandte Chemie International Edition* **2006**, *45*, 7188-7192.
- (41) Manicke, N. E.; Wiseman, J. M.; Ifa, D. R.; Cooks, R. G. *Journal of the American Society for Mass Spectrometry* **2008**, *19*, 531-543.
- (42) Takats, Z.; Koblíha, V.; Sevcik, K.; Novak, P.; Kruppa, G.; Lemr, K.; Havlicek, V. *Journal of Mass Spectrometry* **2008**, *43*, 196-203.
- (43) Dill, A. L.; Ifa, D. R.; Manicke, N. E.; Ouyang, Z.; Cooks, R. G. *Journal of Chromatography B* **2009**, *877*, 2883-2889.
- (44) Huang, M.-Z.; Hsu, H.-J.; Wu, C. I.; Lin, S.-Y.; Ma, Y.-L.; Cheng, T.-L.; Shiea, J. *Rapid Communications in Mass Spectrometry* **2007**, *21*, 1767-1775.
- (45) Uzman, L. L.; Marilyn, K. R. *Journal of Neurochemistry* **1958**, *3*, 170-184.
- (46) Li, Y.; Shrestha, B.; Vertes, A. *Analytical Chemistry* **2007**, *79*, 523-532.
- (47) Li, Y.; Shrestha, B.; Vertes, A. *Analytical Chemistry* **2008**, *80*, 407-420.
- (48) Shrestha, B.; Li, Y.; Vertes, A. *Metabolomics* **2008**, *4*, 297-311.

- (49) Nemes, P.; Vertes, A. *Analytical Chemistry* **2007**, *79*, 8098-8106.
- (50) Nemes, P.; Barton, A. A.; Li, Y.; Vertes, A. *Anal. Chem.* **2008**, *80*, 4575-4582.
- (51) Sripadi, P.; Nazarian, J.; Hathout, Y.; Hoffman, E. P.; Vertes, A. *Metabolomics* **2009**, *5*, 263-276.
- (52) Sampson, J. S.; Murray, K. K.; Muddiman, D. C. *Journal of the American Society for Mass Spectrometry* **2009**, *20*, 667-673.
- (53) Shrestha, B.; Vertes, A. *Analytical Chemistry* **2009**, *81*, 8265-8271.
- (54) Nyadong, L.; Green, M. D.; DeJesus, V. R.; Newton, P. N.; Fernandez, F. M. *Analytical Chemistry* **2007**, *79*, 2150-2157.
- (55) Song, Y.; Cooks, R. G. *Journal of Mass Spectrometry* **2007**, *42*, 1086-1092.
- (56) Peng, I. X.; Ogorzalek Loo, R. R.; Shiea, J.; Loo, J. A. *Analytical Chemistry* **2008**, *80*, 6995-7003.
- (57) Wu, C.; Ifa, D. R.; Manicke, N. E.; Cooks, R. G. *Analytical Chemistry* **2009**, *81*, 7618-7624.
- (58) Tan, P. V.; Laiko, V. V.; Doroshenko, V. M. *Analytical Chemistry* **2004**, *76*, 2462-2469.
- (59) Von Seggern, C. E.; Gardner, B. D.; Cotter, R. J. *Analytical Chemistry* **2004**, *76*, 5887-5893.
- (60) Smith, C. A.; O'Maille, G.; Want, E. J.; Qin, C.; Trauger, S. A.; Brandon, T. R.; Custodio, D. E.; Abagyan, R.; Siuzdak, G. *Therapeutic Drug Monitoring* **2005**, *27*, 747.
- (61) Wishart, D. S.; Tzur, D.; Knox, C.; Eisner, R.; Guo, A. C.; Young, N.; Cheng, D.; Jewell, K.; Arndt, D.; Sawhney, S.; Fung, C.; Nikolai, L.; Lewis, M.; Coutouly, M.

- A.; Forsythe, I.; Tang, P.; Shrivastava, S.; Jeroncic, K.; Stothard, P.; Amegbey, G.; Block, D.; Hau, D. D.; Wagner, J.; Miniaci, J.; Clements, M.; Gebremedhin, M.; Guo, N.; Zhang, Y.; Duggan, G. E.; MacInnis, G. D.; Weljie, A. M.; Dowlatabadi, R.; Bamforth, F.; Clive, D.; Greiner, R.; Li, L.; Marrie, T.; Sykes, B. D.; Vogel, H. J.; Querengesser, L. *Nucleic Acids Research* **2007**, *35*.
- (62) Cotter, D.; Maer, A.; Guda, C.; Saunders, B.; Subramaniam, S. *Nucleic acids research*. **2006**, *34*, D507-D510.
- (63) Watanebe, K.; Yasugi, E.; Oshima, M. *Trends Glycoscience Glycotechnology* **2000**, *12*, 175-184.
- (64) Fahy, E.; Subramaniam, S.; Murphy, R. C.; Nishijima, M.; Raetz, C. R. H.; Shimizu, T.; Spener, F.; van Meer, G.; Wakelam, M. J. O.; Dennis, E. A. *J. Lipid Res.* **2009**, *50*, S9-14.
- (65) Vertes, A.; Nemes, P.; Shrestha, B.; Barton, A.; Chen, Z.; Li, Y. *Applied Physics A: Materials Science & Processing* **2008**.
- (66) O'Connor, P. B.; Costello, C. E. *Rapid Communications in Mass Spectrometry* **2001**, *15*, 1862-1868.
- (67) Garrett, T. J.; Prieto-Conaway, M. C.; Kovtoun, V.; Bui, H.; Izgarian, N.; Stafford, G.; Yost, R. A. *International Journal of Mass Spectrometry* **2007**, *260*, 166-176.
- (68) Rohlfing, A.; Muthing, J.; Pohlentz, G.; Distler, U.; Peter-Katalinic, J.; Berkenkamp, S.; Dreisewerd, K. *Analytical Chemistry* **2007**, *79*, 5793-5808.
- (69) Watanabe, M.; Maemura, K.; Kanbara, K.; Tamayama, T.; Hayasaki, H. *International Review of Cytology* **2002**, *213*, 1-47.

- (70) Zeisel, S. H. *Journal of the American College of Nutrition* **1992**, *11*, 473-481.
- (71) Simons, K.; Ikonen, E. *Science* **2000**, *290*, 1721-1726.
- (72) McDonald, J. G.; Thompson, B. M.; McCrum, E. C.; Russell, D. W.; Brown, H. A. In *Methods in Enzymology*; Academic Press, 2007; Vol. Volume 432, pp 145-170.
- (73) Sandhoff, R.; Brugger, B.; Jeckel, D.; Lehmann, W. D.; Wieland, F. T. *Journal of Lipid Research* **1999**, *40*, 126-132.
- (74) Petkovic, M.; Schiller, J.; Muller, M.; Benard, S.; Reichl, S.; Arnold, K.; Arnhold, J. *Analytical Biochemistry* **2001**, *289*, 202-216.
- (75) Berry, K. A. Z.; Murphy, R. C. *Journal of the American Society for Mass Spectrometry* **2004**, *15*, 1499-1508.
- (76) Schwudke, D.; Oegema, J.; Burton, L.; Entchev, E.; Hannich, J. T.; Ejsing, C. S.; Kurzchalia, T.; Shevchenko, A. *Analytical Chemistry* **2006**, *78*, 585-595.
- (77) Hsu, F.-F.; Bohrer, A.; Turk, J. *Journal of the American Society for Mass Spectrometry* **1998**, *9*, 516-526.
- (78) Jackson, S. N.; Wang, H.-Y. J.; Woods, A. S. *Journal of the American Society for Mass Spectrometry* **2005**, *16*, 2052-2056.
- (79) Sripadi, P.; Nazarian, J.; Hathout, Y.; Hoffman, E.; Vertes, A. *Metabolomics* **2009**, *5*, 263-276.
- (80) Nemes, P.; Svatos, A.; Vertes, A., Philadelphia, PA, USA, May 30-31 **2009**.

CHAPTER 6

IN SITU METABOLIC PROFILING OF SINGLE CELLS BY LASER ABLATION ELECTROSPRAY IONIZATION MASS SPECTROMETRY

Based on material published by B. Shrestha and A. Vertes
in *Anal. Chem.*, **2009**, *81*, 8265-8271.

ABSTRACT

Depending on age, phase in the cell cycle, nutrition and environmental factors, individual cells exhibit large metabolic diversity. To explore metabolic variations in cell populations, laser ablation electrospray ionization (LAESI) mass spectrometry (MS) was used for the *in situ* analysis of individual cells at atmospheric pressure. Single cell ablation was achieved by delivering mid-IR laser pulses through the etched tip of a GeO₂-based glass fiber. Metabolic analysis was performed from single cells and small cell populations of *Allium cepa* and *Narcissus pseudonarcissus* bulb epidermis, as well as single eggs of *Lytechinus pictus*. Of the 332 peaks detected for *A. cepa*, 35 were assigned to metabolites with the help of accurate ion masses and tandem MS. The metabolic profiles from single cells of the two plant species included a large variety of oligosaccharides including possibly fructans in *A. cepa*, and alkaloids, e.g., lycorine in *N. pseudonarcissus*. Analysis of adjacent individual cells with a difference in pigmentation showed that, in addition to

essential metabolites found in both variants, the pigmented cells contained anthocyanidins, other flavonoids and their glucosides. Analysis of single epidermal cells from different scale leaves in an *A. cepa* bulb showed metabolic differences corresponding to their age. Our results indicate the feasibility of using LAESI-MS for the *in situ* analysis of metabolites in single cells with potential applications in studying cell differentiation, changes due to disease states and response to xenobiotics.

INTRODUCTION

Information on the chemical composition within a cell has implications in the understanding of cell metabolism, division, disease states, ecological effects, etc.^{1, 2} Cells of the same type exhibit diverse metabolic makeup depending on their phase in the cell cycle, history and interaction with the environment. *In vivo* analysis of metabolites in a single cell is challenging because of the limited size and complexity of the sample. Spectrochemical analysis, such as Fourier transform infrared (FTIR) spectroscopic imaging,³ coherent anti-Stokes Raman scattering (CARS) microscopy,⁴ and nuclear magnetic resonance⁵ have been utilized to explore the chemical makeup of a single cell. Many of the used techniques, however, require chemical tagging of the analyte by a fluorophore⁶ or the genetic incorporation of green fluorescent protein (GFP),⁷ and do not provide simultaneous detection of more than a few components.⁸ The direct chemical analysis of a single cell by capillary electrophoresis (CE), performed, for example, by inserting a microcapillary into the cell, has broadened the variety of analyzed species.⁹⁻¹² By coupling with electrospray ionization (ESI) mass spectrometry (MS),^{13, 14} multiple components were detected. Other mass spectrometric techniques, such as

matrix-assisted laser desorption ionization (MALDI) and secondary ion mass spectrometry (SIMS), in a vacuum environment have demonstrated the analysis of vesicles and lipid membranes.^{15, 16} Most single cell analysis is performed *in vitro* on isolated cells or cell extracts^{2, 17, 18} and aided by techniques such as laser capture microdissection to select a single cell for mass spectrometric analysis.¹⁹ Current *in situ* MS methods, such as desorption ESI (DESI),^{20, 21} or atmospheric pressure infrared MALDI,^{22, 23} have been used to produce metabolic profiles from biological tissues averaged over cell populations.

Laser ablation electrospray ionization (LAESI) is a new ionization technique that uses a focused mid-IR laser beam with 2.94 μm to sample material directly from tissue based on the strong absorption of water at this wavelength.^{24, 25} In LAESI the ablation plume, consisting mostly of neutrals, is intercepted by an electrospray to efficiently postionize its content. Focusing with conventional optics, e.g., using a single CaF_2 lens, results in a typical ablation diameter of 250 μm that is too large for most single cells. Although the diffraction limit for the $\sim 3 \mu\text{m}$ light used in these studies is $\sim 1.5 \mu\text{m}$, lens aberrations and the long working distance necessary for interfacing with the mass spectrometer result in much larger spot sizes. As most plant and animal cells are in the 20–200 μm and 5–50 μm size range, respectively, single cell analysis by LAESI-MS requires infrared ablation on the 10–100 μm scale. LAESI-MS has demonstrated *in situ* analysis of metabolites and lipids from both plant and animal tissues.^{24, 26} A similar approach has been used to analyze carbohydrates and lipids of milk and egg yolk by infrared (IR) matrix-assisted laser desorption electrospray ionization (MALDESI).²⁷

Here we show that metabolic profiles can be obtained by LAESI-MS from single cells and small cell populations of onion (*Allium cepa*) and daffodil (*Narcissus pseudonarcissus*) bulb epidermal cells. Comparison of the metabolic profiles from these two species reveals a variety of oligosaccharides including possibly fructans and anthocyanins in *A. cepa* and alkaloids, e.g., norpluviine, in *N. pseudonarcissus* cells. Analyzing adjacent cells with or without pigment in the epidermal tissue reveals significant differences in the metabolite content. Accurate mass measurement and structural information, obtained by tandem MS, enable the identification of numerous metabolites from a single cell. Comparing these profiles for cells of different type and of different environmental history provides insight into cellular development and response.

EXPERIMENTAL SECTION

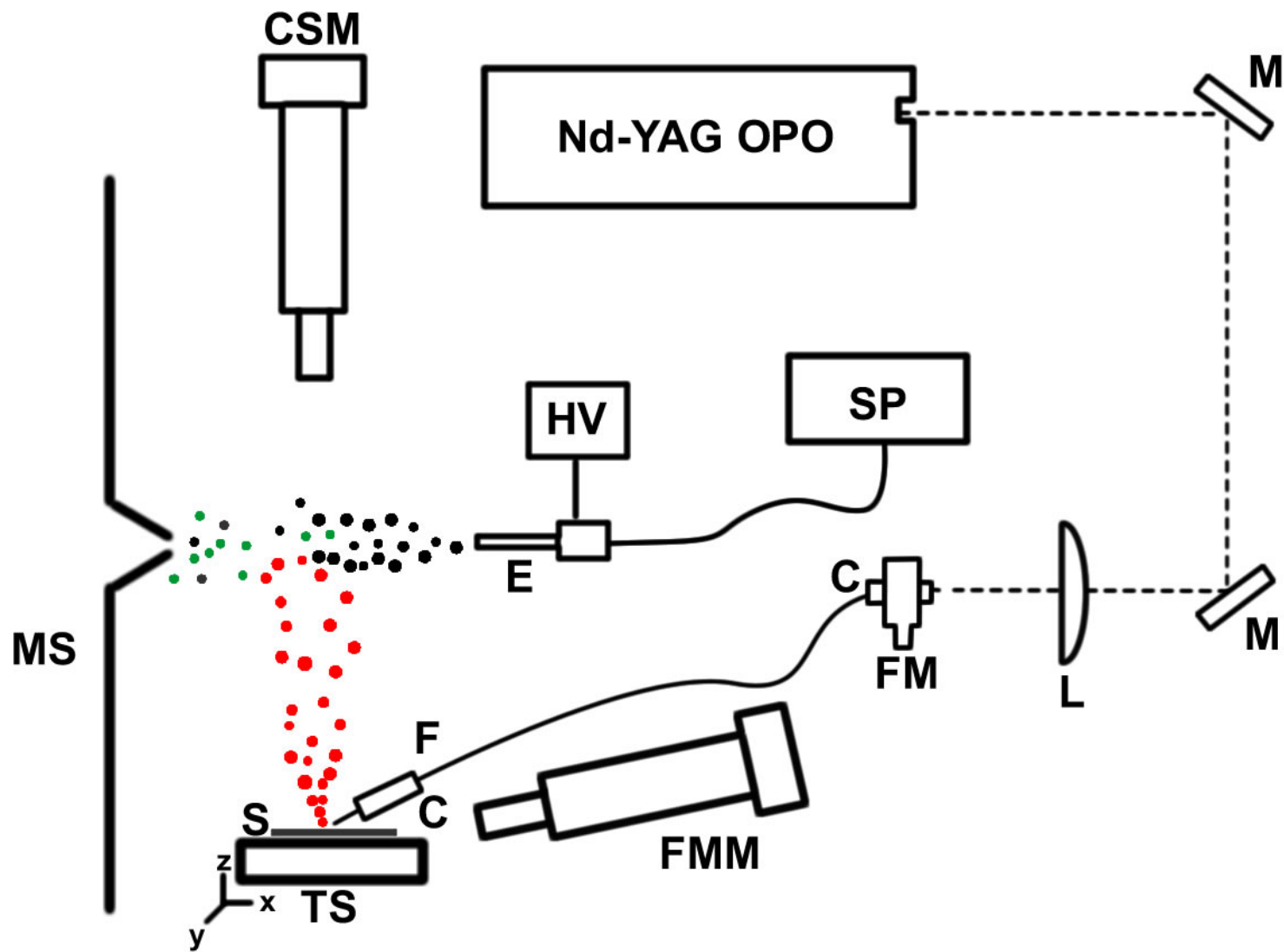
Laser Ablation Electrospray Ionization. Mid-IR laser light was delivered to the target through a germanium oxide (GeO₂)-based optical fiber (450 μm core diameter, HP Fiber, Infrared Fiber Systems, Inc., Silver Spring, MD, USA) with its tip etched to a 15 μm radius of curvature. Laser radiation was produced by a diode pumped Nd:YAG laser-driven optical parametric oscillator (OPO) (Opolette 100, Opotek, Carlsbad, CA, USA) at 2940 nm, 100 Hz repetition rate, and 5 ns pulse width. The energy of a laser pulse before coupling into the optical fiber was 554 ± 26 μJ, thus the pulse-to-pulse energy stability corresponded to ~5%. The laser system was operated at 100 Hz for ~1 sec to ablate a cell, thus, up to 100 laser shots were delivered to a cell for analysis. For the postionization of the ablated neutrals, 50% methanol with 0.1% (v/v) acetic acid was electrosprayed under right angle into the ablation plume. In the home built electrospray

source, a low noise syringe pump (Physio 22, Harvard Apparatus, Holliston, MA, USA) was used to supply the solution at 200 nl/min to a tapered stainless steel emitter (i.d. 50 μm , MT320-50-5-5, New Objective, Woburn, MA, USA). Stable high voltage between 2.7 and 2.9 kV, generated by a regulated power supply (PS350, Stanford Research Systems, Sunnyvale, CA, USA), was applied to the emitter, which was mounted on a manual translation stage for the optimization of the laser ablation electrospray ionization (LAESI) signal.

The mass spectrometer orifice was on the same axis as the electrospray emitter of the LAESI source at a distance of ~ 12 mm from the tip. The sample was placed on a pre-cleaned microscope glass slide (Cat # 125496, Fisher Scientific, Pittsburgh, PA, USA) ~ 15 mm below the spray axis on a stepper motor-driven three-axis precision flexure stage (NanoMax TS, Thorlabs, Newton, NJ, USA). Without the ESI on, no ions were detected by the mass spectrometer, indicating that no ions directly induced by the laser were collected. This was the result of the large (> 15 mm) distance between the orifice of the mass spectrometer and the ablated sample.

The positive ions produced by the LAESI source were analyzed by an orthogonal acceleration time-of-flight mass spectrometer (Q-TOF Premier, Waters Co., MA, USA) (see Figure 6.1) at a mass resolution of 8,000 (FWHM). The orifice of the mass spectrometer had an inner diameter of 127 μm . The interface block temperature was held at 80 $^{\circ}\text{C}$ and its potential was kept at -70 V. Tandem mass spectra were obtained by collision activated dissociation (CAD) with argon as the collision gas at a typical collision cell pressure of 4×10^{-3} mbar and with collision energies between 10 and 25 eV.

Figure 6.1 Schematics of instrumental setup for single cell analysis by LAESI-MS. The mid-IR ablation products (red dots) generated by the etched optical fiber tip (F) are intercepted by the electrospray plume (black dots) and postionized to form ions (green dots) sampled by the mass spectrometer (MS). A long-distance video microscope (fiber monitor, FMM) is utilized to maintain constant distance between the fiber tip and the sample surface (S). The sample is placed on a 3-axis translation stage (TS), and a second video microscope (cell spotting microscope, CSM) is used to target the cells. The electrospray is produced by applying high voltage (HV) to the capillary emitter (E) and by maintaining constant solution flow rate by a syringe pump (SP). Pulses from the mid-IR OPO are coupled to the optical fiber, adjusted by a fiber chuck (C) and a 5-axis fiber mount (FM), using two Au-coated mirrors (M) and a CaF₂ lens (L).



Ablation using optical fiber tips. The laser beam was steered by gold-coated mirrors (PF10-03-M01, Thorlabs, Newton, NJ, USA) and coupled into the cleaved end of the optical fiber by a 50 mm focal length plano-convex calcium fluoride lens (Infrared Optical Products, Farmingdale, NY, USA). The optical fiber, held by a bare fiber chuck (BFC300, Siskiyou Corporation, Grants Pass, OR, USA), was positioned by a 5-axis translator (BFT-5, Siskiyou Corporation, Grants Pass, OR, USA).

The GeO₂-based glass fiber was used because of its high laser-damage threshold due to its high glass transition temperature.²⁸ After stripping off the Hytrel and the polyimide coatings on both ends of the fiber by the application of 1-methyl-2-pyrrolidinone (at 130 to 150 °C for ~1 minute), the fiber ends were cleaved with a Sapphire blade (KITCO Fiber Optics, Virginia Beach, VA, USA) by scoring and gently snapping them. Chemical etching of the fiber tip was achieved by dipping one of the cleaved fiber ends ~0.5 mm deep into 24 °C 1% HNO₃ solution in a wide beaker to provide low meniscus curvature. The meniscus formed at the fiber end gradually etched the 450 μm diameter core into a sharp tip (see Figure 6.2a) with a radius of curvature $R \approx 15 \mu\text{m}$. Prior to use the etched tips were washed with deionized water. No visible change of the fiber tip was observed after the LAESI experiments.

The etched end of the fiber was attached to a micromanipulator (MN-151, Narishige, Tokyo, Japan) and brought to close proximity of the sample. Aligning the coordinate system so that the x-y plane coincided with the sample and the x axis was parallel with the emitter, the optical fiber was positioned at azimuth and zenith angles of 135° and 45°, respectively. Following the LAESI signal as a function of the zenith angle, we determined that 45° provided an acceptable tradeoff between the shape of the

ablation mark and signal intensity reduction by blocking the expanding plume. In a few instances, after ablation a thin material deposit was observed on the fiber tip. In these cases, the fiber was retracted from the surface and elevated laser pulse energy was used to clean the tip. Usually, the distance between the fiber tip and the sample surface, h , was set close to $h \approx 2R$, resulting in an ablation mark with an average diameter $\langle D \rangle \approx 2.5R$.

Microscope images of the ablation marks were obtained in either reflected or transmitted mode by an upright microscope (BX 51, Olympus America Inc., Center Valley, PA, USA).

Visualization system. The distance between the fiber tip and sample surface was monitored by a long distance video microscope (InFocus Model KC, Infinity, Boulder CO, USA) with a 5× infinity-corrected objective lens (M Plan Apo 5×, Mitutoyo Co., Kanagawa, Japan) and the image was captured by a CCD camera (Marlin F131, Allied Vision Technologies, Stadtroda, Germany). With the environmental vibration in the low μm range, an approximate distance of 30-40 μm was easily maintained between the tip and the selected cell. A similar video microscope system was used at right angle to the sample surface to align the fiber tip over the cell of choice for ablation. This system consisted of a 7× precision zoom optic (Edmund Optics, Barrington, NJ, USA), fitted with a 10× infinity-corrected long working distance objective lens (M Plan Apo 10×, Mitutoyo Co., Kanagawa, Japan) and a CCD camera (Marlin F131, Allied Vision Technologies, Stadtroda, Germany).

Chemicals. HPLC grade methanol and water were purchased from Acros Organics (Geel, Belgium) and glacial acetic acid was obtained from Fluka (Munich, Germany). These chemicals were used without further purification.

Cells. Ten organic purple *A. cepa* bulbs (5 to 7 cm transverse diameter) were purchased from a local store (Distributed by, CFF Fresh, Sedro-Woolley, WA, USA, and bought in Washington, DC, USA) and four *N. pseudonarcissus* bulb were obtained from Reston, VA, USA. Prior to the experiments the bulbs were stored at 4 °C. Before LAESI-MS analysis, the bulbs were cut longitudinally by a surgical scalpel. A layer of scale was selected and cut into a strip between 4 and 6 cm². The intact monolayer of the inner epidermal tissue from the concave surface was peeled away from the parenchyma tissue. The wet surface of the epidermis was used to mount the tissue to a glass slide for LAESI-MS analysis.

Unfertilized *Lytechinus pictus* (painted sea urchin) eggs were collected by injecting the animal with 0.5 M KCl solution. Prior to the LAESI-MS analysis, the eggs were stored in a refrigerator (4° C) in artificial seawater. For the ablation experiments, a single egg was held with a holding micropipette (MPH-MED-O, Humagen Fertility Diagnostic, VA, USA) mounted on a micromanipulator (NMN-21, Narishige International USA, Inc., NY, USA). Suction was induced by a manual injector (IM-9A, Narishige International USA, Inc., NY, USA).

Peak assignments. Due to the diversity of structural isomers, assignments of the peaks to specific metabolites required special care. High mass resolution ($m/\Delta m \approx 8,000$, FWHM) and mass accuracy (~ 1 mDa or ~ 5 ppm at m/z 200) helped to identify a selection of potential structures. The measured monoisotopic masses, $m/z_{meas.}$, in Tables 6.1, 6.2 and 6.3 were obtained from single cell spectra, whereas the calculated values, $m/z_{calc.}$, were derived using the NIST Isotope Calculator package (ISOFORM, Version 1.02). The Plant Metabolic Network database (<http://plantcyc.org/>; last accessed on

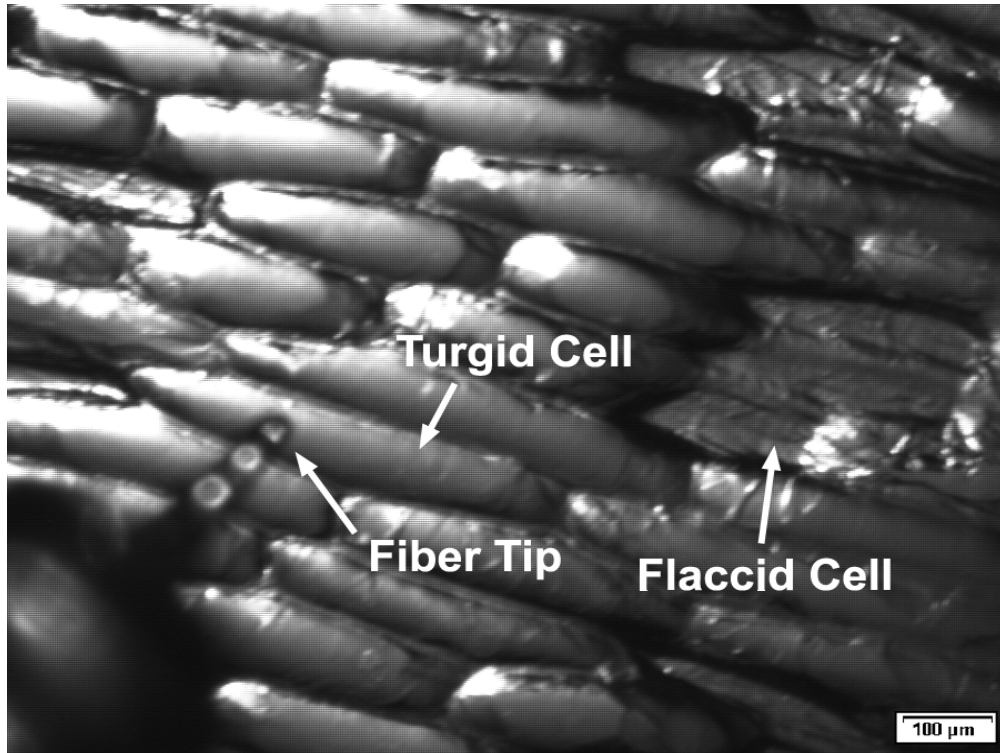
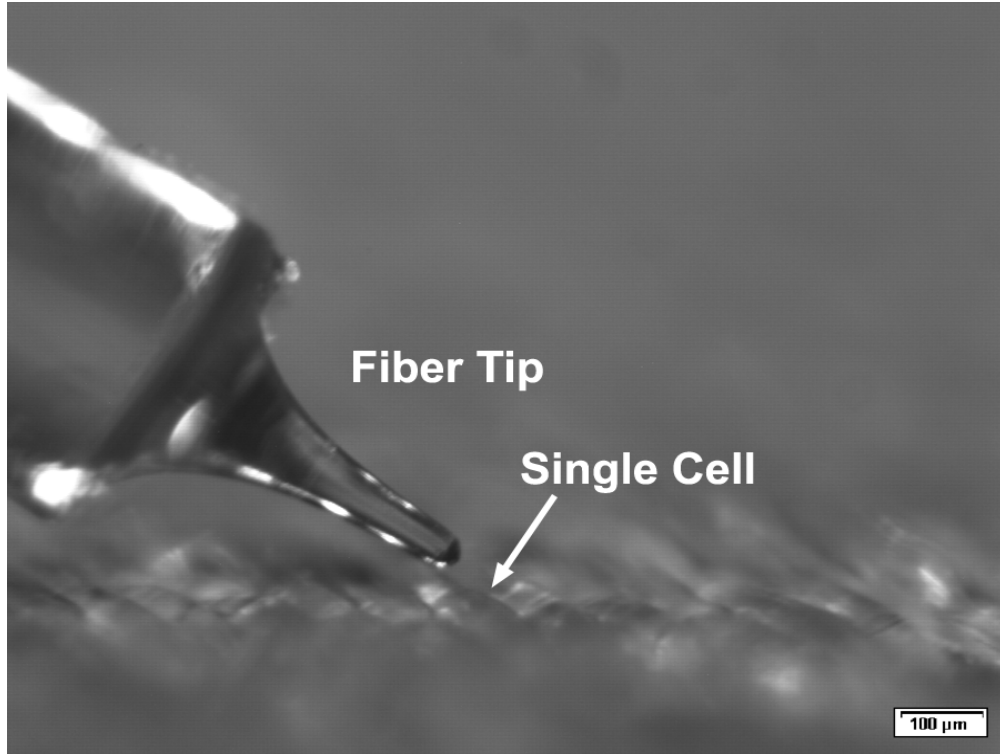
June 8, 2009) and species-specific literature^{29, 30} were also used as input for possible candidates. Tentative peak assignments were made based on the accurate mass, the isotope distribution patterns and, in some cases, the CAD spectra. Final identification of the ions requires additional work based on separation techniques, ultrahigh resolution MS, ¹H and ¹³C NMR, and FTIR.

Relative quantitation. For solutions with only a few components, quantitation capabilities of LAESI-MS were demonstrated throughout a wide dynamic range.²⁴ For more complex biological tissue matrixes, relative quantitation was established.²⁶ For layer-by-layer comparison of relative metabolite abundances in individual cells, LAESI-MS was performed to analyze four cells for each of the studied layers. The spectra were normalized to the base peaks and relative abundances and their standard deviations were calculated for the metabolites of interest.

RESULTS AND DISCUSSION

Laser Ablation of a Single Plant Cell. Smaller ablation craters can be produced by delivering the laser light through an optical fiber with an etched tip to reduce its diameter.³¹ This approach to focusing is similar to the one applied in scanning near-field optical microscopy (SNOM) but in the current study the produced spot size is still well above the diffraction limit. A GeO₂-based glass fiber with an etched tip with $R \approx 15 \mu\text{m}$ radius of curvature was utilized to deliver the 2.94 μm wavelength infrared light. When placed in close proximity of the sample surface, the average diameter of the ablation mark, $\langle D \rangle$, was slightly larger than $2R$. Because an accidental contact between the tip and the cells could break the fiber tip or damage the cell wall, the distance between the

Figure 6.2 (a) Etched optical fiber tip and the raised surface of turgid epidermal cells of *A. cepa* were $\sim 30 \mu\text{m}$ apart. For optimum coupling of the laser energy, this distance was similar to the diameter of the tip. Further removal of the fiber tip from the cell surface resulted in no ablation, whereas closer approach often led to damage to the cell or the fiber tip. **(b)** Cell targeting for ablation was carried out by adjusting the lateral position of the fiber tip over the selected turgid cell in the tissue. Scale bars are $100 \mu\text{m}$.



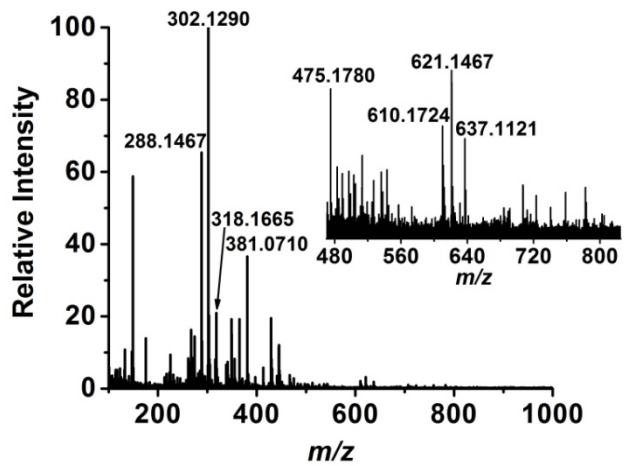
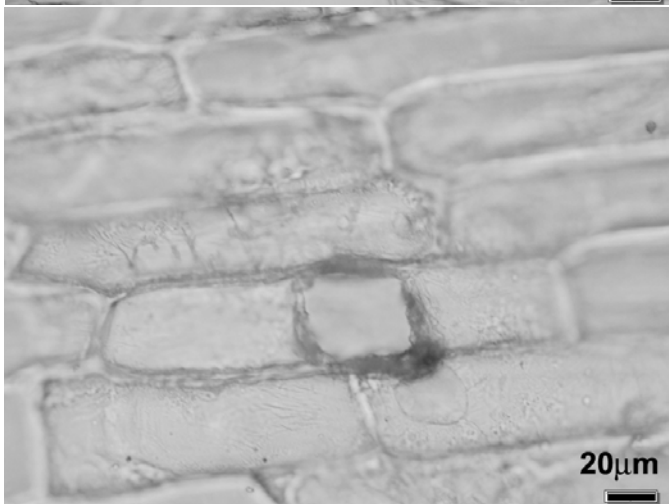
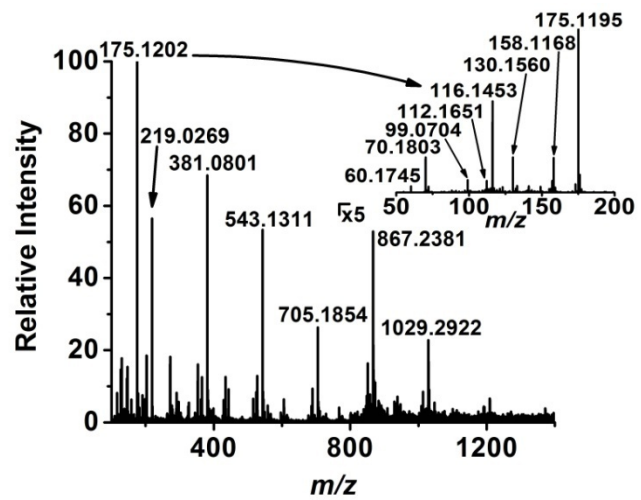
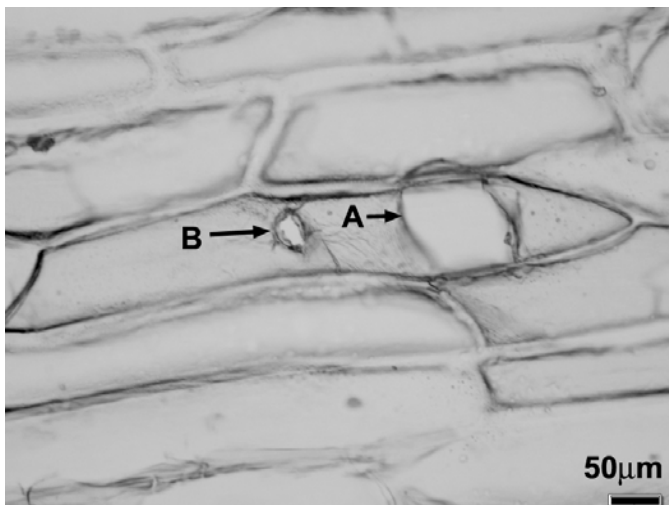
$\frac{A}{B}$

fiber tip and sample surface was adjusted by a micromanipulator and a micropositioning stage with the help of a long distance microscope (see Figure 6.2a). A similar long distance microscope was used to visualize the tissue surface for cell targeting (see Figure 6.2b). Assuming length, width and depth dimensions of 300 μm , 50 μm and 100 μm , respectively, the average volume of a large epidermal cell is ~ 1.5 nL, but the interaction volume is only ~ 30 pL for the 30 to 40 μm ablation spot diameter. Thus the fiber-based LAESI experiments probe only a fraction of these large cells. The schematic of the single cell LAESI-MS system is shown in Figure 6.1.

Large epidermal cells from *A. cepa* bulb, a model system to study plant cell structures,³² and from *N. pseudonarcissus* bulb were used to demonstrate single cell analysis by LAESI-MS. In this tissue, the potential cross-contamination induced by the analysis of neighboring cells in the same layer was negligible because of the large cell size. Due to the monolayer structure, there was no mixing from the underlying tissue either. Perforation marks produced by mid-IR ablation on single turgid epidermal cells of the two samples are shown in Figures 6.3a and 6.3c. These marks indicated the sampling of the selected individual cells, with no visible effect on the neighboring regions. Ablation typically started at the second laser pulse and continued until all the cytoplasm has been ablated and/or leaked out of the cell. Mass spectra were observed starting from the second laser pulse, as well. In case of an *A. cepa* epidermal cell, after ~ 100 laser pulses no additional ablation took place.

There was a remarkable difference between ablating turgid cells and flaccid ones that had lost their cytoplasm. The ablation marked A in Figure 6.3a shows a relatively large opening corresponding to the turgid state, whereas the smaller hole in the same cell

Figure 6.3 Single cell ablation marks on epidermal cell of **(a)** *A. cepa* (unpigmented cell) and **(c)** *N. pseudonarcissus* produced through an etched optical fiber tip. In panel **(a)** the first ablation (marked A) was performed on a turgid cell, whereas the second ablation (marked B) occurred after the loss of cytoplasm when the cell became flaccid. Panels **(b)** and **(d)** show the corresponding LAESI mass spectra produced by 100 laser pulses for *A. cepa* and *N. pseudonarcissus*, respectively. The inset in panel **(b)** depicts the eight fragments in the tandem MS of the nominal m/z 175 ion produced by CAD. The inset in panel **(d)** shows the zoomed portion of the daffodil spectrum at higher m/z .



A|B
C|D

wall was produced in a flaccid state after the cytoplasm had been removed. It is important to emphasize that in the case of every intact cell ablation was successfully carried out. The larger size of the ablation marked A in Figure 6.3a and the ruptured cell wall indicate the explosive nature of cytoplasm sampling in the turgid state. The presence of rapid phase explosion in the ablation of water-rich targets has been demonstrated by modeling studies.³³ In the flaccid state (i.e., in the absence of cytoplasm), however, sampling of the cell wall only is indicated by the smaller opening.

Laser Ablation of a Single Animal Cell. Individual eggs of *L. pictus* (painted sea urchin) were analyzed in sessile configuration. A few minutes before the LAESI-MS analysis, 30 μl of the *L. pictus* egg suspension was mixed with 1 ml of water to decrease the number of eggs per unit volume. This increased the average distance between the eggs and enabled their individual manipulation. Furthermore, the dilution reduced the concentration of salts. This was necessary because the high salt concentration prevented the detection of metabolite ions. Approximately 100 μl of the resulting egg suspension was placed on a glass slide. A single egg of 90 to 100 μm in diameter was selected and immobilized by a holding pipette using suction induced by a manual injector. The pipette was positioned by a micromanipulator. The ablation for LAESI-MS was carried out by moving the etched fiber tip to contact the *L. pictus* egg (see the inset of Figure 6.4). In order to initiate ablation, slightly more efficient coupling of the laser pulse to the optical fiber was achieved, which in relative terms translated into somewhat higher laser fluences at the sharpened fiber tip compared to the epidermal cells.

Figure 6.4 Positive ion LAESI mass spectrum of a single sea urchin (*L. pictus*) egg of $\sim 100 \mu\text{m}$ in diameter. The inset shows the sessile egg immobilized by the holding pipette and touched by the sharpened optical fiber.

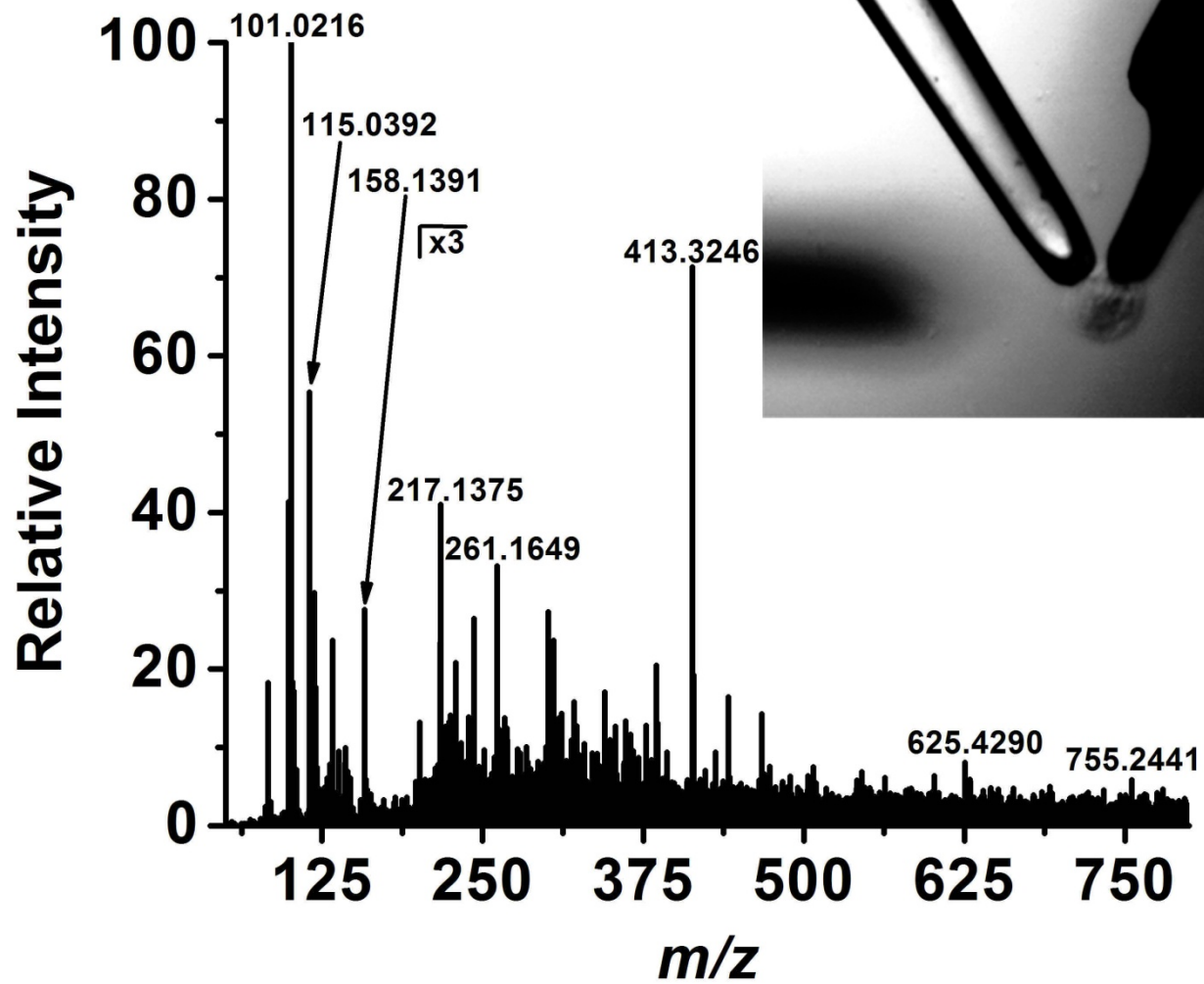


Figure 6.4 shows the LAESI mass spectrum acquired from a single egg. The preliminary analysis of the data shows the presence of ions representing small metabolites along with lipids at higher masses. Some of the prominent ions include species at nominal m/z 83, 101, 105, 115, 119, 138, 158, 217, 243, 261, 413, 625, 755. Further work, including tandem MS, is needed to identify the corresponding metabolites.

LAESI-MS and MS/MS from a Cell. LAESI mass spectra were only produced from turgid cells. Except in the case of *N. pseudonarcissus*, all the tandem MS data were collected from the single cells using up to a 100 laser pulses. Initially single cell spectra were combined to increase the signal-to-noise ratio and enhance the fidelity of peak assignments. The combined positive ion spectra from a population of 13 cells showed 332 peaks with a wide dynamic range. Once the assignments were made single cell spectra were studied. Figures 6.3b and 6.3d give examples of single cell mass spectra from the two plant species. Many of the ions were tentatively identified as primary or secondary metabolites based on accurate masses, isotope distribution patterns and, in some cases, tandem MS. In the onion cell most of the singly charged low m/z ions ($< m/z$ 300) were assigned to smaller metabolites, such as alliin, 2-aminoacrylic acid, thioacrolein found in the alliin degradation cycle. Most of the larger ions corresponded to secondary metabolites and oligosaccharides, possibly fructans, found in the fructan biosynthesis cycle. A number of doubly charged ions were also observed for oligosaccharides, which helped their identification up to a degree of polymerization ten.

Some ions can have multiple assignments. For example, the m/z 175.1202 ion in the *A. cepa* spectrum can be assigned to arginine, acetyl-ornithine, N-methyltryptamine and/or gramine. It was identified as protonated arginine based on better than 0.001 Da

mass accuracy and comparing its CAD fragmentation pattern (see the inset in Figure 6.3b) to the corresponding tandem MS spectrum in the NIST Mass Spectral Search Program (NIST/EPA/NIH Mass Spectral Library, Version 2.0). The ability of performing tandem MS on a single cell *in situ* has promising implications for ion identification in organisms.

To facilitate the data analysis and the peak assignments, averaged LAESI mass spectra were also taken on small cell populations using conventional focusing optics with ~250 μm focal spot size. As expected, these spectra showed higher S/N than the single cell data. Even with this additional information, due to the large variety of structural isomers caution is necessary in making metabolite assignments.²⁹ Unambiguous identification of individual metabolites requires extensive studies relying on multiple methods, e.g., separation techniques, ultrahigh resolution MS, ^1H and ^{13}C NMR, and FTIR.

Metabolites from Same Cell Type in Different Species. The analysis of the anatomically similar single epidermal cells from the two storage organs, showed significantly different metabolic profiles. While the cells from both plants contained oligosaccharides, these species were more prevalent in the onion. The daffodil cells, however, were rich in various alkaloids, such as norpluviine, a lycorine type, and vittatine a haemanthamine type alkaloid. These and other *Narcissus* alkaloids are known to be present in this plant species.²⁹ The lists of peak assignments and mass accuracies for both species are presented in Tables 6.1 (*A. cepa*) and 6.2 (*N. pseudonarcissus*).

Adjacent Colorless and Pigmented Cells. A fraction of the epidermal cells in the purple onion cultivar are pigmented and can be distinguished under the microscope.

Table 6.1 Tentative peak assignments in the mass spectrum of a single unpigmented epidermal cell from *A. cepa* bulb.

Metabolites	Formula	m/z calc.	m/z meas.	Δm (mDa)
pyruvaldehyde	C ₃ H ₄ O ₂ (+H ⁺)	73.0290	73.0188	-10.2
thioacrolein	C ₃ H ₄ S (+H ⁺)	73.0112	73.0188	7.6
5-aminoimidazole	C ₃ H ₅ N ₃ (+H ⁺)	84.0562	84.0452	-11.0
furanone	C ₄ H ₄ O ₂ (+H ⁺)	85.0290	85.0310	2.0
2-aminoacrylic acid	C ₃ H ₅ NO ₂ (+H ⁺)	88.0399	88.0426	2.7
proline	C ₅ H ₉ NO ₂ (+H ⁺)	116.0712	116.0747	3.5
2-oxohexa-4,5-cyclopropyl-5-enoic acid	C ₆ H ₆ O ₃ (+H ⁺)	127.0395	127.0440	4.5
thymine	C ₅ H ₆ N ₂ O ₂ (+H ⁺)	127.0508	127.0440	-6.8
5-oxoproline	C ₅ H ₇ NO ₃ (+H ⁺)	130.0504	130.0527	2.3
p-aminobenzoic acid and/or vitamin L1	C ₇ H ₇ NO ₂ (+H ⁺)	138.0555	138.0493	-6.2
glutamine and/or 3-ureido-isobutyric acid	C ₅ H ₁₀ N ₂ O ₃ (+H ⁺)	147.0770	147.0811	4.1
histidine and/or bacimethrin	C ₆ H ₉ N ₃ O ₂ (+H ⁺)	156.0773	156.0833	6.0
allylcysteine	C ₆ H ₁₁ NO ₂ S (+H ⁺)	162.0589	162.0678	8.9
acetylhomoserine, α -aminoadipic acid	C ₆ H ₁₁ NO ₄ (+H ⁺)	162.0766	162.0678	-8.8
phenylalanine	C ₉ H ₁₁ NO ₂ (+H ⁺)	166.0868	166.0914	4.6
arginine ^b	C ₆ H ₁₄ N ₄ O ₂ (+H ⁺)	175.1195	175.1202	0.7
alliin	C ₆ H ₁₁ NO ₃ S (+H ⁺)	178.0538	178.0606	6.8
galactosamine	C ₆ H ₁₃ NO ₅ (+H ⁺)	180.0872	180.0815	-5.7
tyrosine and/or α -aminoxy- β -phenylpropionic acid	C ₉ H ₁₁ NO ₃ (+H ⁺)	182.0817	182.0807	-1.0
monosaccharide ^a	C ₆ H ₁₂ O ₆ (+K ⁺)	219.0271	219.0269	-0.2
arginino-succinic acid	C ₁₀ H ₁₈ N ₄ O ₆ (+H ⁺)	291.1305	291.1224	-8.1
glucosan or dextrin unit	(C ₆ H ₁₀ O ₅) ₂ (+H ⁺) ^c	325.1135	325.1068	-6.7
disaccharide ^{a,b}	C ₁₂ H ₂₂ O ₁₁ (+K ⁺)	381.0799	381.0801	0.2
trisaccharide ^{a,b}	C ₁₈ H ₃₂ O ₁₆ (+K ⁺)	543.1328	543.1311	-1.7
heptasaccharide ^a	C ₄₂ H ₇₂ O ₃₆ (+H ⁺ +K ⁺)	596.1759	596.1743	-1.6
oligosaccharide (DP 8 units) ^{a,c}	C ₄₈ H ₈₂ O ₄₁ (+H ₂ O+H ⁺ +K ⁺)	686.2076	686.2177	10.1
tetrasaccharide ^{a,b}	C ₂₄ H ₄₂ O ₂₁ (+K ⁺)	705.1856	705.1854	-0.2
oligosaccharide (DP 9 units) ^{a,c}	C ₅₄ H ₉₂ O ₄₆ (+H ₂ O+H ⁺ +K ⁺)	767.2340	767.2286	-5.4
oligosaccharide (DP 10 units) ^{a,c}	C ₆₀ H ₁₀₂ O ₅₁ (+H ₂ O+H ⁺ +K ⁺)	848.2604	848.2584	-2.0
pentasaccharide ^a	C ₃₀ H ₅₂ O ₂₆ (+K ⁺)	867.2384	867.2381	-0.3
hexasaccharide ^{a,b}	C ₃₆ H ₆₂ O ₃₁ (+K ⁺)	1029.2913	1029.2922	0.9

^aOther adduct, and/or quasi-molecular, and/or cluster ions of the chemical species were also observed in the LAESI mass spectra.

^bThese ions were used as internal mass standards.

^cDP = Degree of polymerization.

Table 6.2 Tentative peak assignments in the mass spectrum of a single epidermal cell from *N. pseudonarcissus* bulb.

Metabolites	Formula	m/z calc.	m/z meas.	Δm (mDa)
5-aminoimidazole	C ₃ H ₅ N ₃ (+H ⁺)	84.0562	84.0468	-9.4
furanone	C ₄ H ₄ O ₂ (+H ⁺)	85.0290	85.0295	0.5
proline	C ₅ H ₉ NO ₂ (+H ⁺)	116.0712	116.0725	1.3
succinic acid	C ₄ H ₆ O ₄ (+H ⁺)	119.0344	119.0243	-10.1
homoserine	C ₄ H ₉ NO ₃ (+H ⁺)	120.0661	120.0809	14.8
3-methylene-indolenine	C ₅ H ₇ NO ₃ (+H ⁺)	130.0504	130.0548	4.4
asparagine	C ₄ H ₈ N ₂ O ₃ (+H ⁺)	133.0613	133.0638	2.5
glutamine and/or 3-ureido-isobutyric acid	C ₅ H ₁₀ N ₂ O ₃ (+H ⁺)	147.0770	147.0799	2.9
histidine and/or bacimethrin	C ₆ H ₉ N ₃ O ₂ (+H ⁺)	156.0773	156.0804	3.1
gallic acid	C ₇ H ₆ O ₅ (+H ⁺)	171.0293	171.0203	-9
arginine ^b	C ₆ H ₁₄ N ₄ O ₂ (+H ⁺)	175.1195	175.1218	2.3
caranine and/or crinine and/or vittatine	C ₁₆ H ₁₇ NO ₃ (+H ⁺)	272.1287	272.1302	1.5
norpluviine	C ₁₆ H ₁₉ NO ₃ (+H ⁺)	274.1443	274.1423	-2
galanthamine and/or mesembrenone and/or pluviine	C ₁₇ H ₂₁ NO ₃ (+H ⁺)	288.1600	288.1467	-13.3
crinamine and/or haemanthamine	C ₁₇ H ₁₉ NO ₄ (+H ⁺)	302.1392	302.1290	-10.2
homolycorine	C ₁₈ H ₂₁ NO ₄ (+H ⁺)	316.1549	316.1512	-3.7
galanthine and/or lycorenine and/or papyramine	C ₁₈ H ₂₃ NO ₄ (+H ⁺)	318.1705	318.1665	-4
disaccharides ^{a, b}	C ₁₂ H ₂₂ O ₁₁ (+K ⁺)	381.0799	381.0710	-8.9
trisaccharides ^{a, b}	C ₁₈ H ₃₂ O ₁₆ (+K ⁺)	543.1328	543.1394	6.6
tetrasaccharide	C ₂₄ H ₄₂ O ₂₁ (+H ₂ O+K ⁺)	723.1961	723.1855	-10.6

^aOther adduct, and/or quasi-molecular, and/or cluster ions of the chemical species were also observed in the LAESI mass spectra.

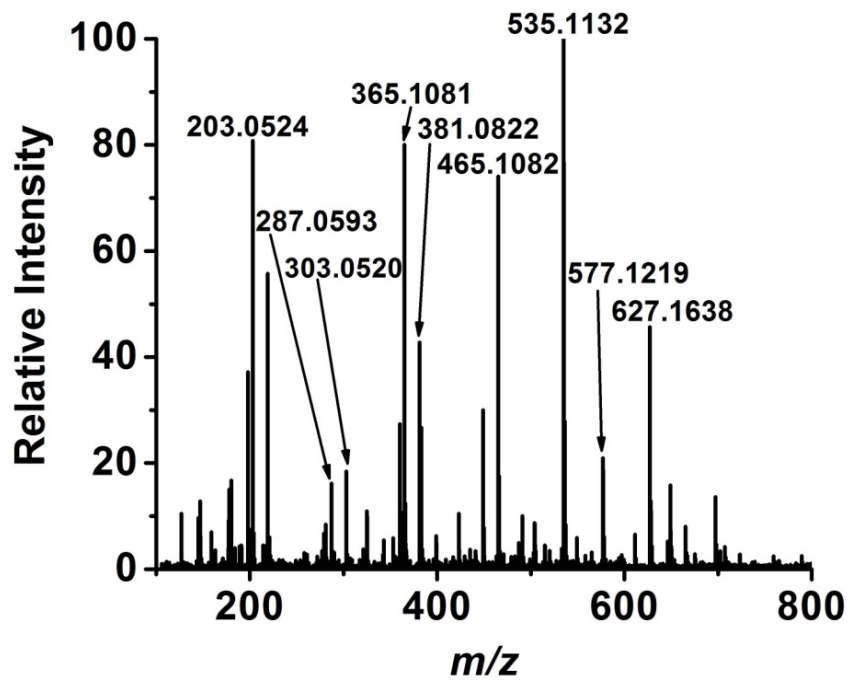
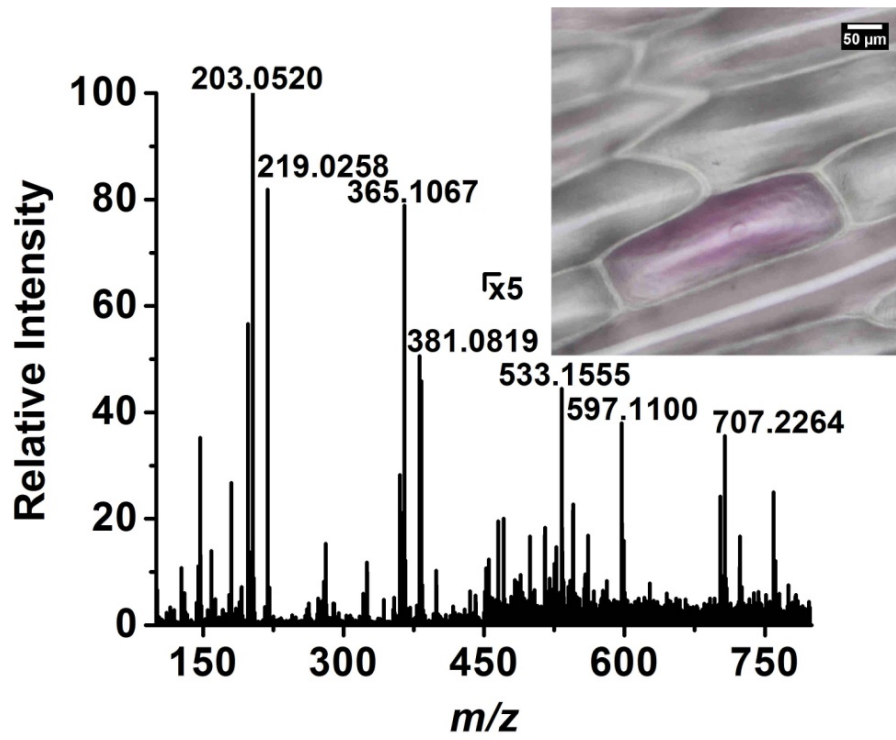
^bThese ions were used as internal mass standards.

Table 6.3 Comparative list of tentative peak assignments for the LAESI mass spectra of the colorless and pigmented cells in the onion bulb epidermis. The purple background in the table indicates ions found exclusively in the pigmented cells.

Metabolites	Formula	Purple	Colorless
furanone	C ₄ H ₄ O ₂ (+H ⁺)	85.0268	85.0262
2-aminoacrylic acid	C ₃ H ₅ NO ₂ (+H ⁺)	88.0388	88.0370
thymine / oxohexacyclopropylenoic acid	C ₅ H ₆ N ₂ O ₂ (+H ⁺)/C ₆ H ₆ O ₃ (+H ⁺)	127.0374	127.0370
oxoproline	C ₅ H ₇ NO ₃ (+H ⁺)	130.0546	130.0469
glutamine and/or 3-ureido-isobutyric acid	C ₅ H ₁₀ N ₂ O ₃ (+H ⁺)	147.0766	147.0753
alliin	C ₆ H ₁₁ NO ₃ S (+H ⁺)	178.0515	178.0525
galactosamine	C ₆ H ₁₃ NO ₅ (+H ⁺)	180.0869	180.0870
monosaccharide ^a	C ₆ H ₁₂ O ₆ (+K ⁺)	219.0259	219.0258
cyanidin and/or kaempferol	C ₁₅ H ₁₁ O ₆ ⁺	287.0593	-
quercetin	C ₁₅ H ₁₀ O ₇ (+H ⁺)	303.0520	-
glucosan and/or dextrin unit ^a	(C ₆ H ₁₀ O ₅) ₂ (+H ⁺)	325.1122	325.1128
disaccharide ^a	C ₁₂ H ₂₂ O ₁₁ (+K ⁺)	381.0822	381.0819
dityrosine	C ₁₈ H ₂₀ N ₂ O ₆ (+Na ⁺)	383.1148	383.1148
disaccharide + quercetin glucoside	C ₁₂ H ₂₂ O ₁₁ (+K ⁺) + C ₂₁ H ₂₀ O ₁₂ (+H ⁺)	423.0884	-
cyanidin glucoside and/or kaempferol glucoside ^a	C ₂₁ H ₂₁ O ₁₁ ⁺	449.1164	-
peonidin glucoside	C ₂₂ H ₂₃ O ₁₁ ⁺	463.1262	-
quercetin glucoside ^a	C ₂₁ H ₂₀ O ₁₂ (+H ⁺)	465.1082	-
adenylyl aminoadipic acid	C ₁₆ H ₂₃ N ₆ O ₁₀ P (+H ⁺)	491.1235	-
trisaccharide + quercetin glucoside	C ₁₈ H ₃₂ O ₁₆ (+K ⁺) + C ₂₁ H ₂₀ O ₁₂ (+H ⁺)	504.1145	-
cyanidin malonyl glucoside	C ₂₄ H ₂₃ O ₁₄ ⁺	535.1132	-
peonidin malonyl glucoside	C ₂₅ H ₂₅ O ₁₄ ⁺	549.1303	-
trisaccharide	C ₁₈ H ₃₂ O ₁₆ (+H ₂ O+K ⁺)	-	561.1495
cyanidin malonyl acetyl glucoside	C ₂₆ H ₂₅ O ₁₅ ⁺	577.1219	-
quercetin rutinoside, quercetin glucoside rhamnoside	C ₂₇ H ₃₀ O ₁₆ (+H ⁺)	611.1697	-
cyanin, cyanidin diglucoside	C ₂₇ H ₃₁ O ₁₆ ⁺	611.1697	-
quercetin diglucoside ^a	C ₂₇ H ₃₀ O ₁₇ (+H ⁺)	627.1638	-
cyanidin malonyl diglucoside	C ₃₀ H ₃₃ O ₁₉ ⁺	697.1754	-
tetrasaccharide	C ₂₄ H ₄₂ O ₂₁ (+H ₂ O+K ⁺)	723.1995	723.2080
peonidin glucoside + quercetin	C ₂₂ H ₂₃ O ₁₁ ⁺ +C ₁₅ H ₁₀ O ₇	765.1505	-
quercetin triglucoside	C ₃₃ H ₄₀ O ₂₂ (+H ⁺)	789.2043	-
2 disaccharides + quercetin glucoside ^a	C ₁₂ H ₂₂ O ₁₁ +C ₂₁ H ₂₀ O ₁₂ (+Na ⁺)	829.2299	-
2 disaccharides + quercetin diglucoside	C ₁₂ H ₂₂ O ₁₁ + C ₂₇ H ₃₀ O ₁₇ (+Na ⁺)	991.2538	-
quercetin triglucoside + quercetin glucoside	C ₃₃ H ₄₀ O ₂₂ +C ₂₁ H ₂₀ O ₁₂ (+H ⁺)	1253.3040	-
quercetin diglucoside + quercetin diglucoside ^a	(C ₂₇ H ₃₀ O ₁₇) ₂ (+H ⁺)	1253.3040	-

^aOther adduct, and/or quasi-molecular, and/or cluster ions of the chemical species were also observed in the LAESI mass spectra.

Figure 6.5 Single cell LAESI mass spectra of neighboring **(a)** colorless and **(b)** pigmented epidermal cells of the purple *A. cepa* cultivar with the optical image of the cells in the inset (scale bar = 50 μm).



$\frac{A}{B}$

The presence of this cell variant enabled a direct comparison between the metabolite composition of the colorless and pigmented cells in the same tissue. In Figure 6.5 the corresponding mass spectra are presented together with the optical image of the two cell types.

Comparison of the LAESI mass spectra revealed that, in addition to the essential metabolites found in the colorless cells, the pigmented variant contained significant amounts of anthocyanidins, other flavonoids and their glucosides. For example, the m/z 449 ion can be assigned to cyanidin glucoside, a known purple pigment contained in the cell membrane vacuoles in purple plants. A comparative list of the ions and the tentative metabolite assignments for the colorless and the pigmented cell are listed in Table 6.3. Close to 70 ionic species were found in single cells. Two thirds of them were tentatively assigned to one or more metabolites that had accurate masses close to the measured values and for some of them the tandem MS that was consistent with known fragmentation patterns. The most significant difference between the colorless and pigmented cells was the presence of anthocyanins and the corresponding anthocyanidins in the latter. Glycosidic flavonoids had been detected by vacuum IR laser MS studies in red rose leaf tissues.³⁴ In addition, the pigmented cells contained high levels of quercetin and its mono-, di- and triglucosides. The elevated presence of quercetin in purple or red onion bulbs is well documented.³⁰ The observation that the metabolites in colorless cells were not contaminated by anthocyanidins and anthocyanins from adjacent pigmented cells points to no or minimal damage of the neighboring cells by the ablation.

Metabolites in Cells of Different Age. To find metabolic changes primarily correlated with age for the same type of cells, we compared the epidermal cells from

different leaf bases (layers) within individual onion bulbs, where the different layers represented older and younger cell populations.³⁵ The relative quantitation capabilities of LAESI-MS in a wide dynamic range had been shown in previous publications.^{24, 26} The relative ion intensities of some metabolites averaged for four cells per layer ($n = 4$) are shown in Table 6.4. Changes from the younger inner leaf base (layer four) to the oldest outer turgid layer (layer eight) illustrate the variations of the related metabolite content. For example, reduced arginine content can be seen in the older cell populations from the gradual drop in its relative ion intensity from 97 ± 5 (layer 4) to 0 (layer 7). Conversely, alliin seems to accumulate more in the cells of the outer layers.

CONCLUSIONS

We have shown that *in situ* metabolic analysis of single cells is possible by a modified version of LAESI-MS. Using a sharpened optical fiber tip, individual cells were ablated for analysis. Comparisons of cells with different pigmentation or age within the same tissue, as well as between cells of the same type in different species demonstrated significant metabolic variations consistent with literature data.

Laser based atmospheric pressure mass spectrometric techniques, such as LAESI-MS, are able to analyze small sample volumes with a tightly focused laser beam. Further developments in single cell analysis should focus on reducing the ablation spot size while maintaining the mass spectrometric signal by optimizing the source geometry and increasing the post-ionization yield. In heterogeneous cell populations, automatic adjustment of the laser parameters based on optical feedback can facilitate the analysis of multilayered populations cell by cell. An important future extension of this method is the

Table 6.4 Relative ion intensities for some metabolites in single cells of an *A. cepa* bulb averaged for four cells.

Metabolites	Leaf Bases				
	Fourth (inner)	Fifth	Sixth	Seventh	Eighth (outer)
arginine	97±5	74±28	6±3	0	0
alliin	9±4	11±2	20±7	19±7	20±3
monosaccharide	47±11	60±30	23±13	40±14	41±51
disaccharide	87±19	96±7	72±13	70±7	77±35
trisaccharide	78±18	85±13	100±0	100±0	48±36
tetrasaccharide	47±13	56±8	80±17	74±11	20±15
pentasaccharide	20±8	27±5	31±7	25±2	7±6
hexasaccharide	6±3	11±2	10±2	7±2	1±0
heptasaccharide	2±2	4±1	3±0	1±1	0

analysis of biological tissues, with the ultimate goal of molecular imaging based on cells as the natural voxels, a three dimensional pixel. Metabolic analysis of single cells helps to better understand cell differentiation, ageing, changes due to disease states and response to xenobiotics and physical stimuli.

ACKNOWLEDGEMENT

The authors acknowledge financial support from the U.S. National Science Foundation (0719232), the U. S. Department of Energy (DEFG02-01ER15129), the W. M. Keck Foundation (041904) and the George Washington University Research Enhancement Fund. Infrared Fiber Systems, Silver Spring, MD, USA, kindly provided the GeO₂-based glass optical fibers for this study, and Mark E. Reeves and Joan A. Hoffmann of GWU helped with the protocol regarding their etching. The sea urchin eggs were kindly provided by Kenneth M. Brown of GWU.

REFERENCES:

- (1) Kehr, J. *Current Opinion in Plant Biology* **2003**, *6*, 617-621.
- (2) Monroe, E. B.; Jurchen, J. C.; Rubakhin, S. S.; Sweedler, J. V. In *New Frontiers in Ultrasensitive Bioanalysis*; Xiao-Hong Nancy, X., Ed., 2007, pp 269-293.
- (3) Malik, Z.; Dishi, M.; Garini, Y. *Photochemistry and Photobiology* **1996**, *63*, 608-614.
- (4) Potma, E. O.; De Boeij, W. P.; Van Haastert, P. J. M.; Wiersma, D. A. *Proceedings of the National Academy of Sciences of the United States of America* **2001**, *98*, 1577-1582.

- (5) Aguayo, J. B.; Blackband, S. J.; Schoeniger, J.; Mattingly, M. A.; Hintermann, M. *Nature* **1986**, *322*, 190-191.
- (6) Miyawaki, A.; Sawano, A.; Kogure, T. *Nature Reviews Molecular Cell Biology* **2003**, *4*, S1-S7.
- (7) Tsien, R. Y. *Annual Review of Biochemistry* **1998**, *67*, 509-544.
- (8) Navratil, M.; Mabbott, G. A.; Arriaga, E. A. *Analytical Chemistry* **2006**, *78*, 4005-4020.
- (9) Kennedy, R. T.; Oates, M. D.; Cooper, B. R.; Nickerson, B.; Jorgenson, J. W. *Science* **1989**, *246*, 57-63.
- (10) Olefirowicz, T. M.; Ewing, A. G. *Analytical Chemistry* **1990**, *62*, 1872-1876.
- (11) Hogan, B. L.; Yeung, E. S. *Analytical Chemistry* **1992**, *64*, 2841-2845.
- (12) Cruz, L.; Moroz, L. L.; Gillette, R.; Sweedler, J. V. *Journal of Neurochemistry* **1997**, *69*, 110-115.
- (13) Hofstadler, S. A.; Severs, J. C.; Smith, R. D.; Swanek, F. D.; Ewing, A. G. *Rapid Communications in Mass Spectrometry* **1996**, *10*, 919-922.
- (14) Tsuyama, N.; Mizuno, H.; Tokunaga, E.; Masujima, T. *Analytical Sciences* **2008**, *24*, 559-561.
- (15) Rubakhin, S. S.; Garden, R. W.; Fuller, R. R.; Sweedler, J. V. *Nature Biotechnology* **2000**, *18*, 172-175.
- (16) Ostrowski, S. G.; Van Bell, C. T.; Winograd, N.; Ewing, A. G. *Science* **2004**, *305*, 71-73.
- (17) Stahl, B.; Linos, A.; Karas, M.; Hillenkamp, F.; Steup, M. *Analytical Biochemistry* **1997**, *246*, 195-204.

- (18) Amantonico, A.; Oh, J. Y.; Sobek, J.; Heinemann, M.; Zenobi, R. *Angewandte Chemie - International Edition* **2008**, *47*, 5382-5385.
- (19) Emmert-Buck, M. R.; Bonner, R. F.; Smith, P. D.; Chuaqui, R. F.; Zhuang, Z.; Goldstein, S. R.; Weiss, R. A.; Liotta, L. A. *Science* **1996**, *274*, 998-1001.
- (20) Takáts, Z.; Wiseman, J. M.; Gologan, B.; Cooks, R. G. *Science* **2004**, *306*, 471-473.
- (21) Talaty, N.; Takats, Z.; Cooks, R. G. *Analyst* **2005**, *130*, 1624-1633.
- (22) Li, Y.; Shrestha, B.; Vertes, A. *Analytical Chemistry* **2007**, *79*, 523-532.
- (23) Shrestha, B.; Li, Y.; Vertes, A. *Metabolomics* **2008**, *4*, 297-311.
- (24) Nemes, P.; Vertes, A. *Analytical Chemistry* **2007**, *79*, 8098-8106.
- (25) Nemes, P.; Barton, A. A.; Li, Y.; Vertes, A. *Analytical Chemistry* **2008**, *80*, 4575-4582.
- (26) Sripadi, P.; Nazarian, J.; Hathout, Y.; Hoffman, E. P.; Vertes, A. *Metabolomics* **2009**, *5*, 263-276.
- (27) Sampson, J. S.; Murray, K. K.; Muddiman, D. C. *Journal of the American Society for Mass Spectrometry* **2009**, *20*, 667-673.
- (28) Harrington, J. A. In *Specialty Optical Fibers Handbook*; Méndez, A., Morse, T. F., Eds.; Academic Press: Burlington, MA, 2007.
- (29) Bastida, J.; Viladomat, F.; Codina, C. In *Studies in natural products chemistry*; Atta-ur-Rahman, Ed.; Elsevier Science B. V., 1998; Vol. 20, pp 323-405.
- (30) Slimestad, R.; Fossen, T.; Vagen, I. M. *Journal of Agricultural and Food Chemistry* **2007**, *55*, 10067-10080.
- (31) Stockle, R.; Setz, P.; Deckert, V.; Lippert, T.; Wokaun, A.; Zenobi, R. *Analytical Chemistry* **2001**, *73*, 1399-1402.

- (32) Wilson, R. H.; Smith, A. C.; Kacurakova, M.; Saunders, P. K.; Wellner, N.; Waldron, K. W. *Plant Physiology* **2000**, *124*, 397-406.
- (33) Chen, Z. Y.; Vertes, A. *Physical Review E* **2008**, *77*, 036316.
- (34) Dreisewerd, K.; Draude, F.; Kruppe, S.; Rohlfing, A.; Berkenkamp, S.; Pohlentz, G. *Analytical Chemistry* **2007**, *79*, 4514-4520.
- (35) Darbyshire, B.; Henry, R. J. *New Phytologist* **1978**, *81*, 29-34.

CHAPTER 7

FUTURE DIRECTIONS

Advances in Metabolomics through LAESI-MS

More than 200 000 metabolites are estimated to exist in the plant kingdom.¹ The initial study of the human metabolome suggests even greater diversity. With the limited mass accuracy of current laser ablation electrospray ionization (LAESI) mass spectrometry (MS) systems, due to the large number of possibilities even the elemental composition of many metabolites cannot be unambiguously discerned. Using conventional ion sources the ultrahigh accuracy measurement of the m/z value obtained from direct infusion Fourier transform ion cyclotron resonance (FTICR) MS has been successfully utilized to identify metabolites in mouse serum.² Coupling LAESI with an ultrahigh resolution mass spectrometer, e.g., based on an FTICR or an orbitrap analyzer, will help in the unambiguous identification of numerous metabolites.

Currently, the statistical methods used in the analysis of tissue and cell metabolites and their correlation with disease states have not been fully established. Some groups have utilized mathematical methods such as principal component analysis (PCA) to compare metabolic profiles in healthy and diseased samples. For example, PCA has been utilized to study metabolic profiles associated with inborn errors of metabolism from urine samples using DESI-MS.³ Similarly, suitable statistical and analysis protocols should be developed for studying a larger number of metabolites using LAESI-MS.

Reactive LAESI

The reactive LAESI method implements chemical reactions between the laser ablation plume produced from the sample and the electrospray droplets or the gas phase environment to induce enhanced or selective ionization of the molecules targeted for analysis. For example, a chemical reagent can be dissolved in the electrospray solvent. When the ablation plume interacts with the electrospray, the reaction for this reagent with the analyte can yield produce new types of ions. An important advantage of this method is the ability to enhance the ionization of targeted analytes without additional sample preparation. Furthermore, reactive LAESI does not require a direct contact between the reactant and the sample, thereby minimizing the contamination of the latter. This is especially significant in case of *in vivo* analysis.

We have demonstrated the utility of reactive LAESI in the analysis of mouse brain samples.⁴ Lithiated ions of glycerophosphocholines were produced from mouse brain sections using reactive LAESI by adding Li_2SO_4 to the spray solution. The resulting lithiated lipid molecules readily fragmented in CAD experiments and the fragments provided direct information on the individual lengths of the acyl chains.

Prerequisites for reactive LAESI-MS are the appropriate selection of a reagent that can dissolve in electrospray solution without significantly changing the spray, a rapid reaction with the targeted molecules, and efficient ion production.

Single Cell Imaging

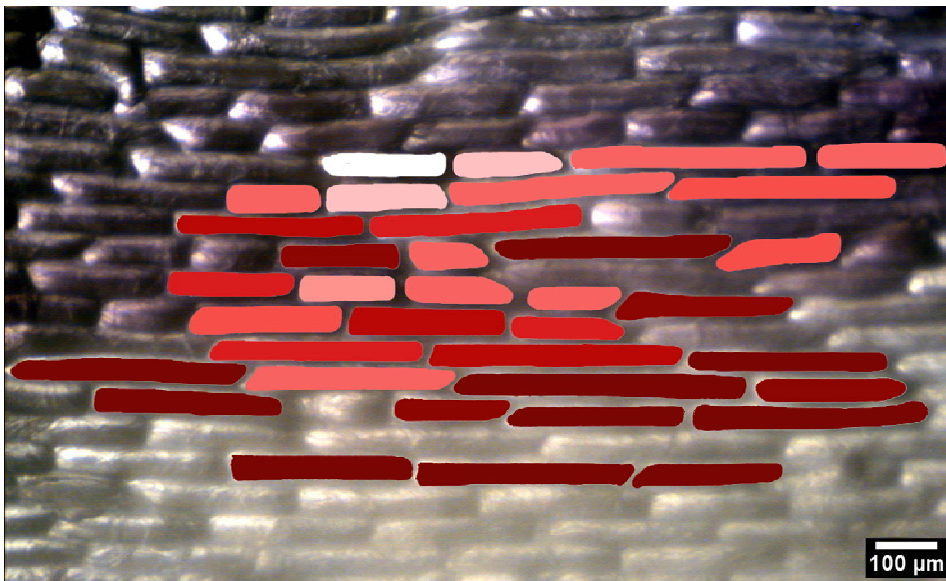
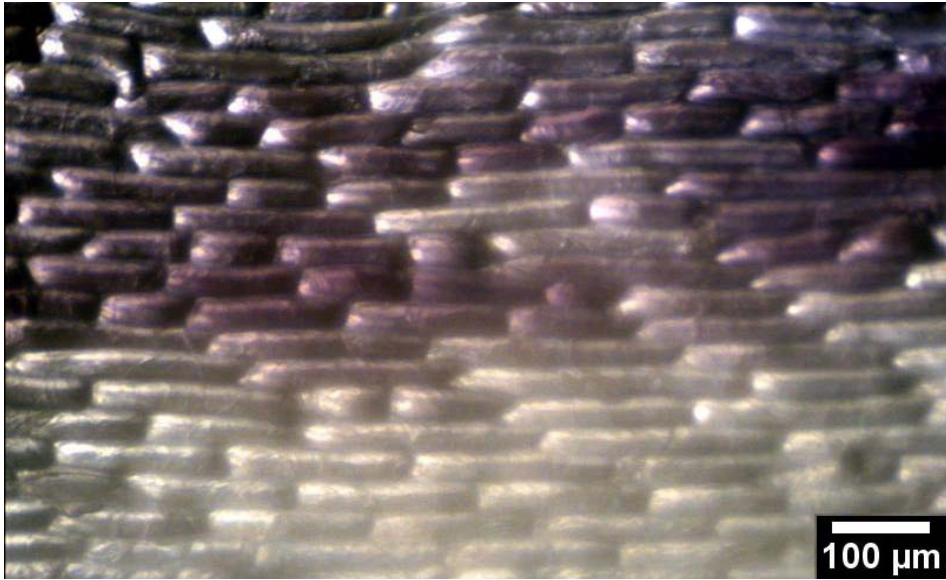
Current methods for the spatial mapping of molecules in tissues by imaging MS rely on rectangular grids for sampling and an artificial choice for the voxel, i.e.,

volumetric pixel, size based on the size of the laser focal volume.⁵ A more natural choice, the single cell, can be adopted for the latter. Accepting the single cell as the voxel in a tissue also dictates a more appropriate imaging grid that follows the distribution of cells. Spatial maps of biomolecules in a tissue produced one cell at a time are more likely to retain information on the spatial organization of biochemical interactions.

Our single cell analysis results described in Chapter 6 indicate the feasibility of such a new approach to tissue imaging.⁶ Figure 7.1 presents some of my preliminary results for the chemical imaging of the epidermal tissue in the purple *Allium Cepa* bulb produced by using single cells as voxels. Extensive experience with this tissue indicated that ablating neighboring cells did not have an influence on the analysis of a targeted cell. The cell-by-cell chemical image in Figure 7.1 was acquired by manually selecting each cell by the operator. A correlation between the chemical contrast and the optical contrast is apparent in the images.

In order to produce images based on a large number of cells, an automated cell contour recognition and computerized grid generation is envisioned. Due to the need to retain the water content in the sample for LAESI ion production, the cell-by-cell imaging of samples with a large number of cells requires an environmental chamber to prevent drying.

Figure 7.1 (a) Optical micrograph of epidermal tissue from purple cultivar of *A. Cepa* showing colorless and pigmented cells. **(b)** Cell-by-cell chemical image based on the intensity of protonated quercetin at nominal m/z 303 superimposed on the microscope image.



A
B

Analysis of smaller cells

Typical eukaryotic cell sizes range from ~ 10 to ~ 100 μm . For example, human erythrocytes, epidermal cells, and neurons are ~ 8 μm , ~ 30 μm and $5\text{-}100$ μm in diameter, respectively. One of the earlier limitations in the analysis of these smaller cells by LAESI-MS was the difficulty in focusing the mid-infrared (IR) laser pulse. Using conventional optics, the focal spot size is limited by the diffraction limit, the divergence of the laser beam and the aberrations of the focusing lens. Using the near field from the etched tip of an optical fiber, the ablated spot size can be reduced beyond the diffraction limit. Indeed, high sensitivity MS in combination with ultraviolet laser ablation using a scanning near-field optical microscopy (SNOM) probe was demonstrated for sample analysis beyond the diffraction limit with a few hundred nanometer lateral resolution.⁷

Currently in LAESI-MS we are not limited by the ablation spot size but by the amount of material presented for the MS analysis. We have successfully demonstrated the analysis of metabolites from a single sea urchin egg with a diameter of 90 μm and with a calculated volume of 382 femtoliters.⁶ The smallest animal cells, e.g., red blood cells at ~ 10 μm , are only one order of magnitude smaller in diameter. However, these 10 μm cells have volume of 524 attoliters, which corresponds to approximately three orders of magnitude less material available for the analysis. The detection of ions from these small volumes by the mass spectrometer remains a challenge. Therefore improving the ion production and collection efficiency is required to analyze the smaller cells.

Gradual reduction in cell sizes can help to map the limits of the current technology. Human skin cells and certain leaf epidermal cells are between 30 and 50 μm in diameter. The volume of a single 50 μm diameter cell is 65 femtoliters, which is only

factor of 6 lower than the currently analyzed smallest volume. As further reductions in the analyzed cell sizes are realized, new classes of tissues become amenable for cell-by-cell inquiry.

Laser Surgery and MS

During surgery the time consuming histological identification of the demarcation between diseased and healthy tissues is often necessary. Takáts *et al.* have recently demonstrated the real time monitoring of lipid ions produced from biological tissues during electrosurgery by using a mass spectrometer.⁸ Exposure to the high-frequency electrical current during electrosurgery produced different lipid ion profiles for a tumor and for the healthy tissue.

Just three years after its invention in 1967, a carbon dioxide laser (10.6 μm), was used to remove corneal tissue.⁹ By the mid-1980s, mid-IR lasers, such as the hydrogen fluoride laser (3.0 μm) and the Er:YAG laser (2.94 μm), were used, to perform corneal incisions in eye surgery and to surgically remove atherosclerotic plaques in human arteries, respectively.^{10, 11} Due to the O-H vibrations, the strongest absorption band of liquid water, the primary constituent of most human tissues, is at 2.94 μm wavelength. The relatively short optical penetration depth of a few micrometers at 2.94 μm wavelength also provides a lower collateral thermal damage, which is desirable in laser surgery.¹² Smaller penetration depth also helps to achieve precise ablation due to the confinement of the deposited laser energy in a small volume. Other factors, however, such as the laser pulse duration and the mechanical properties of the tissue also affect the precision.¹³

The combination of surgical infrared laser ablation methods and LAESI-MS can be utilized to perform laser surgery and simultaneously monitor the metabolic profile of the tissue. Ultimately, the endoscopic visualization and laparoscopic ablation of tissues through fiber optic cables coupled with remote sampling methods can be used to perform minimally invasive mid-IR laser surgery and LAESI-MS identification of tumor boundaries inside the body.

REFERENCES

- (1) Dunn, W. B.; Bailey, N. J. C.; Johnson, H. E. *Analyst* **2005**, *130*, 606-625.
- (2) Han, J.; Danell, R.; Patel, J.; Gumerov, D.; Scarlett, C.; Speir, J.; Parker, C.; Rusyn, I.; Zeisel, S.; Borchers, C. *Metabolomics* **2008**, *4*, 128-140.
- (3) Pan, Z.; Gu, H.; Talaty, N.; Chen, H.; Shanaiah, N.; Hainline, B.; Cooks, R.; Raftery, D. *Analytical and Bioanalytical Chemistry* **2007**, *387*, 539-549.
- (4) Shrestha, B.; Nemes, P.; Nazarian, J.; Hathout, Y.; Hoffman, E. P.; Vertes, A. *Analyst* **2009**, submitted.
- (5) McDonnell, L. A.; Heeren, R. M. A. *Mass Spectrometry Reviews* **2007**, *26*, 606-643.
- (6) Shrestha, B.; Vertes, A. *Analytical Chemistry* **2009**, *81*, 8265-8271.
- (7) Stockle, R.; Setz, P.; Deckert, V.; Lippert, T.; Wokaun, A.; Zenobi, R. *Analytical Chemistry* **2001**, *73*, 1399-1402.
- (8) Schäfer, K.-C.; Dénes, J.; Albrecht, K.; Szaniszló, T.; Balog, J.; Skoumal, R.; Katona, M.; Tóth, M.; Balogh, L.; Takáts, Z. *Angewandte Chemie International Edition* **2009**, *48*, 8240-8242.

- (9) Fine, B. S.; Fine, S.; Peacock, G. R.; Geeraets, W. J.; Klein, E. *American Journal of Ophthalmology* **1967**, *64*, 209.
- (10) Loertscher, H.; Mandelbaum, S.; Parrish, R.; Parel, J. M. *American Journal of Ophthalmology* **1986**, *102*, 217-221.
- (11) Esterowitz, L.; Hoffman, C. A.; Tran, D. C. *Proc. SPIE Optical and Laser Technology in Medicine* **1986**, *605*, 32-36.
- (12) Krasnopoler, A.; George, S. M. *The Journal of Physical Chemistry B* **1998**, *102*, 788-794.
- (13) Apitz, I.; Vogel, A. *Applied Physics A: Materials Science & Processing* **2005**, *81*, 329-338.

BIOGRAPHY

Bindesh Shrestha graduated with a Bachelor of Science degree in chemistry and a Bachelor of Arts in economics from the Moravian College, Pennsylvania, U.S.A., in May of 2003. During college, he served as a teaching assistant and conducted undergraduate research under the supervision of Professor O. Carl Salter, Jr. at the Department of Chemistry of the Moravian College. Prior to college, he finished his high school from National School of Sciences, Kathmandu, Nepal.

In the fall semester of 2004, he enrolled in the Ph.D. program of the Department of Chemistry at the George Washington University, in Washington, D.C., U.S.A. In January 2005, he joined the research group of Professor Akos Vertes.

His research interest included uncovering the fundamentals and developing applications of mass spectrometry-based methods to solve biological problems. In his graduate research projects, he explored the application of mid-infrared laser ablation to study the biomolecular makeup of biological tissues, bodily fluids, and single cells.

He has co-authored 8 research articles. His work has been presented 18 times at national and international conferences. His work has also been featured twice on the cover of *Analytical Chemistry*, the leading journal in his field. Newswire service reports on his work have been featured by numerous media outlets.